MATERIAL AND DEVICE DESIGN FOR ORGANIC PHOTOVOLTAICS

Calvyn T. Howells

A Thesis Submitted for the Degree of PhD
at the
University of St Andrews

2015

MATERIAL AND DEVICE DESIGN FOR ORGANIC PHOTOVOLTAICS

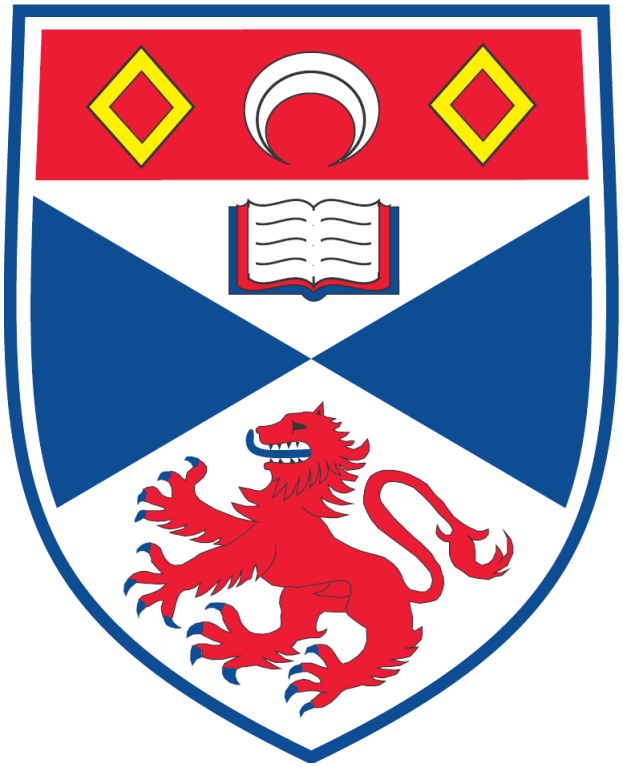

Calvyn T. Howells

A thesis submitted to the School of Physics and Astronomy, University of St Andrews, for the degree of Doctor of Philosophy

September 2014

Abstract

This thesis presents novel materials for photovoltaic conversion. The materials described are solution-processable organic semiconductors and have been used in the fabrication of organic photovoltaic cells (OPVs).

The widely used PEDOT:PSS layer was investigated in P3HT and PTB7 photovoltaics. By doping, the efficiencies recorded were amongst the highest reported in the field using a conventional architecture.

Two low band-gap BODIPY-based polymers were introduced and shown to have properties favourable for optoelectronics. Photovoltaics consisting solely of the polymers as the active component surpassed the performance expected without the use of an acceptor, indicating ambipolar behaviour, which was verified by charge carrier mobility measurements. When blended with an acceptor, the devices demonstrated a short-circuit current density similar to that of P3HT, a well-studied and successful OPV material. They also revealed a broad spectral response and were shown to operate as photodiodes.

Two small molecules containing diketopyrrolopyrrole (DPP) and BODIPY were introduced and characterised. The addition of thiophenes red shifted the absorption but did not result in a sufficient bathochromic shift. Instead, a propensity to aggregate limited the performance. PLQY measurements showed the aggregation to quench luminescence. The study demonstrated the importance of controlling aggregation for efficient devices.

Two solution-processable small molecules with a germanium-bridged spiro centre were investigated, and the molecular, electrochemical and optical properties discussed. The small molecule with shorter conjugation length exhibited an interesting packing motif shown to be favourable for charge transport. The mobility measurements were an order of magnitude higher than those reported for sexithiophene, a small molecule analogue, and the same order of magnitude as P3HT. The two-dimensional charge transporting nature of the material was verified with two independent techniques: time of flight (TOF) and organic field-effect transistor (OFET) measurements. The mobility of the material was found to vary with annealing, a result of morphological changes. These were studied with optical, electron and scanning probe microscopies. By controlling the morphology with the implementation of a well-defined annealing method, it was possible to improve the performance of OFETs and planar-heterojunction OPVs. Solution-processed bulk-heterojunction OPVs were fabricated, characterised and optimised with Ge spiro molecules. A PCE similar to that of P3HT, 2.66 %, was achieved for the one, whilst a PCE of 1.60 % was obtained for the other. The results are encouraging, and there is scope for improvement by increasing the overlap between the absorption and solar spectrum, for example.

Declaration

I, Calvyn T. Howells, hereby certify that this thesis, which is approximately 60,000 words in length, has been written by me, that it is the record of work carried out by me and that it has not been submitted in any previous application for a higher degree.

I was admitted as a research student in September 2009 and as a candidate for the degree of Doctor of Philosophy in September 2009; the higher study for which this is a record was carried out in the University of St Andrews between 2009 and 2013.

Calvyn T. Howells September 26, 2014

I hereby certify that the candidate has fulfilled the conditions of the Resolution and Regulations appropriate for the degree of Doctor of Philosophy in the University of St Andrews and that the candidate is qualified to submit this thesis in application for that degree.

Ifor D. W. Samuel September 26, 2014

Copyright Declaration

In submitting this thesis to the University of St Andrews I understand that I am giving permission for it to be made available for use in accordance with the regulations of the University Library for the time being in force, subject to any copyright vested in the work not being affected thereby. I also understand that the title and the abstract will be published, and that a copy of the work may be made and supplied to any bona fide library or research worker, that my thesis will be electronically accessible for personal or research use unless exempt by award of an embargo as requested below, and that the library has the right to migrate my thesis into new electronic forms as required to ensure continued access to the thesis. I have obtained any third-party copyright permissions that may be required in order to allow such access and migration, or have requested the appropriate embargo below. The following is an agreed request by candidate and supervisor regarding the electronic publication of this thesis: Access to printed copy and electronic publication of thesis through the University of St Andrews.

Calvyn T. Howells September 26, 2014

Ifor D.W. Samuel September 26, 2014

Embargo

The following is an agreed request by candidate and supervisor regarding the electronic publication of this thesis:

Access to all of the printed copy but embargo of all of the electronic publication of thesis for a period of 1 year on the following ground: publication would preclude future publication.

Calvyn T. Howells September 26, 2014

Ifor D.W. Samuel September 26, 2014

Acknowledgements

First and foremost, I would like to thank my supervisor, Professor Ifor D. W. Samuel, and my second supervisor, Dr. Graham Turnbull, for giving me the opportunity to undertake a PhD at the University of St Andrews, and for their invaluable supervision and guidance. St Andrews has been a truly special place to study, from its history and setting to its great lecturers, clubs and community. I feel very fortunate and grateful to have been part of it.

I would like to extend my gratitude to Professor Peter Skabara, an exceptional scientist, genuine person and inspiring man, for being a mentor, collaborator and friend, and encouraging me to continue with the PhD. Furthermore, I would like to thank Professor Skabara's team at the Department of Pure and Applied Chemistry at the University of Strathclyde for fruitful collaborations.

Dr. Iain Wright, thanks for the work on the synthesis and electrochemical characterisation of the germanium-bridged spiro-centred small molecules, and Dr. Anto Regis Inigo, thanks for the work on the organic field-effect (OFET) transistors and atomic force microscopy. Dr. Pascal Andre, thank you for allowing me to be part of an interesting project and having faith in my work. Dr. Diego Cortizo Lacalle, I thoroughly enjoyed working with you, thank you for the synthesis and electrochemical characterisation of the BODIPY-based conjugated polymers, and small molecules containing BODIPY and DPP. To project student Khalid Marbou, the world needs more scientists like you! I have no doubt you will make a great contribution to science. And to Stuart Thomson, thank you for all your hard work with the time of flight (TOF) measurements.

To my colleagues, thank you for putting up with my eccentricities. Dr. Gordon J. Hedley you are a brilliant scientist and good friend. Thank you ever so much for involving me in interesting science, it was a pleasure working with you. Dr. Arvydas Ruseckas thank you for providing me with interesting insights, different perspectives and motivating me by showing an interest in my work and believing that it is important. Thanks to Dr. Ashu Bansal for making me persevere and not give up, and for being a strong role model. I admire your work ethic, dedication to your family and friends and kindness. Dr. Ajay Pandey, thank you for introducing me to organic solar cells and Dr. Yue Wang, thanks for helping me learn how to use the AFM. Dr. Salvatore Gambino, many thanks for the time of flight (TOF) measurements, and Scott Pearson

and Zarifi Masri, thank you both for sending me interesting and relevant papers. Dr. Georgios Tsiminis, thanks for all the laughs and consistently putting life into context. Dr. Jack Levell, thank you for your encouragement, and Dr. Paul Dalgarno, I think you are OK despite your bizarre taste in music and t-shirts. To Dr Emiliano Rexende Martins, though none of our ideas worked despite their sound methodology, thanks for divulging in them with me. Alexander Ward, always a great one for a good debate, I admire you very much as a scientist. Amy Illingworth, you showed me so much and helped me through the early years of my PhD, from the bottom of my heart, I wish you every success in life. Bernd Ebenhoch, what can I say? Thank you so much for assisting me in developing the solar cell lab, I was sad to only have it like I wanted towards the end, but that is science! Olena Kulyk and Guy Whitworth, thank you for limiting the damage done by me to mankind. Olena, you are an amazing person, keep going and do not give up! As Winston Churchill eloquently said, *"If you are going through hell, keep going!"*

A special thanks to my friends for all the help, support and encouragement provided throughout the course of my degree. In particular, I extend heartfelt thanks to David Barlow, for your handsome face and always being there. John and Ryan Taney, for your crazy antics and showing me a good time. Laura Robinson, for all the movie nights and memorable party planning. Camille Bilger, for your genuineness and friendship. Olena Kulyk and Guy Whitworth, "… all for one, one for all - that is our motto, is it not?". You two go beyond colleagues and I know our friendship will be life-long. Also the most sincere thanks is due to Major Paul Veenhuizen of Earlshall Castle and Dr. Minou Foadi M.D., for altering my perspective on what truly matters and what I want out of this life. Paul, I hope to own my own castle one day. Minou, your strength knows no bounds! I have learned so much from your outlook on life. Thank you.

Last but not least, this thesis would not have been possible without the support of my family. Karen, Alan, Conner, and Violet and Graham, thanks for everything. I can promise you this rollercoaster is now over and that my time as a student has now truly come to an end! Thanks as well to the soon to be new members of my family, the Van Eerde's. Christa, thanks for your patience and faith in me. Here is to LIVING once again!

Publications Arising from this Work

- Calvyn T. Howells, Khalid Marbou, Haeri Kim, Seiichi Furukawa, Aiko Nakao, Tetsuya Aoyama, Ju-Hyung Kim, Masanobu Uchiyama, Chihaya Adachi, Jeong-Weon Wu, Dong-Wook Kim, Jean-Charles Ribierre, Ifor D.W. Samuel and Pascal Andre. Enhanced Solar Cells Efficiency through Conjugated Polymer Morphology Alteration driven by Fluorinated Doped PEDOT-PSS. Article submitted.

- Diego Cortizo-Lacalle, Calvyn T. Howells, Upendra K. Pandey, Joseph Cameron, Neil J. Findlay, Anto R. Inigo, Tell Tuttle, Peter J. Skabara and Ifor D. W. Samuel. Solution processable Diketopyrrolopyrrole (DPP) cored small molecules with BODIPY end groups as novel donors for organic solar cells. Beilstein Journal of Organic Chemistry.
Article published: November 2014.

- Gordon J. Hedley, Alexander J. Ward, Alexander Alekseev, Calvyn T. Howells, Emiliano R. Martins, Luis Antonio Serrano González, Graeme Cooke, Arvydas Ruseckas and Ifor D. W. Samuel. Determining the optimum morphology in high-performance polymer-fullerene organic photovoltaic cells. Nature communications.
Article published: December 2013.

- Sasikumar Arumugam, Iain A. Wright, Anto R. Inigo, Salvatore Gambino, Calvyn T. Howells, Alexander L. Kanibolotsky, Peter J. Skabara and Ifor D. W. Samuel. Charge transport in a two-dimensional molecular organic semiconductor. Journal of Material Chemistry C.
Article published: November 2013.

- Diego Cortizo-Lacalle, Calvyn T. Howells, Salvatore Gambino, Filipe Vilela, Zuzana Vobecka, Neil J. Findlay, Anto R. Inigo, Stuart A. J. Thomson, Peter J. Skabara and Ifor D. W. Samuel. BODIPY-based conjugated polymers for broadband light sensing and harvesting applications. Journal of Material Chemistry.
Article published: June 2012.

- Dr. Iain A. Wright, Dr. Alexander L. Kanibolotsky, Joseph Cameron, Dr. Tell Tuttle, Prof. Dr. Peter J. Skabara, Dr. Simon J. Coles, Calvyn T. Howells, Stuart A. J. Thomson, Dr. Salvatore Gambino, Prof. Dr. Ifor D. W. Samuel. Oligothiophene Cruciform with a Germanium Spiro Center: A Promising Material for Organic Photovoltaics. Angewandte Chemie International Edition.
Article published: March 2012.

To my parents, Alan and Karen, thank you for everything. To my brother, Conner, there are no prizes for second place.

"You, the people have the power - the power to create machines. The power to create happiness! You, the people, have the power to make this life free and beautiful, to make this life a wonderful adventure."

-Charlie Chaplin, The Great Dictator

Contents

Chapter 1
Introduction 1
1.1 References 7
Chapter 2
Theory of organic semiconductors 9
2.1 Introduction 9
2.2 Organic semiconductors 10
2.2.1 Electronic properties 13
2.2.2 Optical properties 20
2.3 Organic semiconducting devices 24
2.4 Conclusion 31
2.5 References 32
Chapter 3
Organic photovoltaics 36
3.1 Introduction 36
3.2 Principles of operation 37
3.3 Performance parameters 43
3.4 Device design 45
3.5 Conclusion 47
3.6 References 48
Chapter 4
Experimental methods 51
4.1 Introduction 51
4.2 Absorption and photoluminescence spectroscopy 51
4.3 Photoluminescence quantum yield 53
4.4 Time-resolved luminescence 54
4.5 Contact angle measurements 55
4.6 Conductivity measurements 56
4.7 Photovoltaic fabrication and characterisation 57
4.8 References 64

Chapter 5
Photovoltaic efficiency enhancement by fluorinated doped PEDOT:PSS... 65
Overview ... 65
5.1 Introduction ... 66
5.2 Materials ... 67
5.2.1 Molecular structures ... 68
5.2.2 Electrochemical and optical properties ... 69
5.3 Photovoltaic cells ... 77
5.3.1 Experimental methods ... 78
5.3.2 Materials ... 79
5.3.3 Optimisation ... 79
5.3.4 Characterisation ... 84
5.4 Conclusion ... 88
5.5 Appendix ... 90
5.6 References ... 100
Chapter 6
BODIPY-based conjugated polymers for broadband light sensing and solar energy harvesting ... 104
Overview ... 104
6.1 Introduction ... 105
6.2 Materials-Polymers ... 106
6.2.1 Molecular structures ... 108
6.2.2 Electrochemical and optical properties ... 109
6.3 Polymer OPVs ... 110
6.3.1 Fabrication ... 112
6.3.2 Optimisation ... 116
6.3.3 Characterisation ... 121
6.4 Conclusion ... 129
6.5 Appendix ... 130
6.6 References ... 132
Chapter 7
BODIPY-based solution-processable small molecules with a DPP core for organic photovoltaics ... 135
Overview ... 135

7.1 Introduction 136
7.2 Materials-Small molecules 137
7.2.1 Molecular structures 138
7.2.2 Electrochemical and optical properties 139
7.3 Small molecule OPVs 144
7.3.1 Fabrication 145
7.3.2 Optimisation 146
7.3.3 Characterisation 148
7.4 Conclusion 154
7.5 Appendix 156
7.6 References 157

Chapter 8

Oligothiophene with a Germanium Spiro-centre: A promising photovoltaic material with a fascinating packing motif 160

Overview 160
8.1 Introduction 161
8.2 Materials 163
8.2.1 Molecular structures 165
8.2.2 Electrochemical and optical properties 167
8.2.3 Stacking in mutually orthogonal directions 169
8.3 Mobility measurements 170
8.3.1 Morphological studies 174
8.4 Planar heterojunctions 178
8.4.1 Fabrication 180
8.4.2 Characterisation 182
8.5 Bulk heterojunctions 185
8.5.1 Fabrication 186
8.5.2 Optimisation 188
8.5.3 Characterisation 202
8.6 Time-resolved photophysics 206
8.7 Conclusions 212
8.8 Appendix 214
8.9 References 224

Chapter 9
Conclusion 230
9.1 References 237

Chapter 1

Introduction

As the human population grows [1] so too does the global demand for energy [2]. To ensure economic growth and political stability it is important that we not only satisfy this demand, but that we do it, without destroying the environment. Renewable technologies have the capability of harnessing energy from the natural world without or with low emission of harmful pollutants. Developing this technology will help reduce humanity's dependence on fossil fuels and tackle climate change [3]. A plethora of technologies are available. These include: wind, geothermal, solar thermal, solar photovoltaic energy, and hydroelectricity.

The focus of this thesis is on the topic of photovoltaics: a promising renewable technology that converts sunlight into electricity - the photovoltaic effect. The conversion, was discovered by the physicist, A. E. Becquerel, in 1839 whilst investigating liquid electrolytes [4]. However, photovoltaic cells were only realised as a feasible technology in 1954 when Chapin et al. demonstrated a silicon-based photovoltaic cell with power conversion efficiency (PCE) of 6 % [5]. Since, photovoltaic cells have found many applications in the market place [6-8], and with the energy crisis and growing demand for clean and sustainable energy there is now considerable interest in developing photovoltaics for energy production [9].

The sun is the most significant source of renewable energy. It delivers more energy to the Earth in one hour than all the energy consumed in a year [9]. If we employed the technology currently available for solar energy harvesting, taking into account the practical limitations, we would be able to generate more than 3 times the world's primary energy consumption [10]. However, the cost of implementing the technology on a large scale is too expensive. Hence, photovoltaic technologies account for less than 0.1 % of energy production [11].

Therefore, for photovoltaics to become competitive with fossil fuels, work needs to be done on reducing the cost of the technology. The present solar cell market is 99 % based on inorganic silicon wafers [11]. The assembly, i.e. fabrication, and amount of absorbing material and infrastructure required for these photovoltaics cells, are where the costs arise [12].

It is for this reason that in the last two decades or so there has been significant interest amongst the research community to develop thin-film photovoltaic technologies [13]. These, so called second-generation photovoltaics

are based on inorganic semiconducting materials, but require less absorbing material than the first-generation and can be processed on large area substrates. Second-generation photovoltaics include but are not exclusive to: amorphous silicon (a-Si), cadmium telluride (CdTe), copper indium selenide (CIS) and copper indium gallium selenide (CIGS). These photovoltaic cells show promising performance with typical PCEs between 10-16 % [14]. However, vacuum and high temperature processing makes large scale implementation of the aforementioned technology challenging. Additionally, some of these photovoltaic devices rely on scarce and or toxic elements in their manufacture. [12].

The search for novel materials that are plentiful, low cost in their manufacture and require limited infrastructure to implement [9] has resulted in the development of organic semiconductors for applications in photovoltaics. Organic photovoltaics, which are the focus of this thesis, are often referred to as the third-generation. However, the third-generation includes all device types that do not operate by means of conventional single p-n junctions, so also including dye-sensitized [15], multijunction [16] and hybrid technologies [17].

Organic semiconducting materials have energy levels that correspond to the UV-VIS spectrum and have many advantages over their inorganic counterparts. These include: (i) low fabrication costs, as they are solution-processable and do not require high-temperature processing, which means, they can be manufactured in bulk using well-established manufacturing techniques, for example ink-jet printing and roll-to-roll processing; (ii) high absorption coefficients allow for the fabrication of efficient devices with limited material; (iii) and ease of chemical engineering permits the investigation of a seemingly endless number of semiconducting materials [18]. Furthermore, it is possible to fabricate light-weight and flexible photovoltaics with these materials. That said the most attractive feature is the ability to fabricate modules by means of roll-to-roll processing. There are a wide variety of techniques for example slot die, gravure, spray, screen and others that have been used for OPV production [19]; however, lifetimes prevent their implementation on an industrial scale.

Organic photovoltaics have achieved efficiencies beyond 9 % (single junction) [20] and up to 12 % (tandem) [21]. If we can solve the issue with the lifetimes, it would be possible to roll-out the technology on a large scale. For example, a single assembly line can produce approximately 100 000 m^2 of film per day, and if we were to assume an efficiency of 5 % (50 W m^{-2}), which equates to 5 MW a day, a single printing press would be able to produce over 1 GW a year [19, 22, 23].

There are three main categories of organic semiconductors: small molecules, dendrimers, and polymers. The choice of semiconducting material is largely dependent on the application. As this thesis is on the topic of photovoltaics, it will focus on the use of small molecules and polymers. That is not necessarily to say that it is not possible to fabricate photovoltaics with dendrimers [24]. However, for reasons which will be apparent in due course, small molecules and polymers are the preferred choices.

The first observation of an organic compound (anthracene) exhibiting semiconducting behaviour was reported in 1906 by Pochettino [25]. Although, the photoconductivity properties of poly(N-vinyl-carbazole) (PVK) were reported in 1957 [26], it was the discovery of the conductive properties of polyacetylene [27] that propelled the study of electronically active polymers. Previously, polymers were thought only to have non-conductive applications such as electrical and thermal insulators. Since, they, along with small molecules, have been employed as light emitters [28], sensors [29], optical amplifiers [30] and photovoltaics [31].

The field of organic photovoltaics is interesting and fast moving [21, 32]. Whilst significant progress has been made in our understanding of the underlying science governing device operation, there are still many unanswered questions. The reason for this is that the field is comparatively new in relation to inorganics and the operational principle of organic photovoltaics is different. Hence, while some of the theory is analogous, some of it is not applicable. A good example is the nature of optically excited states. On absorption, in an organic semiconductor, there is the formation of an exciton, i.e. a coulombically bound electron-hole pair with typical binding energies $\geq$ 500 meV [33, 34], whilst inorganic semiconductors have binding energies of a few meV [12]. Therefore, inorganic semiconductors have the ability to generate an electrical current on absorption, whereas for organic semiconductors to readily generate an electrical current it is necessary to dissociate the excitons into free charge carriers. Fortunately, the incorporation of an electron acceptor, typically a fullerene derivative, efficiently dissociates the excitons [35]. This is but one of many differences between inorganic and organic photovoltaics which impact on the material and device design. As a result there is significant interest in improving organic photovoltaic performance by developing new materials and device architectures [20, 36-39].

A conventional organic photovoltaic (OPV) cell consists of an electron donor and acceptor. The donor is typically a conjugated polymer and the acceptor is usually a fullerene derivative. The absorption of light occurs largely in the donor with the formation of an exciton. For the exciton to contribute to

photocurrent it is necessary for it to diffuse to the donor-acceptor interface within the exciton diffusion length (L_D) [40]. Here, exciton dissociation, i.e. the separation of charge occurs. After which the electron and hole are transported through the acceptor and donor phases to the electrodes, respectively. To ensure efficient OPVs it is necessary to blend the donor and acceptor, therefore ensuring the excitons can reach the donor-acceptor interface within the exciton diffusion length (L_D) [41, 42].

The majority of progress in the field of organic photovoltaics has resulted from investigating new materials and improving device design. This is not to say that investigating the fundamentals is not important. They are extremely significant in developing our understanding of the principles behind OPV operation. However, these are usually carried out retrospectively on proven materials. There will come a time when the aforementioned will facilitate the development of measurements to filter undesirable materials for OPV applications. But until then, the real test of a material is to investigate its performance in an OPV device.

In this thesis I present novel materials for organic photovoltaic applications. The materials are used for photovoltaic conversion (electron donors) or to improve device design. I discuss their molecular, electrochemical and optical properties. In addition, I fabricate, characterise and optimise OPVs with the materials and investigate their film forming properties i.e. morphology with a wide variety of photophysical and microscopic techniques.

This thesis consists of eight parts, chapters 2-9, in addition to this introduction. In Chapter 2, I present an overview of the theory of organic semiconductors and discuss their electronic and optical properties in addition to their applications in optoelectronics. In Chapter 3, I review the literature on organic photovoltaics and present the principles of operation. I briefly mention the performance parameters and how they are extracted from the characterisation, and discuss how the material properties impact device performance. In doing so, I highlight the current obstacles organic photovoltaics face in commercialisation. In Chapter 4, the experimental methods used to investigate the optical and electronic properties of the materials are presented along with microscopic techniques used to investigate film morphology. Additionally, the fabrication and characterisation of organic photovoltaic cells are described.

The first experimental chapter of the thesis is Chapter 5. In this chapter, I discuss the importance of controlling bulk-heterojunction morphology for achieving efficient solution-processable organic photovoltaic cells, and describe how the performance of these optimal OPVs can be enhanced by

altering the anode interlayer, poly(3,4-ethylenedioxylenethiophene): poly(styrenesulfonate) (PEDOT:PSS) by means of doping with either a sulfonic acid surfactant (PFOS) or a sulfonic fluorinated ionomer (PFI). A 15 % increase in efficiency is observed for two different types of organic photovoltaic cell, the well-studied poly(3-hexylthiophene): [6,6]-phenyl-C_{61}-butyric acid methyl ester (P3HT:PC_{61}BM) and the lesser studied but highly efficient poly[4,8-bis[(2-ethylhexyl)oxy]benzo[1,2-b:4,5-b']dithiophene-2,6-diyl][3-fluoro-2-[(2ethyl-hexyl)carbonyl]thieno[3,4-b]-thiophenediyl] (PTB7) in combination with PC_{71}BM. Whilst, a similar increase in performance is observed for both cell types, I provide evidence and suggest that the main mechanism behind the increase in performance is different for each cell type. I describe the properties of these two doping agents, and to understand the reason for the observed increase in OPV performance, the properties of the PEDOT:PSS interlayer are investigated upon doping. These studies include but are not exclusive to: wettability, conductivity and work function. I also present results of a degradation study on P3HT:PC_{61}BM OPVs fabricated with the anode interlayer doped with PFI and discuss the implications.

In Chapter 6, I introduce two 4, 4-difluoro-4-bora-3a, 4a-diaz-s-indacene BODIPY-based conjugated polymers, elucidate their optoelectronic properties, and demonstrate their use for broad band light sensing and solar energy harvesting by means of fabricating photodiodes and photovoltaics, respectively. Chapters 7 and 8 focus on solution-processable small molecules for bulk-heterojunction photovoltaics. In Chapter 7, I further discuss the advantages small molecules have over conjugated polymers and mention the difficulties in implementing them in solution-processable bulk-heterojunction OPVs, which I demonstrate with small molecules containing diketopyrrolopyrrole (DPP) and BODIPY. The small molecules are fully characterised and are unfortunately shown to have PCEs less than 1 %. However, this was an extremely ambitious project, incorporating two compounds, successfully demonstrated for OPV applications into a single small molecule.

A small molecule with a germanium-bridged spiro-centre is introduced in Chapter 8. I discuss the properties of this material in great detail as the chemical structure is extremely interesting and enables the molecule to pack in a way that is favourable for charge transport and by extension device performance. The multi-dimensional charge transport properties, achieved through the three-dimensional packing motif are verified with two independent techniques, time of flight (TOF) and organic field-effect transistor (OFET) measurements. These techniques, measure the charge carrier mobility perpendicular and parallel to the film, respectively. The mobility of the

compound is shown to be superior to several other compounds. Additionally, when compared with results reported for linear analogues in the literature, the results are impressive. The mobility is an order of magnitude greater than that reported for sexithiophene [43] and the same order of magnitude as the conjugated polymer P3HT [44, 45]. The mobility of the compound was found to vary with annealing and shown to be concomitant with changes in morphology. By controlling this morphology, I show that it is possible to improve device performance. Finally, I demonstrate OPVs with PCEs similar to P3HT:$PC_{61}BM$ without thermal annealing. A similar compound with an extended conjugation length was studied, however a lower PCE was observed.

1.1 References

1. USCB, *U.S. and World Population Clock.* http://www.census.gov/popclock/ 2010 Census data and the most recent national population estimates.
2. Howells, M., et al., *Integrated analysis of climate change, land-use, energy and water strategies.* Nature Clim. Change, 2013. **3**(7): p. 621-626.
3. Luthi, D., et al., *High-resolution carbon dioxide concentration record 650,000-800,000[thinsp]years before present.* Nature, 2008. **453**(7193): p. 379-382.
4. Becquerel, A.E., *Mémoire sur les effets électriques produits sous l'influence des rayons solaires.* C. R. Acad. Sci., 1839. **9**(561-567).
5. Chapin, D.M., C.S. Fuller, and G.L. Pearson, *A New Silicon p-n Junction Photocell for Converting Solar Radiation into Electrical Power.* Journal of Applied Physics, 1954. **25**(5): p. 676-677.
6. Wurfel, P., *Physics of Solar Cells.* Wiley VCH, 2005.
7. Green, M.A., *Solar Cells.* The University of New South Wales, Kensington, Australia, 1998.
8. Bube, R.H., *Photovoltaic Materials.* Imperial College Press, 1998.
9. Lewis, N.S., et al., *Basic Research Needs for Solar Energy Utilization. Report of the Basic Energy Sciences Workshop on Solar Energy Utilization, April 18-21, 2005*, 2005. p. Medium: ED.
10. Arvizu, D.e.a., *In IPCC Special Report on Renewable Energy Sources and Climate Change Mitigation.* Cambridge University Press: Cambridge, U. K. and New York, NY, USA, 2011.
11. BERNÈDE, J.C., *ORGANIC PHOTOVOLTAIC CELLS: HISTORY, PRINCIPLE AND TECHNIQUES.* Journal of the Chilean Chemical Society, 2008. **53**: p. 1549-1564.
12. Kippelen, B. and J.-L. Bredas, *Organic photovoltaics.* Energy & Environmental Science, 2009. **2**(3): p. 251-261.
13. Hegedus, S., *Thin film solar modules: the low cost, high throughput and versatile alternative to Si wafers.* Progress in Photovoltaics: Research and Applications, 2006. **14**(5): p. 393-411.
14. Hamakawa, Y., *Thin-Film Solar Cells: Next Generation Photovoltaics and Its Applications.* Springer Science & Business Media, 2004.
15. Gratzel, M., *Photoelectrochemical cells.* Nature, 2001. **414**(6861): p. 338-344.
16. Dimroth, F. and S. Kurtz, *High-Efficiency Multijunction Solar Cells.* MRS Bulletin, 2007. **32**(03): p. 230-235.
17. Huynh, W.U., J.J. Dittmer, and A.P. Alivisatos, *Hybrid Nanorod-Polymer Solar Cells.* Science, 2002. **295**(5564): p. 2425-2427.
18. Mishra, A. and P. Bäuerle, *Small Molecule Organic Semiconductors on the Move: Promises for Future Solar Energy Technology.* Angewandte Chemie International Edition, 2012. **51**(9): p. 2020-2067.
19. Ameri, T., N. Li, and C.J. Brabec, *Highly efficient organic tandem solar cells: a follow up review.* Energy & Environmental Science, 2013. **6**(8): p. 2390-2413.
20. He, Z., Zhong, Chengmei, Su, Shijian, Xu, Miao, Wu, Hongbin, Cao, Yong, *Enhanced power-conversion efficiency in polymer solar cells using an inverted device structure.* Nat Photon, 2012(591–595
).
21. *Heliatek consolidates its technology leadership by establishing a new world record for organic solar technology with a cell efficiency of 12%.* Press release, 2013.
22. Brabec, C.J. and J.R. Durrant, *Solution-Processed Organic Solar Cells.* MRS Bulletin, 2008. **33**(07): p. 670-675.
23. Brabec, C.J., et al., *Production Aspects of Organic Photovoltaics and Their Impact on the Commercialization of Devices.* MRS Bulletin, 2005. **30**(01): p. 50-52.

24. Ma, C.-Q., et al., *Solution-Processed Bulk-Heterojunction Solar Cells Based on Monodisperse Dendritic Oligothiophenes.* Advanced Functional Materials, 2008. **18**(20): p. 3323-3331.
25. Pochettino, A., *Acad. Lincei Rend.* 1906. **15**: p. 355.
26. Hoegl, H., *On Photoelectric Effects in Polymers and Their Sensitization by Dopants1.* The Journal of Physical Chemistry, 1965. **69**(3): p. 755-766.
27. Shirakawa, H., et al., *Synthesis of electrically conducting organic polymers: halogen derivatives of polyacetylene, (CH).* Journal of the Chemical Society, Chemical Communications, 1977. **0**(16): p. 578-580.
28. Friend, R.H., et al., *Electroluminescence in conjugated polymers.* Nature, 1999. **397**(6715): p. 121-128.
29. Harrison, M.G., J. Grüner, and G.C.W. Spencer, *Analysis of the photocurrent action spectra of MEH-PPV polymer photodiodes.* Physical Review B, 1997. **55**(12): p. 7831.
30. Ribierre, J.C., et al., *Amplified spontaneous emission and lasing properties of bisfluorene-cored dendrimers.* Applied Physics Letters, 2007. **91**(8): p. -.
31. Tang, C.W., *Two-layer organic photovoltaic cell.* Applied Physics Letters, 1986. **48**(2): p. 183-185.
32. Liu, Y., et al., *Solution-processed small-molecule solar cells: breaking the 10% power conversion efficiency.* Sci. Rep., 2013. **3**.
33. Alvarado, S.F., et al., *Direct Determination of the Exciton Binding Energy of Conjugated Polymers Using a Scanning Tunneling Microscope.* Physical Review Letters, 1998. **81**(5): p. 1082-1085.
34. Brédas, J.-L., J. Cornil, and A.J. Heeger, *The exciton binding energy in luminescent conjugated polymers.* Advanced Materials, 1996. **8**(5): p. 447-452.
35. Sariciftci, N.S., et al., *PHOTOINDUCED ELECTRON-TRANSFER FROM A CONDUCTING POLYMER TO BUCKMINSTERFULLERENE.* Science, 1992. **258**(5087): p. 1474-1476.
36. Luhman, W.A. and R.J. Holmes, *Enhanced exciton diffusion in an organic photovoltaic cell by energy transfer using a phosphorescent sensitizer.* Applied Physics Letters, 2009. **94**(15): p. 153304.
37. Morfa, A.J., et al., *Plasmon-enhanced solar energy conversion in organic bulk heterojunction photovoltaics.* Applied Physics Letters, 2008. **92**(1): p. 013504-013504-3.
38. Lampande, R., et al., *A highly efficient transition metal oxide layer for hole extraction and transport in inverted polymer bulk heterojunction solar cells.* Journal of Materials Chemistry A, 2013. **1**(23): p. 6895-6900.
39. Sista, S., et al., *Highly Efficient Tandem Polymer Photovoltaic Cells.* Advanced Materials, 2009. **9999**(9999): p. NA.
40. Shaw, P.E., A. Ruseckas, and I.D.W. Samuel, *Exciton Diffusion Measurements in Poly(3-hexylthiophene).* Advanced Materials, 2008. **20**(18): p. 3516-3520.
41. Yu, G., et al., *POLYMER PHOTOVOLTAIC CELLS - ENHANCED EFFICIENCIES VIA A NETWORK OF INTERNAL DONOR-ACCEPTOR HETEROJUNCTIONS.* Science, 1995. **270**(5243): p. 1789-1791.
42. Halls, J.J.M., et al., *Efficient photodiodes from interpenetrating polymer networks.* Nature, 1995. **376**(6540): p. 498-500.
43. Delannoy, P., et al., *Transient electroluminescence of monolayer and bilayer sexithiophene diodes.* Synthetic Metals, 1994. **67**(1–3): p. 197-200.
44. Mozer, A.J., et al., *Charge carrier mobility in regioregular poly(3-hexylthiophene) probed by transient conductivity techniques: A comparative study.* Physical Review B, 2005. **71**(3): p. 035214.
45. Binh, N.T., L.Q. Minh, and H. Bässler, *Photoconduction in poly(3-alkylthiophene) II. Charge transport.* Synthetic Metals, 1993. **58**(1): p. 39-50.

Chapter 2

Theory of organic semiconductors

2.1 Introduction

If you were asked to describe modern day electronics in one word, what word would you choose? At a guess, I would say you decided on "semiconductor" and if not then how about "silicon". It is no secret that semiconductors are the very foundation of modern electronics. Continual developments in the semiconductor industry over the course of several decades have completely changed the way in which we live our lives, work and communicate. This is to such an extent that for many of us there is not a single day that goes by without some interaction with a device containing a semiconductor. Semiconductors have a wide variety of applications including transistors, integrated circuits and optoelectronics. As the name suggests, a semiconductor exhibits electrical conductivity in between that of a conductor and an insulator. The properties of a semiconducting material, i.e. electrical conductivity can be altered by means of doping etc. The reason for this behaviour is due to semiconductors having a band gap, i.e. an energy gap where no electronic states are allowed to exist. Therefore, in order to, for example conduct electricity, a sufficient amount of energy is required to excite the charge carriers from the valence band, across the energy gap and into the conduction band. An interesting property which allows semiconductors to be used in a wide variety of applications is the various and indeed many forms of energy that can be used for excitation. These include optical, electrical and thermal excitation. The majority of technologies rely on inorganic semiconductors. Considering the periodic table, these include a few of the Group IV elements, i.e. silicon (Si), germanium (Ge) etc. They can also include combinations of certain elements from different Groups, i.e. II and VI, IV and VI and III and V i.e. gallium arsenide (GaAs) etc. In the past three decades or so there has been significant interest amongst the research community in developing organic materials as semiconductors and implementing them in technologies [1-4].

I begin this chapter, by further discussing the advantages organic semiconductors have over their inorganic counterparts and availability as small molecules, dendrimers and conjugated polymers. In addition, I discuss how the choice of conjugated system is dependent on the desired technological application as each conjugated system has unique characteristics. I present

some of the theory of organic semiconductors. In doing so, I demonstrate the aforementioned as functional electronic materials with optical properties that make them favourable for various technological applications. Additionally, I show that although organic semiconductors can be used in the fabrication of devices, some of which are similar to those fabricated with inorganic semiconductors, organic semiconductors are molecularly, structurally, electronically and optically very different.

2.2 Organic semiconductors

What makes organic, i.e. carbon (nitrogen, oxygen or sulphur) based systems a promising semiconductor technology is largely related to their synthesis. In contrast with the rigidity of crystalline inorganic semiconductors, organic semiconductors exhibit chemical docility. The ease of which these systems can be synthesised combined with their tuneable nature allows them to be used in a wide variety of technologies with interesting properties. With a growing interest in organic semiconductors new applications for these systems are being discovered. At present, they are largely used for organic field-effect transistors (OFETs) [5-7], photovoltaics (OPVs) [4, 8-11], light-emitting diodes (OLEDs) [12-14], optical amplifiers [15] and sensors [16, 17]. In addition to the chemical properties, their electronic, optical and mechanical properties, enables technology with a difference. Organic semiconductors can be easily synthesised for a desired application and deposited using conventional deposition techniques, i.e. vacuum deposition, but they are also solution-processable, enabling their deposition by means of ink-jet printing and roll to roll processing. Hence, they can be used in the high volume fabrication of large area, lightweight and flexible devices, for example photovoltaics. Furthermore, as they are solution-processable and don't require high temperature processing they are low cost and can be deposited on a wide variety of substrates, which include paper and plastic. This also means that they can have very low energy of manufacture.

In the previous chapter, I discussed the possibility of a single printing press being able to produce over 1 GW of power a year [18-20], and how this can only be realised, once we have solved the issues related to OPV lifetime. As soon as we have a solution to this problem, the next challenge would be to roll-out the technology on an industrial scale to reduce the cost. This would make organic photovoltaics competitive with other technologies such as inorganic photovoltaics, hydro, wind and biomass [21]. To get an idea of the cost, we begin by comparing Indium-Tin Oxide (ITO) with HC (highly conductive) PEDOT:PSS.

Indium-Tin Oxide is a transparent conductor widely used in display technologies and organic photovoltaics. It is an expensive material as it uses the rare earth metal Indium and is typically deposited using energy intensive techniques, for example vacuum sputtering. PEDOT:PSS is a solution-processable conductive polymer manufactured on an industrial scale. The properties of the material for example the conductivity are easily tuneable by means of doping with solvents such as DMSO, ethylene glycol, diethylene glycol etc. In doing so, it is possible to achieve sheet resistances comparable to that of ITO [22, 23]. Furthermore, ITO-free organic photovoltaics can exhibit PCEs similar to those fabricated with ITO [24, 25]. The cost of using ITO in an OPV ranges from €14.64 to €65.50 per m^2 compared with €8.63 to €9.79 per m^2 for HC-PEDOT:PSS. These estimates include the cost of the PET substrate, €8.52 per m^2. Therefore, the cost of HC-PEDOT:PSS ranges from €0.11 to €1.27 per m^2 [22, 26]. The total material cost for a P3HT:PC_{61}BM photovoltaic fabricated using the same procedure in [26] ranges from €40.71 to €154.70 per m^2. These results show that the cost of a mass produced conjugated polymer can be inexpensive, and that a significant portion of the total material cost of a P3HT:PC_{61}BM module is due to the use of ITO.

If we are to estimate the potential cost of the technology, it is logical to assume any future technology would have the ITO replaced with an organic alternative, for example HC-PEDOT:PSS. We will now look at the total cost of implementing the technology on three different scales kW (current), 100 MW (scaled-up) and 100 GW (industrial) and compare these costs with inorganic photovoltaics. It is not uncommon for the cost of a photovoltaic technology to be expressed in terms of € per W_p. The conversion from € per m^2 is accomplished by dividing the cost, by the geometric fill factor (GFF), illumination intensity (1000 Wm^{-2}) and power conversion efficiency (PCE). The modules we will be considering are based on P3HT:PC_{61}BM, a well-studied organic photovoltaic combination. The cost analysis summarised here is from [21, 26]. It is worth mentioning that even though we have replaced the ITO with a low-cost alternative, the majority of the total material cost is for the electrodes. In the said cost analysis organic photovoltaics are produced by means of roll-to-roll processing [27, 28]. In doing so, the processing costs are negligible [21]. Therefore, in our comparison we need only compare material costs in order to estimate the cost of implementing the technology.

The cost of producing an organic photovoltaic technology today (kW) ranges from €1.2 to €3.9 per W_p. This estimate is for P3HT:PC_{61}BM (single junction) devices with power conversion efficiencies (PCEs) between 2 and 6.5

%, and a GFF of 37 %. The estimate is accurate as the analysis takes into consideration current material costs and achievable PCEs and GFF. If we consider the active components of the device, including the solvents required for fabrication, the majority of the cost, results from using Ag as an electrode. Replacing the Ag electrodes with Al or a carbon alternative would result in a cost reduction of 77 % or 90 % for the electrodes, respectively [21]. Therefore, the cost of the electrodes can be excluded when up scaling to 100 MW or 100 GW (industrial), as the active layer accounts for the majority of the total cost of the photovoltaic cell. The current cost of $PC_{61}BM$ is approximately €70 per g, this is over 60 % more expensive than P3HT. Experts believe the cost of $PC_{61}BM$ to be approximately €20 or €10 per g for scaled up or industrial scenarios, respectively [21]. It is likely that the future cost of P3HT will be under that of $PC_{61}BM$, nevertheless, if we assume a similar cost for both materials, the total cost for the scaled up scenario, i.e. 100 MW would be approximately €1.31 per m^2. Using the aforementioned PCEs and a GFF of 75 %, which is a result of up scaling and optimising the printing process, the overall cost for an organic photovoltaic will be between €0.03 and €0.09 per W_p. On an industrial scale a GFF of 98 % can be achieved with laser ablation, a process compatible with roll to roll processing [21, 29, 30]. With an approximate material cost of €0.66 per m^2, a module would cost between €0.01 and €0.03 per W_p. If we were able to roll-out a 10 % technology, a module may cost as little as €0.007 per W_p. To put all of this into perspective we consider the early roof program in Germany. Here, customers had to pay €13 per W_p in 1990. By 2000 the cost had decreased to €8 per W_p. Looking forward, assuming an annual decrease of around 5 % holds, in the near future we can expect for crystalline silicon, module costs of about €2 per W_p [31]. In a similar time frame, we can expect costs of €0.95 per W_p for amorphous silicon with module efficiencies of 10 %, €1.2 per W_p for CIGS with efficiencies of 14 % and €1.0 per W_p for 12 % efficient CdTe modules [26].

The fabrication of photovoltaic cells using the current technology, crystalline Si, requires intensive energy processing. In addition, as it is an indirect semiconductor, it therefore requires a thick layer of hundreds of microns to absorb light, whereas, the active layer thickness of an organic photovoltaic cell is typically around 100 nm, and hence, the material requirements of organic semiconductors are sustainable. The above cost analysis shows organic photovoltaics to be a competitive technology that not only can outperform crystalline Si but also other thin-film photovoltaic

technologies [18, 21, 22, 26, 31]. Therefore, there is a significant interest amongst the research community and industry to develop photovoltaic cells with organic semiconductors.

Organic semiconducting systems are usually categorised as small molecules, dendrimers or polymers. The encompassing elements and usage of a particular system is dependent on the desired application. Regardless of the elements selected for inclusion the backbone of the system is carbon. Hence, in order to understand by what means the aforementioned can act as a functional electronic system, it is necessary to consider the electron configuration of carbon and by extension the molecular orbitals (MOs) of carbon systems.

2.2.1 Electronic properties

Carbon is an abundant and naturally occurring chemical element. Like silicon and germanium, it is a member of Group IV of the periodic table. The most common isotope of carbon is ^{12}C. The nucleus contains six neutrons and six protons. Hence, carbon has charge Z=6. The number of protons is equal to the number of electrons in a neutral atom. The first two of these six electrons fill the lowest energy 1s orbital. The next two electrons fill the slightly higher energy 2s orbital, with the remaining two electrons filling the highest energy 2p orbital. Hence, carbon has an electron configuration of $1s^2 2s^2 2p^2$. The 1s and 2s orbitals are complete, while the 2p orbitals, along the x, y and z axis, have two unpaired electrons. This results in carbon requiring four electrons to complete its valence. Carbon can form single, double, and triple bonds with itself as well as other chemical elements with a similar atomic structure, for example nitrogen or oxygen. This makes carbon an ideal chemical element for synthesising conjugated systems. Through conjugation, non-metallic organic systems can exhibit semiconductor behaviour. Conjugation is realized with the overlapping of p-orbitals. If these orbitals are distributed along the backbone of an organic molecule or polymeric system, it can act as a functional electronic system due to the delocalisation of the electrons. Hence, conjugation relies on the chemical configuration of the system. An alternating single and double bond among other configurations can facilitate in conjugation. To comprehend the delocalisation of electrons it is necessary to understand the way in which the MOs mix. In organic chemistry this is known as hybridisation.

The mixing or hybridisation of MOs results in an alternate (hybrid) structure composed of the original orbitals; the classification of which is dependent on atomic bonding. Consider the electron configuration of the carbon atom. The two electrons in the lowest energy state closest to the nucleus do not participate in bonding with other atoms. However, the 2s and 2p orbitals containing the valence electrons may partake in bonding. If carbon bonds with four other atoms by covalent σ-bonds i.e. single bonds, it exhibits a

tetrahedral structure in which all the bonds are equivalent. This is achieved by means of promoting one of the 2s electrons into the p-orbital that does not have an electron present. Thus creating four partially filled orbitals, each of which containing an electron. These incomplete orbitals can be filled by sharing an electron with another atom. The four orbitals are said to be degenerate sp^3 hybridised orbitals as they are hybrids of the 2s and $2p_x$, $2p_y$ and $2p_z$ orbitals. Methane is an example of a sp^3 hybridised molecule. Here, the four orbitals are sp^3 hybridised and are at an angle of 109.5 degrees from each other (tetrahedral). Each of these orbitals forms a σ-bond with a hydrogen atom (CH_4).

To achieve an electro-active system, a different type of hybridisation is required, sp^2 hybridisation. Similar to Sp^3 hybridisation an electron is promoted from the 2s into the empty p-orbital of the carbon atom. Unlike sp^3 hybridisation where we formed four hybrid orbitals, in sp^2 hybridisation only three hybrid orbitals form, leaving one p-orbital not hybridised. The three sp^2 orbitals lie in plane at ~ 120 degrees from each other, while the p-orbital that is not hybridised lies perpendicular to the sp^2 orbitals with the dumbbell shaped orbital distributed above and below the plane. It is the unhybridised p-orbital that facilitates covalent π-bonds and thus enables conjugation. It is worth mentioning that although the π-bond and σ-bond are orientated perpendicular to each other the orbitals overlie one another forming the double bond. Figure 2.1 depicts chemical compounds that are examples of sp^3 and sp^2 hybridisation, ethane (C_2H_6) and ethene (C_2H_4), respectively. With ethane we see a tetrahedral structure and a C-C bond (single), whereas for ethene we observe a C=C bond (double). The single bond in ethane results from the overlapping of sp^3 hybridised orbitals forming a σ-bond. The double bond in ethene is due to the overlapping of the associated sp^2 hybridised and unhybridised p orbital, forming σ and π bond, respectively. The two carbons of ethene are closer together than the carbons of ethane due to the double bond.

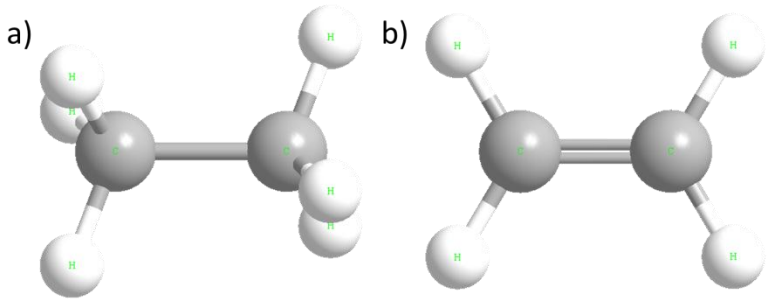

Figure 2.1 *Molecular structure of (a) ethane (C_2H_6) and (b) ethene (C_2H_4).*

In addition, the carbons can rotate in ethane, whereas the double bond between the carbons of ethene prevent any rotation around the axis of the σ-bond. Hybridisation is an interesting concept which helps explain the energy of bonds between atoms and their respective shapes. In terms of semiconducting systems, hybridisation shows that the electrons of the p-orbital occupy a large spatial region and are delocalised. The polymer polyacetylene, shown in Figure 2.2 is a good example of a conjugated system. Here, an alternating single and double bond exists for the full length of the polymer chain with three of the four valence electrons covalently bonded with σ-bonds, resulting in electron delocalisation along the backbone of the conjugated polymer.

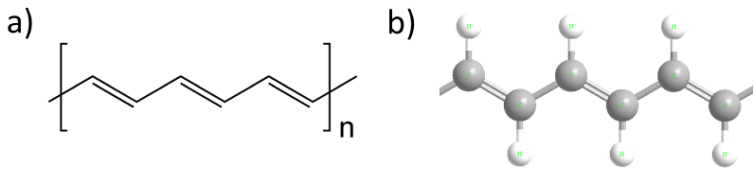

Figure 2.2 *Structure of electro-active polyacetylene (a) skeletal diagram (b) ball-and-stick model.*

Through reviewing the molecular structures of ethane and ethene we have gained an understanding of the means by which organic systems consisting of multiple carbon atoms can show electronic conduction. While the aforementioned is extremely useful and applicable to existing systems for example the conductive polymer polyacetylene and others which contain elements other than carbon for example sulphur, those systems currently under study due to their interesting properties and possible commercial applications demonstrate a more complex molecular structure for example polythiothene. Hence, it is necessary to consider similar systems to those currently employed.

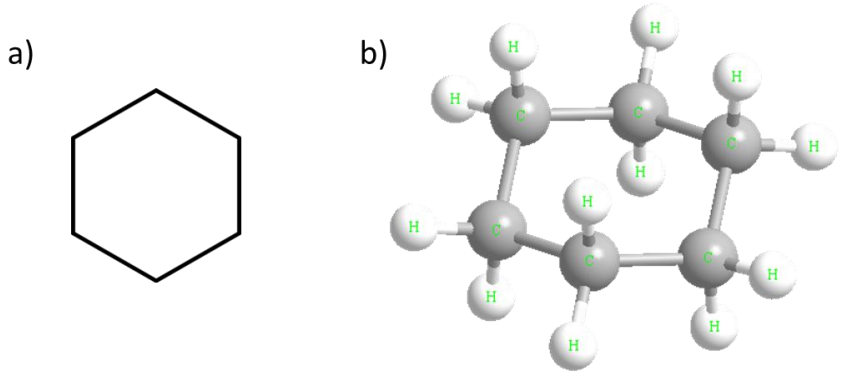

Figure 2.3 *Molecular structure of cyclohexane $(CH_2)_6$ (a) skeletal diagram (b) ball-and-stick model.*

Rings of atoms are common in organic semiconductors. These rings can be fused with other rings or exist as a chain of rings. They can consist entirely of carbon or be a combination of carbon and other elements. The theory covered thus far is the same as for rings containing carbon atoms, but it is interesting to see how the electrons are delocalised for the molecular structures that are rings. The molecule cyclohexane $(CH_2)_6$ shown in Figure 2.3 is similar to the ethane molecule shown in Figure 2.1 (a), as the carbon atoms of cyclohexane are sp^3 hybridised. The molecule is composed of a ring of 6 carbon atoms, with each atom bonded to two other carbons and two hydrogen atoms. Hence, each carbon has four single σ-bonds. The conformation of the molecule is not planar as that would result in significant torsion strain. Thus, the molecule has a 2-dimensional molecular structure allowing each carbon to be tetrahedral with bond angles of 109.5 degrees. The aforementioned molecular structure of cyclohexane has no delocalised electrons and hence it is not a conductive system. However, what would happen, if we were to incorporate a double bond into the system?

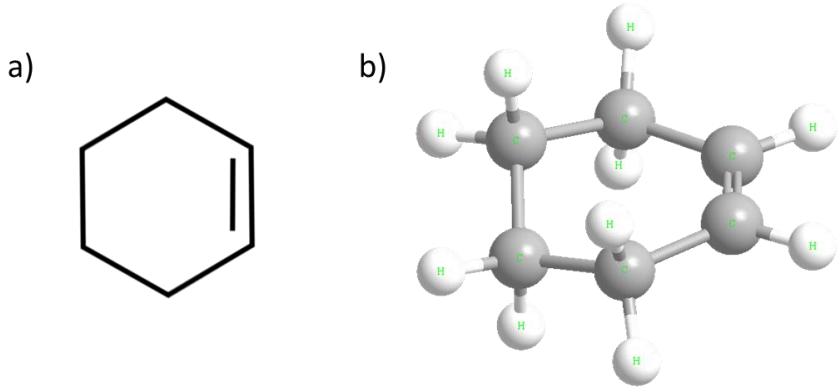

Figure 2.4 *Molecular structure of cyclohexene (C_6H_{10}) (a) skeletal diagram (b) ball-and-stick model.*

The molecular structure of cyclohexene (C_6H_{10}) is shown in Figure 2.4 and is similar to cyclohexane but has a single double bond incorporated into the molecular structure and hence has two less hydrogen atoms than cyclohexane. Considering the ball-stick-model Figure 2.4 (b) we see that the other four atoms have a tetrahedral shape and are σ-bonded to two hydrogen and two carbon atoms. Therefore, as with cyclohexane, cyclohexene is not a conductive system. This is because the double bond contained in the molecular structure is fixed and can't move around the ring, as the other carbon atoms are covalently bonded with four other elements.

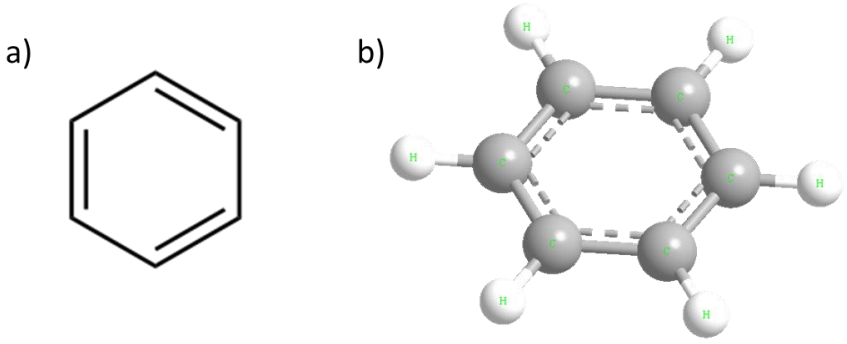

Figure 2.5 *Molecular structure of benzene (C_6H_6) (a) skeletal diagram (b) ball-and-stick model.*

However, if we consider benzene (C_6H_6), shown in Figure 2.5, where we have two additional double bonds, we observe a system that has the ability to be electrically conductive. Benzene is a sp^2 hybridised system containing six carbons and six hydrogen atoms. The molecular structure is planar and each carbon has a bonding angle of 120 degrees with three elements: two carbons and one hydrogen atom. While Figure 2.5 (a) shows the double bonds to be fixed, in reality the molecule exhibits resonance with the electrons delocalised around the entire ring. Hence, benzene is a conductive system and by means of fusing benzene rings together it is possible to synthesis an organic semiconductor for example anthracene, shown in Figure 2.6. Here, the molecular orbital is distributed along the entire molecule and therefore the whole molecule can partake in electronic conduction.

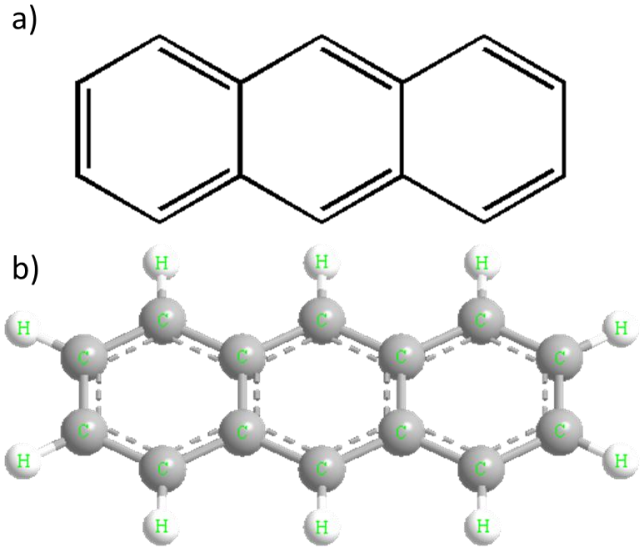

Figure 2.6 *Molecular structure of anthracene ($C_{14}H_{10}$) (a) skeletal diagram (b) ball-and-stick model.*

MO theory has helped explain how organic systems can electronically conduct. The theory can also provide accurate information on electronic transitions i.e. excited states that can occur within a molecule. As valuable as the depicted molecular structures are they fail to provide a quantum mechanical description of the molecular orbitals, for example benzene and anthracene shown in Figure 2.5 and 2.6, respectively. Electrons are not fixed in time and space, and instead of a molecular orbital we have a molecular wavefunction, with the square of the wavefunction being equal to the probability density of finding an electron within some volume of the molecule. Hence, atomic orbitals are waves and when we bring two atoms together they form a molecular wavefunction with the valence electrons delocalised rather than confined to an individual atom or bond. Therefore, the superposition of atomic orbitals allows for in phase (constructive) and out of phase (destructive) interference. These orbitals are known as bonding and anti-bonding orbitals, respectively. Due to the complexity of large systems we will only consider ethene, Figure 2.1 (b), as it is a homo-nuclear diatomic molecule i.e. contains two atoms both of which are the same. On formation of ethene the bonding and anti-bonding orbitals are π and π^*, respectively, shown in Figure 2.7. The lowest energy orbital forms in phase (π orbital) while the highest energy orbital forms out of phase (π^* orbital). It is important to note that the opposite of bonding is anti-bonding and not non-bonding i.e. anti-bonding≠non-bonding. Hence, the bonding orbital is lower in energy than the non-bonding orbitals and the anti-bonding orbital is higher in energy than the non-bonding orbitals.

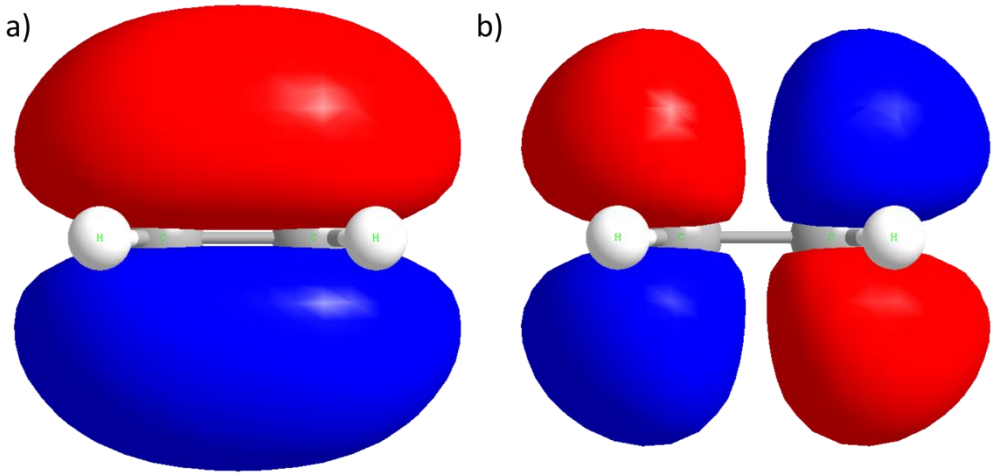

Figure 2.7 *Showing for ethene the (a) π bonding orbital and (b) π^* anti-bonding orbital.*

The theory allows us to determine whether a molecule is stable by means of calculating the bond order. The bond order is defined as half of the difference between the number of bonding and anti-bonding electrons. Calculating the bond order for ethene gives us 2 i.e. ethene has a double bond and is a stable molecule. The aforementioned orbitals, π and π^* are referred to as the highest occupied molecular orbital (HOMO) and the lowest unoccupied molecular orbital (LUMO), respectively, and are analogous to the valence and conduction band of an inorganic semiconductor. Hence, on excitation with an energy greater than or equal to the difference between the HOMO and LUMO i.e. band gap or energy gap an electron can be displaced from the π orbital into the π^* orbital [32]. Through altering the MO distribution it is possible to easily tune the energy difference between the HOMO and the LUMO [33]. This is one of the many interesting properties that make organic semiconducting materials useful in optoelectronic [34-36]. When an electron is excited from π to the π^* orbital or relax back into the π orbital it must be in accordance with the selection rules governing the transition. Usually the MOs of the ground state are occupied with two electrons. These electrons have opposite spin and contribute $\pm 1/2$ to the total angular spin momentum S. Hence, for this ground state the multiplicity, using $2S+1$ is a singlet. On excitation from π into the π^* the electron can either have the same spin or opposite spin to the electron remaining in the π orbital, making one of two configurations possible, a triplet or singlet, respectively. If the electrons have the same spin they are parallel, if they have different spins they are said to be anti-parallel. From the selection rules we know that the spin rule forbids an electron changing its spin while undergoing an electronic transition i.e. $\Delta S=0$, making the aforementioned system a singlet, spin-allowed, as a singlet to triplet transition is spin-forbidden, Figure 2.8. In the unusual case where we have a ground state consisting of two degenerate MOs for example in the case of molecular oxygen (O_2), each containing a single electron a triplet would exist and here a triplet to triplet transition would be spin-allowed.

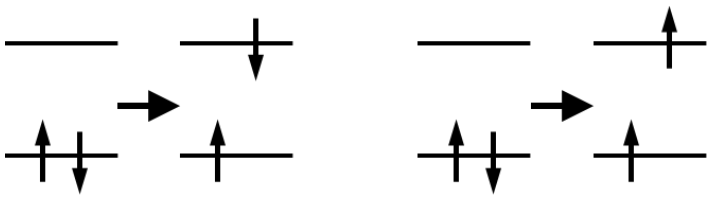

Figure 2.8 *Showing a spin-allowed (left) and spin-forbidden (right) transition.*

2.2.2 Optical properties

Having shown singlet to singlet transitions to be spin-allowed I will now discuss the implications. The first implication is fundamental to the operation of photovoltaic cells, absorption. Absorption by optical excitation and the post absorption emission by means of electronic relaxation are well-known to exist in certain organic molecular systems and have been for a long time [37]. Such processes can occur naturally and may be observed in pigments of living organisms for example chlorophyll, melanin and the well-studied green fluorescent protein (GFP) [38-40], and mineralogy and petrology where fluorescence is observed in for example anthracene and petroleum, respectively [41, 42]. In order to understand how these systems are used as semiconducting materials for optoelectronics, it is necessary to provide a brief description of the processes and timescales thereof. This is illustrated with the help of a Jablonski diagram [43, 44], shown in Figure 2.9. As I previously discussed optical absorption (Abs) i.e. absorption of a photon (~ 10^{-15} s) results in an excited state, S_n [45]. After absorption non-radiative vibrational relaxation (VR) to the lowest vibrational level of an excited state occurs. If lower energy states are available, internal conversion (IC) ensues to a state with the same multiplicity. Like VR, IC is a non-radiative vibrationally mediated process (~ $10^{-12 \text{ to } -14}$ s) [46]. Considering the timescales it is understandable why in most circumstances we observe radiative emission (~1 ns) from the lowest vibrational level [47] of S_1, Kasha's rule [48]. In the lowest vibrational level of S_1 it is also possible for the conversion to a state with a different multiplicity, i.e. a triplet T_1. This is known as intersystem crossing (ISC). The probability of ISC occurring is low, as it requires spin-flipping of the electron (~ $10^{-6 \text{ to } -3}$ s). However, it is worth mentioning that through strong spin-orbital coupling it is possible to achieve ISC timescales that make it competitive with VR and IC. The ground state can be repopulated by means of non-radiative processes, IC and ISC, through VR or radiative processes from the single or triplet state, known fluorescence (~ 10^{-9} s) and phosphorescence (~ $10^{-3 \text{ to } 1}$ s), respectively. The difference in timescales between the two radiative processes, fluorescence and phosphorescence, is due to fluorescence (S_1:S_0) being a fully spin-allowed process and hence exhibiting strong emission, whereas phosphorescence (T_1:S_0) requires an additional spin-flip and hence has a low probability of occurring, and therefore exhibits weak emission [49].

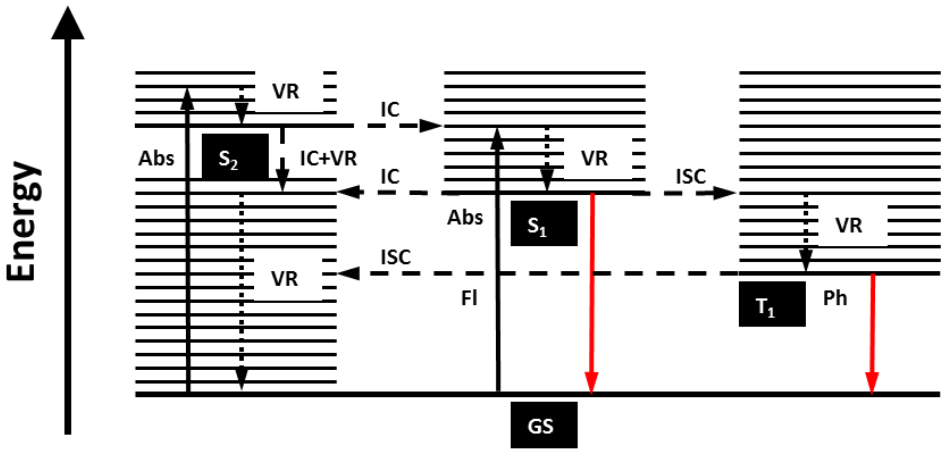

Figure 2.9 *Jablonski diagram showing common processes in organic molecular systems. Post absorption (Abs) non-radiative processes which include: vibrational relaxation (VR), internal conversion (IC) and intersystem crossing (ISC) are illustrated with dot and dash lines, whereas radiative processes which include: fluorescence (Fl) and phosphorescence (Ph) are presented with solid red lines. Figure inspired by reference [50].*

As explained, absorption of light can excite an electron from the ground state to a state that is higher in energy. This excited state, consists of electronic and vibrational energy. The addition of which, must be equal to that of the absorbed light, i.e. energy of a photon, ensuring conservation of energy. Unlike atomic spectra where we observe single wavelength transitions, organic molecules exhibit wavelength-dependent peaks which vary in intensity. By means of the Beer-Lambert law it is possible to determine the intensity of the absorption, the absorbance (A_λ) at a given wavelength (λ) [51]:

$$A_\lambda = \log\left(\frac{I_{0,\lambda}}{I_\lambda}\right) = \varepsilon_\lambda c l \tag{2.1}$$

Where $I_{0,\lambda}$ and I_λ are the incident and transmitted light intensities, respectively, ε_λ is the extinction coefficient, c the concentration in solution, and l is the distance light travels though the solution, i.e. the path length. In solution we are operating in a regime where amongst other requirements our molecules are dissolved, don't interact with one another and absorb similar amounts of light, and hence follow the linear relationship shown in Equation 2.1 between absorbance and concentration of the absorbing species. The measurement itself is extremely useful in providing us with information about the molecular system under study. However, when a material is employed in an organic optoelectronic device the material is deposited as a thin-film. In most

circumstances our films will follow Beer-Lambert's law, with the absorption scaling linearly with film thickness. An example of a scenario where deviation from the linear regime arises is when aggregates of a material are present within a film, resulting in loss of absorption due to the chromophore no longer being able to absorb the light. Another example where deviation occurs that has direct implications on devices arises with increasing light intensity. This thesis is on the topic of organic photovoltaics, hence I will limit my discussion to thereof. As intensity increases, at some point less and less of the material is able to absorb the light. The implications in an OPV can be profound. With increasing light intensity the excited states, i.e. excitons (coulombically bound electron-hole pairs) are created closer and closer together until they are so close they annihilate, two excitons become one. This exciton is higher in energy than the original excitons, but it is not possible to harvest this additional energy due to fundamental limitations in the conversion process, discussed in Chapter 3. Under high illumination you can also have a situation where lots of charges are generated and these mobile charges annihilate an exciton. Fortunately, the aforementioned scenarios are not an issue under normal OPV operation [52].

The absorption and emission spectra for the systems discussed in this thesis lie between ~ 300 and ~ 1100 nm. To understand these spectra it is necessary to further consider the nature of the excited states. Figure 2.10 depicts two Morse-like potentials, S_0 and S_1, for the ground and excited state, respectively. The potentials contain energy levels associated with vibrational energy from the lowest, $\nu=0$ to the highest in energy, $\nu=n$. On excitation of the ground state we populate the vibrational levels corresponding to high energy of the excited state, S_1 to S_n. The schematic shows the nuclear co-ordinates for the ground state and excited state to be different. This difference arises from a geometric rearrangement of the molecule in the excited state. The Born-Oppenheimer approximation tells us that an electronic transition to a higher state occurs rapidly compared to the rearrangement of the nucleus [53]. Therefore, with electronic transitions we observe little or no change in the geometry of the molecular system, and hence electronic transitions are said to be vertical transitions. Post absorption the excited state VRs to the lowest vibrational level of the excited state, and it is here where fluorescence occurs, according to Kasha's rule [48, 49], to a higher energy vibrational level of the ground state. The probability of an optical transition occurring is governed by the overlap of vibrational wavefunctions of the ground and excited state, known as the Frank-Condon principle [54, 55]. For example, as shown in Figure 2.10, strong absorption is a result of populating vibrational levels which have a significant wavefunction overlap. Due to the electronic transitions being vertical and the geometry of the excited state being different as described, generally we observe population of higher vibrational levels of the excited state,

shown here as a transition from ν=0 to ν=2. The overlap in wavefunction allows for high and low probability transitions, resulting in an absorption spectra. The observed emission spectra is similar to the absorption spectra but reversed, i.e. from ν=2 to ν=0, and owing to the conversion of energy through VR is shifted [56].

In this section concerning the optical properties of organic molecular systems, I have provided a description of the main processes and their associated timescales, explained the rules and laws governing certain transitions, discussed how non-radiative and radiative transitions compete with each other and described the character of absorption and emission spectra. In addition, a quantity of experimental significance can be measured from the aforementioned, known as Photoluminescence Quantum Yield (PLQY), which is the number of photons emitted divided by the number of photons absorbed [57], and is determined by means of considering the radiative and non-radiative decays, k_r and k_{nr}, respectively, shown in Equation 2.2.

$$PLQY = \frac{k_r}{k_r + k_{nr}} \tag{2.2}$$

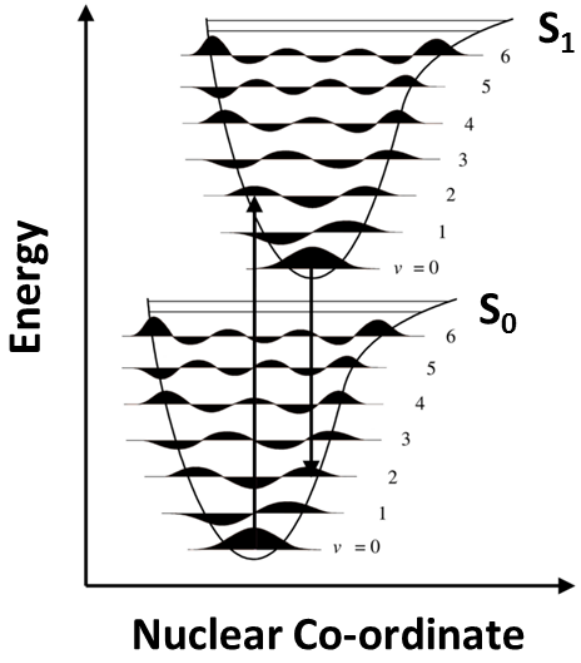

Figure 2.10 *Schematic diagram of the Franck-Condon principle. The diagram shows the probability of absorption and emission with the overlap of vibrational wavefunctions. The potentials illustrate favourable transitions between ν=0 and ν=2.*

2.3 Organic semiconducting devices

Having discussed the fundamentals, I will now provide an overview of several technologies that rely on semiconductors, and in doing so, introduce common terminology used in semiconductor physics. Once established, I will discuss excitons, electron transfer, energy transfer and the use of organic semiconductors in different technologies. My discussion on the technological aspects of organic semiconductors will be brief, owing to many of the technologies being out with the focus of this thesis, and those which are will be discussed in subsequent chapters. This section is merely to provide a flavour of the use of organic semiconductors, and how technologies fabricated with these materials operate.

The development of the transistor by John Bardeen, Walter Brattain [58] and William Shockley completely revolutionised the electronics industry. The use of semiconductors in the fabrication thereof, allows for rapid switching or amplification, made possible by operating without the need for moving parts, and enables thousands of millions to be incorporated in a single integrated circuit. These so called microprocessors are found in many electronics. A transistor in its simplest form, a bipolar npn transistor, can be considered as a semiconducting material sandwiched between two electrodes. Where the electrodes are connected the semiconductor is doped n-typed, i.e. contains excess electrons (negative). The gap between the two n-type regions is doped p-type, i.e. contains excess holes (positive). A hole is the absence of an electron. At each interface between the p-type and n-type a depletion layer exists, i.e. a potential barrier. These layers act as an insulator and prevent the flow of electrons through the material. However, if we were to add a third electrode to the semiconductor it is possible to control the flow of electrical current through the semiconductor by means of applying a voltage. A similar result is observed with a PNP transistor. It is worth mentioning that transistors have many applications and configurations, and that the aforementioned is for the purpose of illustration.

When we excite an electron into a higher state we are left with an empty state, and as mentioned, an empty state in which there is the absence of an electron is known as a hole. On excitation the creation of an electron-hole pair is referred to as an exciton. Introducing energy into a system can result in the formation and separation of an exciton. Once the exciton has been separated into its constituents, the constituent charges can be extracted from the semiconductor. This effect can be achieved with different forms of energy. For example, when exposed to heat or illuminated with light, it is possible for a semiconductor to produce an electrical current, and hence be used as a

temperature sensor [59] or a photovoltaic device [60], respectively. If we inject charges, as opposed to extracting charges, it is feasible by means of recombination to fabricate a device that produces light, i.e. a light-emitting diode (LED) [61]. The mechanisms which govern the operation of these devices differ greatly, so alternative materials and device architectures are understandably required to ensure optimal performance. For example, for a photovoltaic cell, it is essential to dissociate and extract the charges from the device as speedily as possible to prevent recombination or loss of energy through radiative or non-radiative decay, whereas for an LED, it is important to control recombination in an attempt to ensure that the majority of recombination is radiative.

Inorganic semiconductors are used in the fabrication of myriad technological devices. Many of these technological devices can be fabricated with organic semiconductors. However, due to the substantial difference in material properties, often the principle of operation and device architecture are dissimilar. Arguably, the most significant difference between the two is related to their dielectric constants. Inorganic semiconductors exhibit high dielectric constants and hence show lots of screening. This results in free carrier transitions with the electron and hole able to move away from each other with ease on excitation. Whereas, in an organic semiconductor on excitation we have the formation of an excited state, which is a coulombically bound electron-hole pair i.e. an exciton. Like inorganic semiconductors, organic semiconductors are doped p-type or n-type. We characterise an n-type or p-type semiconductor as an electron or hole transporting material, respectively. The charge carriers found in organic semiconductors are polarons, an electron or hole with an induced polarization that together move through a molecular or polymeric system, whereas in inorganic semiconductors we refer to mobile charge carriers and the atoms that make the crystalline lattice. Generally, organic semiconductors are amorphous and inorganic semiconductors crystalline. That said we similarly consider those which alter the mobility as impurities, defects or traps. Charge transport in technological devices fabricated with organic semiconductors can be achieved with thermal energy and an applied electric field. Hence, charge carrier mobility measurements on organic semiconducting materials show both temperature and electric field dependence. The ability for a charge carrier, i.e. a polaron to travel from one site to another, depends on its energy and to some extent the wavefunction overlap [62]. For efficient charge transfer between sites it is important to ensure there is a suitable separation thereof [63]. Hence, where the charge is situated on a molecule and the molecules conformation and orientation with other molecules impacts charge

transport [64]. A few good examples include: multi-dimensional stacking of small molecules and chain alignment of polymeric systems. Both cases show a strong correlation with charge transport [65, 66]. In addition, these and subsequent works show that charge transport in molecular and polymeric systems is to some extend controllable by means of altering processing conditions [67] and that the mobility is anisotropic. Therefore, unlike inorganic semiconductors where it is usually possible to build an accurate model of charge transport, in organic systems it is difficult to develop a reliable model [68, 69].

For simplicity I have, in this thesis, used band diagrams to explain how the devices I have fabricated work. Whilst, correct in the field of inorganic semiconductors and common practice in organic semiconductors, it does not paint an accurate picture of our molecular or polymeric systems. A more suitable description is provided with state diagrams. For our purposes band diagrams are sufficient, but it is important to remember the difference between the two. The reasons for this difference are several-fold. As mentioned our organic systems can have different conformations and orientations. Such differences may result in energy disorder and shifting of the energy levels. Amongst other reasons it is also possible to have chemical impurities within the system. These factors lead to broadening of the density of states. In addition, from a practical perspective a band diagram does not show the energy levels of the optically excited exciton and incorrectly depicts the energy of the charge transfer (CT) state or CT exciton. A CT state or CT exciton occurs during the charge transfer process. It is a bound state that exists at the donor acceptor interface. Here, the electron and hole are in their respective charge carrier transport material, but are still bound to each other by an energy of approximately 350 mV and separated by a distance of order of a nm. Therefore, in an energy diagram the CT state should be shown to have less energy than the unbound free charge carriers. This is not the case in a band diagram, but is in state diagrams [35]. Nevertheless, it is common practice and for reasons of simplicity and clarity we use the band diagrams.

Electron transfer and energy transfer are associated with the mitigation of energy. Electron transfer involves the movement of an electron from a donor to an acceptor site, resulting in a cation on the donor and an anion on the acceptor, as shown in Figure 2.11. The process can occur with an excited donor or acceptor state by means of photo-reduction or photo-oxidation, respectively. These processes are critical for the generation of charges in artificial photosynthesis and organic photovoltaic cells, and can be explained with Marcus theory [70, 71].

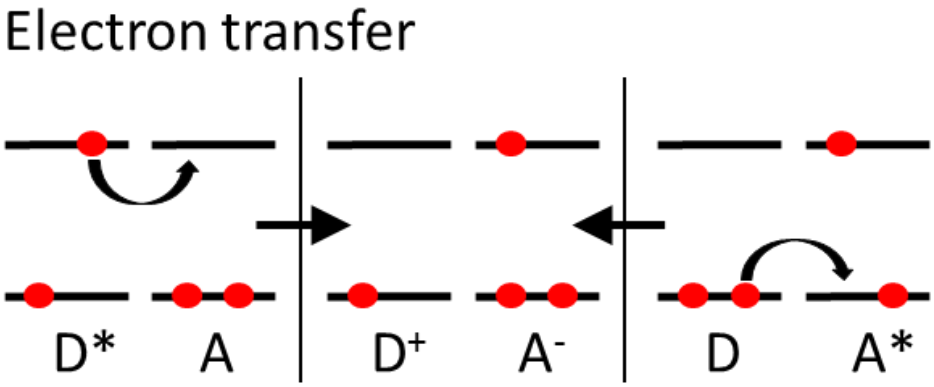

Figure 2.11 *Illustrating electron transfer from a donor, D, to an acceptor, A.*

Like electron transfer, the process of energy transfer involves the movement of electrons. However, with energy transfer there are two electron exchanges instead of one. Two mechanisms can result in energy transfer. The first is a short range collision process that involves an electron exchange from the excited state of the donor into the LUMO of the acceptor, while another electron exchange occurs from the HOMO of the acceptor into the lower lying singly occupied MO of the donor. The result of the process is an excited state donor and ground state acceptor molecule becoming a ground state donor and an excited state acceptor molecule. Förster energy transfer is the second mechanism and occurs by means of dipole-dipole coupling. This mechanism has a longer range than the first mechanism and is usually the mechanism responsible for energy transfer from one chromophore to another in an organic photovoltaic cell [72], shown in Figure 2.12.

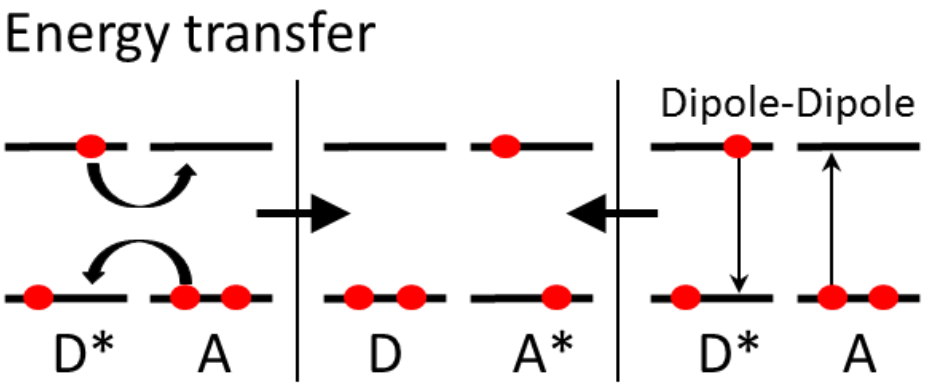

Figure 2.12 *Illustrating energy transfer from a donor, D, to an acceptor, A.*

Organic semiconductors are exciting materials for technological devices. I have discussed the fundamentals and covered the mechanisms that enable them to be used as such, and mentioned the advantages they have over their inorganic counterparts, which in brief includes: energy transitions corresponding to the visible, strong coupling with light, ease of bulk synthesis, highly tuneable properties and may be used in the fabrication of low cost devices, as they are solution processable and require no high temperature processing. They can also be used in a wide-range of technological applications, the most common being organic field effect transistors (OFETs), photovoltaics (OPVs) and light-emitting diodes (OLEDs). Like inorganic transistors, organic transistors may operate in different configurations with a particular application in mind. They are widely used in the study of charge transport and have facilitated the development of organic semiconducting materials with superior mobilities.

In just over a decade, within the field of organic semiconductors we have seen an increase in charge carrier mobility of five orders of magnitude, a remarkable achievement. However, charge carrier mobilities are still several orders of magnitude lower than those measured for inorganic semiconductors, therefore limiting the thickness of the active or absorbing layer in an OPV. Another issue with using organic semiconductors for photovoltaics concerns lifetime. The performance of an OPV degrades significantly when exposed to moisture and oxygen. If not encapsulated an OPV will stop working within days. With a flexible barrier an OPV may last two to three years, and ten plus years with rigid glass, however, encapsulation with the rigid glass is expensive and makes the module heavy and not flexible [73]. That said there has been fruitful research and development into encapsulating barriers, active layer materials and stable electrodes. The aforementioned combined with the properties of these semiconducting materials for example high absorption coefficients enable their use in efficient devices.

On a similar timescale a dramatic improvement in performance has been observed in both OPV and OLED devices. While efficiencies for OPVs are lower than inorganics, the dramatic increase in performance has resulted in efficiencies of almost 10 % with non-tandem solution-processable bulk-heterojunction photovoltaic devices [74] and in tandem, OPVs have been reported with certified efficiencies of 12 % [75]. Having almost crossed the 10 % efficiency milestone generally perceived as a requirement for non-tandem OPVs to be a viable technology [76], it is certainly an interesting time to be working in the field of OPVs, shown in Figure 2.13.

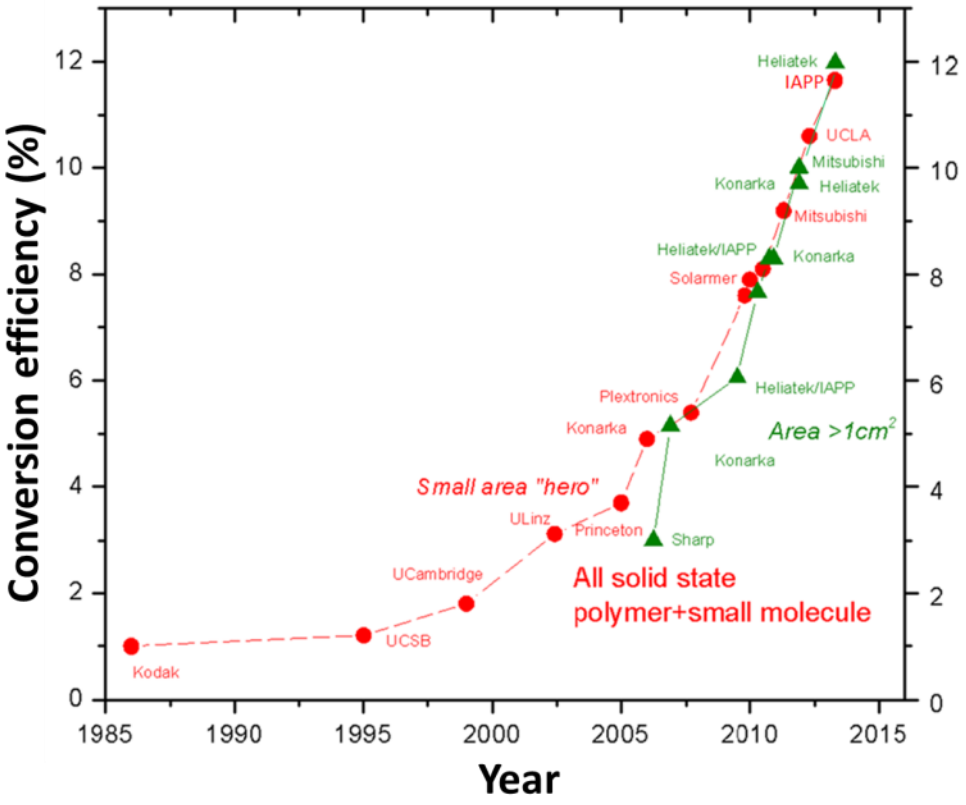

Figure 2.13 *Illustrating the development of OPV efficiencies. Figure courtesy of Karl Leo and modified to show the photovoltaic technologies of interest.*

Unlike OLEDs, there are many challenges that remain to be addressed before we begin to see the large-scale commercialisation of the technology. These challenges will be discussed in detail in chapter 3. However, some of the fundamental challenges which impact device performance will be discussed here. The first, involves the nature of the excited state. In photovoltaics, absorption of light results in the promotion of an electron to a state that is higher in energy leaving behind a vacant position called a hole. These two quasi-particles may interact electrostatically and form a bound state known as an exciton i.e. an electron-hole pair, as previously described [77]. The binding energy of an exciton in an inorganic semiconductor is relatively low due to the high dielectric constant. Therefore, in these systems on excitation it is possible to observe the direct excitation of free charge carriers. However, at low temperatures where the excitation energy is below that of the band-gap, excitons may be observed. These excitons are known as Mott-Wannier excitons, where screening or damping of the electric field reduces the electrostatic interactions between opposite charges, resulting in the charges orbiting each other at a radius much larger than the lattice spacing. In organic

semiconductors the materials have low dielectric constants and hence have a higher binding energy. Unlike the picture described for inorganic semiconductors, where we have an electron and hole orbiting each other, in organic semiconductors the nature of an exciton can be thought of as an excited state of a molecule governed by MO theory, as described in section 2.2.1. The formation of excitons in these materials with low dielectric constants, results in the electron-hole pair being tightly bound by means of the Coulomb interaction and hence these excitons are referred to as Poole-Frenkel excitons and must not be confused with charge transfer (CT) excitons, which extend across both donor and acceptor molecules in a blend. These tightly bound Poole-Frenkel excitons have large binding energies greater than or of order 500 meV [36]. This has serious consequences on OPV device operation, as energies greater than or equal to the aforementioned is required to dissociate the exciton into its constituent charges for current generation. To achieve charge separation we have to sacrifice energy through incorporation of an acceptor. The choice of acceptor must be carefully selected and is typically a type of fullerene derivative. There is much on-going research to aid our understanding of the mechanisms involved in dissociation. There is therefore hope that through a better understanding of the mechanisms involved we will one day be able to efficiently dissociate excitons without having to sacrifice too much energy. Another challenge the technology faces, which is universal to photovoltaics, is on the subject of absorption. Understandably, we would like to maximise absorption of the solar spectrum, but in practice are limited by the mechanisms that govern operation. Hence, we find ourselves unable to absorb the lower energy photons, and through VR and IC unable to convert all the energy of the higher energy photons.

The development of OLEDs as a technology has been very successful with many high-end smartphones using them as their primary display. The operation principle for an OLED is the reverse of an OPV. Charges are injected at the electrodes into the device. The charges form excitons, and it is the decay or recombination of these excitons that produce the luminescence. However, the success of OLEDs strongly suggests the engineering challenges for OPV can be met.

2.4 Conclusion

I began this chapter underlining the importance of inorganic semiconductors and how they have facilitated the development of many technologies. A group of organic materials were introduced that show semiconductor-like behaviour, organic semiconductors. These organic semiconducting materials were shown to exhibit many advantages over their inorganic counterparts, which include the ability to be easily synthesised in bulk with various shapes, sizes and properties.

The organic semiconductors presented in this thesis are either small molecules or polymers. Small molecules are molecules with a low molecular weight ($<$ 900 Da), for example anthracene shown in Figure 2.6. Polymers on the other hand are large molecules that are composed of many small molecules, i.e. monomers. These monomers are repeated throughout the polymer chain. An example of a polymer is polyacetylene, shown in Figure 2.2. To give an indication of the molecular weight of a polymer used in organic photovoltaics, we look to P3HT. The most efficient OPVs acquired with P3HT have molecular weights $>$ 40 KDa [78].

The synthesis of an organic semiconducting system is dependent on the desired application. I went on to discuss some of the theory of organic semiconductors and demonstrate how their electronic and optical properties enable their use in the fabrication of different technologies. I finished the chapter with a brief overview of some of these technologies and discuss a few challenges organic semiconductors face in terms of their use in photovoltaics.

2.5 References

1. Shirakawa, H., et al., *Synthesis of electrically conducting organic polymers: halogen derivatives of polyacetylene, (CH).* Journal of the Chemical Society, Chemical Communications, 1977. **0**(16): p. 578-580.
2. Chiang, C.K., et al., *Electrical Conductivity in Doped Polyacetylene.* Physical Review Letters, 1977. **39**(17): p. 1098.
3. Delannoy, P., et al., *Transient electroluminescence of monolayer and bilayer sexithiophene diodes.* Synthetic Metals, 1994. **67**(1–3): p. 197-200.
4. Tang, C.W., *Two-layer organic photovoltaic cell.* Applied Physics Letters, 1986. **48**(2): p. 183-185.
5. Garnier, F., et al., *All-Polymer Field-Effect Transistor Realized by Printing Techniques.* Science, 1994. **265**(5179): p. 1684-1686.
6. Dimitrakopoulos, C.D. and P.R.L. Malenfant, *Organic Thin Film Transistors for Large Area Electronics.* Advanced Materials, 2002. **14**(2): p. 99-117.
7. Zen, A., et al., *Solution Processable Organic Field-Effect Transistors Utilizing an α,α'-Dihexylpentathiophene-Based Swivel Cruciform.* Journal of the American Chemical Society, 2006. **128**(12): p. 3914-3915.
8. Yu, G., et al., *POLYMER PHOTOVOLTAIC CELLS - ENHANCED EFFICIENCIES VIA A NETWORK OF INTERNAL DONOR-ACCEPTOR HETEROJUNCTIONS.* Science, 1995. **270**(5243): p. 1789-1791.
9. Bube, R.H., *Photovoltaic Materials.* Imperial College Press, 1998.
10. Nelson, J., *Organic photovoltaic films.* Current Opinion in Solid State and Materials Science, 2002. **6**(1): p. 87-95.
11. Hamakawa, Y., *Thin-Film Solar Cells: Next Generation Photovoltaics and Its Applications.* Springer Science & Business Media, 2004.
12. Brabec, C.J., et al., *A Low-Bandgap Semiconducting Polymer for Photovoltaic Devices and Infrared Emitting Diodes.* Advanced Functional Materials, 2002. **12**(10): p. 709-712.
13. Lee, T.-W., et al., *Hole-injecting conducting-polymer compositions for highly efficient and stable organic light-emitting diodes.* Applied Physics Letters, 2005. **87**(23): p. -.
14. Tan, C.H., et al., *The morphological dependence of charge transport in a soluble luminescent conjugated polymer.* Organic Electronics, 2002. **3**(2): p. 81-88.
15. Ribierre, J.C., et al., *Amplified spontaneous emission and lasing properties of bisfluorene-cored dendrimers.* Applied Physics Letters, 2007. **91**(8): p. -.
16. Halls, J.J.M., et al., *Efficient photodiodes from interpenetrating polymer networks.* Nature, 1995. **376**(6540): p. 498-500.
17. Harrison, M.G., J. Grüner, and G.C.W. Spencer, *Analysis of the photocurrent action spectra of MEH-PPV polymer photodiodes.* Physical Review B, 1997. **55**(12): p. 7831.
18. Ameri, T., N. Li, and C.J. Brabec, *Highly efficient organic tandem solar cells: a follow up review.* Energy & Environmental Science, 2013. **6**(8): p. 2390-2413.
19. Brabec, C.J. and J.R. Durrant, *Solution-Processed Organic Solar Cells.* MRS Bulletin, 2008. **33**(07): p. 670-675.
20. Brabec, C.J., et al., *Production Aspects of Organic Photovoltaics and Their Impact on the Commercialization of Devices.* MRS Bulletin, 2005. **30**(01): p. 50-52.
21. Machui, F., et al., *Cost analysis of roll-to-roll fabricated ITO free single and tandem organic solar modules based on data from manufacture.* Energy & Environmental Science, 2014. **7**(9): p. 2792-2802.
22. Emmott, C.J.M., A. Urbina, and J. Nelson, *Environmental and economic assessment of ITO-free electrodes for organic solar cells.* Solar Energy Materials and Solar Cells, 2012. **97**(0): p. 14-21.
23. Choi, D.Y., et al., *Annealing-free, flexible silver nanowire-polymer composite electrodes via a continuous two-step spray-coating method.* Nanoscale, 2013. **5**(3): p. 977-983.

24. Na, S.-I., et al., *Fully spray-coated ITO-free organic solar cells for low-cost power generation.* Solar Energy Materials and Solar Cells, 2010. **94**(8): p. 1333-1337.
25. Na, S.-I., et al., *Efficient and Flexible ITO-Free Organic Solar Cells Using Highly Conductive Polymer Anodes.* Advanced Materials, 2008. **20**(21): p. 4061-4067.
26. Azzopardi, B., et al., *Economic assessment of solar electricity production from organic-based photovoltaic modules in a domestic environment.* Energy & Environmental Science, 2011. **4**(10): p. 3741-3753.
27. Hösel, M., et al., *Fast Inline Roll-to-Roll Printing for Indium-Tin-Oxide-Free Polymer Solar Cells Using Automatic Registration.* Energy Technology, 2013. **1**(1): p. 102-107.
28. Andersen, T.R., et al., *Scalable, ambient atmosphere roll-to-roll manufacture of encapsulated large area, flexible organic tandem solar cell modules.* Energy & Environmental Science, 2014. **7**(9): p. 2925-2933.
29. Kubis, P., et al., *Patterning of organic photovoltaic modules by ultrafast laser.* Progress in Photovoltaics: Research and Applications, 2015. **23**(2): p. 238-246.
30. Kubis, P., et al., *High precision processing of flexible P3HT/PCBM modules with geometric fill factor over 95%.* Organic Electronics, 2014. **15**(10): p. 2256-2263.
31. Hoffmann, W., *PV solar electricity industry: Market growth and perspective.* Solar Energy Materials and Solar Cells, 2006. **90**(18–19): p. 3285-3311.
32. J. Clayden, N.G., S. Warren, and P. Wothers, *Organic chemistry.* Oxford University Press, 2008.
33. Mishra, A. and P. Bäuerle, *Small Molecule Organic Semiconductors on the Move: Promises for Future Solar Energy Technology.* Angewandte Chemie International Edition, 2012. **51**(9): p. 2020-2067.
34. Bredas, J.-L. and J.R. Durrant, *Organic Photovoltaics.* Accounts of Chemical Research, 2009. **42**(11): p. 1689-1690.
35. Bradas, J.-L., et al., *Molecular Understanding of Organic Solar Cells: The Challenges.* Accounts of Chemical Research, 2009. **42**(11): p. 1691-1699.
36. Kippelen, B. and J.-L. Bredas, *Organic photovoltaics.* Energy & Environmental Science, 2009. **2**(3): p. 251-261.
37. Herschel, J.F.W., Philosophical Transactions of the Royal Society of London, 1845. **135**: p. 147-153.
38. Kollias, N. and A. Baqer, *Spectroscopic Characteristics of Human Melanin In Vivo.* J Investig Dermatol, 1985. **85**(1): p. 38-42.
39. Lichtenthaler, H.K., *[34] Chlorophylls and carotenoids: Pigments of photosynthetic biomembranes*, in *Methods in Enzymology*, R.D. Lester Packer, Editor. 1987, Academic Press. p. 350-382.
40. Zimmer, M., *GFP: from jellyfish to the Nobel prize and beyond.* Chemical Society Reviews, 2009. **38**(10): p. 2823-2832.
41. De Ment, J.A., *Fluorescent techniques in petroleum exploration.* Geophysics, 1947. **12**(1): p. 72-98.
42. Schwarz, F.P. and S.P. Wasik, *Fluorescence measurements of benzene, naphthalene, anthracene, pyrene, fluoranthene, and benzo[e]pyrene in water.* Analytical Chemistry, 1976. **48**(3): p. 524-528.
43. Jablonski, A., *Uber den Mechanismus der Photolumineszenz von Farbstoffphosphoren.* Zeitschrift für Physik, 1935. **94**: p. 38-46.
44. Jablonski, A., *Efficiency of anti-stokes fluorescence in dyes.* Nature, 1933. **131**: p. 839-841.
45. Hedley, G.J., *Ultrafast photophysics of iridium complexes.* Doctoral Dissertation, 2010.
46. R Engleman, J.J., Molecular Physics, 1970. **18**: p. 145-164.
47. Elsaesser, T. and W. Kaiser, *Vibrational and Vibronic Relaxation of Large Polyatomic Molecules in Liquids.* Annual Review of Physical Chemistry, 1991. **42**(1): p. 83-107.
48. Kasha, M., Discussions of the Faraday Society 1950. **9**: p. 14-19.
49. Kasha, M., Chemical Reviews, 1947. **41**: p. 401-419.

50. Osterman, T., *Excited State Processes in Solar Energy Materials.* Doctoral Dissertation, 2014.
51. Lambert, J.H., *Photometria sive de mensura et gradibus luminis, colorum et umbrae.* Germany, Eberhardt Klett, 1760: p. 391.
52. Shaw, P.E., A. Ruseckas, and I.D.W. Samuel, *Exciton Diffusion Measurements in Poly(3-hexylthiophene).* Advanced Materials, 2008. **20**(18): p. 3516-3520.
53. M, B. and O. R, *Annalen der Physik.* 1927. **84**: p. 457.
54. Condon, Physics Review, 1926. **28**: p. 1182.
55. Franck and Dymond, Transactions of the Faraday Society, 1926. **21**: p. 536-542.
56. Stokes, G., *Philosophical Transactions of the Royal Society of London.* 1852. **142**: p. 463-562.
57. I. D. W. Samuel, G. Rumbles, and R.H. Friend, *Primary Photoexcitations in Conjugated Polymers: Molecular Excitation Versus Semiconductor Band Model, ed. N. S. Sariciftci.* World Scientific Publishing Company, 1998.
58. Bardeen, J. and W.H. Brattain, *The Transistor, A Semi-Conductor Triode.* Physical Review, 1948. **74**(2): p. 230-231.
59. v. Ettingshausen, A. and W. Nernst, *Ueber das Auftreten electromotorischer Kräfte in Metallplatten, welche von einem Wärmestrome durchflossen werden und sich im magnetischen Felde befinden.* Annalen der Physik, 1886. **265**(10): p. 343-347.
60. Chapin, D.M., C.S. Fuller, and G.L. Pearson, *A New Silicon p-n Junction Photocell for Converting Solar Radiation into Electrical Power.* Journal of Applied Physics, 1954. **25**(5): p. 676-677.
61. Holonyak, N. and S.F. Bevacqua, *COHERENT (VISIBLE) LIGHT EMISSION FROM Ga(As1−xPx) JUNCTIONS.* Applied Physics Letters, 1962. **1**(4): p. 82-83.
62. Brédas, J.L., et al., *Organic semiconductors: A theoretical characterization of the basic parameters governing charge transport.* Proceedings of the National Academy of Sciences, 2002. **99**(9): p. 5804-5809.
63. Markham, J.P.J., et al., *Charge transport in highly efficient iridium cored electrophosphorescent dendrimers.* Journal of Applied Physics, 2004. **95**(2): p. 438-445.
64. Yamada, T., et al., *Revealing bipolar charge-transport property of 4,4'-N,N'-dicarbazolylbiphenyl (CBP) by quantum chemical calculations.* Organic Electronics, 2011. **12**(1): p. 169-178.
65. Wright, I.A., et al., *Oligothiophene Cruciform with a Germanium Spiro Center: A Promising Material for Organic Photovoltaics.* Angewandte Chemie International Edition, 2012. **51**(19): p. 4562-4567.
66. Sirringhaus, H., et al., *Two-dimensional charge transport in self-organized, high-mobility conjugated polymers.* Nature, 1999. **401**(6754): p. 685-688.
67. Arumugam, S., et al., *Charge transport in a two-dimensional molecular organic semiconductor.* Journal of Materials Chemistry C, 2014. **2**(1): p. 34-39.
68. Vukmirović, N. and L.-W. Wang, *Carrier hopping in disordered semiconducting polymers: How accurate is the Miller–Abrahams model?* Applied Physics Letters, 2010. **97**(4): p. -.
69. MacKenzie, R.C.I., J.M. Frost, and J. Nelson, *A numerical study of mobility in thin films of fullerene derivatives.* The Journal of Chemical Physics, 2010. **132**(6): p. -.
70. Marcus, R.A., *On the Theory of Oxidation-Reduction Reactions Involving Electron Transfer. I.* The Journal of Chemical Physics, 1956. **24**(5): p. 966-978.
71. Marcus, R.A., *Electrostatic Free Energy and Other Properties of States Having Nonequilibrium Polarization. I.* The Journal of Chemical Physics, 1956. **24**(5): p. 979-989.
72. Scheblykin, I.G., et al., *Excited State and Charge Photogeneration Dynamics in Conjugated Polymers.* The Journal of Physical Chemistry B, 2007. **111**(23): p. 6303-6321.

73. Dr Harry Zervos, R.D.a.D.K.G., *Organic Photovoltaics (OPV) 2013-2023: Technologies, Markets, Players.* IDTechEx, 2013.
74. He, Z., et al., *Enhanced power-conversion efficiency in polymer solar cells using an inverted device structure.* Nat Photon, 2012. **6**(9): p. 591-595.
75. Heliatek, *Heliatek reaches efficiency record with 40 % transparent organic solar cells.* Press release, 2014.
76. C. Brabec, U. Scherf, and L. Dyakonov, *Organic photovoltaics: materials, device physics, and manufacturing technologies.* Wiley 2014.
77. Wannier, G.H., *The Structure of Electronic Excitation Levels in Insulating Crystals.* Physical Review, 1937. **52**(3): p. 191-197.
78. Holmes, N.P., et al., *The effect of polymer molecular weight on P3HT:PCBM nanoparticulate organic photovoltaic device performance.* Solar Energy Materials and Solar Cells, 2014. **128**(0): p. 369-377.

Chapter 3

Organic photovoltaics

3.1 Introduction

To achieve an efficient organic photovoltaic (OPV), it is necessary for the active layer of the device to contain both donor and acceptor materials. These materials can be molecular or polymeric. Typically, an active layer will consist of a conjugated polymer as the donor and a fullerene derivative as the acceptor. In order to extract a current from the device, the active layer must be sandwiched between two electrodes. To enable absorption, at least one of these electrodes must be transparent. Light is usually absorbed by the donor, resulting in the formation of an exciton that has an associated diffusion length (L_D). To generate a current it is essential to dissociate the exciton into its constituent charges within L_D [1]. This is achieved with an acceptor by means of photo-induced charge transfer, and is a result of the acceptor having a high electron affinity (EA). Post dissociation, the charges travel under the influence of an electric field to the electrodes, where they are extracted from the device. The electric field is a result of the electrodes having asymmetric work functions. The mechanisms involved in the operation of a typical OPV device are shown in Figure 3.1. To maximise device performance it is necessary to focus on each mechanism. Therefore, in this section I discuss each mechanism and the improvements that can be made to ensure optimal performance.

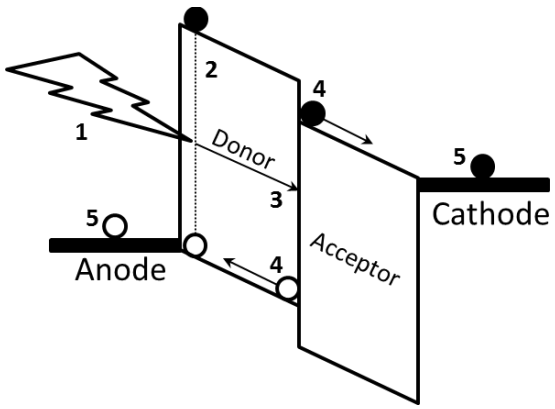

Figure 3.1 *Illustration demonstrating the operation of a typical organic photovoltaic cell. The absorption of a photon (1) results in an exciton (2). The exciton diffuses to the donor-acceptor interface (3). Here, exciton dissociation occurs, resulting in the generation of free charge carriers (4). These charge carriers are swept to the electrodes, where they are extracted to the external circuit (5).*

3.2 Principles of operation

I will discuss the various mechanisms in the order of operation and therefore begin by considering absorption. Organic semiconductors usually have high absorption coefficients ~10^5 cm^{-1} [2] and therefore, unlike their inorganic counterparts, can absorb almost all the incident photons for a given wavelength range in a thin-film of thickness ~100 nm [3]. This is an important aspect in their use for applications in OPV as they exhibit low charge carrier mobilities [4]. The majority of organic semiconductors have a band gap greater than or equal to ~2 eV (620 nm) [5]. This is not ideal for solar energy harvesting, as shown in the solar irradiance spectrum in Figure 3.2. A very successful and well-studied donor acceptor combination is that of poly (3-hexylthiophene) (P3HT) and [6, 6]-phenyl-C61-butyric acid methyl ester ($PC_{61}BM$). In this combination the acceptor is largely passive in terms of absorption i.e. the majority of absorption occurs in the donor, which I will demonstrate in Chapter 5 of this thesis. The success of this combination is somewhat surprising as the donor has only a slightly more favourable band gap of ~1.9 eV (~653 nm) [6]. Hence, one of the ways in which we can improve performance is to focus on increasing the absorption of the materials. Efforts are underway to achieve this by light trapping with spacers [7], lenses [8], gratings [9] or folding [10]; and by synthesising novel materials with lower band gaps [11].

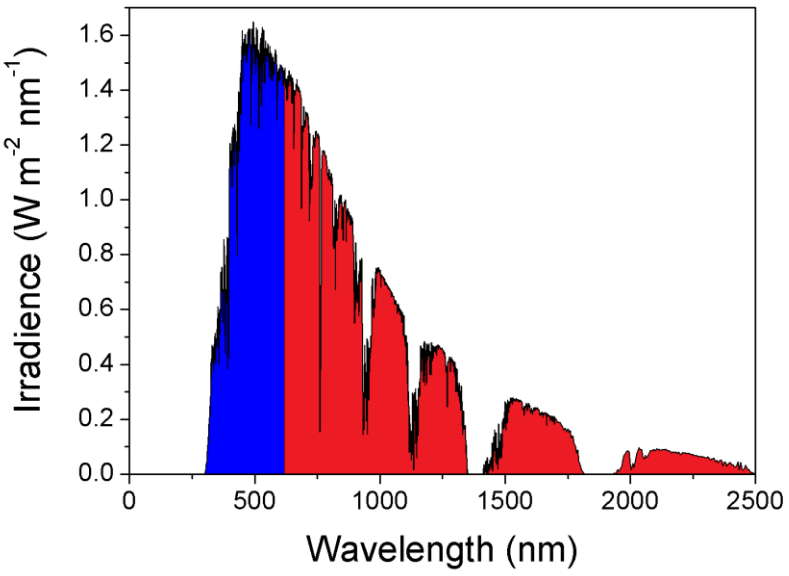

Figure 3.2 *AM 1.5G spectrum. The blue and red parts correspond to wavelengths above and below 2 eV (620 nm), respectively.*

The absorption of light leads to the formation of an exciton, i.e. a bound electron-hole pair. The exciton has a large binding energy due to the semiconductor having a low dielectric constant. In order to obtain free charge carriers we require energy much greater than the thermal energy (KT) to dissociate the exciton [12]. For example, if we were to fabricate an OPV solely with the donor polymer P3HT, and generate excitons in therein, the device would show a poor photovoltaic response [13]. In order to obtain an efficient device it is necessary to incorporate an acceptor [14], for example PCBM. The use of an acceptor provides us with an energy offset greater than the exciton binding energy, enabling exciton dissociation. This energy is sometimes referred to as the LUMO offset. It is worth mentioning that there is an on-going debate as to the nature of this driving force; however, there is good evidence to suggest that the process is governed by photo-induced electron transfer, which can be understood in terms of Marcus theory [15]. The timescale for this photo-induced charge transfer for a donor next to an acceptor is ~45 fs [16], much faster than the competing radiative relaxation process of ~1 ns [17].

Where the donor and acceptor meet, i.e. the donor-acceptor interface is called a heterojunction. The generation of free charge carriers in a typical organic photovoltaic device is a result of excitons forming in a donor and diffusing to the heterojunction for exciton dissociation. As previously mentioned excitons have an associated diffusion length, L_D. An ideal scenario is one where all the excitons formed within the donor diffuse to the heterojunction within their lifetime, i.e. within the exciton diffusion length, L_D. These lengths are small when compared with the film thicknesses required to absorb sufficient light [18, 19]. For this reason we observe a low exciton dissociation efficiency and poor device performance in planar-heterojunction devices [20], where the donor and acceptor lie in separate layers. Such a device is fabricated by depositing an acceptor on a previously deposited donor or vice versa. Here, the majority of excitons are formed within the donor at a distance larger than L_D from the heterojunction and therefore don't contribute to photocurrent as they recombine before reaching the heterojunction. Therefore, the exciton diffusion length, L_D, limits the generation of free charge carriers in organic photovoltaic devices and is intrinsically related to device performance. The most common method used to maximise the exciton dissociation efficiency is to dissolve the donor and acceptor in a common solvent and deposit them together, resulting in a film consisting of an interpenetrating network of donor and acceptor [21, 22]. In doing so, excitons formed in the donor are likely to diffuse to the donor-acceptor interface within L_D. Post exciton dissociation due

to the high hole mobility of the donor and high electron mobility of the acceptor, the holes and electrons can travel through the percolated pathways to the electrodes where they can be extracted from the device. The structure is called a bulk-heterojunction. To understand how an efficient organic photovoltaic device operates, it is necessary to consider exciton diffusion in combination with the morphology of the bulk-heterojunction [23]. For simplicity, I have only considered absorption in a donor material. However, if we were to replace $PC_{61}BM$ with an acceptor that absorbs strongly in the visible, for example $PC_{71}BM$, the acceptor may also contribute to the generation of free charge carriers [24].

On generation of free charge carriers we require them to travel to the electrodes where they can be extracted from the device. For this to occur it is essential that there are conductive pathways of each material within the active layer to the electrodes. Thus, allowing charges to travel to the necessary electrode within their lifetime. Ideally, charges should be extracted from the device as fast as possible to prevent recombination. If opposite charges meet they will recombine. The mechanisms largely responsible for charge transport are drift and diffusion [6]. The first mechanism involves holes and electrons "drifting" to the anode and cathode, respectively, under the influence of a built-in electric field. The built-in field is a potential gradient that arises from the electrodes having different work functions. The field aids in the collection of electrons and holes and is achieved by using a low and high work function metal, respectively. The other mechanism is the result of a concentration gradient, where the electrons and holes "diffuse" away from the heterojunction due to higher concentrations thereof at the heterojunction. Therefore, with a strong internal electric field we can have regime where charge transport is dominated by drift and in the scenario where we have no internal electric field charge transport can be driven by diffusion.

Inorganic semiconductors generally have a crystalline structure and therefore exhibit high charge carrier mobilities, whereas organic semiconductors are generally amorphous and therefore have low charge carrier mobilities. Low charge carrier mobilities impact strongly on device performance. For instance, restricting the active layer thickness and requiring a careful balance of donor and acceptor mobilities in order to prevent entering a regime of space-charge limited current (SCLC). Here an imbalance in charge extraction efficiency, i.e. where one charge is extracted with a greater efficiency than the other, results in the accumulation of charge at one of the electrodes and hence alters the charge transporting properties of the active layer, limiting charge extraction. Consider a semiconductor sandwiched between a cathode and an anode

electrode. The semiconductor is un-doped and free of traps or impurities. Thus, only the injected charge of density, n, may carry current. We assume the flow of current through the device to be the result of charge injection at the cathode and collection at the anode. The charge is in the form of electrons and is supplied by a reservoir contact i.e. an unlimited source. Neglecting the diffusion term, the current density, J, is given by:

$$J = \mathrm{ne}\mu\mathrm{E} \tag{3.1}$$

The distribution of charge i.e. the charge carrier density, n(x), will decrease with increasing distance, d, from the cathode:

$$n(x) = \frac{3\epsilon V}{4ed^2}\left(\frac{d}{x}\right)^{1/2} \tag{3.2}$$

While the field, E(x), increases:

$$E(x) = \frac{3V}{2d}\left(\frac{x}{d}\right)^{1/2} \tag{3.3}$$

The distribution of charge and profile of the electric field within our semiconducting material is easily visualised, and by making the substitution, one observes the current density, J_{SCLC}, under the SCLC regime:

$$J_{SCLC} = \frac{9}{8}\epsilon\mu\frac{V^2}{d^3} \tag{3.4}$$

Where ϵ and μ are the dielectric permittivity and charge carrier mobility, respectively. The equation comes in various forms and may be referred to as the Mott-Gurney square law, Child's law for solids, or the trap-free square law depending on its application [25]. Critically, the law shows the system to be space-charge limited, the result of a sufficiently large injection of a charge carrier density that leads to fields stronger than the applied bias [26]. Here, a current-voltage characteristic of the system would not follow Ohm's law, where:

$$E = V/d \tag{3.5}$$

Hence, one of the many requirements necessary to achieve an efficient organic photovoltaic device is to balance the transport of electrons and holes within the active layer, thus ensuring the charges can be extracted before they recombine [27, 28]. The final mechanism I wish to discuss is charge extraction. For efficient devices we need to ensure the charges having travelled to the electrodes can be extracted from the device without having to cross a high potential barrier, making the choice of electrodes important in the operation

and performance of devices. Generally, we obtain optimal performance when the work functions of the anode and cathode electrodes are matched to the HOMO of the donor and LUMO of the acceptor, respectively. These matched contacts are non-rectifying i.e. Ohmic. If the contacts are not matched they are referred to as Schottky contacts. Ohmic contacts tend not to distort or limit the performance of a device as the contact resistance between the semiconductor and the electrode is insignificant. The situation is very different with a Schottky contact. Here, a significant contact resistance results in rectifying behaviour. The type of contact achieved depends on the equalisation of the chemical potential or Fermi level between the electrode and semiconductor, on contact.

To demonstrate the formation of each contact, we consider an electrode and a semiconductor with work functions Φ_E and Φ_S, respectively. The work function of the semiconductor, Φ_S, corresponds to the difference in energy between the Fermi and Vacuum level. If the semiconductor is n-type an Ohmic contact can be achieved by means of ensuring $\Phi_E < \Phi_S$. In doing so, electrons will diffuse from the electrode into the semiconductor, resulting in the formation of an accumulation layer that is no barrier to the flow of electrons. When $\Phi_E > \Phi_S$, the electrons diffuse from the semiconductor into the electrode leaving behind a region or layer of positive charge, i.e. depletion region or layer. This layer acts as a potential barrier against the flow of electrons and is a rectifying Schottky contact. With a p-type semiconductor an Ohmic contact forms when $\Phi_E > \Phi_S$. On contact, the electrons flow from the semiconductor into the electrode leaving behind an accumulation layer containing empty states i.e. holes. With no potential barrier preventing the flow of electrons, they can travel from the electrode into the empty states of the semiconductor. This corresponds to the flow of holes from the semiconductor into the electrode. If $\Phi_E < \Phi_S$, the holes diffuse from the semiconductor into the electrode, resulting in the formation of a depletion layer and a Schottky contact. The aforementioned is an idealised picture that neglects the effect of surface states [29]. Naturally, a p-n junction with two depletion layers will result when an n-type and p-type semiconductor are brought together. This is usually the case as generally $\Phi_{p\text{-type}} > \Phi_{n\text{-type}}$. Efficient charge extraction is generally achieved by considering electrodes of different work functions. Typically, organic photovoltaic cells use a transparent electrode, indium tin oxide (ITO) as an anode and a reflecting electrode, aluminium as the cathode [30]. The reason for this, is that aluminium has a work function of ~4.2 eV [31], making it suitable for matching the LUMO of commonly used acceptors, for example $PC_{61}BM$ [6].

ITO, on the other hand, is not an ideal electrode as it has a work function (untreated) of ~4.7 eV [32] and therefore it is likely that $\Phi_E < \Phi_S$. There are many other reasons that make ITO an unfavourable electrode for organic photovoltaic cells, these include but are not limited to: requiring high temperature deposition, not solution-processable, finite resource and can exhibit structures greater than the thickness of the active layer, which can lead to a short-circuit in the device. However, we use ITO, as it is very effective when used in combination with poly (3, 4-ethylenedioxylenethiophene): poly (styrenesulfonate) (PEDOT:PSS) [33]. PEDOT:PSS, is a solution-processable interlayer, that is deposited on the ITO prior to deposition of the active layer. It prevents the ITO making contact with the cathode and provides a favourable work function alignment between the semiconductor and the ITO. In addition, the interlayer further improves device performance by acting as an electron-blocking (EBL) hole-transporting (HTL) layer. Interlayers are a hot topic in the field of organic photovoltaics [34, 35] and can be used between the semiconductor and the anode or cathode. Significant improvements in performance can be observed with the utilisation of such interlayers, as they exhibit interesting properties favourable for OPV applications [36].

Another effective method for ensuring an Ohmic contact, implemented at the cathode, is to deposit a low work function metal, for example calcium [37], lithium fluoride [38] etc. These low work function electrodes are deposited by thermal evaporation before the aluminium contact. Metal oxides can also be used, but these can be used at both the cathode and anode interface, for example TiO_2 [39] and MoO_3 [40, 41], respectively. In addition, they can be used as optical spacers [42, 43] to improve device performance by means of controlling the optical electric field distribution. Unlike PEDOT:PSS and calcium, metal oxides are not hygroscopic or reactive, respectively, and hence, improve device stability [39]. It is important to mention that when the cathode and anode form Ohmic contacts, the open-circuit voltage, Voc, for an ideal organic photovoltaic cell, is equal to the difference between the HOMO of the donor and the LUMO of the acceptor, i.e. $Voc \approx HOMO_D\text{-}LUMO_A$ [44]. However, if the contacts are non-Ohmic the Voc is governed by the difference in electrode work functions [45]. Other methods for improving charge extraction efficiency include but are not limited to: increasing the interface area between the electrodes and the semiconductor [10], inclusion of plasmonic structures on the electrodes [46] and the use of ferroelectric polymers [47]. Obviously, when and where we use the aforementioned charge extraction enhancing methods is entirely dependent on the device architecture and the properties of the active layer.

3.3 Performance parameters

Characterisation of a photovoltaic cell involves measuring the current-voltage (I-V) response in the dark and under illumination. In the dark, the response for an ideal cell is equivalent to a standard diode governed by the Shockley diode equation [29]:

$$I = I_s\left(exp\left(\frac{qV}{kT}\right) - 1\right) \tag{3.6}$$

Where: I is the diode current, I_s the saturation current, q the elementary charge, V the bias, i.e. the voltage across the diode, T the temperature, and k the Boltzmann constant. The equivalent circuit model can be used to help understand the current-voltage characteristics under illumination. This model was developed for inorganic photovoltaic cells, however, it can be applied to organic photovoltaic cells [48, 49]. The equivalent circuit for an ideal cell under illumination is shown in Figure 3.3 (left) [50].

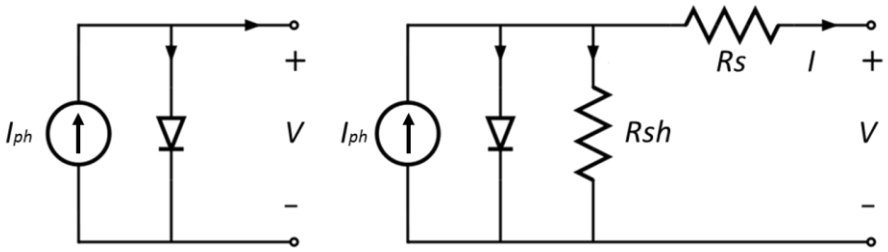

Figure 3.3 *Equivalent circuit of an ideal (left) and real (right) photovoltaic cell under illumination. Figure inspired by reference [51].*

Thus, the current is given by:

$$I = I_s\left(exp\left(\frac{qV}{kT}\right) - 1\right) - I_{ph} \tag{3.7}$$

Where, I_{ph} is the photo-induced current. The strength of the equivalent circuit model is that it allows us to use elementary circuit elements to explain some of the processes that occur in a photovoltaic device on illumination. Under the right conditions the model can accurately predict the current-voltage characteristic of an organic photovoltaic device [52]. Figure 3.3 (right), shows the equivalent circuit for a real photovoltaic device. Like an ideal cell, we have a current source and diode connected in parallel; however we also have parallel and series resistances, the shunt, R_{sh}, and series, R_s, resistance, respectively. These resistances account for losses in the device. These losses are discussed in later chapters, but in general R_s accounts for any drops in voltage across the

device, i.e. at the contacts and within the bulk, while R_{sh} accounts for the recombination of charge carriers, i.e. at the donor acceptor interface for example [53]. Hence, in a real device the equation from the equivalent circuit is given by [54]:

$$I\left(1+\frac{R_s}{R_{sh}}\right)-\frac{V}{R_{sh}}=I_s\left(exp\frac{q}{BKT}(V-IR_s)-1\right)-I_{ph} \tag{3.8}$$

Having the equation in this form, we can see an ideal scenario is one where the ideality factor, B, is equal to 1, R_{sh} is large and R_s is small. The result, equation 3.7 and a large fill factor, as shown in Figure 3.4. Various methods are available for extracting the R_{sh} and R_s, a popular method is to take the reciprocal of the slope at V=0 and > Voc, respectively [53].

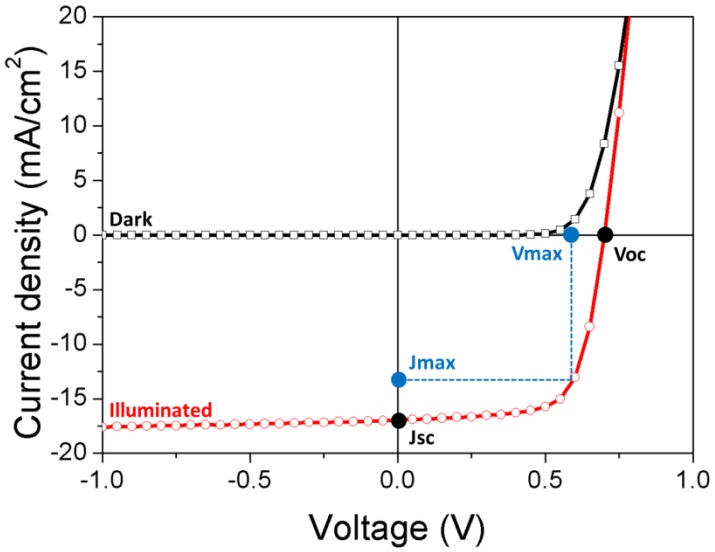

Figure 3.4 *J-V characteristics of an organic photovoltaic cell in the dark and under illumination.*

Fill factor, is a performance parameter, defined as the ratio of the maximum power output, i.e. where the product of the current and voltages are maximised, Jmax and Vmax, respectively, as shown in Figure 3.4 to the theoretical maximum obtainable power for the Jsc and Voc of the device:

$$Fill\ factor=\frac{Vmax\cdot Jmax}{Voc\cdot Jsc} \tag{3.9}$$

Where Voc is the open-circuit voltage and Jsc is the short-circuit current density.

The power conversion efficiency (PCE) is the main performance parameter used to compare photovoltaic technologies and is essentially the ratio of electrical power generated to incident optical power:

$$n = \frac{Vmax \cdot Jmax}{Pin} = \frac{Voc \cdot Jsc \cdot fill\ factor}{Pin} \tag{3.10}$$

Where, Pin is the photon flux incident on the cell, which usually corresponds to AM1.5 conditions (100 mW cm^{-2}).

Another important performance parameter is the external quantum efficiency (EQE). This quantity is sometimes referred to as the internal photon to current conversion efficiency (IPCE) and is a measure of the ability of the photovoltaic device to convert an incident photon of wavelength, λ (μm), into current:

$$EQE\ (\%) = \frac{1240 \cdot Jsc}{\lambda \cdot Pin} \tag{3.11}$$

Where Jsc is in A cm^{-2} and the incident photon flux at λ, Pin, is in W cm^{-2}. Measurements of EQE are vital in the characterisation of photovoltaic cells. They show the wavelength photo-response of the device and the integral of with the solar spectrum independently verifies the Jsc measured under the solar simulator shown in Chapter 4.

3.4 Device design

The two main types of architecture associated with organic photovoltaic cells are planar heterojunction, i.e. bilayer and bulk heterojunction devices, shown in Figure 3.5 (a) and (b), respectively. Planar heterojunction devices are achieved by depositing the acceptor and donor separately, while bulk heterojunctions are fabricated by depositing a blend of donor-acceptor.

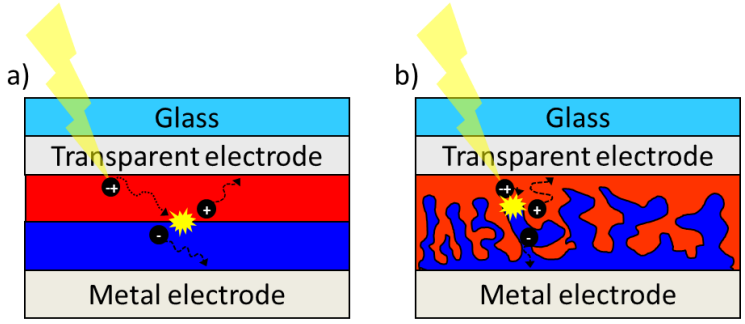

Figure 3.5 *Diagram illustrating the operation of a planar and bulk heterojunction organic photovoltaic cell, with the donor red and acceptor blue.*

In this thesis, I limit my discussion to the aforementioned types of architecture. Other architectures include but are not limited to: tandem [55-58], folded [10, 31] and structured photovoltaic cells [59-61]. The fabrication of organic photovoltaics is done either by vacuum deposition or solution-processing. Vacuum deposition is limited to small molecules as polymers decompose when exposed to heat. Hence, polymers are deposited using solution-processing techniques. It is also possible to fabricate devices with small molecules from solution. However, they used to exhibit low performances due to poor solubility [62]. However, recently there has been a dramatic increase in performance of small molecule devices [63-66]. Bulk heterojunction devices, achieved through deposition by means of solution-processing or co-evaporation usually outperform planar heterojunction devices, as the excitons are able to reach the donor-acceptor interface before they decay, as previously mentioned and shown in Figure 3.5. In keeping with the cost effective methodology of solution-processing, all the photovoltaic devices fabricated for this thesis have been by means of solution-processing. This excludes the deposition of the electrodes.

Having explored some of the critical challenges organic photovoltaics face, I will now discuss where my thesis contributes. In summary, the main limiting factors to organic photovoltaic performance include but are not limited to: incomplete absorption of the solar spectrum (as they usually exhibit narrow absorption bands), recombination of excitons by means of surface quenching at the electrodes or decay due to not reaching the donor-acceptor interface within the exciton diffusion length, low charge carrier mobilities which restrict the thickness of the active layer and mean that careful balancing of the charge carrier mobility is required, and ensuring appropriate contacts in regards to their stability and performance. This thesis attempts to address these challenges by means of investigating novel organic semiconducting materials for photovoltaic applications. Briefly, by chapter rather than order of operation, I demonstrate the importance of morphology and device design, investigate broad absorbing materials, and finally, I consider a small molecule with an interesting morphology that facilitates charge transport and device performance. To-date, optimisation of organic photovoltaic cells (and hence the process that govern operation) is best achieved by means of fabricating devices and considering the changes in morphology. This is done through altering the fabrication conditions, i.e. solvent, annealing, donor-acceptor concentration, electrodes etc.

3.5 Conclusion

In this chapter, I reviewed some of the literature on organic photovoltaics and discussed the principles of operation, including: absorption, exciton diffusion and dissociation and charge transport and extraction. In doing so, I introduced a few of the challenges they face and what can be done to overcome these in order to improve device performance. I demonstrated how the performance parameters are extracted from current-voltage (J-V) characteristics and what they mean in terms of the equivalent circuit model and finish the chapter by discussing the challenges my thesis attempts to address through investigating novel materials and device architectures.

3.6 References

1. Shaw, P.E., A. Ruseckas, and I.D.W. Samuel, *Exciton Diffusion Measurements in Poly(3-hexylthiophene).* Advanced Materials, 2008. **20**(18): p. 3516-3520.
2. Brütting, W., *Introduction to the Physics of Organic Semiconductors*, in *Physics of Organic Semiconductors*. 2006, Wiley-VCH Verlag GmbH & Co. KGaA. p. 1-14.
3. Coakley, K.M. and M.D. McGehee, *Conjugated Polymer Photovoltaic Cells.* Chemistry of Materials, 2004. **16**(23): p. 4533-4542.
4. Kim, G., et al., *Acceptor-acceptor type isoindigo-based copolymers for high-performance n-channel field-effect transistors.* Chemical Communications, 2014. **50**(17): p. 2180-2183.
5. Hoppe, H. and N.S. Sariciftci, *Organic solar cells: An overview.* Journal of Materials Research, 2004. **19**(07): p. 1924-1945.
6. Choy, W., *Organic solar cells: materials and device physics.* Springer-Verlag London, 2013.
7. Kyaw, A.K.K., et al., *Improved Light Harvesting and Improved Efficiency by Insertion of an Optical Spacer (ZnO) in Solution-Processed Small-Molecule Solar Cells.* Nano Letters, 2013. **13**(8): p. 3796-3801.
8. Peer, A. and R. Biswas, *Nanophotonic Organic Solar Cell Architecture for Advanced Light Trapping with Dual Photonic Crystals.* ACS Photonics, 2014.
9. Min, C., et al., *Enhancement of optical absorption in thin-film organic solar cells through the excitation of plasmonic modes in metallic gratings.* Applied Physics Letters, 2010. **96**(13): p. -.
10. Kim, J.B., et al., *Wrinkles and deep folds as photonic structures in photovoltaics.* Nat Photon, 2012. **6**(5): p. 327-332.
11. Cortizo-Lacalle, D., et al., *BODIPY-based conjugated polymers for broadband light sensing and harvesting applications.* Journal of Materials Chemistry, 2012. **22**(28): p. 14119-14126.
12. Gomes da Costa, P. and E.M. Conwell, *Excitons and the band gap in poly(phenylene vinylene).* Physical Review B, 1993. **48**(3): p. 1993-1996.
13. Novotny, C.J., E.T. Yu, and P.K.L. Yu, *InP Nanowire/Polymer Hybrid Photodiode.* Nano Letters, 2008. **8**(3): p. 775-779.
14. Tang, C.W., *Two-layer organic photovoltaic cell.* Applied Physics Letters, 1986. **48**(2): p. 183-185.
15. Coffey, D.C., et al., *An Optimal Driving Force for Converting Excitons into Free Carriers in Excitonic Solar Cells.* The Journal of Physical Chemistry C, 2012. **116**(16): p. 8916-8923.
16. Günes, S., H. Neugebauer, and N.S. Sariciftci, *Conjugated Polymer-Based Organic Solar Cells.* Chemical Reviews, 2007. **107**(4): p. 1324-1338.
17. Sariciftci, N.S., et al., *PHOTOINDUCED ELECTRON-TRANSFER FROM A CONDUCTING POLYMER TO BUCKMINSTERFULLERENE.* Science, 1992. **258**(5087): p. 1474-1476.
18. Ruseckas, A., P.E. Shaw, and I.D.W. Samuel, *Probing the nanoscale phase separation in binary photovoltaic blends of poly(3-hexylthiophene) and methanofullerene by energy transfer.* Dalton Transactions, 2009(45): p. 10040-10043.
19. Markov, D.E., et al., *Accurate Measurement of the Exciton Diffusion Length in a Conjugated Polymer Using a Heterostructure with a Side-Chain Cross-Linked Fullerene Layer.* The Journal of Physical Chemistry A, 2005. **109**(24): p. 5266-5274.
20. Antohe, S. and L. Tugulea, *Electrical and Photovoltaic Properties of a Two-Layer Organic Photovoltaic Cell.* physica status solidi (a), 1991. **128**(1): p. 253-260.
21. Yu, G., et al., *POLYMER PHOTOVOLTAIC CELLS - ENHANCED EFFICIENCIES VIA A NETWORK OF INTERNAL DONOR-ACCEPTOR HETEROJUNCTIONS.* Science, 1995. **270**(5243): p. 1789-1791.

22. Halls, J.J.M., et al., *Efficient photodiodes from interpenetrating polymer networks.* Nature, 1995. **376**(6540): p. 498-500.
23. Hedley, G.J., et al., *Determining the optimum morphology in high-performance polymer-fullerene organic photovoltaic cells.* Nat Commun, 2013. **4**.
24. Wright, I.A., et al., *Oligothiophene Cruciform with a Germanium Spiro Center: A Promising Material for Organic Photovoltaics.* Angewandte Chemie International Edition, 2012. **51**(19): p. 4562-4567.
25. M. Lampert and P. Mark, *Current injection in Solids.* Academic Press New York and London, 1970.
26. M, N. and R.W. Gurney, *Electronic Processes in Ionic Crystals, 1st ed.* Oxford University Press, 1940.
27. Sha, W.E.I., X. Li, and W.C.H. Choy, *Breaking the Space Charge Limit in Organic Solar Cells by a Novel Plasmonic-Electrical Concept.* Sci. Rep., 2014. **4**.
28. Mihailetchi, V.D., J. Wildeman, and P.W.M. Blom, *Space-Charge Limited Photocurrent.* Physical Review Letters, 2005. **94**(12): p. 126602.
29. Neamen, *Semiconductor Physics and Devices Basic Principles.* McGraw-Hill Companies, 2003. **Third Edition**.
30. Scharber, M.C., et al., *Design Rules for Donors in Bulk-Heterojunction Solar Cells—Towards 10 % Energy-Conversion Efficiency.* Advanced Materials, 2006. **18**(6): p. 789-794.
31. Lipomi, D.J. and Z. Bao, *Stretchable, elastic materials and devices for solar energy conversion.* Energy & Environmental Science, 2011. **4**(9): p. 3314-3328.
32. Parker, I.D., *Carrier tunneling and device characteristics in polymer light-emitting diodes.* Journal of Applied Physics, 1994. **75**(3): p. 1656-1666.
33. Meng-Yueh, L., et al. *Accurate measurement of performance of polymer solar cell with highly conductive PEDOT:PSS*. in *Photovoltaic Specialists Conference (PVSC), 2009 34th IEEE*. 2009.
34. Gu, C., et al., *Achieving High Efficiency of PTB7-Based Polymer Solar Cells via Integrated Optimization of Both Anode and Cathode Interlayers.* Advanced Energy Materials, 2014. **4**(8): p. n/a-n/a.
35. He, Z., et al., *Simultaneous Enhancement of Open-Circuit Voltage, Short-Circuit Current Density, and Fill Factor in Polymer Solar Cells.* Advanced Materials, 2011. **23**(40): p. 4636-4643.
36. He, Z., Zhong, Chengmei, Su, Shijian, Xu, Miao, Wu, Hongbin, Cao, Yong, *Enhanced power-conversion efficiency in polymer solar cells using an inverted device structure.* Nat Photon, 2012(591–595
).
37. Gupta, D., M. Bag, and K.S. Narayan, *Correlating reduced fill factor in polymer solar cells to contact effects.* Applied Physics Letters, 2008. **92**(9): p. -.
38. Tatsuki, Y., et al., *Flexible PTB7:PC 71 BM bulk heterojunction solar cells with a LiF buffer layer.* Japanese Journal of Applied Physics, 2014. **53**(2S): p. 02BE05.
39. Oh, H., et al., *Comparison of various sol–gel derived metal oxide layers for inverted organic solar cells.* Solar Energy Materials and Solar Cells, 2011. **95**(8): p. 2194-2199.
40. Cattin, L., et al., *MoO3 surface passivation of the transparent anode in organic solar cells using ultrathin films.* Journal of Applied Physics, 2009. **105**(3): p. -.
41. Hori, T., et al., *MoO3 buffer layer effect on photovoltaic properties of interpenetrating heterojunction type organic solar cells.* Thin Solid Films, 2009. **518**(2): p. 522-525.
42. Kim, J.Y., et al., *New Architecture for High-Efficiency Polymer Photovoltaic Cells Using Solution-Based Titanium Oxide as an Optical Spacer.* Advanced Materials, 2006. **18**(5): p. 572-576.
43. An, K.H., et al., *Organic photodetector with spectral response tunable across the visible spectrum by means of internal optical microcavity.* Organic Electronics, 2009. **10**(6): p. 1152-1157.

44. Mihailetchi, V.D., L.J.A. Koster, and P.W.M. Blom, *Effect of metal electrodes on the performance of polymer:fullerene bulk heterojunction solar cells.* Applied Physics Letters, 2004. **85**(6): p. 970-972.
45. Mihailetchi, V.D., et al., *Cathode dependence of the open-circuit voltage of polymer:fullerene bulk heterojunction solar cells.* Journal of Applied Physics, 2003. **94**(10): p. 6849-6854.
46. Morfa, A.J., et al., *Plasmon-enhanced solar energy conversion in organic bulk heterojunction photovoltaics.* Applied Physics Letters, 2008. **92**(1): p. 013504-013504-3.
47. Yuan, Y., et al., *Efficiency enhancement in organic solar cells with ferroelectric polymers.* Nat Mater, 2011. **10**(4): p. 296-302.
48. Yoo, S., B. Domercq, and B. Kippelen, *Intensity-dependent equivalent circuit parameters of organic solar cells based on pentacene and C60.* Journal of Applied Physics, 2005. **97**(10): p. -.
49. Xue, J., et al., *4.2% efficient organic photovoltaic cells with low series resistances.* Applied Physics Letters, 2004. **84**(16): p. 3013-3015.
50. Sze, S.M., *Physics of semiconductor devices, 2nd edition.* John Wiley & Sons, New York, 1981.
51. Mcphee, *http://en.wikipedia.org/wiki/Theory˙of˙solar˙cells*. Solar cell equivalent circuit-wiki common. **Theory of solar cells**.
52. Potscavage, W.J., A. Sharma, and B. Kippelen, *Critical Interfaces in Organic Solar Cells and Their Influence on the Open-Circuit Voltage.* Accounts of Chemical Research, 2009. **42**(11): p. 1758-1767.
53. Li, Y., et al., *Evaluation of methods to extract parameters from current–voltage characteristics of solar cells.* Solar Energy, 2013. **90**(0): p. 51-57.
54. BERNÈDE, J.C., *ORGANIC PHOTOVOLTAIC CELLS: HISTORY, PRINCIPLE AND TECHNIQUES.* Journal of the Chilean Chemical Society, 2008. **53**: p. 1549-1564.
55. You, J., et al., *A polymer tandem solar cell with 10.6% power conversion efficiency.* Nat Commun, 2013. **4**: p. 1446.
56. Sista, S., et al., *Highly Efficient Tandem Polymer Photovoltaic Cells.* Advanced Materials, 2009. **9999**(9999): p. NA.
57. Kim, J.Y., et al., *Efficient Tandem Polymer Solar Cells Fabricated by All-Solution Processing.* Science, 2007. **317**(5835): p. 222-225.
58. Rand, B.P., P. Peumans, and S.R. Forrest, *Long-range absorption enhancement in organic tandem thin-film solar cells containing silver nanoclusters.* Journal of Applied Physics, 2004. **96**(12): p. 7519-7526.
59. Fabregat-Santiago, F., et al., *Characterization of nanostructured hybrid and organic solar cells by impedance spectroscopy.* Physical Chemistry Chemical Physics, 2011. **13**(20): p. 9083-9118.
60. Park, J.Y., N.R. Hendricks, and K.R. Carter, *Solvent-Assisted Soft Nanoimprint Lithography for Structured Bilayer Heterojunction Organic Solar Cells.* Langmuir, 2011. **27**(17): p. 11251-11258.
61. Soldera, M., E. Estrada, and K. Taretto, *Geometric Light Trapping in 2D and 3D Structured Small Molecule Organic Solar Cells.* MRS Online Proceedings Library, 2013. **1493**: p. 317-322.
62. Liu, Y., et al., *Solution-processed small-molecule solar cells: breaking the 10% power conversion efficiency.* Sci. Rep., 2013. **3**.
63. Poe, A.M., et al., *Small molecule BODIPY dyes as non-fullerene acceptors in bulk heterojunction organic photovoltaics.* Chemical Communications, 2014. **50**(22): p. 2913-2915.
64. Lim, N., et al., *High-Performance Organic Solar Cells with Efficient Semiconducting Small Molecules Containing an Electron-Rich Benzodithiophene Derivative.* Chemistry of Materials, 2014. **26**(7): p. 2283-2288.
65. Mishra, A. and P. Bäuerle, *Small Molecule Organic Semiconductors on the Move: Promises for Future Solar Energy Technology.* Angewandte Chemie International Edition, 2012. **51**(9): p. 2020-2067.
66. Shang, H., et al., *A Solution-Processable Star-Shaped Molecule for High-Performance Organic Solar Cells.* Advanced Materials, 2011. **23**(13): p. 1554-1557.

Chapter 4

Experimental methods

4.1 Introduction

This chapter details the equipment and methods used to investigate novel materials for applications in organic photovoltaics. Several photophysical methods are considered. These include: absorption and photoluminescence spectroscopy, photoluminescence quantum yield (PLQY) and time-resolved luminescence. The methodology employed to measure contact angle and conductivity is described and details of the equipment used for morphological studies given. The chapter concludes on material and substrate preparation, and device fabrication and characterisation.

4.2 Absorption and photoluminescence spectroscopy

Absorption is important for any photovoltaic technology. Hence, when considering materials for solar energy harvesting, it is necessary to determine the strength and wavelengths at which a material absorbs. In addition, significant information can be obtained from the absorption spectra, regarding the properties of a material. This is very useful in the field of organic photovoltaics, as we often compare a material with some analogue. The theory governing the absorption of light in organic semiconducting materials was described in Chapter 2. The absorbance or optical density for a sample is defined as:

$$A = -log_{10}(T) \tag{4.1}$$

where T is the transmittance:

$$T = \left(\frac{I}{I_0}\right) \tag{4.2}$$

The fraction of light transmitted through a sample, I, to that entering the sample, I_0. This is related to the molar absorption coefficient, ε, through the equation:

$$A = \varepsilon \cdot c \cdot l \tag{4.3}$$

where, c is the concentration and l the optical path length of the sample.

In this work, steady state absorption measurements were performed with either a Varian Cary spectrophotometer or a Perkin-Elmer Lambda 950. Both instruments operate by means of a double beam configuration. Before acquiring absorption spectra, a reference sample is placed into each arm of the instrument in order to perform a baseline. In the majority of cases, this is achieved with cleaned fused silica substrates or solvent containing cuvettes, depending on whether the spectra of interest is to be acquired from a film or solution, respectively. In doing so, any difference between the arms is corrected with the instrument set to 100 % transmission. On completion, a reference sample is replaced with a fused silica substrate coated with an organic film or a cuvette containing a solution. With the reference in one arm and a sample in the other, the spectrum of absorption is recorded by means of equation 4.2 by scanning the wavelength of a monochromated lamp. While the instrument takes into consideration the absorption, reflection and scattering by the substrate or solvent containing cuvette, it does not account for any reflection or scattering by the organic film or solution. This is particularly important to bear in mind when characterising organic semiconductor films for photovoltaic applications, as tails in the absorption spectra at longer wavelengths may in some circumstances not arise from the absorption in the ~100 nm thick film, but as a result of reflection losses. These losses may occur at the air and film or film and substrate interface and can be comparable with the internal absorption losses [1]. In addition, molecular or polymer orientation and crystallisation can result in tails in the absorption spectra [2-4]. However, these reflection losses may be determined by means of an integrating sphere, for example [5].

Another useful steady state photophysical technique involves the measurement of photoluminescence (PL). In my studies a Jobin Yvon Fluoromax 2 fluorimeter was used to acquire photoluminescence spectra. The instrument uses a xenon lamp in combination with a monochromator to excite the sample. A photomultiplier tube (PMT) in single photon counting mode with a monochromator perpendicular to the excitation is used to collect the emission. The acquired emission spectra were corrected with a calibration curve provided by Jobin Yvon. This calibration curve corrects for the PMT exhibiting reduced sensitivity at longer wavelengths. During scans the instrument maintains a constant bandpass. Therefore, one must be acutely aware that the conversion of a fluorescence spectrum measured in wavelength, λ, into units of energy is not as straight-forward as one may perceive:

$$E = \frac{hc}{\lambda} \tag{4.4}$$

With a spacing of intervals in wavelength, dλ, being uneven a scaling factor must be applied to the recorded spectra, f(λ). The scaling factor can be derived by considering the conservation of energy:

$$f(E)dE = -f(\lambda)\mathrm{d}\lambda \tag{4.5}$$

where the minus arises from an increase in E causing a decrease in λ. Substituting equation 4.4 into 4.5:

$$f(E) = -f(\lambda)\frac{d\lambda}{dE} = -f(\lambda)\frac{d}{dE}\left(\frac{hc}{E}\right) = f(\lambda)\left(\frac{\lambda^2}{hc}\right) \tag{4.6}$$

Therefore, when carrying out the conversion with equation 4.4, the recorded spectra must be multiplied by (λ^2/hc). This factor is sometimes referred to as the Jacobian transformation [6]. For OPVs no emission is desired. However, if emission is observed, it may help our understanding of how a given material operates within a device [7-9].

4.3 Photoluminescence quantum yield

Photoluminescence quantum yield (PLQY) is a useful quantity to measure when considering materials for application in organic optoelectronics and is defined as:

$$\Phi = \frac{number\ of\ photons\ emitted}{number\ of\ photons\ absorbed} \tag{4.7}$$

in a photoluminescence measurement. When investigating materials for OLEDs, the measurement provides an upper limit on the efficiency of electroluminescence (EL) [5]. For OPVs, PLQY can provide a measure of efficiency at which photoluminescence of the donor is quenched by the acceptor [10]. PLQY measurements were performed under nitrogen with a Hamamatsu (C9920-02) absolute PLQY measurement system. The system consisted of an excitation source, monochromator, integrating sphere and CCD spectrometer, as shown in Figure 4.1.

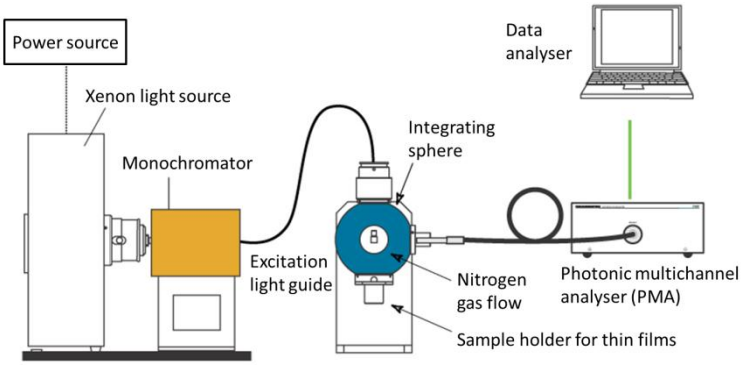

Figure 4.1 *Illustration of the Hamamatsu (C9920-02) absolute PLQY measurement system, adapted from reference [11].*

4.4 Time-resolved luminescence

Time-resolved luminescence measurements are useful for acquiring information relating to the dynamics of excited states. To prevent quenching by oxygen, organic semiconductor coated fused silica substrates were placed in a vacuum chamber. At ~2×10^{-5} mbar, the organic semiconductor film was excited with frequency doubled pulses (400 nm) from a titanium sapphire femtosecond laser (800 nm). The luminescence is resolved with a Hamamatsu streak camera. A schematic of the experimental setup is shown in Figure 4.2.

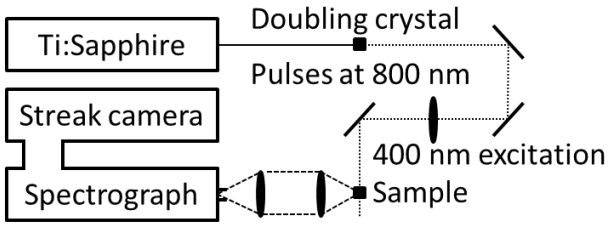

Figure 4.2 *Schematic of time-resolved luminescence experimental setup. Excitation source shown is a titanium sapphire femtosecond laser, 100 fs pulses with a repetition rate of 80 MHz.*

The luminescence from the sample is focussed on and collected by a spectrograph, as shown in Figure 4.2. The spectrograph disperses the light onto the photocathode of the streak camera. The photocathode converts the light into electrons which are then accelerated along the streak tube. When they make contact with the phosphor screen, photons are emitted and recorded by a CCD camera. The instrument response or resolution is ~1-2 ps and is limited by the scanning of the electric field back and forth along the length of the tube. It is the acceleration and arrival of electrons from the photocathode to the phosphor screen, respectively, under the presence of a time-varying electric field that gives rise to photoluminescence spectra with temporal information, as shown in Figure 4.3.

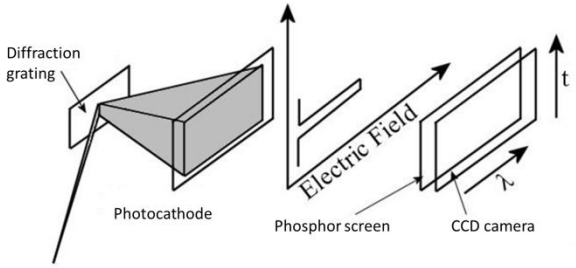

Figure 4.3 *Schematic illustrating the streak camera's principle of operation, adapted from reference [12].*

4.5 Contact angle measurements

When fabricating photovoltaic cells by means of solution-processing, it is essential to consider wetting, especially when using techniques such as spin-coating. Poor wettability of a surface can lead to the inadequate deposition of subsequent layers, resulting in low efficiencies and making device fabrication difficult, as the solution detaches easily from the substrate. In a conventional OPV, wettability comes into play when depositing the hole-transporting (HTL) electron-blocking layer (EBL) PEDOT:PSS and the active layer. Contact angle, α, is a measure of wettability, as shown in Figure 4.4.

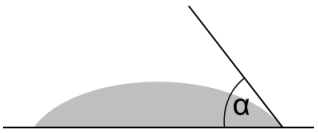

Figure 4.4 *Schematic showing the contact angle for a liquid drop on a solid surface.*

The contact angle provides information on whether a surface is hydrophobic, hydrophilic or somewhere in-between, as shown in Figure 4.5. Typically, contact angles of 90 degrees or greater show poor wettability, while those under 90 degrees may have good or typical wettability.

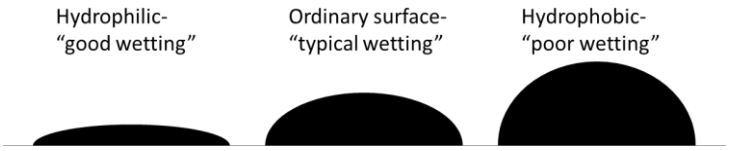

Figure 4.5 *Schematic illustrating: good, typical and poor wettability.*

Contact angle measurements were performed with a positioning stage, dosing needle and a Nikon D5200. Drop analysis was carried out with Image J software using two different approaches, one based on the Young-Laplace equation (LB-ADSA) [13] and the other on a B-spline snake-based approach [14]. Figure 4.6 shows an image of a drop of deionised water on an untreated substrate. The contact angle was determined for the reference to be 90.9 ± 0.3 and 91.4 ± 0.3 degrees using the aforementioned approaches, respectively.

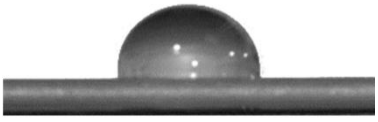

Figure 4.6 *Image of a drop of deionised water on glass substrate.*

4.6 Conductivity measurements

Two techniques were used to measure the conductivity: a fully automated four-point probe method using a Jandel instrument, and a two-point electrode method. The Jandel instrument operates by using two sets of electrodes for current-sourcing and voltage-sensing, and is a useful instrument for determining conductivity of inorganic semiconductors, conductive polymers and electrodes, for example indium tin oxide (ITO). However, when measuring soft films the method can be ineffective, and in this scenario we resort to using the two-point electrode approach, shown in Figure 4.7.

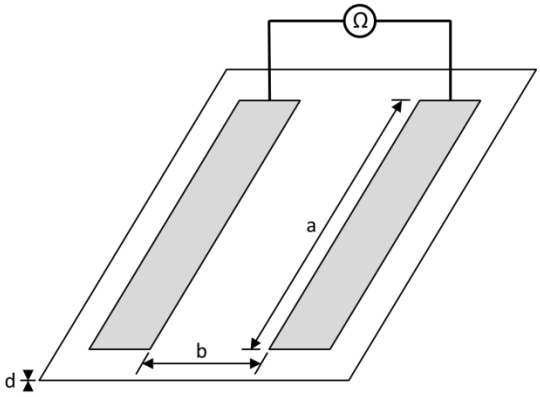

Figure 4.7 *Schematic illustrating a two-point probe experimental setup used to measure conductivity.*

The resistivity, ρ, of a film measured using the two-point electrode approach shown in Figure 4.7, is given by:

$$\rho = R \cdot d \cdot \frac{a}{b} \tag{4.8}$$

Where a: length of the contacts
b: distance between the contacts
d: film thickness
R: resistance

Thus, the conductivity is:

$$\sigma = \frac{1}{\rho} \tag{4.9}$$

When comparing thin-films we generally use sheet resistance:

$$R_S = \frac{\rho}{d} \tag{4.10}$$

4.7 Photovoltaic fabrication and characterisation

Before fabricating a device, the morphology of the active layer was studied. This was achieved by depositing the active layer on fused silica substrates and investigating the morphology with some of the aforementioned techniques in combination with several microscopies. These microscopies included: atomic force microscopy (AFM), scanning electron microscopy (SEM), far-field microscopy and confocal fluorescence microscopy.

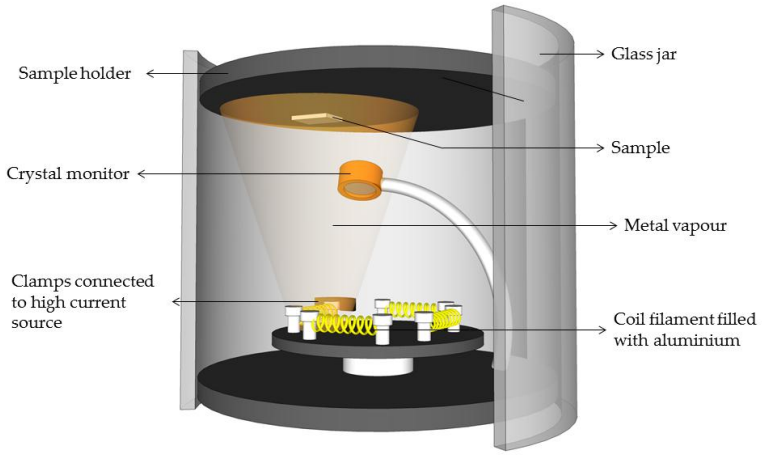

Figure 4.8 *Schematic of a thermal evaporator. Courtesy of Kapil Debnath [15].*

Satisfied with the morphology and quality of a film, OPVs were fabricated. The OPVs fabricated in this work were done so using a bottom up approach. Hence, fabrication started with the bottom contact, ITO. ITO coated glass substrates were etched in hydrochloric acid to pattern a 4 mm wide anode. The substrates were cleaned in an ultrasonic bath with acetone, isopropyl alcohol (IPA) and de-ionised water successively. Once cleaned, the substrates were dried with nitrogen and placed into a plasma asher. Post ashing, a layer of PEDOT:PSS was deposited by spin-coating. The PEDOT:PSS coated ITO substrates were then dried on a hotplate before being placed into a glovebox for active layer deposition. After spin-coating the active layer, devices were placed into an evaporator, Figure 4.8, for deposition of the top contact. A completed device is shown in Figure 4.9.

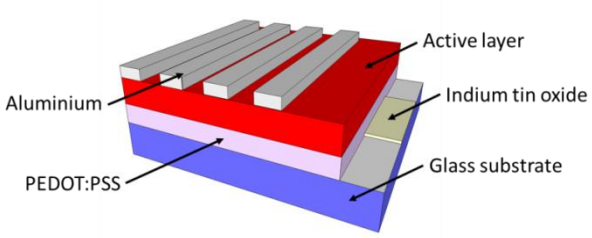

Figure 4.9 *Schematic of a typical organic photovoltaic device.*

Before removing devices from the glovebox for characterisation, the devices are encapsulated with a UV activated optical adhesive. Encapsulation helps prevent moisture and oxygen from entering the device and degrading OPV performance. In operation, light travels through the PEDOT:PSS coated ITO glass substrate into the active layer where is it absorbed. The thickness of the active layer is determined with a Dektak 150 M stylus profiler. Typical thicknesses are ~100 nm. The active area is defined as the region where the electrodes overlap, as shown in Figure 4.10. However, for reasons that will soon become clear, this overlap does not describe the active area of the device. The fabrication procedure discussed serves as a brief overview, as a detailed description is provided in each experimental chapter. This is a consequence of the procedure being adapted to each study. Additionally, information on where the materials were sourced and their characteristics are also presented in the experimental section of each chapter.

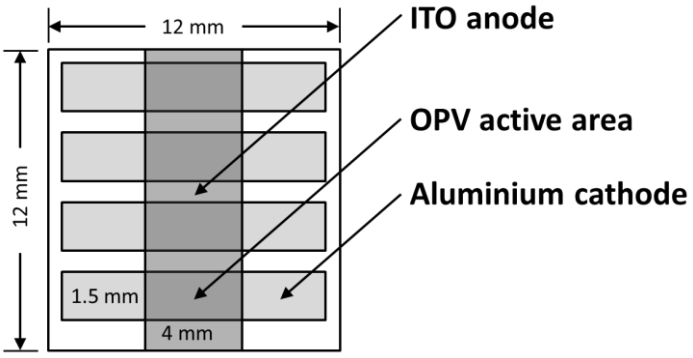

Figure 4.10 *Schematic showing a plane view of an OPV device and illustrates four individual devices each with an active area of 0.06 cm². For some studies OPVs were fabricated with an active area of 0.08 cm².*

Electrical characterisation is an essential component of assessing materials for photovoltaic applications. Furthermore, using the performance parameters outlined in Chapter 3, we can identify the shortfalls and optimise accordingly. The optimisation of an OPV can be broken down into two categories: device architecture and active layer morphology. These two categories are not independent from each other. Often varying a single parameter in either category leads to or requires changes in another, and alters the properties of the category under consideration. This makes the optimisation of OPVs challenging. To facilitate the optimisation we refer back to the aforementioned techniques in order to identify and understand the changes, for example in morphology, and correlate these changes with those of performance.

To give some examples, first we consider the device architecture. Here, we may wish to change the contacts or alter their thickness or properties. It is also possible to explore different device structures, as described in Chapter 3. In terms of the active layer, we may wish to vary: thickness, solvent, annealing conditions, and the materials and concentrations thereof, i.e. the donor-acceptor ratio. In doing so, one would hope to achieve optimal performance, i.e. power conversion efficiency (PCE), for a given material. Measurements of PCE are performed at 100 mW cm^{-2} with a solar simulator from KHS, Germany. The spectrum of the solar simulator is overlaid with a standard reference spectrum, AM 1.5G for the purpose of comparison, Figure 4.11. AM refers to the air mass coefficient and represents the path length that light must travel through the atmosphere normalised to the shortest possible path length, i.e. directly overhead. If we assume the atmosphere to be flat we can use the relation that AM is equal to one divided by COS(Θ). Therefore, the approximate angle from the zenith path length, i.e. directly overhead for an AM of 1.5 is 48.2 degrees. This angle is representative of mid-latitudes and therefore has been adopted by the solar industry for all standardised testing of terrestrial photovoltaic modules. The reference spectra includes direct and diffusive radiation. This is indicated by the G, which stands for global. Having a standard reference spectrum helps research groups and companies around the world to compare photovoltaic modules with each other. Light intensities from the solar simulator are verified with a calibrated reference cell.

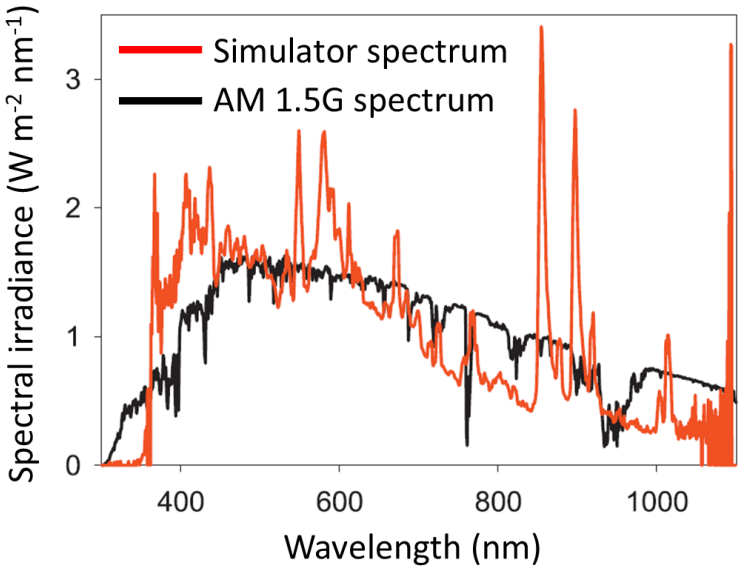

Figure 4.11 *Spectrum of solar simulator (red) and AM 1.5G standard spectrum (black).*

An important aspect of fabrication that can impact characterisation is the top contact. It is essential to evaporate the top contact slowly in order not to short-circuit the device, and to make certain the contact is of a suitable thickness ~200 nm, so as not to be damaged by the spring-loaded contacts of the sample holder. The characterisation itself involves applying a range of voltages to a device using a Keithley 2400 source-measure unit, typically, -1 to 1 V with a voltage step of 0.05 V every 200 ms, depending on the device type. The result is a J-V characteristic that can be used to extract performance parameters and compare with other photovoltaic technologies.

To acquire spectral information on the cell's response and to verify the short-circuit current density (Jsc), or to be able to apply a spectral mismatch correction factor, M, it is necessary to perform an incident photon to current conversion efficiency (IPCE) or external quantum efficiency (EQE) measurement. The experimental setup consisted of a Xenon lamp, Bentham TMc300 monochromator, optical fibre, Keithley 6517A picoammeter and an NPL calibrated photodiode. Monochromatic light is coupled into the optical fibre, which is used to illuminate the reference photodiode in the dark from short to long wavelengths in steps of 1 nm. The photocurrent is monitored at 0 V. The procedure is repeated for the test cell thus allowing the external quantum efficiency (EQE), denoted as QE_{SC}, of the test cell to be determined using the following equation:

$$QE_{SC}(\lambda) = \frac{QE_{NPL} \cdot I_{SC}}{I_{NPL}} \cdot 100\,\% \tag{4.11}$$

Where: QE_{NPL} is the quantum efficiency (λ) of the NPL photodiode, which is provided by the company. I_{SC} and I_{NPL} are the currents measured for the test cell and NPL photodiode at a given wavelength (λ), respectively. When performing this measurement it is essential that all of the light coming out of the optical fibre is incident on the device, thus ensuring the incident light intensity is the same on both the NPL photodiode and test cell. If the size of the imaged spot is larger than the active area of the device it underestimates the EQE and therefore the calculated Jsc, as the Jsc can be calculated by means of integrating the EQE with the AM 1.5G solar spectrum.

A strong desire amongst the research community for efficient photovoltaic devices combined with the fact that efficiency is often used as the sole performance parameter for evaluating and comparing photovoltaics with other photovoltaic technologies, means that care must be taken when carrying out efficiency measurements. While, a J-V characteristic is simple to

understand and acquire, the errors arising from the measurement can be difficult to interpret and understand. A great source of error, which is still causing issues today, is defining the active area of a photovoltaic cell incorrectly. The field of organic photovoltaics has grown dramatically in recent years with many new researchers from a variety of backgrounds. Having such an influx of researchers from areas other than the photovoltaic community resulted in a tendency for researchers to use the overlap of the electrodes to define the active area of a device. This practice has made it difficult to compare some photovoltaic technologies, as it results in an over estimation in performance. Unfortunately, some groups have yet to adopt masking their devices and are still publishing erroneous efficiencies [16]. The use of an opaque mask with a well-defined aperture can be used to ensure the active area is correct. A suitable mask should not reflect or scatter light and must be thin so as not to shadow the cell being tested [17]. The reasons for the active area being larger than that defined by the electrode overlap, is a result of polymer based cells exhibiting an increase in conductivity when under illumination and the use of conductive PEDOT:PSS as a hole-transporting (HTL) electron-blocking layer (EBL).

Device characterisation with a simulator is never going to be perfect, even the best simulators are divergent [17]. Hence, one must be extremely careful when positioning samples under a simulator. The position must be clearly marked, kept constant and away from hot spots to allow for good comparison of devices. In addition, it is common practice to have more than one device on a single substrate. To ensure they all experience a similar illumination they should all be positioned close together. It would be extremely difficult and time consuming to replicate the testing conditions of the certified national laboratories and this is not necessary, but it is good practice to try and mitigate the source of potential errors within the measurement. Another potential error regards the light source in the solar simulator. What lamp the simulator uses with which filters is important, but also monitoring the lamp with age is essential as the intensity and spectra will change with time.

In terms of calibrating the solar simulator a technique that is becoming ever more popular among the organic photovoltaic community is to use a calibrated Si reference cell with meter [18]. These are available from Newport. It is important to choose a reference cell that has a similar response to the test cells. In this work I largely used a calibrated Si reference cell with a KG-5 window. In certain situations it is necessary to apply a spectral mismatch factor, M, to the J-V characteristic this arises when the reference cell and the test cell have dissimilar spectral responses and the reference AM 1.5G spectrum

is different from the spectrum of the source, both cases are inevitable. However, in some situations the error can't be ignored. Whether or not the error is significant can be established by considering the short-circuit current density calculated from the EQE to that measured under the solar simulator, as shown in equation 4.12.

$$I_{TR} = A_T \int_{\lambda_1}^{\lambda_2} E_R(\lambda) S_T(\lambda) d\lambda \tag{4.12}$$

This equation provides the short-circuit current of a test cell with a spectral response $S_T(\lambda)$ under a reference spectral irradiance $E_R(\lambda)$. Here, the area of the test cell is denoted by A_T and the integral limits of λ govern the spectral range of the test cell. Therefore, the fractional error of the test cell under the simulator I_{TS} to that when it is under the reference spectrum I_{TR} is given by:

$$F = \frac{I_{TS}}{I_{TR}} = \frac{\int_{\lambda_1}^{\lambda_2} E_S^*(\lambda) S_T(\lambda) d\lambda}{\int_{\lambda_1}^{\lambda_2} E_R(\lambda) S_T(\lambda) d\lambda} \tag{4.13}$$

Where $E^*_S(\lambda)$ is the spectral irradiance of the solar simulator and the A_T cancels out algebraically. As mentioned, we use a calibrated reference cell to adjust the simulator until $I_{RS}=I_{RR}$. In doing so:

$$\frac{I_{RS}}{I_{RR}} = 1 = \frac{\int_{\lambda_1}^{\lambda_2} E_S^*(\lambda) S_R(\lambda) d\lambda}{\int_{\lambda_1}^{\lambda_2} E_R(\lambda) S_R(\lambda) d\lambda} \tag{4.14}$$

Rearranging:

$$1 = \frac{I_{RS}}{I_{RR}} \cdot \frac{\int_{\lambda_1}^{\lambda_2} E_R(\lambda) S_R(\lambda) d\lambda}{\int_{\lambda_1}^{\lambda_2} E_S^*(\lambda) S_R(\lambda) d\lambda} \tag{4.15}$$

By multiplying equation 4.13 with 4.15:

$$F = \frac{I_{TS}}{I_{TR}} = \frac{I_{RS}}{I_{RR}} \cdot \frac{\int_{\lambda_1}^{\lambda_2} E_S^*(\lambda) S_T(\lambda) d\lambda}{\int_{\lambda_1}^{\lambda_2} E_R(\lambda) S_T(\lambda) d\lambda} \cdot \frac{\int_{\lambda_1}^{\lambda_2} E_R(\lambda) S_R(\lambda) d\lambda}{\int_{\lambda_1}^{\lambda_2} E_S^*(\lambda) S_R(\lambda) d\lambda} \tag{4.16}$$

This can be simplified to give:

$$\frac{I_{TS}}{I_{TR}} = \frac{I_{RS}}{I_{RR}} \cdot M \tag{4.17}$$

Thus, we have the well-known for of the spectral mismatch factor:

$$I_{TR} = \frac{I_{TS}}{M} \cdot \frac{I_{RR}}{I_{RS}} \tag{4.18}$$

Hence, if we were to ensure $I_{RS}=I_{RR}$ then the short circuit current would be given by:

$$I_{TR} = \frac{I_{TS}}{M} \tag{4.19}$$

One of the parameters necessary to calculate the spectral mismatch factor, M, is the spectral response of the test cell. As previously mentioned, this can be acquired by carrying out an IPCE measurement. It is therefore important to make sure the measurement is accurate by ensuring the output of the optical fibre is confined to the active area of the reference and test cell.

4.8 References

1. Kajzar, *Organic Thin Films for waveguiding non-linear optics.* Gordon and Breach Publishers, 1996.
2. Wright, I.A., et al., *Oligothiophene Cruciform with a Germanium Spiro Center: A Promising Material for Organic Photovoltaics.* Angewandte Chemie International Edition, 2012. **51**(19): p. 4562-4567.
3. Arumugam, S., et al., *Charge transport in a two-dimensional molecular organic semiconductor.* Journal of Materials Chemistry C, 2014. **2**(1): p. 34-39.
4. Kim, Y., et al., *A strong regioregularity effect in self-organizing conjugated polymer films and high-efficiency polythiophene:fullerene solar cells.* Nat Mater, 2006. **5**(3): p. 197-203.
5. Greenham, N.C., et al., *Measurement of absolute photoluminescence quantum efficiencies in conjugated polymers.* Chemical Physics Letters, 1995. **241**(1-2): p. 89-96.
6. Mooney, J. and P. Kambhampati, *Get the Basics Right: Jacobian Conversion of Wavelength and Energy Scales for Quantitative Analysis of Emission Spectra.* The Journal of Physical Chemistry Letters, 2013. **4**(19): p. 3316-3318.
7. Shaw, P.E., A. Ruseckas, and I.D.W. Samuel, *Exciton Diffusion Measurements in Poly(3-hexylthiophene).* Advanced Materials, 2008. **20**(18): p. 3516-3520.
8. Shaw, P.E., A. Ruseckas, and I.D.W. Samuel, *Distance dependence of excitation energy transfer between spacer-separated conjugated polymer films.* Physical Review B (Condensed Matter and Materials Physics), 2008. **78**(24): p. 245201.
9. Ruseckas, A., P.E. Shaw, and I.D.W. Samuel, *Probing the nanoscale phase separation in binary photovoltaic blends of poly(3-hexylthiophene) and methanofullerene by energy transfer.* Dalton Transactions, 2009(45): p. 10040-10043.
10. Schwenn, P.E., et al., *A Small Molecule Non-fullerene Electron Acceptor for Organic Solar Cells.* Advanced Energy Materials, 2011. **1**(1): p. 73-81.
11. Photonics, H., *Hamamatsu (C9920-02) absolute PLQY measurement system.* Manual, 2009.
12. Wood, P., *Conformational disorder and the degree of conjugation in conjugated polymers.* Thesis (PhD) University of St Andrews, 2002.
13. Stalder, A.F., et al., *Low-bond axisymmetric drop shape analysis for surface tension and contact angle measurements of sessile drops.* Colloids and Surfaces A: Physicochemical and Engineering Aspects, 2010. **364**(1–3): p. 72-81.
14. Stalder, A.F., et al., *A snake-based approach to accurate determination of both contact points and contact angles.* Colloids and Surfaces A: Physicochemical and Engineering Aspects, 2006. **286**(1–3): p. 92-103.
15. Kapil Debnath, *Photonic crystal cavity based architecture for optical interconnects.* Thesis (PhD) University of St Andrews, 2013.
16. Meng-Yueh, L., et al. *Accurate measurement of performance of polymer solar cell with highly conductive PEDOT:PSS*. in *Photovoltaic Specialists Conference (PVSC), 2009 34th IEEE*. 2009.
17. Snaith, H.J., *How should you measure your excitonic solar cells?* Energy & Environmental Science, 2012. **5**(4): p. 6513-6520.
18. Shrotriya, V., et al., *Accurate Measurement and Characterization of Organic Solar Cells.* Advanced Functional Materials, 2006. **16**(15): p. 2016-2023.

Chapter 5

Photovoltaic efficiency enhancement by fluorinated doped PEDOT:PSS

Overview

In this chapter, I describe an on-going study investigating organic photovoltaic efficiency enhancement through alteration of the PEDOT:PSS interlayer by means of fluorinated doping. As the investigation is focussed on refining device design, it requires reproducible cells, i.e. cells with consistent active layer morphology. To satisfy this requirement we have based our devices on P3HT:$PC_{61}BM$ and PTB7:$PC_{71}BM$. Fluorinated doping was implemented with two different doping agents, a sulfonic acid surfactant (FOS) and a sulfonic fluorinated ionomer (PFI), and were individually studied and found to alter the wettability, conductivity and work function of the PEDOT:PSS interlayer. By controlling these parameters it was possible to increase the efficiency of our photovoltaic cells by ~15 %. In doing so, we have managed to achieve EQEs and PCEs that are amongst the highest reported in the field of organic photovoltaics with a conventional architecture, i.e. not inverted, tandem etc. For the most successful cell, a PCE of 8.26 % was realised.

Photophysical, conductivity (two-probe) and contact angle measurements, combined with the preparation and characterisation of photovoltaic cells were performed under the supervision of Dr Pascal Andre and Professor Ifor D. W. Samuel, at the University of St Andrews. Project student Khalid Marbou assisted in the preparation of solutions. Haeri Kim and Professor Dong-Wook Kim were in charge of the near-field characterisation at Ewha Womans University. Dr Tetsuya Aoyama performed the Kelvin probe and UPS measurements with Aiko Nakao at Riken, Wako, Saitama.

5.1 Introduction

PEDOT:PSS is widely used in organic photovoltaics for the purposes described in Chapter 3. The sulfonate groups withdraw electrons from the backbone of the PEDOT, transforming the electronic state of the chain from neutral to polycationic. Hence, the PSS serves a dual purpose of oxidising the PEDOT moieties and stabilising the otherwise insoluble polymer in an aqueous solution. PEDOT:PSS has been intensely investigated and used for a wide-variety of applications due to its properties. Studies on PEDOT:PSS have shown that subtle changes in molecular conformation can dramatically alter the electronic properties, amongst others. A wide-variety of methods can be used to alter the properties. These include the use of co-solvents or post treatments for example, alcohols, acids and surfactants etc. Treatments can result in work functions ranging from 4.0-5.7 eV and conductivities greater than 1000 S cm^{-1} [1-13]. The ease at which these can be performed and their ability to tune the properties of PEDOT:PSS has resulted in the use thereof in a wide-variety of technologies including: light emitting diodes [14-18], sensors [19, 20], transistors [21-24] and photovoltaic cells [25-28]. For the latter, modified PEDOT:PSS interlayers have resulted in improved PCEs and facilitated the development of innovative cells for example, semi-transparent, flexible and ITO free photovoltaic cells with comparable efficiencies [29-36].

Having solution properties orthogonal to water and oil derivatives, fluorinated materials can be of significance in creating barriers or controlling colloidal solubilisation, surface properties, or even in completing chemical reactions in their original environments [37-40]. Due to its high electronegativity, fluor is commonly used in push-pull molecular design [41]. In order to develop PDMS based stretchable electrodes for P3HT:$PC_{61}BM$ OPVs, a non-ionic ethoxylated fluorosurfactant was employed [32]. While a similar non-ionic material was blended with PEDOT:PSS to facilitate inverted photovoltaic cells with tunable efficiency and prolonged lifetimes [42]. (Heptadecafluoro-1,1,2,2-tetra-hydrodecyl) triethoxysilane spin-coated on-top of PEDOT:PSS and annealed at 180 ˚C created a silica-based fluorinated spacer above which pentacene could be deposited. The interface facilitated 3-dimenstional crystalline growth, the development of interfacial dipole moments through the accumulation of negative charges that enhanced the built-in potential across the devices, resulting in increased open-circuit voltages, hole transport and device efficiency [43]. Germack et al. studied SiO_2, PEDOT:PSS and poly(thienothiophene):perfluorinated ionomer interfaces in P3HT:$PC_{61}BM$ devices and revealed that whilst segregation at the buried interface near the

HTL could be greatly impacted by its surface energy, devices made with the latter two blends led to OPVs with similar characteristics [44].

In this chapter, I demonstrate the use of two anionic fluorinated materials, a perfluorinated ionomer (PFI) and perfluorooctanesulfonic acid (FOS), as doping agents for PEDOT:PSS. The selection of these materials was driven by their similar composition (fluorinated and sulfonic acid) and allows for comparison of the effects of doping with a polymer (PFI) or small molecule (FOS) on the properties of PEDOT:PSS and device performance. In doing so, I attempt to contradistinguish the relative impacts of work function, conductivity, and surface alterations on organic photovoltaic device performance.

5.2 Materials

The two photoactive blends used in this work, were P3HT:$PC_{61}BM$ and PTB7:$PC_{71}BM$. These blends were selected for their ability to form active layers with a reproducible morphology. The procedure employed in order to achieve an optimal P3HT:$PC_{61}BM$ morphology was acquired from [45] and [46]. However, post-fabrication annealing at 140 °C for 30 minutes, produced aggregates through the molecular diffusion of $PC_{61}BM$, shown in Figure 5.18 of the appendix. The aggregates are believed to be $PC_{61}BM$, which is evidence by fluorescence microscopy, shown in Figure 5.19 of the appendix and is supported in [47]. Hence, in order to prevent crystal or aggregate growth annealing was performed at 130 °C for 15 minutes, shown in Figure 5.20 of the appendix.

To achieve an optimal PTB7:$PC_{71}BM$ morphology it is necessary to include additive diiodooctane (DIO) into the solution prior to spin-coating the active layer. The use of additive has profound implications on device performance if the host solvent is chlorobenzene. We have shown said OPVs without additive to suffer from high levels of recombination, and that this leads to poor charge extraction and limits device performance [48].

Aggregates of $PC_{71}BM$ are responsible for the high levels of recombination. These are not present with additive; instead elongated polymer and fullerene-rich fibre like structures are observed. These elongated domains are shown to minimise recombination and improve charge extraction efficiency by providing a concentration gradient for directional charge diffusion. The charge extraction efficiencies determined with and without additive are approximately 80 and 45 %, respectively [48]. Additives like DIO are most effective when the boiling point is higher than the host solvent. This prolongs the time for thin film formation and the interaction between the additive and the less soluble component of the blend, which in our case is the $PC_{71}BM$ [49].

Figure 5.21 of the appendix shows J-V characteristics for PTB7:$PC_{71}BM$ cells fabricated from chlorobenzene with and without DIO. With adding 3 % of DIO per volume the short-circuit current density goes from 9.17 to 15.45 mA/cm^2. Consequently, the PCE increases from 3.15 to 6.34 %. Naturally, a dramatic change in morphology through the addition of DIO is unfavourable for our investigation, as small variations, for example in the quality and quantity of DIO, can lead to large variations in device performance. Figure 5.22 of the appendix shows the J-V characteristics for organic photovoltaic cells fabricated from dichlorobenzene with and without DIO. The results show that with the inclusion of 3 % per volume of DIO, the short-circuit current density increases from 14.86 to 15.94, and with this increase so increases the PCE from 6.13 to 7.18 %. The variation in device performance with and without additive is not as profound in these devices as it is for those fabricated from chlorobenzene. The reason for this is that $PC_{71}BM$ is more soluble in dichlorobenzene than it is in chlorobenzene, and dichlorobenzene and DIO both have higher boiling points than chlorobenzene (131 °C) of 180.5 and 169 °C, respectively [49]. Additionally, PTB7:$PC_{71}BM$ OPVs fabricated with dichlorobenzene and DIO outperform those we have fabricated with chlorobenzene and DIO. Therefore, dichlorobenzene was selected as the host solvent to be used in our investigation.

5.2.1 Molecular structures

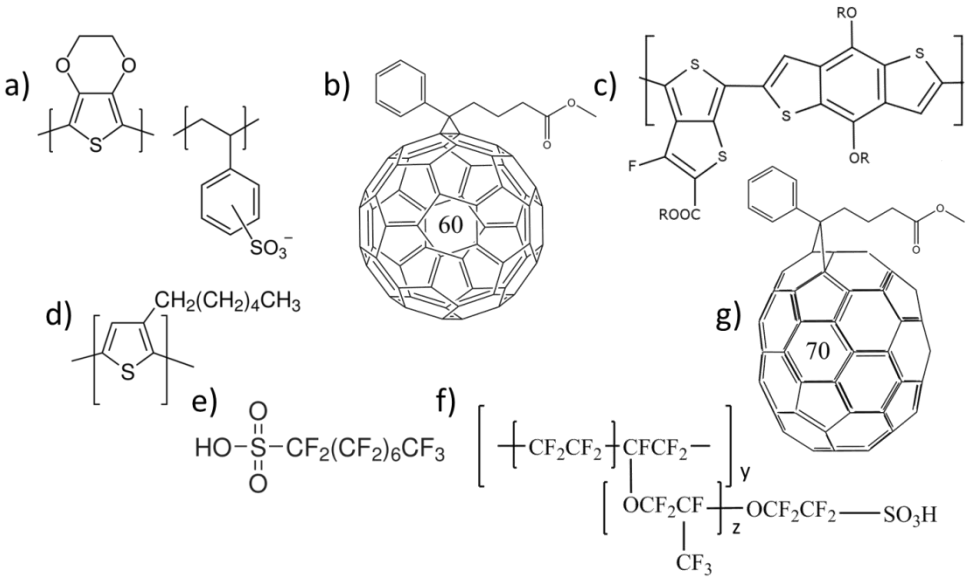

Figure 5.1 *Chemical structures of (a) PEDOT:PSS (b) $PC_{61}BM$ (c) PTB7 (d) P3HT (e) FOS (f) PFI and (g) $PC_{71}BM$.*

The photoactive blends P3HT:$PC_{61}BM$ and PTB7:$PC_{71}BM$ are shown in Figure 5.1 (d):(b) and (c):(g), respectively. P3HT:$PC_{61}BM$ is the most studied OPV model system with typical efficiencies of around 2-3 % using a conventional architecture [50]. PTB7:$PC_{71}BM$ is a comparatively new model system. PCEs of 9.2 % have been achieved with an inverted architecture and using poly [(9,9-bis(3′-(N, N-dimethylamino) propyl)-2,7-fluorene)-alt-2,7-(9,9-ioctylfluorene)] (PFN) [51]. The perfluorooctanesulfonic acid (FOS) and perfluorinated ionomer (PFI) are also shown in Figure 5.1, (e) and (f), respectively. Previously report of the use of PFI in organic electronics concerns OLEDs. Here, PFI was used to improve performance and degradation [17, 52]. To date, there are no reports of the use of PFI in OPVs or FOS in optoelectronics. A variety of studies have focused on the effects of additives [53-59], molecular weight [60], processing [61, 62], and substrate [63-65], on the BHJ morphology and by extension OPV device efficiency. Interestingly, charge separation along the PTB7 backbone appeared to be enhanced by intramolecular charge separation associated with the alternating donor-acceptor group delocalising the excitons, lowering their binding energy and reducing charge carrier recombination [66]. The combination of both photoactive blends is therefore convenient to draw relevant comparisons [64, 67]. I show that doping PEDOT:PSS with PFI or FOS can improve the performance of P3HT and PTB7-based OPVs. Doping is carried out by dissolving the doping agent in PEDOT:PSS solution prior to spin-coating the interfacial layer. The mechanisms responsible for the improvement are investigated and appear to be different for each device type. In the best case scenario we observe a 15 % improvement in PCE for both types of device. However, the observed improvement in P3HT:$PC_{61}BM$ is likely due to changes of the electronic properties at the electrode, whilst for PTB7:$PC_{71}BM$, the improvement may be a result of a change in BHJ morphology through alteration of the surface energy.

5.2.2 Electrochemical and optical properties

The purpose of this study was to determine if it is possible to improve OPV device performance through doping of the PEDOT:PSS interlayer. We believed that this could be achieved if the doping agent altered the work function of the interlayer such as to make an Ohmic contact. The energy levels for the two types of OPV under investigation, i.e. P3HT:$PC_{61}BM$ and PTB7:$PC_{71}BM$ are shown in Figures 5.9 (b) and 5.10 (b), respectively. The energy levels show that in order to achieve a good contact with the donor, the work function of the interlayer needs to move down, i.e. further away from vacuum, as described in Chapter 3. In terms of device performance an improved contact would likely lead to a reduction in recombination and

improved charge carrier extraction. If successful we would therefore expect to see in our devices an increase in open-circuit voltage and fill factor.

Several techniques were used to measure the work function of our interlayers. The first technique I wish to discuss is Kelvin probe force microscopy (KPFM). It is a modified version of atomic force microscopy (AFM), which simultaneously measures topography and the electronic work function of the surface of a sample. The technique relies on a measurement of potential offset between the tip of a probe and the sample, like a macroscopic Kelvin probe. However, here an AFM is used with a cantilever as the reference electrode. For KPFM the cantilever operates in a non-contact mode and scans the surface at a constant height. A XE-100 (Park Systems Co.) was used to perform our measurements and these were carried out in an inert atmosphere at ambient temperature. The tips used for our measurements were Pt-coated Si cantilevers (NT-MDT). Topography was acquired in AC mode with a resonance frequency of 280 kHz. Simultaneously, measurements of work function were obtained by applying an AC modulation voltage of 2V and 20 kHz across the tip. To estimate the work function a Pt coated tip of 4.7 eV was calibrated with a pyrolytic graphite reference sample. In order to extract the work function ($W_{\text{f-KPFM}} = W_{\text{sample}}$) from our data, we measured the contact potential difference (V_{CPD}) and then calibrated the work function of the SPM tip (W_{tip}). The work function of the sample could then be deduced using the following equation:

$$V_{\text{CPD}} = \frac{(W_{\text{tip}} - W_{\text{sample}})}{q} \tag{5.1}$$

Where q is the electronic charge of an electron. The topographic images acquired with KPFM are shown in Figure 5.2. In solution, PEDOT:PSS forms micelles around a PEDOT crystalline core, which has been shown to grow by scattering techniques when subjected to solvent treatments [10].

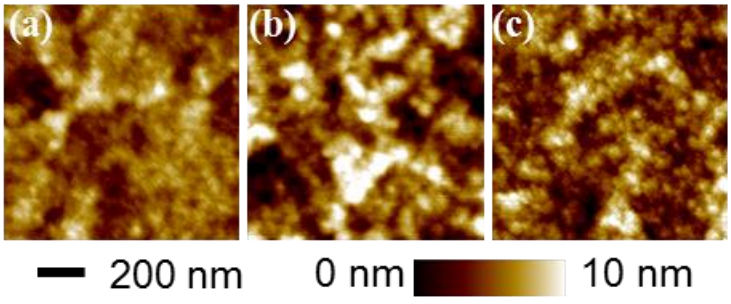

Figure 5.2 *Topographic images acquired by Kelvin probe force microscopy of PEDOT:PSS: (a) un-doped, (b) doped with PFI and (c) doped with FOS.*

The images show bright (dark) areas commonly associated with PEDOT:PSS (PSS) rich regions once spin-coated [5-7, 16, 31-33, 35, 68]. On doping we move away from a binary composition to a ternary with the PSS and doping agent competing to stabilise the polymeric chains of the PEDOT. With the dark domains corresponding to the PSS, it is likely that the bright domains are associated with PEDOT-rich regions. On doping, we observed brighter domains with even brighter structures corresponding to doping by polymer rather than surfactant. However, more structure was evident with the surfactant. The structures appear to be small grains aggregating together. This however may be a result of the surfactant, which is a small molecule, having a different solubility. These images provide evidence of conformational changes of the polymer chains on doping. It is worth mentioning the variation in RMS and peak-to-peak heights are not significantly different between the doped and un-doped samples. We can therefore conclude that changes in device performance are not the result of topographical changes.

As I previously mentioned work function measurements were performed simultaneously with the topographic scan in order to compare local surface potential with topography. Figure 5.3 shows the surface potential mapping. The maps show three different averaged values: -220 mV, -720 mV and -250 mV for the (a) un-doped, (b) PFI doped and (c) FOS doped PEDOT:PSS, respectively. The variations in local surface potential are small, shown in Figure 5.3, 5.4 and 5.23 (appendix). Figures 5.4 and 5.23 (appendix) show the surface potential overlaid on the topography and there appears to be no distinctive correlation. This is likely a result of probing the various orientations of the PEDOT crystalline grains distributed within the interlayer under the PSS, PFI and or the FOS rich layer, as the literature suggests the top of the PEDOT:PSS interlayer to be rich of insulating PSS, PFI and or FOS [17, 69]. This argument is consistent with the contact angle measurements and degradation studies I have carried out, which I will cover later on in this chapter.

A wide variety of doping concentrations were explored in the fabrication of OPVs and for several other measurements. However, for the KPFM and near-field characterisation only the most successful concentrations determined from the OPVs were investigated, i.e. PEDOT:PSS:PFI or PEDOT:PSS:FOS of 1:6:30. All the concentrations investigated were weighted ratios between PEDOT, PSS and the doping agent in solution. The ratio is based on the weight concentration of each material and is indicated by the manufacturer. It is worth mentioning that some of the concentrations we have used are similar to those in [17] for the purpose of comparison.

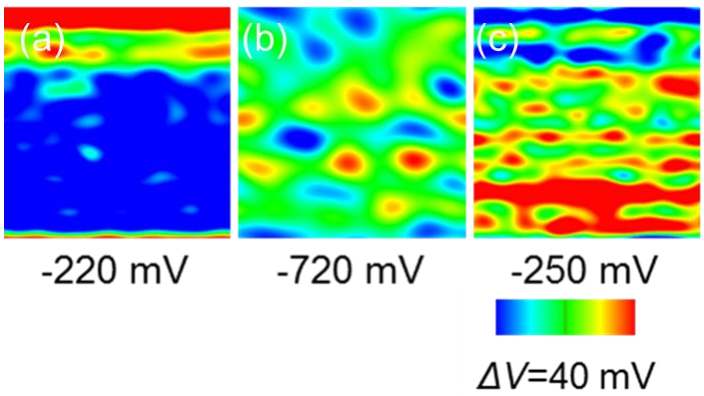

Figure 5.3 *Surface potential maps acquired by Kelvin probe force microscopy for (a) un-doped, (b) PFI doped and (c) FOS doped PEDOT:PSS.*

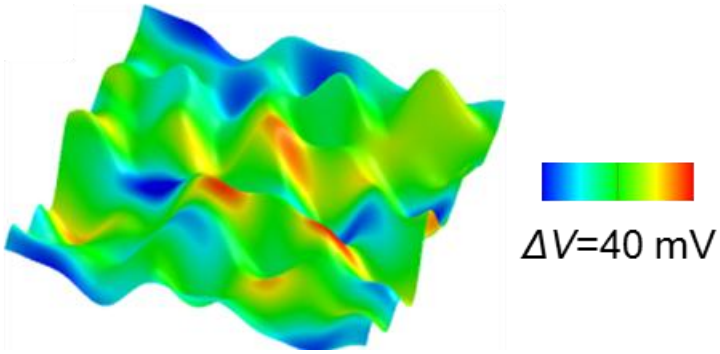

Figure 5.4 *Surface potential overlaid on the topography for a PFI doped PEDOT:PSS sample.*

From the electrostatic measurements in the near-field, local work functions were determined and averaged. The averaged values are presented in Table 5.1. The doped interlayers exhibit a deeper average work function than the un-doped PEDOT:PSS interlayer, which is consistent with previous reports of PEDOT:PSS doped with fluorinated materials [17, 70].

Table 5.1 *Thin film morphology of PEDOT:PSS characterized by AFM: root mean square (RMS, ±0.1 nm) and peak-to-valley height (hPtV), nanoscopic and macroscopic work functions (Wf-KPFM, Wf-mKP ±0.02 eV).*

Doping	*RMS* (nm)	h_{PtV} (nm)	$W_{f\text{-}KPFM}$ (eV)	$W_{f\text{-}mKP}$ (eV)
--	1.5	11 ± 2	4.70 ± 0.02	5.20
PFI	2.5	17 ± 1	5.40 ± 0.03	5.72
FOS	2.0	14 ± 2	4.90 ± 0.03	5.56

Table 5.1 also contains measurements from a macroscopic Kelvin probe (FAC-1, RIKEN KEIKI). As before measurements were performed in an inert atmosphere. The area measured was 1 cm in diameter and the calibration was carried out with a thin gold plate (5.10 eV). Comparing these measurements with the KPFM measurements, we observe the work functions to be different. However, like the UPS measurements, the results of which are shown in the appendix, they follow a similar trend. In an attempt to further understand the properties of the interlayer on doping, conductivity measurements were performed using the two-point probe technique mentioned in Chapter 4. However, the measurements were determined to be unreliable. The inconsistency in the measurements was correlated to changes in the humidity. Figure 5.24 of the appendix shows how the conductivity was discovered to vary with humidity exposure. The process as shown appears to be reversible, allowing for PEDOT:PSS to be used in humidity sensors [71]. This is a result of PEDOT:PSS being hygroscopic. Hence, for reliable measurements samples were prepared and stored in nitrogen and sent for characterisation. The value acquired for the conductivity of the pristine interlayer was similar to that reported in the literature, 0.70 ± 0.05 mS/cm, curiously, a slightly lower conductivity was measured for the PFI and FOS doped interlayers of 0.55 $\pm$ 0.02 and 0.49 ± 0.03 mS/cm, respectively.

We know films of PEDOT:PSS to exhibit a rich upper PSS phase [8, 17, 18, 69], and hence the observation of a decrease in conductivity is assumed to be the result of a larger fraction of insulating material, PFI or FOS) near the upper surface of the film. This may inhibit the hygroscopic properties of PEDOT:PSS, which are well-known to contribute to OPV degradation. To test this, photovoltaic cells were fabricated without encapsulation and characterised in air. This is an on-going study, so I will limit my analysis and discussion on the topic. However, the results are shown in Figures 5.26 through 5.28 of the appendix and indicate improved OPV stability when using PFI in the PEDOT:PSS interlayer. FOS is still to be investigated. Our study monitored P3HT:$PC_{61}BM$ device performance for a period of 24 hours under constant illumination with an AM 1.5 G source at 100 mW cm^{-2}. A J-V characteristic was taken every 30 minutes. Temperature and humidity were monitored for the length of the study and found to be stable throughout the investigation. Looking at the results there appears to be two mechanisms responsible for degradation, an initial fast decay followed by a much slower decay. The latter appears unaffected with the use of PFI. A considerable difference in performance is observed between devices fabricated with and without PFI within the first two hours of operation. We have normalised the efficiencies for comparison, as the device fabricated with PFI is more efficient than that without PFI, exhibiting a larger Voc and fill factor. The decrease in conductivity does not explain the observed improvement in device performance.

Figure 5.5 and 5.6 show the transmittance spectra for un-doped and doped with varying concentrations of PFI and FOS, respectively. For both PFI and FOS, increasing the concentration of the doping agent reduces the transmittance of the sample. However, the reduction is not significant and is likely due to an increase in thickness of the PEDOT:PSS interlayer, shown in Figure 5.29 of the appendix. Furthermore, there is no significant change in the overall shape of the spectra with doping.

Contact angle measurements were performed and reveal an increase in angle on doping. The contact angle for un-doped PEDOT:PSS deposited on a quartz substrate was 11.6 °. At a ratio of 1:6:1 an angle of 11.9 and 29.6 ° was measured for PFI and FOS. For 1:6:2.5, 11.9 ° increased to 16.2 °, while 29.6 ° increased to 38.6 °. The contact angle levels off with increasing the ratio to 1:6:13.4. For PFI an angle of 16.9 ° was measured, while for FOS an angle of 37.8 ° was attained. The concentration was further increased, to the maximum ratio of 1:6:30, angles of 21.2 and 37.7 ° were measured for PFI and FOS, respectively. For the optimal ratio, 1:6:30. Contact angle measured were performed with dichlorobenzene. When deposited on the un-doped PEDOT:PSS interlayer an angle of 2.6 ° was measured. However, when deposited on the doped samples angles of 38.1 and 47.8 ° were measured for PFI and FOS, respectively. The contact angle measurements are summarised in a table alongside the images in Figure 5.30 of the appendix.

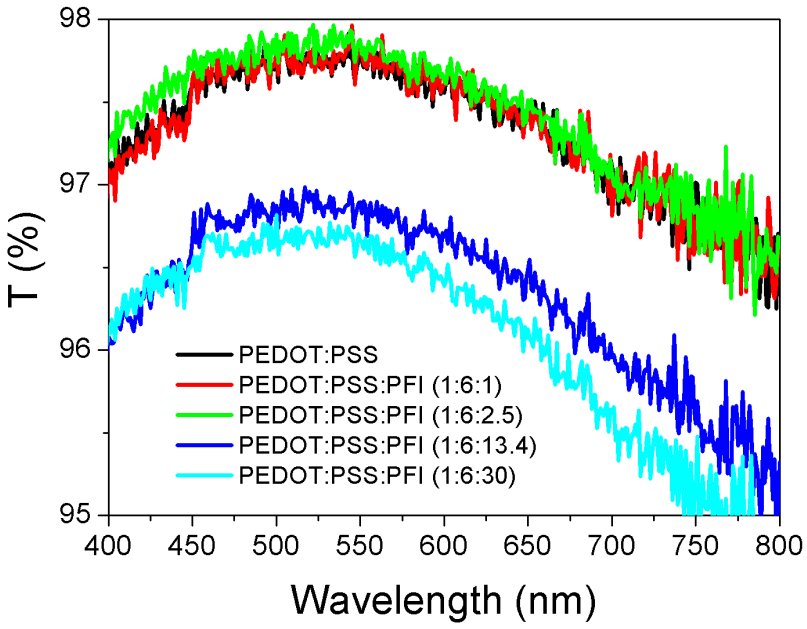

Figure 5.5 *Transmittance spectra for PEDOT:PSS films spin-coated on quartz substrates: un-doped and doped with various concentrations by weight of PFI.*

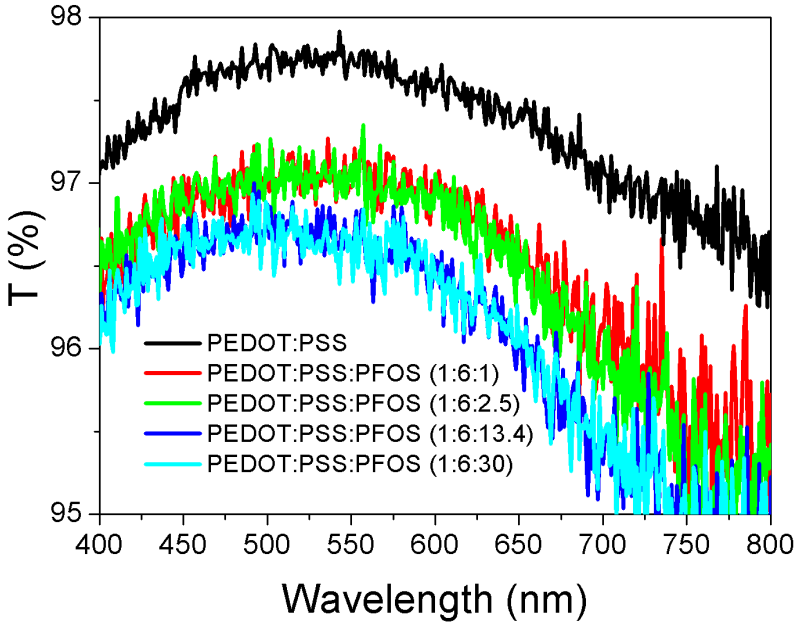

Figure 5.6 *Transmittance spectra for PEDOT:PSS films spin-coated on quartz substrates: un-doped and doped with various concentrations by weight of FOS.*

The change in contact angle with doping is significant and therefore may alter the BHJ morphology during the deposition, thus influencing device performance. The main mechanism by which PEDOT:PSS conducts is associated with the acid groups protonating the PEDOT and the charge hopping along the PEDOT polymer chain. The effect of doping is largely thought to promote structural changes in the PEDOT from coiled to an extended coiled conformation. This leads to larger PEDOT crystals. The fact that we obtained slightly lower conductivities with doping is consistent with the literature [72] alongside with the observed changes in conformation and morphology. The doping does not prevent protonation of the PEDOT by the PSS. It has been shown that films of PEDOT:PSS exhibit an upper rich PSS phase [8, 17, 18, 69] and the slight decrease in conductivity combined with contact angle and degradation measurements etc. implies that a larger fraction of the insulating material is at the surface of the film.

The normalised absorbance spectra for P3HT, $PC_{61}BM$ and composite P3HT:$PC_{61}BM$ are shown in Figure 5.7. While, the spectra for PTB7, $PC_{71}BM$ and the composite PTB7:$PC_{71}BM$ are shown in Figure 5.8. Clearly, with a wider spectral range, PTB7 is a better photovoltaic material. In addition, the fullerene derivative, $PC_{71}BM$ has a favourable absorption compared to $PC_{61}BM$.

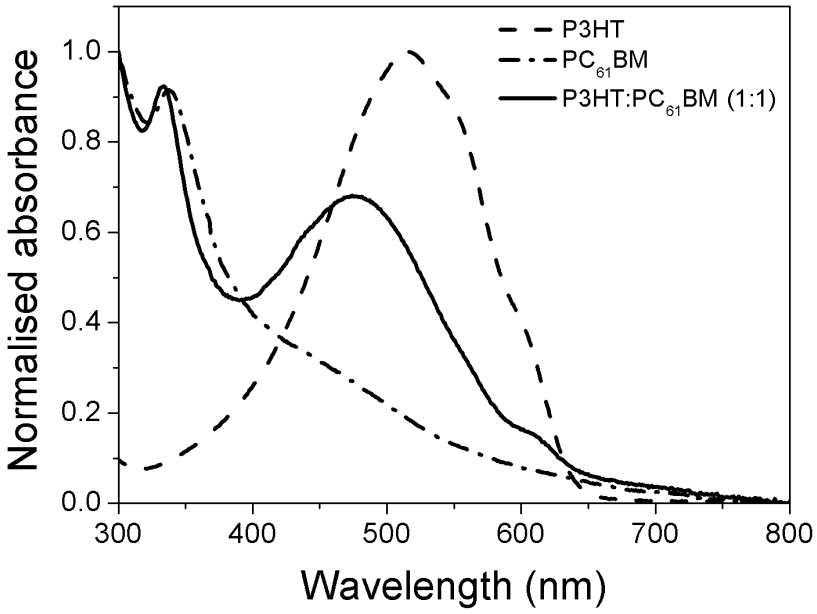

Figure 5.7 *Absorption spectra for P3HT, $PC_{61}BM$ and composite P3HT:$PC_{61}BM$ used in the photovoltaic cells..*

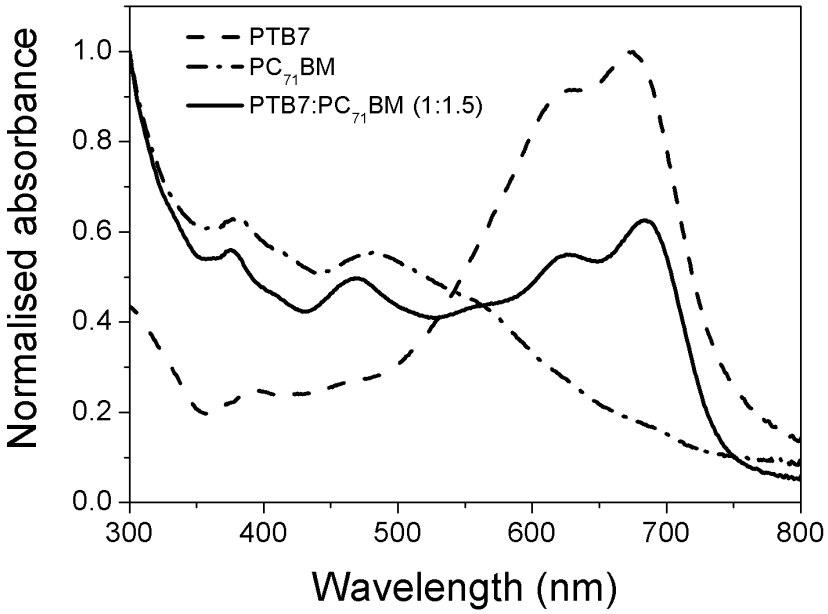

Figure 5.8 *Absorption spectra for PTB7, $PC_{71}BM$ and composite PTB7:$PC_{71}BM$ used in the photovoltaic cells.*

5.3 Photovoltaic cells

The device architectures and energy levels are shown in Figure 5.9 and 5.10. Here, the doped PEDOT:PSS interlayers are employed as hole transporting (HTL) electron blocking (EBL) layers. As described, the devices were based on two different device types, P3HT:$PC_{61}BM$ and PTB7:$PC_{71}BM$, Figure 5.9 and 5.10, respectively. For P3HT:$PC_{61}BM$ aluminium was evaporated as the top contact, whilst for efficient PTB7:$PC_{71}BM$ devices a calcium aluminium top contact was required. The devices were encapsulated to address the reactivity of the calcium layer and were characterised in ambient conditions accordingly. The initial concept for the use of PFI and FOS in OPVs was to ensure the contact between the interlayer and the donor of the photoactive blend, i.e. P3HT and PTB7 as Ohmic.

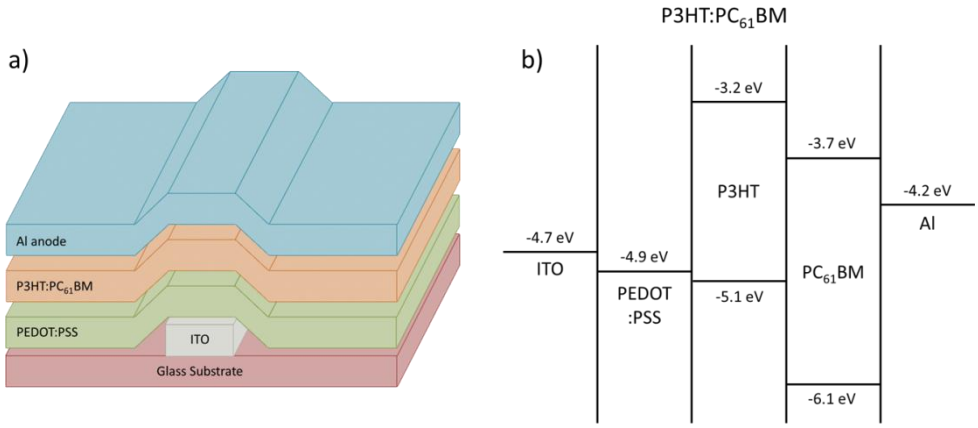

Figure 5.9 *Schematic showing (a) device architecture and (b) energy levels for the P3HT:$PC_{61}BM$ organic photovoltaic cells [73].*

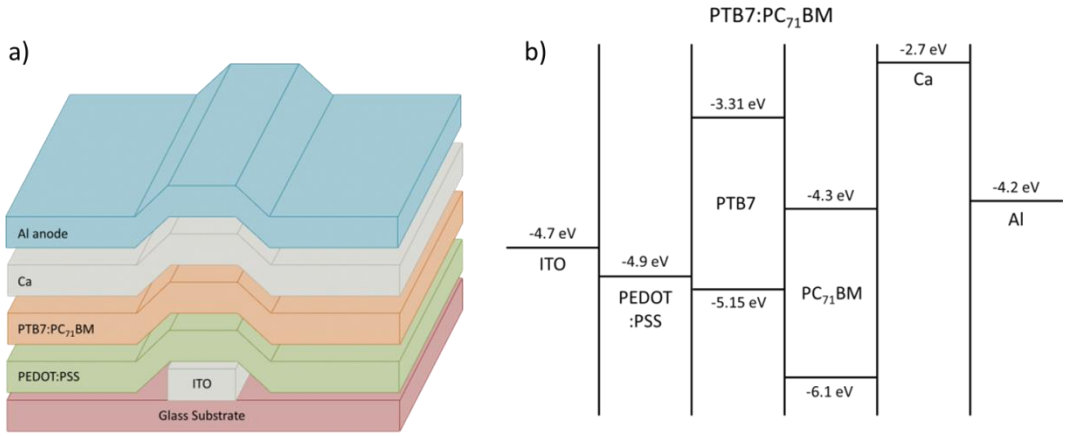

Figure 5.10 *Schematic showing (a) device architecture and (b) energy levels for the PTB7:$PC_{71}BM$ organic photovoltaic cells [74].*

5.3.1 Experimental methods

ITO coated glass substrates were masked with an adhesive tape and etched in HCl (37 %) for 20 minutes to define the active area of the bottom contact. The mask was removed and the substrates now patterned were subsequently cleaned by means of sonication in deionized water, acetone and isopropanol successively for 15 minutes. The substrates were then dried with nitrogen flow before treatment by oxygen plasma for 5 minutes. Solutions of PEDOT:PSS were prepared with varying concentrations of doping agent. These were prepared based on the weight concentrations indicated by the manufacturers. The PEDOT:PSS and PFI solutions were used as received. However, the FOS was diluted with DI water. The appropriate concentrations of doping agents were added to the PEDOT:PSS solution and stirred vigorously overnight. Before using the solutions, they were sonicated, filtered (0.45 μm) and spin-coated at 4000 rpm. The PEDOT:PSS coated ITO patterned substrates were then annealed at 120 °C for 15 minutes on a hotplate in a nitrogen-filled glove-box.

The organic semiconductor compositions were dissolved by stirring at 50 °C (P3HT:$PC_{61}BM$) or 70 °C (PTB7:$PC_{71}BM$) overnight. Chlorobenzene was used for the P3HT-based devices, while dichlorobenzene was used for the PTB7-based devices. 3 % v/v DIO was added to the solution containing PTB7 an hour prior to spin-coating the active layer. No DIO was used for the P3HT-based devices. Solutions of P3HT:$PC_{61}BM$ at a ratio of 1:1 and PTB7:$PC_{71}BM$ at a ratio of 1:1.5 were spin-coated at 1000 rpm on top of the HTL. P3HT-based devices were annealed post active layer deposition at 130 °C for 15 minutes. The top electrode was evaporated under a 2.10^{-6} mBar vacuum. PTB7:$PC_{71}BM$ received a 20 nm calcium layer followed by a 200 nm aluminum layer, while P3HT:$PC_{61}BM$ was only coated with aluminum. PTB7:$PC_{71}BM$ devices were immediately removed from the evaporator and encapsulated inside the glovebox with a UV optical adhesive and a glass coverslip. P3HT:$PC_{61}BM$ devices were not encapsulated. Devices removed from the glovebox were masked and subsequently characterized in air with a Keithley 2400 source-measure unit and a K.H. Steuernagel AM1.5G solar simulator providing an illumination intensity of 100 $mWcm^{-2}$, which was verified with an NREL-calibrated monosilicon detector with KG-5 filter.

The external quantum efficiency (*EQE*) measurements were completed with an incident photon to charge carrier efficiency setup, made of an NPL-calibrated photodiode, a Keithley 6517A picoammeter and a TMc300 monochromator.

Transmission measurements were completed with a Perkin-Elmer Lambda 950 UV/Vis/NIR spectrometer on ITO coated substrates. The contact angle measurements were measured with a positioning stage, dosing needle and a Nikon D5200 with a macroscopic lens and analysed with Image J software as described by Stalder et al [75].

5.3.2 Materials

Indium tin oxide (ITO) coated glass substrates (15 Ω/square) were purchased from Xin Yan Technology Ltd. Hydrochloric acid (HCl, 37 %), acetone, isopropanol, dichlorobenzene, chlorobenzene were all HPLC grade and purchased from Sigma-Adrich. Perfluorinated ionomer solution (PFI, Nafion DE 520, 5 wt. % in alcohols and 45 % water) and perfluorooctanesulfonic acid solution (FOS, M_w = 500.13, D, ~ 40 % in water) were also from Sigma-Adrich. 1, 8-diiodooctane (DIO) was from Fluka. Poly(3, 4-ethylenedioxythiophene: poly (styrenesulfonate) (PEDOT:PSS, AI4083) was from Clevios, poly(–4,8-bis[(2-ethylhexyl)oxy]benzo[1,2-b:4,5-b']dithiophene-2,6-diyl–3-fluoro-2-[(2-ethylhexyl)carbonyl]thieno[3,4-b] thiophenediyl) (PTB7, M_w = 92 kDa, pdi = 2.6) was from 1-Material; regioregular poly(3-hexylthiophene) (P3HT, M_w = 57 kDa, pdi = 2.9) was from Rieke Metals. The soluble fullerenes [6,6]-phenyl-C_{61}/C_{71} butyric acid methyl ester ($PC_{61}BM$ / $PC_{71}BM$) were both purchased from Solenne (99 % purity). The UV optical adhesive (Norland Optical Adhesive 68) and glass coverslips used for the encapsulation were purchased from Thorlabs and Fisher Scientific, respectively.

5.3.3 Optimisation

P3HT:$PC_{61}BM$ photovoltaic cells with varying concentrations of PFI or FOS doped in the PEDOT:PSS interlayer were fabricated and characterised, as described. The results are shown in Figure 5.11 and 5.13 for PFI and FOS, respectively. The reference cell, i.e. a cell containing an un-doped PEDOT:PSS interlayer, showed a PCE of 2.53 %. This PCE is the result of a short-circuit current density (Jsc), open-circuit voltage (Voc) and fill factor of 8.84 mA cm^{-2}, 0.59 V and 49 %, respectively. First, we will consider the polymer doping agent, PFI. At a PEDOT:PSS:PFI ratio of 1:6:1, we observe a substantial decrease in PCE of just over 1 % to 1.49 %. This decrease in PCE is a result of a lower Jsc and fill factor of 7.89 mA cm^{-2} and 31 %, respectively. While these two parameters decreased, the Voc increased from 0.59 V without doping to 0.61 V with doping. A Voc of 0.62 V and Jsc of 8.54 mA cm^{-2} were acquired at a ratio of 1:6:2.5. A similar PCE to 1:6:1 of 1.50 % was obtained. This is the result of a fill factor of 28 %. For a ratio of 1:6:13.4 a PCE of 2.34 % was

acquired, which is still below the 2.53 % of the reference cell. The lower PCE compared to the reference cell is due to a Jsc of 8.21 mA cm^{-2}, as we observe a larger Voc of 0.62 V and a similar fill factor of 47 %. Further increasing the concentration of PFI to a ratio of 1:6:30, we observe an approximate 15 % increase in PCE compared to the reference cell. With a similar Jsc of 8.85 mA cm^{-2}, the increase arises from an increase in fill factor and Voc to 54 % and 0.62 V, respectively.

Considering photovoltaic cells doped with the small molecule, FOS. At a PEDOT:PSS:FOS ratio of 1:6:1 we observe a slight increase in PCE to 2.59 %. Although we observe a lower Jsc of 8.00 mA cm^{-2}, an increase in both the Voc and fill factor of 0.63 V and 51%, respectively, is sufficient to compensate for the decrease in Jsc. For a ratio of 1:6:2.5 the Voc does not change. However, an increase in both the Jsc and fill factor of 8.32 mA cm^{-2} and 53 %, respectively, results in a larger PCE of 2.79 %. With increasing the concentration of FOS to a ratio of 1:6:13.4 the PCE increased to 2.84 %. This increase in PCE is a result of a slightly larger fill factor of 54 % and Jsc of 8.42 mA cm^{-2}. Increasing the concentration to the maximum doping ratio of 1:6:30 a PCE of 2.91 % was acquired. With a similar Voc and fill factor to 1:6:13.4 the improvement in PCE is a result of an increase in the Jsc to 8.63 mA cm^{-2}. This is lower than that of the reference cell. Nevertheless, a larger Voc and fill factor results in a PCE approximately 15 % greater than that of the reference cell.

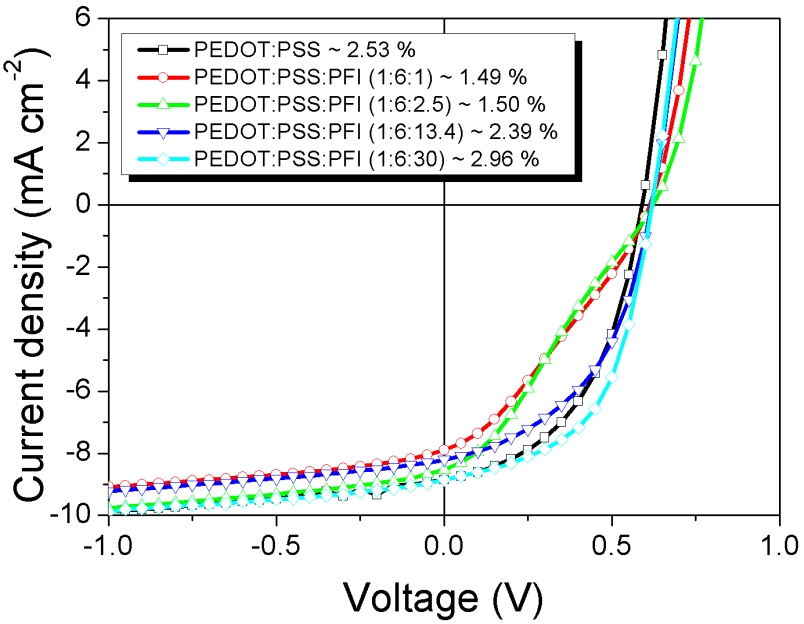

Figure 5.11 *J-V characteristics for a number of P3HT:$PC_{61}BM$ photovoltaic cells with varying concentrations of PFI doping of the PEDOT:PSS interlayer.*

The aforementioned performance parameters are summaried in Table 5.2. The most efficient photovoltaic cells for PFI and FOS were acquired at a ratio of 1:6:30. A similar increase in PCE was observed for PFI and FOS at this ratio of approximately 15 %. Larger concentrations of doping agent, made deposition of the PEDOT:PSS interlayer difficult due to the use of a filter. The filter was used in order to ensure good film quality. The concentrations used in the study were similar to those employed in an investigation of PFI doping of PEDOT:PSS for OLEDs [17]. For PFI and FOS doping we observe an increase in Voc. The increase is larger for photovoltaic cells where the PEDOT:PSS interlayer has been doped with FOS rather than PFI. The increase in Voc is likely to be the result of an improved Ohmic contact [76, 77]. A dissimilar trend is noticeable between doping with PFI or FOS. For FOS we observe good fill factors for all doping concentrations compared to the reference cell. However, for PFI we observe an initial decrease in fill factor, and as we approach larger concentrations of doping agent the fill factor improves, shown in Figure 5.12. To further validate these results additional concentrations were investigated. These are in agreement with the results shown in Figure 5.12 and are found in Figure 5.31 of the appendix.

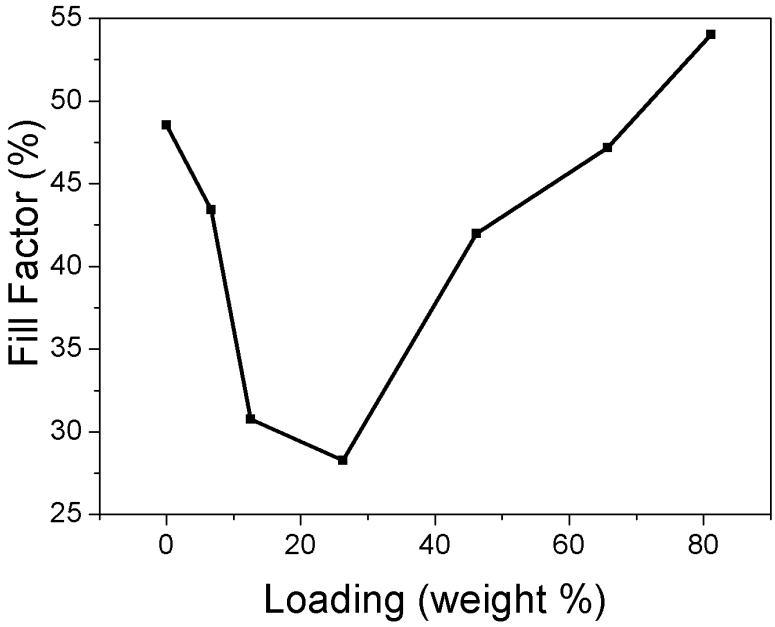

Figure 5.12 *Fill factors extracted from the J-V characteristics depicted in Figure 5.11. PFI doped PEDOT:PSS by percentage weight.*

The low fill factors with PFI are due to S-kinks in the J-V characteristics, i.e. S-shaped J-V characteristics observed in Figure 5.11. The most likely cause of an S-kink is an imbalance of charge carrier mobilities, resistance of the interfacial layer or the presence of interface dipoles etc. It is difficult to determine the mechanism responsible for the occurrence of the S-kink without carrying out additional measurements. Where we observe these low fill factors we observe poor rectification (dark-current), shown in Figure 5.31 of the appendix. The conductivity measurements show the conductivity for PFI and FOS doped films (1:6:30) to be less than that of the un-doped films. The Jsc is, in most circumstances lower when the PEDOT:PSS interlayer is doped with PFI or FOS, and the improvement in PCE is the result of an increase in Voc and the fill factor. The lower Jsc suggests a possible change in the conductivity of the PEDOT:PSS interlayer with doping. It is possible that at low concentrations of PFI, the doping agent is either preventing the PSS from protonating the PEDOT or disrupting the continuity of the PEDOT. If viable, the reason we may not observe a similar result with FOS, is due to FOS being a small molecule and not a polymer. From the device fabrication it was evident that PFI is more soluble than FOS. This is not surprising as polymers usually exhibit better solubility than small molecules.

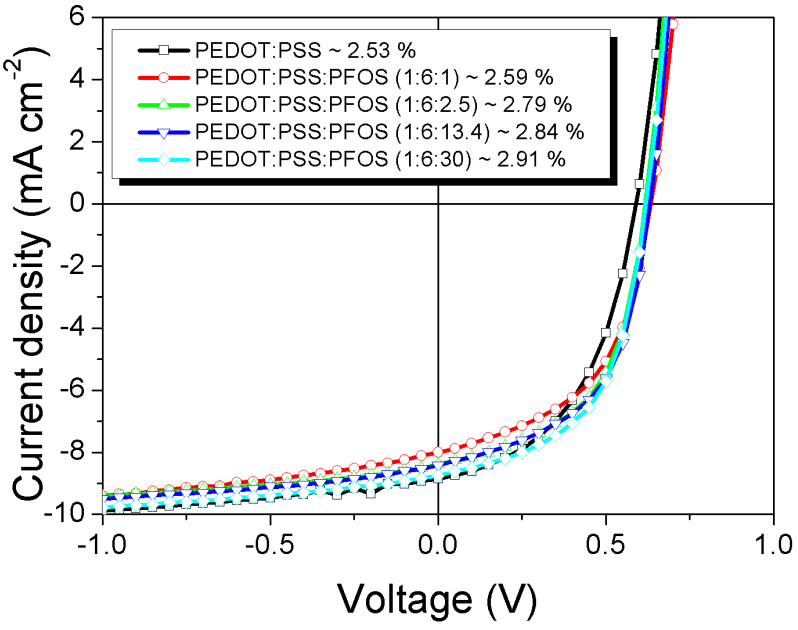

Figure 5.13 *J-V characteristics for a number of P3HT:$PC_{61}BM$ photovoltaic cells with varying concentrations of FOS doping of the PEDOT:PSS interlayer.*

Hence, it is likely that at low concentrations of PFI the soluble polymer is distributed within the PEDOT:PSS interlayer, whereas with FOS it is likely that even at low concentrations the majority is at the surface of the interlayer. Comparing the contact angle measurements for PFI and FOS doped PEDOT:PSS, this is justifiable. Additionally, at low concentrations of PFI we don't observe large changes in the contact angle when compared with the un-doped PEDOT:PSS. At high concentrations we know the majority of PFI is at the surface of the film. This is evident from the contact angle measurements, morphology and studies into degradation (Figures 5.26 to 5.28 of the appendix). For the latter, the PFI acts as an insulator on the surface of the PEDOT:PSS, preventing water from penetrating and degrading the sample. Hence, although we observe an approximate 15 % increase in PCE for PFI and FOS at 1:6:30, we observe different PCEs at similar concentrations below 1:6:30. For FOS we observe small increases in efficiency with increasing the concentration of the doping agent, whilst for PFI we observe a drop in PCE with doping until we get to larger doping concentrations where we see an increase. To understand the difference between PFI and FOS doping it would be useful to carry out further degradation measurements for both doping agents at the aforementioned concentrations and in parallel perform further conductivity measurements.

Table 5.2 *Performance statistics of P3HT:$PC_{61}BM$ photovoltaics with un-doped, PFI doped and FOS doped PEDOT:PSS.*

Device type	**Ratio**	**Loading [%]**	**Jsc [mA/cm^2]**	**Voc [V]**	**FF [%]**	**PCE [%]**
Conventional	1:6:0	0	8.84	0.59	49	2.53
PFI	1:6:1	12.5	7.89	0.61	31	1.49
	1:6:2.5	26.32	8.54	0.62	28	1.50
	1:6:13.4	65.69	8.21	0.62	47	2.39
	1:6:30	81.08	8.85	0.62	54	2.96
FOS	1:6:1	12.5	8.00	0.63	51	2.59
	1:6:2.5	26.32	8.32	0.63	53	2.79
	1:6:13.4	65.69	8.42	0.63	54	2.84
	1:6:30	81.08	8.63	0.63	53	2.91

5.3.4 Characterisation

To compare the photovoltaic responses, the J-V characteristics for the optimal cells containing PFI and FOS were graphed alongside the reference cell with an un-doped PEDOT:PSS interlayer, shown in Figure 5.14. Considering Figure 5.14 we observe a good improvement with doping and there is little difference between using the PFI or FOS doping agent. PTB7:$PC_{71}BM$ photovoltaic cells were fabricated and characterised. The results are shown in Figure 5.15. The doping ratio used in these cells was taken from the optimal P3HT:$PC_{61}BM$ cells (1:6:30). A very different result was observed with the PTB7-based cells. Whilst we observed a slightly larger Voc than the reference cell, the improvement in PCE was the result of an increase in the Jsc. A larger fill factor was obtained with FOS of 70 % compared to the 65 % for PFI. It is possible that the photovoltaic cell with PFI was not operating correctly as the fill factor acquired is lower than that obtained with the reference cell. The reference cell had a PCE of 7.18 % made possible by a Voc, Jsc and fill factor of 0.67 V, 15.94 mA cm^{-2} and 67 %, respectively. With PFI doping the PCE increased to 7.49 % with a Jsc and Voc of 16.89 mA cm^{-2} and 0.65, respectively. Whilst, for FOS a PCE of 8.26 % was achieved, made possible by an increase in Voc, fill factor and Jsc of 0.70 V, 70 % and 16.94 mA cm^{-2}, respectively.

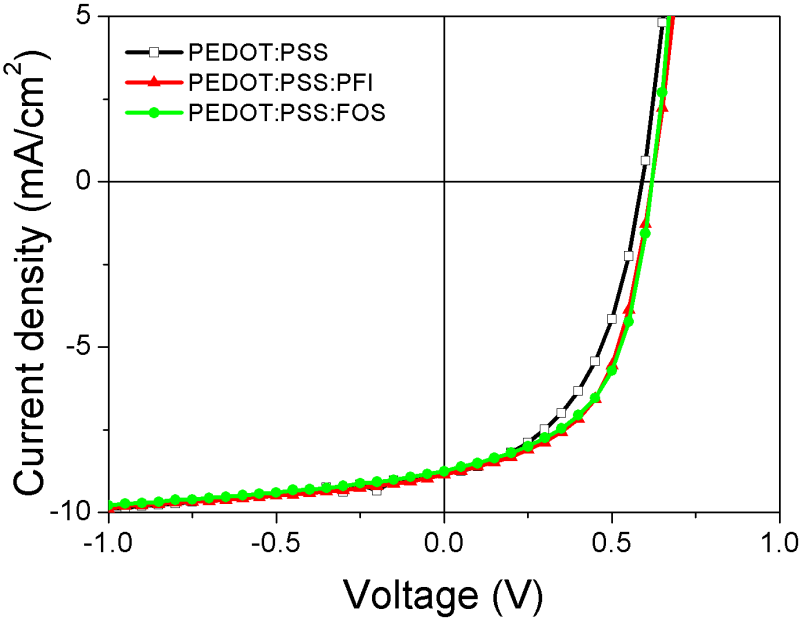

Figure 5.14 *J-V characteristics of P3HT:$PC_{61}BM$ with un-doped, PFI doped (1:6:30) and FOS doped (1:6:30) PEDOT:PSS.*

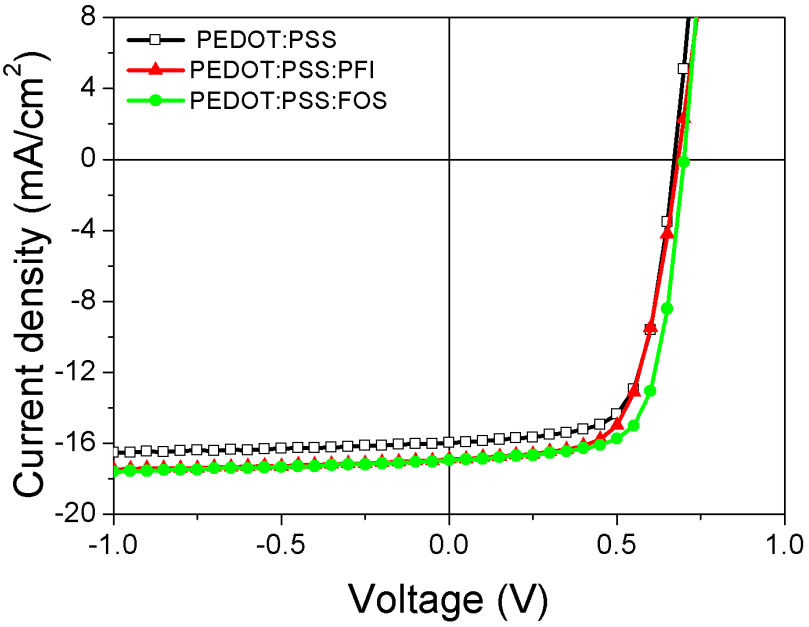

Figure 5.15 *J-V characteristics of PTB7:$PC_{71}BM$ with un-doped, PFI doped (1:6:30) and FOS doped (1:6:30) PEDOT:PSS.*

The Jsc for PFI and FOS doped PEDOT:PSS PTB7-based cells are similar, 16.89 mA cm^{-2} compared with 16.94 mA cm^{-2}, respectively. The performance parameters extracted from the J-V characteristics are shown in Table 5.3. The performance parameters acquired for the un-doped PEDOT:PSS interlayers are consisted to those in the literature. To summarise the results, larger PCEs were observed for those devices with a doped PEDOT:PSS interlayer. An increase in efficiency of ~15 % is seen for PFI and FOS doping of P3HT:$PC_{61}BM$. A similar increase is observed with FOS in PTB7-based cells.

Table 5.3 *Summary of performance statistics for photovoltaic devices with an un-doped, PFI doped (1:6:30) and FOS doped (1:6:30) PEDOT:PSS interlayer.*

	Interlayer	*PCE* [%]	V_{OC} [V]	J_{SC} [mA/cm^2]	*FF* [%]
PTB7:$PC_{71}BM$	PEDOT:PSS	7.18	0.67	15.94	67
	PEDOT:PSS:PFI	7.49	0.68	16.89	65
	PEDOT:PSS:FOS	8.26	0.70	16.94	70
P3HT:$PC_{61}BM$	PEDOT:PSS	2.53	0.59	8.84	49
	PEDOT:PSS:PFI	2.96	0.62	8.85	54
	PEDOT:PSS:FOS	2.91	0.63	8.63	53

The J-V characteristics for P3HT and PTB7-based photovoltaic cells under illumination and in the dark are shown in Figure 5.25 of the appendix. To help us understand the mechanisms responsible for the efficiency enhancement, EQE measurements were performed. These are shown for P3HT and PTB7-based devices in Figures 5.16 and 5.17, respectively. The measurements were carried out on devices fabricated with and without doping of the PEDOT:PSS interlayer. Both doping agents were investigated, but only at a PEDOT:PSS:PFI or PEDOT:PSS:FOS ratio of 1:6:30, as this ratio produce the best results.

For the P3HT-based devices we see little change in the shape and magnitude of the EQE spectra. This is consistent with the J-V characteristics where we see almost no change in the short-circuit density (Jsc) with and without doping. The measurements agree with the postulate that the improvement in performance of P3HT-based devices is the result of a better Ohmic contact between the donor of the active layer and the PEDOT:PSS interlayer, as the efficiency enhancement arises from an increase in fill factor and open-circuit voltage, a result of improved charge extraction efficiency, i.e. reduced recombination.

For the PTB7-based photovoltaic cells we observe a very different result. Here, there is a change in both the shape and magnitude of the EQE spectra. It is possible that some of this improvement in performance is a result of a better Ohmic contact. However, it is the change EQE that is largely responsible for the increase in efficiency. The underlying mechanism behind the improvement, i.e. the increase in EQE and Jsc is unclear. Two possible reasons for the increase include a change in the thin film morphology of the active layer during the deposition. A change in the thickness of the PEDOT:PSS interlayer and or the active layer may also be responsible for the improvement. The aforementioned are feasible considering the results acquired from the contact angle measurements.

It would be interesting to carry out ellipsometry measurements to determine the thickness of the active layer on top of the PEDOT:PSS interlayer and to map out the optic field intensity within the device to ensure the enhancement is not a result of thin film interference effects. The later would be an unlikely culprit due to the thicknesses and materials involved. It is worth mentioning that the PCE and EQE measurements for the FOS device are amongst the highest reported in the field of organic photovoltaics.

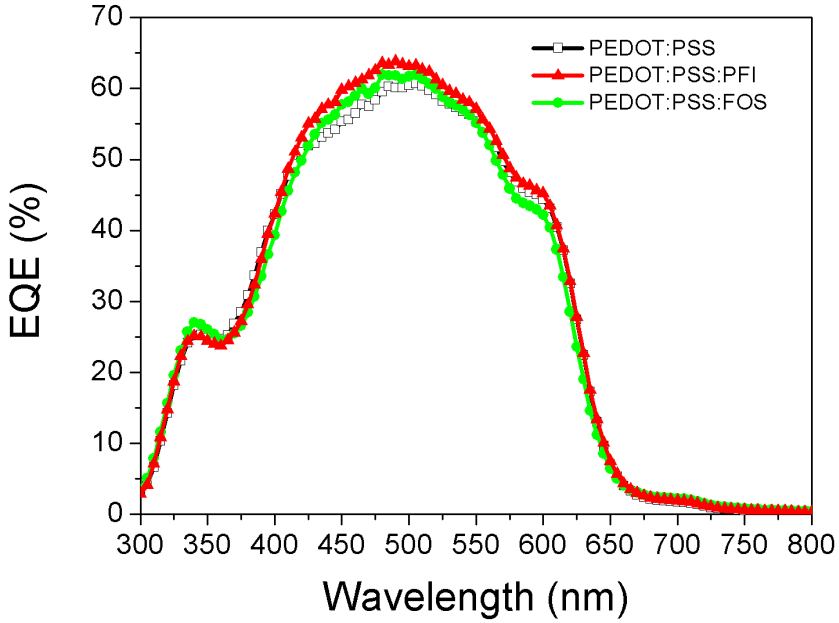

Figure 5.16 *External quantum efficiency (EQE) measurements for P3HT:$PC_{61}BM$ with un-doped, PFI doped (1:6:30) and FOS doped (1:6:30) PEDOT:PSS interlayer.*

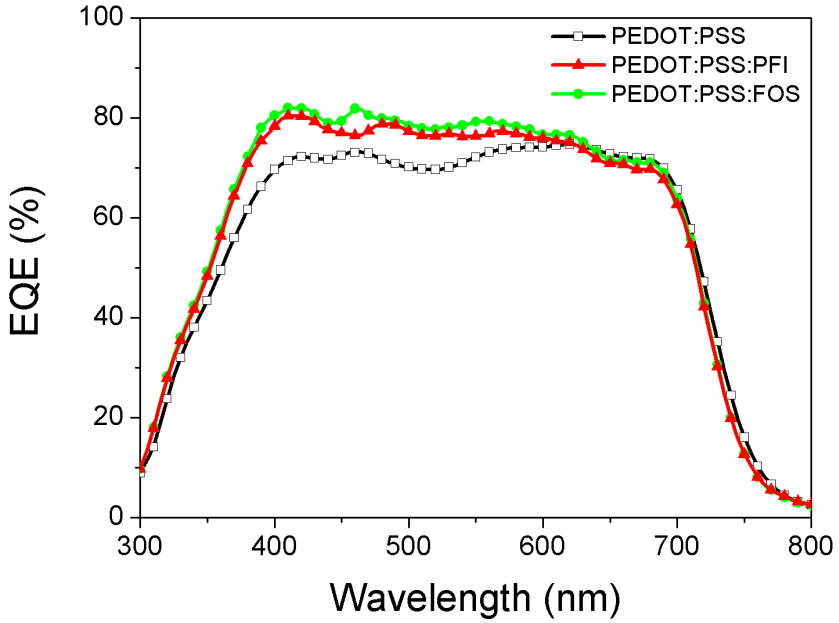

Figure 5.17 *External quantum efficiency (EQE) measurements for PTB7:$PC_{71}BM$ with un-doped, PFI doped (1:6:30) and FOS doped (1:6:30) PEDOT:PSS interlayer.*

5.4 Conclusion

In this chapter I have investigated the influence of two doping agents on the properties of the interlayer, PEDOT:PSS. The two different doping agents that were studied are the polymer, perfluorinated ionomer (PFI) and the small molecule, perfluorooctanesulfonic acid (FOS). To-date, there are no reports of the use of PFI in OPVs or the use of FOS in optoelectronics. There have been reports of the use of PFI in PEDOT:PSS, but these are in the context of OLEDs. Here, the use of PFI improved the stability and performance of the OLED devices.

Doping of the PEDOT:PSS interlayer was shown to change the morphological and electronic properties of the interlayer. At a PEDOT:PSS:PFI or PEDOT:PSS:FOS ratio of 1:6:30 by weight the majority of the doping agent is near the surface of the interlayer. The dopant rich region encapsulates the PEDOT:PSS preventing water from degrading the sample. This is in agreement with reports in the literature, morphological studies, and contact angle and degradation measurements. Doping also decreased the conductivity and altered the work-function of the PEDOT:PSS interlayer. The change in work-function was thought to be favourable for OPVs to ensure an Ohmic contact as hole accumulation has been reported in P3HT:$PC_{61}BM$ photovoltaic cells when under illumination, implying an energy level mismatch between the PEDOT:PSS interlayer and the donor, P3HT.

P3HT and PTB7-based devices were fabricated and characterised. For P3HT-based devices any improvement in PCE was likely the result of an improved Ohmic contact. A similar increase in PCE of approximately 15 % was achieved with both doping agents at a ratio of 1:6:30, at lower concentrations the results were dissimilar. A likely reason for the disparity is due to the PFI being a polymer and the FOS a small molecule. With the polymer having a better solubility, at low concentrations it is likely to be well-distributed in the interlayer, this may prevent the PSS from protonating the PEDOT or alter the connectivity of the PEDOT and therefore change the conductivity of the sample. Unfortunately, we have no conductivity measurements for these concentrations. However, our measurements at 1:6:30 do show a decrease in conductivity compared to the reference, i.e. the un-doped PEDOT:PSS interlayer.

For the PTB7-based devices the increase in PCE is largely the result of an increase in Jsc, which is different to those devices containing P3HT, even though devices exhibit a similar increase of 15 % when doped with FOS. Considering the EQE measurements, we see that the improvement in Jsc is the

result of a change in the shape and magnitude of the EQE. Whilst a change in the electronic properties is likely to have improved the PCE of the P3HT-based cells and may contribute in some way to the improved efficiency of PTB7-based cells, the main reason for the improvement is likely to be the result of a change in the morphology or thickness during the deposition, a result of a very different contact angle.

To understand the mechanisms responsible for the disparity between PFI and FOS doped films it would be interesting to carry out conductivity and degradation measurements for both doping agents at the necessary concentrations. In terms of the PTB7-based devices it would be useful to investigate the morphology and carryout ellipsometry measurements to determine the thicknesses of the layers and to map the optic field intensity within the device. In doing so, we hope to determine the reason for the improvement in Jsc and by extension PCE.

5.5 Appendix

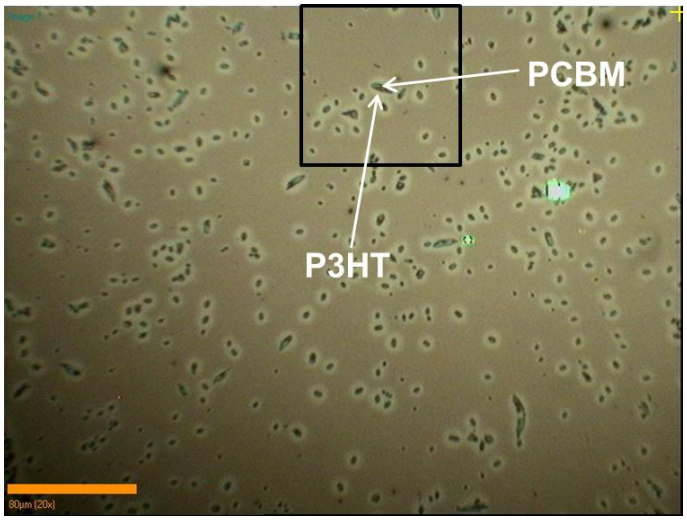

Figure 5.18 *P3HT:$PC_{61}BM$ (1:1) annealed at 140 °C for 30 minutes. The image depicts aggregates of $PC_{61}BM$ surrounded by regions that are rich in P3HT.*

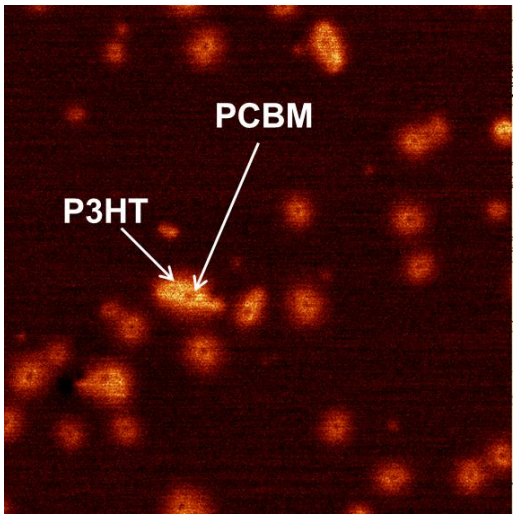

Figure 5.19 *Image obtained with a fluorescent microscope with an excitation of 532 nm. The area imaged is outlined by the black square shown in Figure 5.18.*

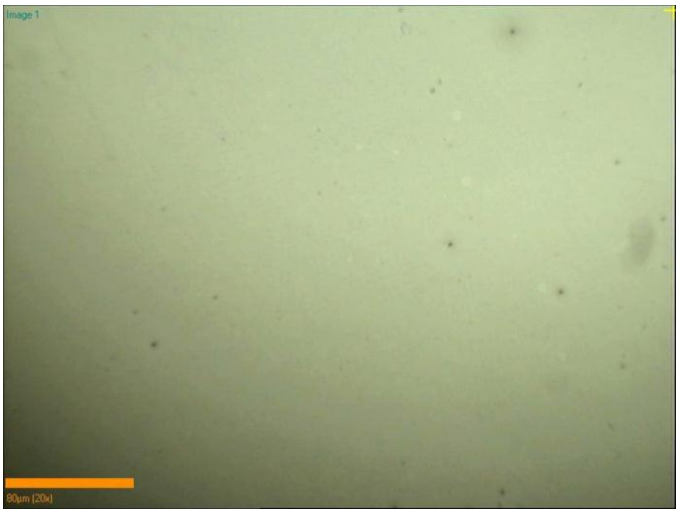

Figure 5.20 *P3HT:$PC_{61}BM$ (1:1) annealed at 130 °C for 15 minutes.*

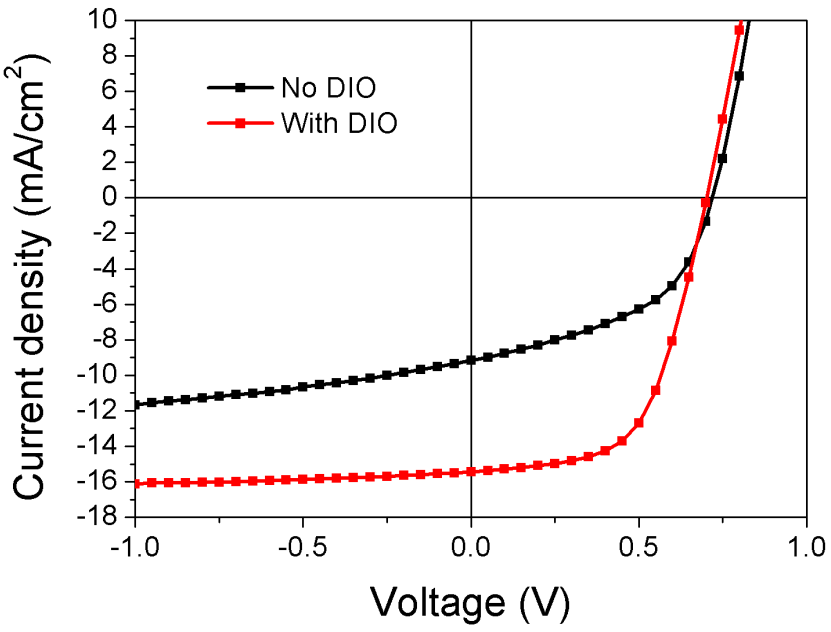

Figure 5.21 *J-V characteristic for PTB7:$PC_{71}BM$ (1:1.5) photovoltaics fabricated from chlorobenzene with and without additive.*

Table 5.4 *Performance parameters for PTB7:$PC_{71}BM$ (1:1.5) photovoltaics fabricated from chlorobenzene with and without additive. Statistics extracted from J-V characteristics shown in Figure 5.21.*

	No Dio	With Dio
Efficiency [%]	3.15	6.34
Jsc [mA/cm^2]	9.17	15.45
Voc [V]	0.72	0.70
FF [%]	48	59

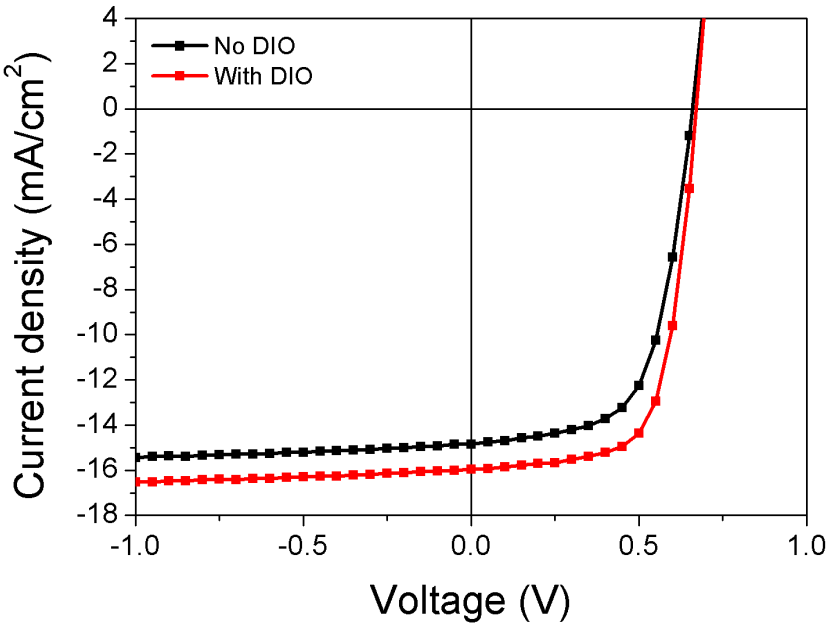

Figure 5.22 *J-V characteristic for PTB7:$PC_{71}BM$ (1:1.5) photovoltaics fabricated from dichlorobenzene with and without additive.*

Table 5.5 *Performance parameters for PTB7:$PC_{71}BM$ (1:1.5) photovoltaics fabricated from dichlorobenzene with and without additive. Statistics extracted from J-V characteristics shown in Figure 5.22.*

	No Dio	With Dio
Efficiency [%]	6.13	7.18
Jsc [mA/cm^2]	14.86	15.94
Voc [V]	0.66	0.67
FF [%]	63	67

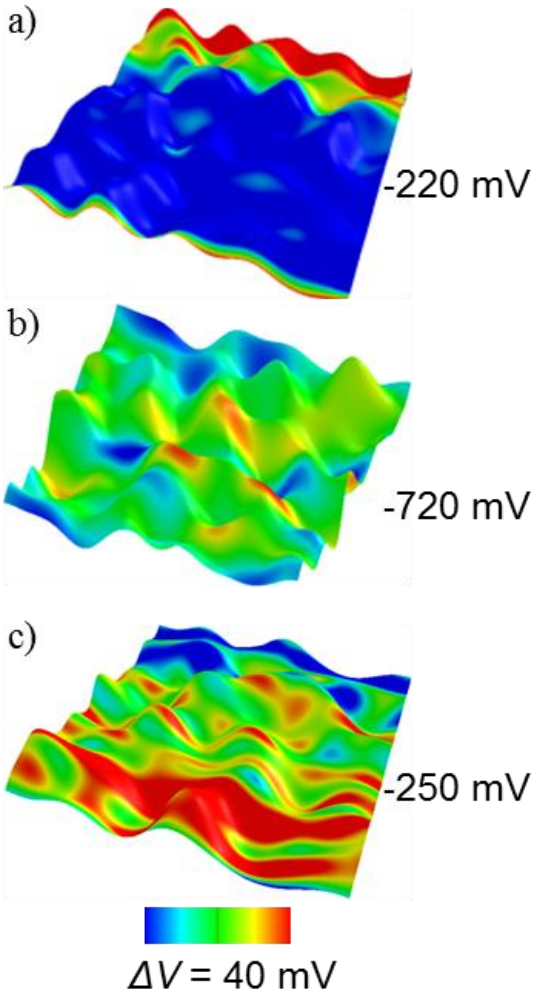

Figure 5.23 *Surface potential overlaid on topography for PEDOT:PSS thin films: (a) un-doped, (b) PFI doped and (c) FOS doped.*

Table 5.6 *Ionization potential as deduced from UPS measurements (I_p) along with nanoscopic and macroscopic work functions of PEDOT:PSS films.*

Doping	I_P (eV)	$W_{f\text{-}KPFM}$ (eV)	$W_{f\text{-}mKP}$ (eV)
--	5.19 ± 0.02	4.70 ± 0.02	5.20 ± 0.02
PFI	7.32 ± 0.02	5.40 ± 0.03	5.72 ± 0.02
FOS	7.09 ± 0.02	4.90 ± 0.03	5.56 ± 0.02

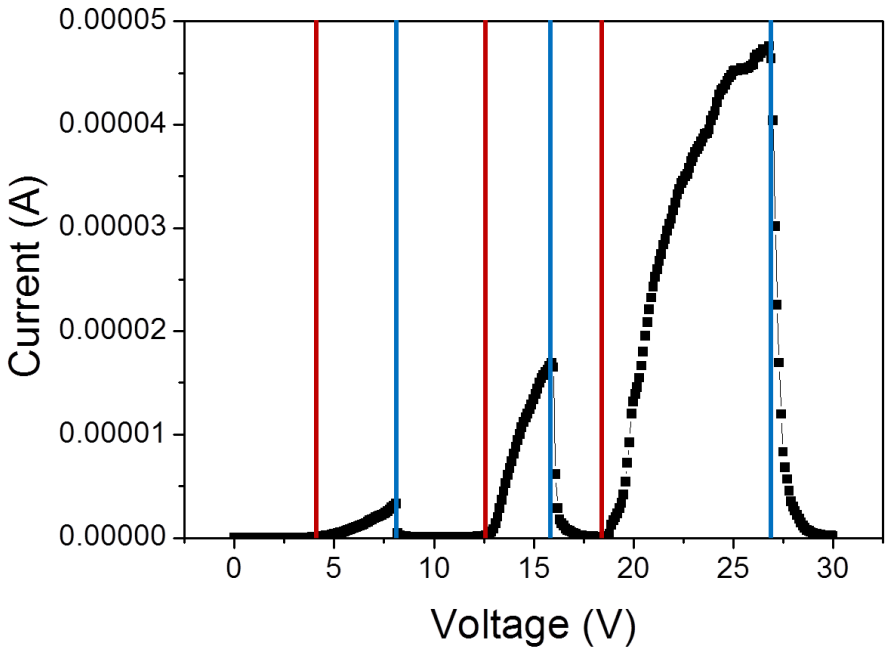

Figure 5.24 *Two-probe conductivity measurement. The vertical red and blue lines indicate the on and off switching of the humidifier, respectively.*

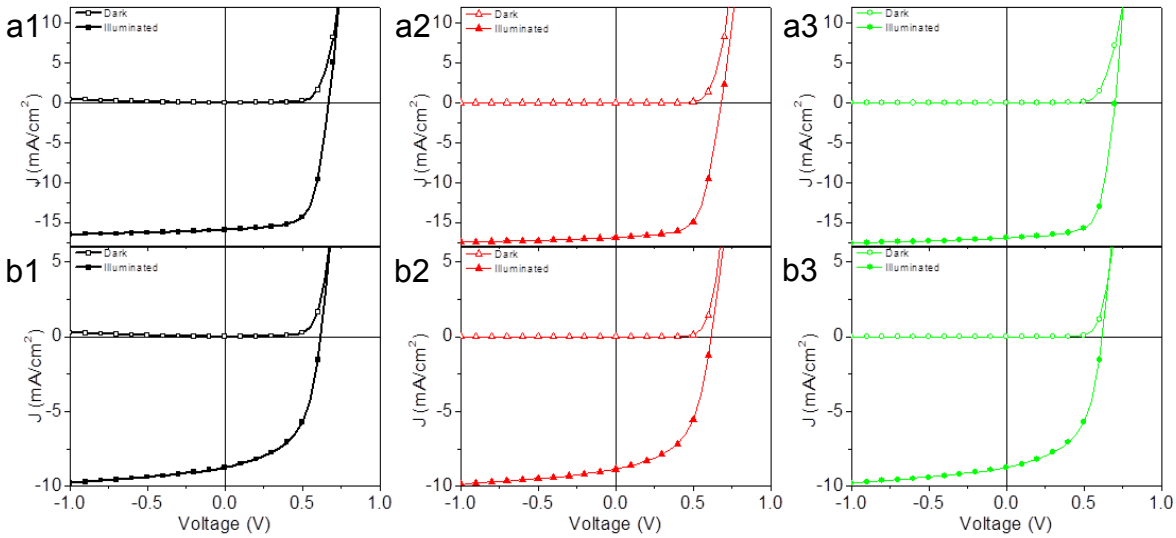

Figure 5.25 *PTB7:$PC_{71}BM$ (a) and P3HT:$PC_{61}BM$ photovoltaic cells using PEDOT:PSS (1), PEDOT:PSS:PFI (2) and PEDOT:PSS:FOS as the hole transport layer.*

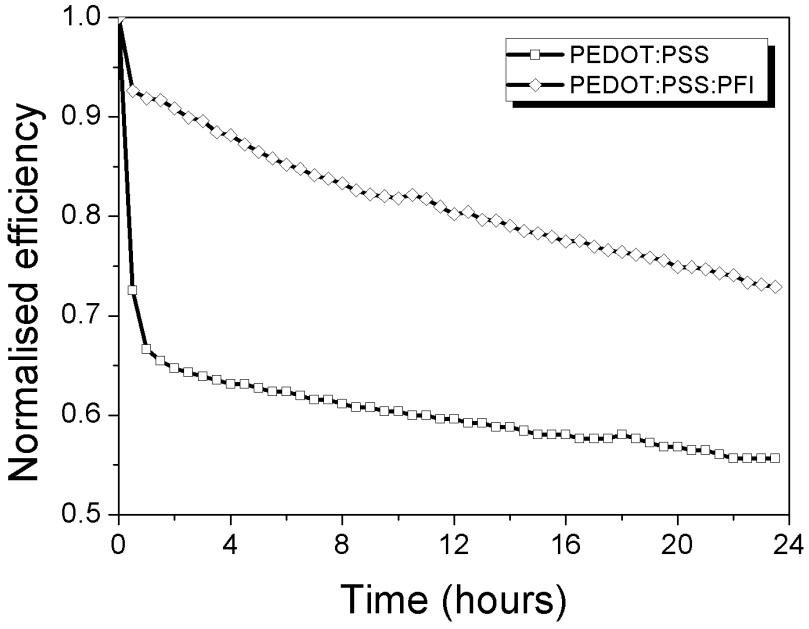

Figure 5.26 *Degradation of P3HT:PC_{61}BM cells with an un-doped or PFI doped (1:6:30) PEDOT:PSS interlayer (normalised PCE).*

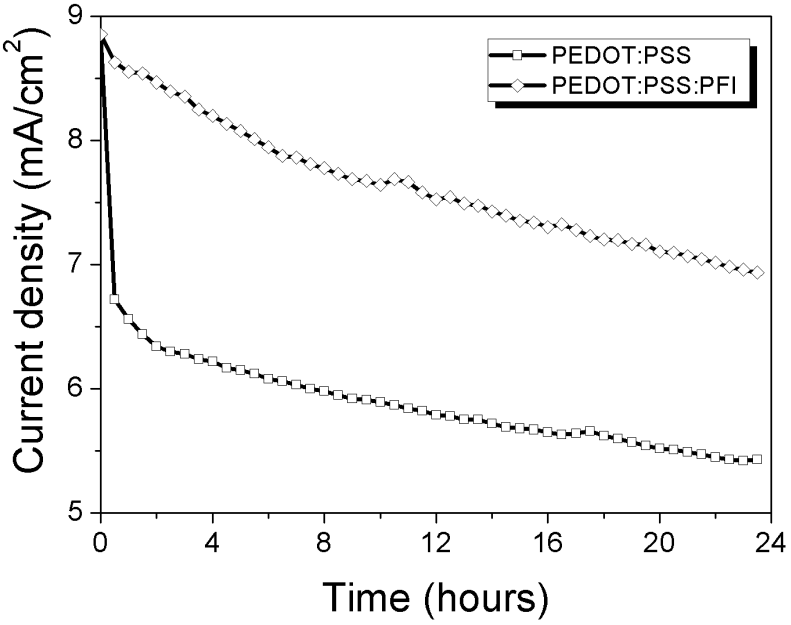

Figure 5.27 *Degradation of P3HT:PC_{61}BM cells with an un-doped or PFI doped (1:6:30) PEDOT:PSS interlayer (short-circuit current density).*

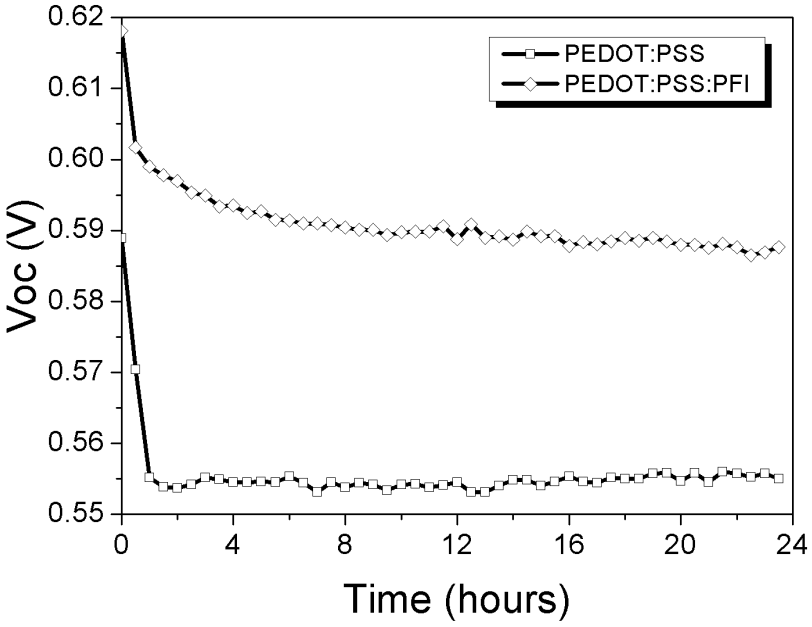

Figure 5.28 *Degradation of P3HT:$PC_{61}BM$ cells with an un-doped or PFI doped (1:6:30) PEDOT:PSS interlayer (open-circuit voltage).*

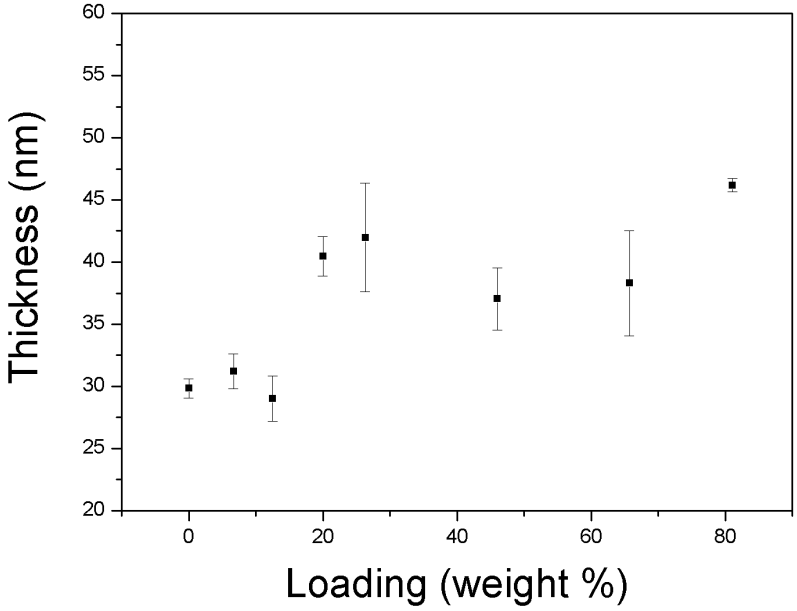

Figure 5.29 *Film thickness measured with a profiler. Figure shows films of PEDOT:PSS doped with different concentrations of PFI by percentage weight.*

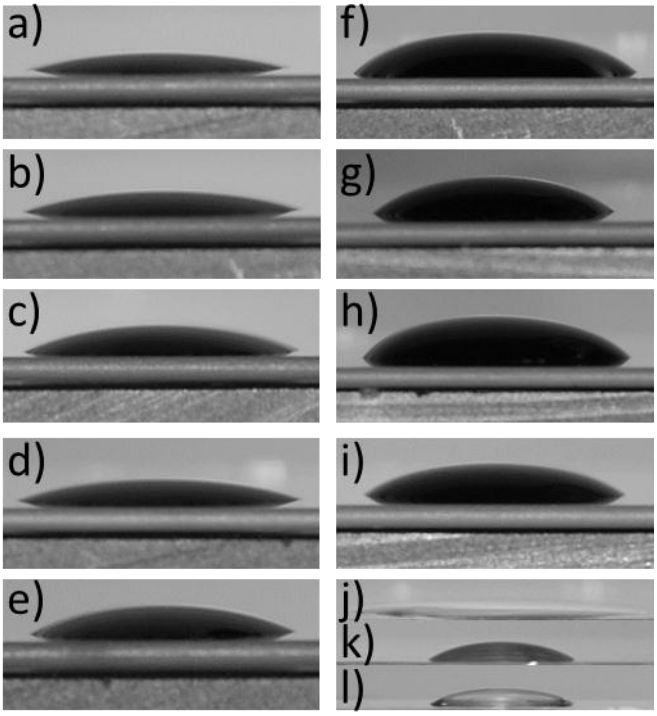

Figure 5.30 *Contact angle measurements for (a) un-doped, PFI doped (b) 1:6:1 (c) 1:6:2.5 (d) 1:6:13.4 (e) 1:6:30 and FOS doped (f) 1:6:1 (g) 1:6:2.5 (h) 1:6:13.4 (i) 1:6:30 PEDOT:PSS. (j), (k) and (l) are for measurements of dichlorobenzene deposited on the surface of the un-doped, PFI doped (1:6:30) or FOS doped (1:6:30) PEDOT:PSS interlayer.*

Table 5.7 Contact angles measurements for un-doped, PFI doped and FOS doped PEDOT:PSS. Measurements correspond to the images shown in Figure 5.30.

Coating	Ratio	Loading [%]	Contact angle [^{o}]
Conventional	1:6:0	0	11.62
PFI	1:6:1	12.5	11.88
	1:6:2.5	26.32	16.23
	1:6:13.4	65.69	16.88
	1:6:30	81.08	21.18
FOS	1:6:1	12.5	29.62
	1:6:2.5	26.32	38.56
	1:6:13.4	65.69	37.81
	1:6:30	81.08	37.74
Conventional	1:6:0	0	2.64
PFI	1:6:30	65.69	38.14
FOS	1:6:30	81.08	47.78

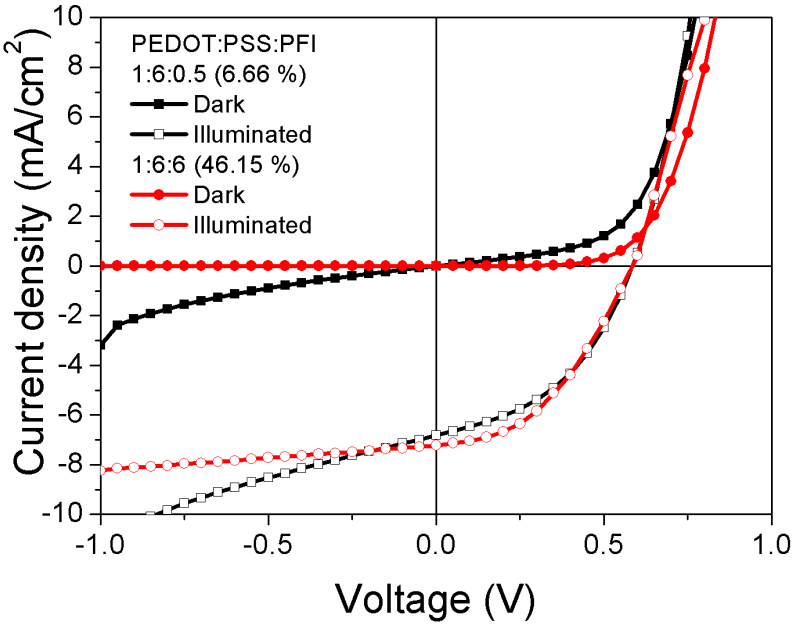

Figure 5.31 *J-V characteristics for two additional concentrations of PFI doping in PEDOT:PSS.*

5.6 References

1. Greczynski, G., et al., *Photoelectron spectroscopy of thin films of PEDOT–PSS conjugated polymer blend: a mini-review and some new results.* Journal of Electron Spectroscopy and Related Phenomena, 2001. **121**(1-3): p. 1-17.
2. Nardes, A.M., et al., *Microscopic Understanding of the Anisotropic Conductivity of PEDOT:PSS Thin Films.* Advanced Materials, 2007. **19**(9): p. 1196-1200.
3. Huang, J.S., et al., *Investigation of the effects of doping and post-deposition treatments on the conductivity, morphology, and work function of poly (3,4-ethylenedioxythiophene)/poly (styrene sulfonate) films.* Advanced Functional Materials, 2005. **15**(2): p. 290-296.
4. Nardes, A.M., R.A.J. Janssen, and M. Kemerink, *A Morphological Model for the Solvent-Enhanced Conductivity of PEDOT:PSS Thin Films.* Advanced Functional Materials, 2008. **18**(6): p. 865-871.
5. Huang, J.-H., et al., *Electrochemical characterization of the solvent-enhanced conductivity of poly(3,4-ethylenedioxythiophene) and its application in polymer solar cells.* Journal of Materials Chemistry, 2009. **19**(22): p. 3704-3712.
6. Xia, Y.J. and J.Y. Ouyang, *Significant Conductivity Enhancement of Conductive Poly(3,4-ethylenedioxythiophene): Poly(styrenesulfonate) Films through a Treatment with Organic Carboxylic Acids and Inorganic Acids.* ACS Applied Materials & Interfaces, 2010. **2**(2): p. 474-483.
7. Ouyang, J., et al., *On the mechanism of conductivity enhancement in poly (3,4-ethylenedioxythiophene): poly(styrene sulfonate) film through solvent treatment.* Polymer, 2004. **45**(25): p. 8443-8450.
8. Mauger, S.A., et al., *Directional dependence of electron blocking in PEDOT:PSS.* Organic Electronics, 2012. **13**(11): p. 2747-2756.
9. Lipomi, D.J., et al., *Electronic Properties of Transparent Conductive Films of PEDOT:PSS on Stretchable Substrates.* Chemistry of Materials, 2012. **24**(2): p. 373-382.
10. Takano, T., et al., *PEDOT Nanocrystal in Highly Conductive PEDOT:PSS Polymer Films.* Macromolecules, 2012. **45**(9): p. 3859-3865.
11. Xia, Y., K. Sun, and J. Ouyang, *Solution-processed metallic conducting polymer films as transparent electrode of optoelectronic devices.* Advanced materials, 2012. **24**(18): p. 2436-40.
12. McCarthy, J.E., et al., *Fabrication of highly transparent and conducting PEDOT:PSS films using a formic acid treatment.* Journal of Materials Chemistry C, 2014. **2**(4): p. 764.
13. Xia, Y., H. Zhang, and J. Ouyang, *Highly conductive PEDOT:PSS films prepared through a treatment with zwitterions and their application in polymer photovoltaic cells.* Journal of Materials Chemistry, 2010. **20**(43): p. 9740.
14. Makinen, A.J., et al., *Hole injection barriers at polymer anode/small molecule interfaces.* Applied Physics Letters, 2001. **79**(5): p. 557-559.
15. Fung, M.K., et al., *Anode modification of polyfluorene-based polymer light-emitting devices.* Applied Physics Letters, 2002. **81**(8): p. 1497-1499.
16. Crispin, X., et al., *The Origin of the High Conductivity of Poly(3,4-ethylenedioxythiophene)−Poly(styrenesulfonate) (PEDOT−PSS) Plastic Electrodes.* Chemistry of Materials, 2006. **18**(18): p. 4354-4360.
17. Lee, T.W., et al., *Self-Organized Gradient Hole Injection to Improve the Performance of Polymer Electroluminescent Devices.* Advanced Functional Materials, 2007. **17**(3): p. 390-396.
18. Lee, T.-W. and Y. Chung, *Control of the Surface Composition of a Conducting-Polymer Complex Film to Tune the Work Function.* Advanced Functional Materials, 2008. **18**(15): p. 2246-2252.
19. Luo, J., et al., *Enhancement of the thermoelectric properties of PEDOT:PSS thin films by post-treatment.* Journal of Materials Chemistry A, 2013. **1**(26): p. 7576.

20. Massonnet, N., et al., *Improvement of the Seebeck coefficient of PEDOT:PSS by chemical reduction combined with a novel method for its transfer using free-standing thin film.* Journal of Materials Chemistry C, 2014. **2**: p. 1278.
21. Li, D.W. and L.J. Guo, *Organic thin film transistors and polymer light-emitting diodes patterned by polymer inking and stamping.* Journal of Physics D-Applied Physics, 2008. **41**(10).
22. Sholin, V., et al., *High work function materials for source/drain contacts in printed polymer thin film transistors.* Applied Physics Letters, 2008. **92**(6): p. 3.
23. Pang, I., et al., *Aminosilane monolayer-assisted patterning of conductive poly(3,4-ethylenedioxythiophene) source/drain electrodes for bottom contact pentacene thin film transistors.* Organic Electronics, 2010. **11**(2): p. 338-343.
24. Tang, H., et al., *Highly sensitive dopamine biosensors based on organic electrochemical transistors.* Biosensors & Bioelectronics, 2011. **26**(11): p. 4559-4563.
25. Ko, C.-J., et al., *Modified buffer layers for polymer photovoltaic devices.* Applied Physics Letters, 2007. **90**(6): p. 063509.
26. Ouyang, J., et al., *High-Conductivity Poly(3,4-ethylenedioxythiophene):Poly(styrene sulfonate) Film and Its Application in Polymer Optoelectronic Devices.* Advanced Functional Materials, 2005. **15**(2): p. 203-208.
27. Nardes, A.M., et al., *Conductivity, work function, and environmental stability of PEDOT:PSS thin films treated with sorbitol.* Organic Electronics, 2008. **9**(5): p. 727-734.
28. Eom, S.H., et al., *Polymer solar cells based on inkjet-printed PEDOT:PSS layer.* Organic Electronics, 2009. **10**(3): p. 536-542.
29. Na, S.I., et al., *Evolution of nanomorphology and anisotropic conductivity in solvent-modified PEDOT:PSS films for polymeric anodes of polymer solar cells.* Journal of Materials Chemistry, 2009. **19**(47): p. 9045-9053.
30. Rahman, M.A., et al., *ITO-free low-cost organic solar cells with highly conductive poly(3,4 ethylenedioxythiophene): p-toluene sulfonate anodes.* Solar Energy Materials and Solar Cells, 2011. **95**(12): p. 3573-3578.
31. Kim, Y.H., et al., *Highly Conductive PEDOT:PSS Electrode with Optimized Solvent and Thermal Post-Treatment for ITO-Free Organic Solar Cells.* Advanced Functional Materials, 2011. **21**(6): p. 1076-1081.
32. Vosgueritchian, M., D.J. Lipomi, and Z.A. Bao, *Highly Conductive and Transparent PEDOT:PSS Films with a Fluorosurfactant for Stretchable and Flexible Transparent Electrodes.* Advanced Functional Materials, 2012. **22**(2): p. 421-428.
33. Alemu, D., et al., *Highly conductive PEDOT:PSS electrode by simple film treatment with methanol for ITO-free polymer solar cells.* Energy & Environmental Science, 2012. **5**(11): p. 9662-9671.
34. Zhang, W., et al., *High-efficiency ITO-free polymer solar cells using highly conductive PEDOT:PSS/surfactant bilayer transparent anodes.* Energy & Environmental Science, 2013. **6**(6): p. 1956.
35. Mengistie, D.A., P.C. Wang, and C.W. Chu, *Effect of molecular weight of additives on the conductivity of PEDOT: PSS and efficiency for ITO-free organic solar cells.* Journal of Materials Chemistry A, 2013. **1**(34): p. 9907-9915.
36. Mengistie, D.A., et al., *Highly Conductive PEDOT:PSS Treated with Formic Acid for ITO-Free Polymer Solar Cells.* ACS Appl Mater Interfaces, 2014.
37. DeSimone, J.M. and W. Tumas, *Green chemistry using liquid and supercritical carbon dioxide*. 2003, Oxford: Oxford University Press.
38. Lacroix-Desmazes, P., et al., *Macromolecular Surfactants for Supercritical Carbon Dioxide Applications: Synthesis and Characterization of Fluorinated Block Copolymers Prepared by Nitroxide-Mediated Radical Polymerization.* Journal of Polymer Science Part A: Polymer Chemistry, 2004. **42**(14): p. 3537-3552.

39. Guo, J., et al., *Solution properties of a fluorinated alkyl methacrylate polymer in carbon dioxide.* Macromolecules, 2006. **39**(9): p. 3427-3434.
40. Andre, P., et al., *Solubility of fluorinated homopolymer and block copolymer in compressed CO2.* Journal of Supercritical Fluids, 2006. **37**(2): p. 263-270.
41. Nalwa, H.S. and S.o. Miyata, *Nonlinear optics of organic molecules and polymers*. 1996, Boca Raton, Fla. ; London: CRC.
42. Lim, F.J., et al., *Influence of a novel fluorosurfactant modified PEDOT:PSS hole transport layer on the performance of inverted organic solar cells.* Journal of Materials Chemistry, 2012. **22**(48): p. 25057-25064.
43. Han, H.C., et al., *Enhancing efficiency with fluorinated interlayers in small molecule organic solar cells.* Journal of Materials Chemistry, 2012. **22**(43): p. 22899-22905.
44. Germack, D.S., et al., *Interfacial Segregation in Polymer/Fullerene Blend Films for Photovoltaic Devices.* Macromolecules, 2010. **43**(8): p. 3828-3836.
45. Pandey, A.K. and I.D.W. Samuel, *Photophysics of Solution-Processed Transparent Solar Cells Under Top and Bottom Illumination.* Selected Topics in Quantum Electronics, IEEE Journal of, 2010. **16**(6): p. 1560-1564.
46. Ma, W., et al., *Thermally Stable, Efficient Polymer Solar Cells with Nanoscale Control of the Interpenetrating Network Morphology.* Advanced Functional Materials, 2005. **15**(10): p. 1617-1622.
47. Campoy-Quiles, M., et al., *Morphology evolution via self-organization and lateral and vertical diffusion in polymer:fullerene solar cell blends.* Nat Mater, 2008. **7**(2): p. 158-164.
48. Hedley, G.J., et al., *Determining the optimum morphology in high-performance polymer-fullerene organic photovoltaic cells.* Nat Commun, 2013. **4**.
49. Lou, S.J., et al., *Effects of Additives on the Morphology of Solution Phase Aggregates Formed by Active Layer Components of High-Efficiency Organic Solar Cells.* Journal of the American Chemical Society, 2011. **133**(51): p. 20661-20663.
50. Li, G., et al., *Manipulating regioregular poly(3-hexylthiophene) : [6,6]-phenyl-C61-butyric acid methyl ester blends-route towards high efficiency polymer solar cells.* Journal of Materials Chemistry, 2007. **17**(30): p. 3126-3140.
51. He, Z., et al., *Enhanced power-conversion efficiency in polymer solar cells using an inverted device structure.* Nat Photon, 2012. **6**(9): p. 591-595.
52. Lee, T.-W., et al., *Hole-injecting conducting-polymer compositions for highly efficient and stable organic light-emitting diodes.* Applied Physics Letters, 2005. **87**(23): p. 231106.
53. Liang, Y., et al., *For the bright future-bulk heterojunction polymer solar cells with power conversion efficiency of 7.4%.* Advanced Materials, 2010. **22**(20): p. E135-8.
54. Lou, S.J., et al., *Effects of additives on the morphology of solution phase aggregates formed by active layer components of high-efficiency organic solar cells.* Journal of the American Chemical Society, 2011. **133**(51): p. 20661-3.
55. Chen, W., et al., *Hierarchical nanomorphologies promote exciton dissociation in polymer/fullerene bulk heterojunction solar cells.* Nano Letters, 2011. **11**(9): p. 3707-13.
56. Hammond, M.R., et al., *Molecular order in high-efficiency polymer/fullerene bulk heterojunction solar cells.* ACS Nano, 2011. **5**(10): p. 8248-57.
57. Cox, P.A., et al., *Mapping nanoscale variations in photochemical damage of polymer/fullerene solar cells with dissipation imaging.* ACS Nano, 2013. **7**(11): p. 10405-13.
58. Li, Z., et al., *Voltage-dependent photocurrent transients of PTB7:PC70BM solar cells: Experiment and numerical simulation.* Journal of Applied Physics, 2013. **114**(3): p. 034502.

59. Guo, S., et al., *Influence of Solvent and Solvent Additive on the Morphology of PTB7 Films Probed via X-ray Scattering.* Journal of Physical Chemistry B, 2014. **118**(1): p. 344-350.
60. Liu, C., et al., *Molecular weight effect on the efficiency of polymer solar cells.* ACS Applied Materials & Interfaces, 2013. **5**(22): p. 12163-7.
61. No, I.-J., et al., *Fabrication and Characteristics of Organic Thin-film Solar Cells with Active Layer of Interpenetrated Hetero-junction Structure.* Applied Physics Research, 2012. **4**(4).
62. Kumar, P., et al., *High-performance organic solar cells based on a low-bandgap poly-thienothiophene-benzodithiophene polymer and fullerene composite prepared by using the airbrush spray-coating technique.* Journal of the Korean Physical Society, 2013. **62**(8): p. 1169-1175.
63. Yanagidate, T., et al., *Flexible PTB7:PC70BM Bulk-Heterojunction Solar Cells with Lif Cathode Buffer Layer.* ECS Transactions, 2013. **58**(11): p. 39-48.
64. Zhou, N., et al., *Ultraflexible Polymer Solar Cells Using Amorphous Zinc-Indium-Tin Oxide Transparent Electrodes.* Advanced materials, 2013.
65. Yanagidate, T., et al., *Flexible PTB7:PC71BM bulk heterojunction solar cells with a LiF buffer layer.* Japanese Journal of Applied Physics, 2014. **53**(2S): p. 02BE05.
66. Szarko, J.M., et al., *Photovoltaic Function and Exciton/Charge Transfer Dynamics in a Highly Efficient Semiconducting Copolymer.* Advanced Functional Materials, 2014. **24**(1): p. 10-26.
67. Guerrero, A., et al., *Charge carrier transport and contact selectivity limit the operation of PTB7-based organic solar cells of varying active layer thickness.* Journal of Materials Chemistry A, 2013. **1**(39): p. 12345.
68. Xia, Y.J. and J.Y. Ouyang, *PEDOT:PSS films with significantly enhanced conductivities induced by preferential solvation with cosolvents and their application in polymer photovoltaic cells.* Journal of Materials Chemistry, 2011. **21**(13): p. 4927-4936.
69. Choi, M.-R., et al., *Soluble Self-Doped Conducting Polymer Compositions with Tunable Work Function as Hole Injection/Extraction Layers in Organic Optoelectronics.* Angewandte Chemie, 2011. **123**(28): p. 6398-6401.
70. Kim, J.S., et al., *Control of the electrode work function and active layer morphology via surface modification of indium tin oxide for high efficiency organic photovoltaics.* Applied Physics Letters, 2007. **91**(11): p. 112111.
71. Jaruwongrungsee, K., et al. *High-sensitivity humidity sensor utilizing PEDOT/PSS printed quartz crystal microbalance*. in *Electrical Engineering/Electronics, Computer, Telecommunications and Information Technology (ECTI-CON), 2011 8th International Conference on*. 2011.
72. Zhu, Y.W., et al., *Efficient organic-inorganic hybrid Schottky solar cell: The role of built-in potential.* Applied Physics Letters, 2013. **102**(11): p. 113504.
73. Teran-Escobar, G., et al., *Low-temperature, solution-processed, layered V2O5 hydrate as the hole-transport layer for stable organic solar cells.* Energy & Environmental Science, 2013. **6**(10): p. 3088-3098.
74. Lu, L., et al., *Ternary blend polymer solar cells with enhanced power conversion efficiency.* Nat Photon, 2014. **8**(9): p. 716-722.
75. Stalder, A.F., et al., *A snake-based approach to accurate determination of both contact points and contact angles.* Colloids and Surfaces A: Physicochemical and Engineering Aspects, 2006. **286**(1–3): p. 92-103.
76. Mihailetchi, V.D., L.J.A. Koster, and P.W.M. Blom, *Effect of metal electrodes on the performance of polymer:fullerene bulk heterojunction solar cells.* Applied Physics Letters, 2004. **85**(6): p. 970-972.
77. Mihailetchi, V.D., et al., *Cathode dependence of the open-circuit voltage of polymer:fullerene bulk heterojunction solar cells.* Journal of Applied Physics, 2003. **94**(10): p. 6849-6854.

Chapter 6

BODIPY-based conjugated polymers for broadband light sensing and solar energy harvesting

Overview

In this chapter, two low band-gap BODIPY-based conjugated polymers, p(BDP-bisEDOT) and p(BDP-bisEDTT) are introduced and shown to have properties favourable for optoelectronics. The performance of photovoltaic cells consisting solely of p(BDP-bisEDOT) or p(BDP-bisEDTT) as the active component, surpasses the typical performance expected of an organic photovoltaic cell without an acceptor. This indicates ambipolar behaviour, which is verified with time of flight (TOF) mobility measurements. The performance of the photovoltaic cells is dramatically increased with the addition of a fullerene acceptor, $PC_{71}BM$. The polymer-fullerene devices demonstrate a short-circuit current density (Jsc) similar to that of P3HT:$PC_{61}BM$. However, lower power conversion efficiencies (PCE) are observed as the open-circuit voltage (Voc) is half that of P3HT:$PC_{61}BM$. The lower Voc is a result of the gap between the HOMO of the donor and the LUMO of the acceptor being smaller than that of P3HT:$PC_{61}BM$. The polymer-fullerene devices can be used as photodiodes for sensing. I have measured the external quantum efficiency (EQE) under short-circuit conditions and under reverse bias and show that these devices have a broad spectral response. The devices can also be used for an absolute measurement of light intensity. Therefore, these novel low band-gap BODIPY-based conjugated polymers can be used for broadband sensing and solar energy harvesting.

Time of flight (TOF) mobility measurements were in collaboration with project student Stuart A. J. Thomson and Dr Salvatore Gambino under the supervision of Professor Ifor D. W. Samuel at the University of St Andrews. The synthesis and electrochemical characterisation was by Dr Diego Cortizo-Lacalle under the supervision of Professor Peter J. Skabara at the University of Strathclyde.

6.1 Introduction

Since the discovery of organic semiconductors [1-3] there has been considerable interest amongst researchers in using these materials as the active components in optoelectronic devices [4-6]. This interest arises from the possibility of being able to fabricate mechanically flexible, low-cost, light-weight devices from solution, with materials that have a readily tuneable band-gap [7]. Organic semiconductors are now-used as the active components in a plethora of optoelectronic devices including organic light-emitting diodes (OLED), organic field-effect transistors (OFET), organic photovoltaic (OPV) cells and organic lasers. However, their use in photodiodes for sensing applications has only just begun to be explored. The prospect of using organic semiconductors for photodiodes was realised after the development of the bulk heterojunction (BHJ) in 1995 [8, 9]. The interpenetrating network of donor and acceptor formed in the BHJ structure revolutionised the world of OPV. The most promising donor acceptor composition is a blend of conjugated polymer with soluble fullerene, respectively. It is the ultrafast electron transfer from polymer to fullerene in BHJ that allows us to make photodiodes for sensing applications [10]. It is also this polymer-fullerene composition that has been responsible for the extraordinary increase in OPV power conversion efficiency (PCE). By allowing excitons formed in the active layer to diffuse to the donor-acceptor interface within the exciton diffusion length [11, 12], as described. To date, polymer-fullerene devices may exhibit PCEs greater than 7 % [13, 14]. The most studied of all polymer-fullerene blends is that of poly (3-hexylthiophene) (P3HT) and [6, 6]-phenyl C_{61}butyric acid methyl ester (PCBM). Here charge transfer is from the lowest unoccupied molecular orbital (LUMO) of the photo-excited polymer to the LUMO of the acceptor. Standard P3HT:PCBM OPVs can have PCEs of up to 5 % [15]. However, the blends demonstrate a poor spectral response above 650 nm [16] as the band-gap of P3HT is ~1.9 eV [17]. To improve spectral responsively low band-gap polymers are required. An approach for obtaining low band-gap polymers is alternating the donor-acceptor units along the polymer back bone. This approach increases the highest occupied molecular orbital (HOMO) whilst at the same time decreasing the LUMO level.

In this chapter, I introduce and discuss the design of low band-gap polymers based on the 4, 4-difluoro-4-bora-3*a*, 4*a*-diaza-*s*-indacene (BODIPY) core with either bis (3, 4-ethylenedioxythiophene) (bisEDOT) or its all-sulfur analogue bis (3, 4-ethylenedithiathiophene) (bisEDTT). The BODIPY core is the electron acceptor unit and bisEDOT or bisEDTT the electron donor unit. I will then go on to discuss the fabrication, characterisation and optimisation of two types of optoelectronic device with these polymers as the active component and demonstrate them for broadband sensing and solar energy harvesting.

6.2 Materials-Polymers

The alternating donor-acceptor units often found in low band-gap polymers are usually synthesised by cross-coupling reactions of the donor and acceptor units [7]. There are an enormous number of units and an almost limitless number of possible organic semiconductors. The most common donor units are thiophenes and their derivatives [18]. Some others, include fluorene, carbazole, silafluorene, cyclopentadithiophene and their derivatives [19]. Common acceptor units include benzothiadiazole [20], thienopyrazine [21] and diketopyrrolopyrrole [22]. The polymers in this investigation have been synthesised with a BODIPY core, Figure 6.1, as the electron acceptor and either bisEDOT or bisEDTT as the electron donor.

The first BODIPY dye was synthesised by Treibs and Kreuzer in 1968 [23]. Since then, derivatives of BODIPY have been shown to have properties of interest to the research community. These properties which include strong absorption-emission spectra and chemical robustness [24-26] have resulted in BODIPY derivatives being used for a wide variety of applications including and not exclusive to chemosensors [24], labelling reagents [24], electroluminescent devices [27], electronically generated chemiluminescence [28], laser dyes [29], logic gates [30] and photovoltaic cells [31-33]. The BODIPY core shown in Figure 6.1 was originally synthesised by Arroyo et al in 2009 [34]. The rational for synthesising polymers with a BODIPY core for optoelectronics was 1) absorption $\lambda > 500$ nm 2) negligible triplet formation, degradation by self-produced single oxygen is low [35] 3) thermal stability and solubility in common solvents and 5) large quantities can be synthesised with short and simple synthetic routes.

3, 4-Ethylenedioxythiophene (EDOT) and its derivatives have been widely used in conjugated polymers. The well-known transparent conductive polymer PEDOT is synthesised using the polymerisation of EDOT. This polymer has properties which make it the most widely used organic semiconductor to date. PEDOT is often blended with sodium polystyrene sulfonate, resulting in poly(3, 4-ethylenedioxythiophene) poly(styrenesulfonate) (PEDOT: PSS). The most common usage for PEDOT: PSS is an antistatic agent. However, it is also widely used in organic optoelectronics for electrode fabrication. For comparison of BODIPY with EDOT, p(BDP-bisEDOT), the all-sulfur analogue of EDOT, 3, 4-Ethylenedithiathiophene (EDTT) was investigated, p(BDP-bisEDTT).

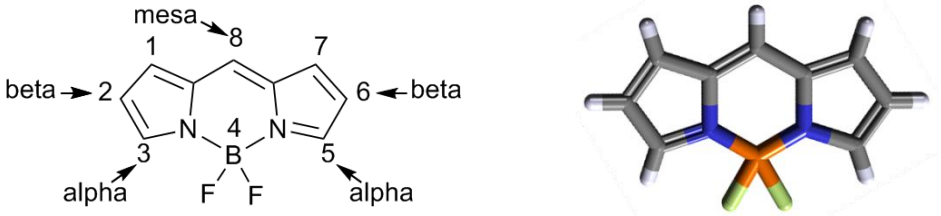

Figure 6.1 *Chemical structure of BODIPY core.*

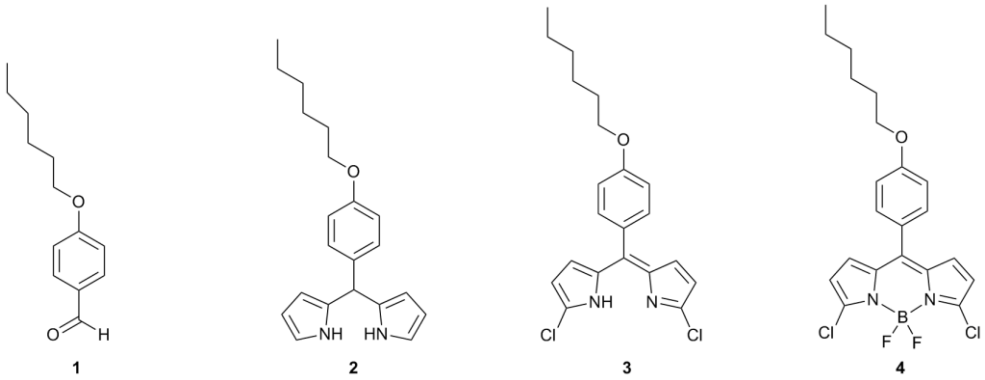

Figure 6.2 *Synthesis of the BODIPY core.*

The majority of BODIPY based polymers have been electrochemically synthesised through the beta-positions of the pyrrole rings [36], our polymers have been polymerised through the alpha positions, as shown in Figure 6.1. These polymers were synthesised for OPVs [37]. To make the polymers soluble a hexyloxy chain has been added to the para-position of the benzene ring at the meso-position of the BODIPY, compound **1**, Figure 6.2. This para-substituted benzaldehyde has been condensed with pyrrole using high excess pyrrole in the presence of catalytic amounts of trifluoroacetic acid (TFA), resulting in compound **2**. Compound **2**, was chlorinated on the two the available alpha-positions and oxidised with 2,3-Dichloro-5,6-dicyano-1,4-benzoquinone (DDQ), compound **3**. Here we see an extension of the conjugation between the pyrrole rings through the methylene unit. To complete the synthesis of the BODIPY core compound **4**, compound **3** was deprotonated with triethylamine and reacted with $BF_3.Et_2O$.

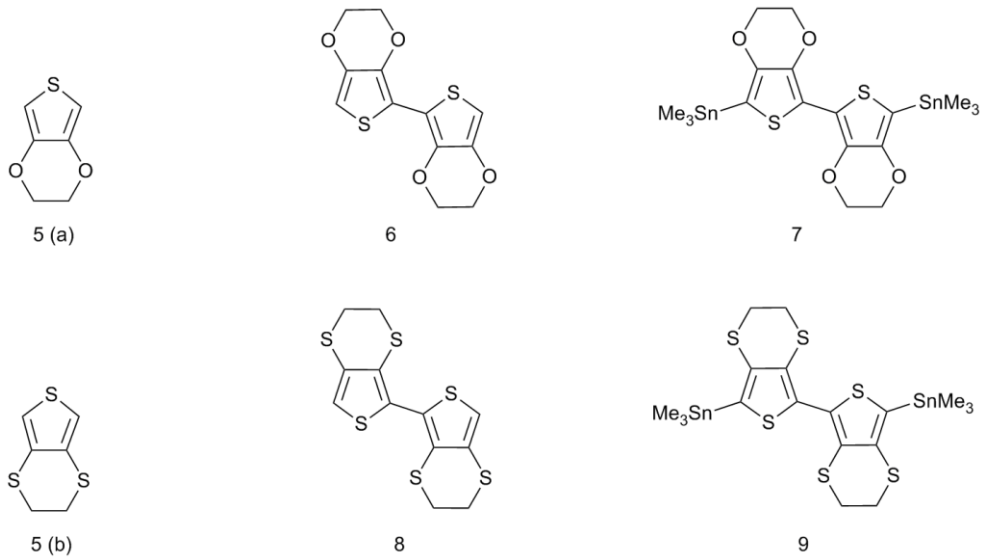

Figure 6.3 *Synthesis of bisEDOT and bisEDTT.*

6.2.1 Molecular structures

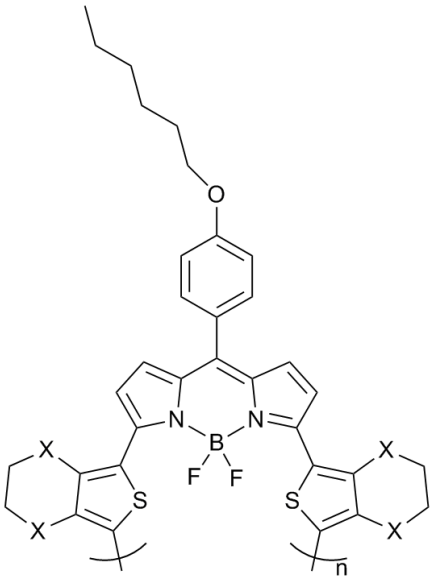

X = O, **p(BDP-bisEDOT)** **10**

X = S, **p(BDP-bisEDTT)** **11**

Figure 6.4 *Chemical structures of BODIPY-based conjugated polymers.*

EDOT and its all-sulfur analogue EDTT are shown in Figure 6.3, compound **5 (a)** and **5 (b)**, respectively. The synthesis of bisEDOT was initiated by Ullman coupling after lithiation of the EDOT unit and subsequent reaction with $CuCl_2$. The same procedure was implemented for EDTT. To obtain bisEDOT and bisEDTT, compounds **6** and **8** were lithiated with n-BuLi before reacting with Me_3SnCl, resulting in compounds **7** and **9**. The polymers p(BDP-bisEDOT) and p(BDP-bisEDTT) were synthesised via stille coupling of **4** with either **7** or **9**, respectively. The polymers p(BDP-bisEDOT) and p(BDP-bisEDTT) are shown in Figure 6.4 as compounds **10** and **11**, respectively. The polymers were dissolved in several solvents at concentrations similar to that used in device fabrication to assess solubility (10 mg/ml). The most promising solvent was dichloromethane, shown in Figure 6.5.

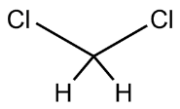

Figure 6.5 *Chemical structure of solvent dichloromethane.*

6.2.2 Electrochemical and optical properties

It is imperative to know the position of the HOMO and LUMO level of the polymers before device fabrication. Thereby, allowing for the correct choice of device architecture. The energy difference between the HOMO of the donor and the LUMO of the acceptor is proportional to the Voc. To maximise the Voc an appropriate acceptor must be selected to ensure that this gap is as large as possible, whilst ensuring that there is a sufficient driving force for exciton dissociation. A typical energy offset of $\geq$ 0.3 eV between the LUMO's of the donor and acceptor is required [38-40].

The HOMO and LUMO levels of p(BDP-bisEDOT) and p(BDP-bisEDTT) were determined by cyclic voltammetry, Figure 6.6. The bisEDOT and bisEDTT unit are responsible for oxidation and the BODIPY core for the reduction of the polymers [37]. The oxidation of p(BDP-bisEDOT) is lower than p(BDP-bisEDTT). This is due to the bisEDOT unit being a stronger electron donor than bisEDTT. The onset of the oxidation for p(BDP-bisEDOT) was +0.20 V and for p(BDP-bisEDTT), +0.47 V. HOMO levels of -5.00 eV and -5.27 eV were determined with ferrocene (-4.8 eV) as the reference for polymers p(BDP-bisEDOT) and p(BDP-bisEDTT), respectively. As the LUMO is dependent on the BODIPY core similar values were obtained for both polymers from the onset of reduction -1.15 V for p(BDP-bisEDOT) and -1.18 V for p(BDP-bisEDTT), giving LUMOs of -3.65 eV and -3.62 eV, respectively.

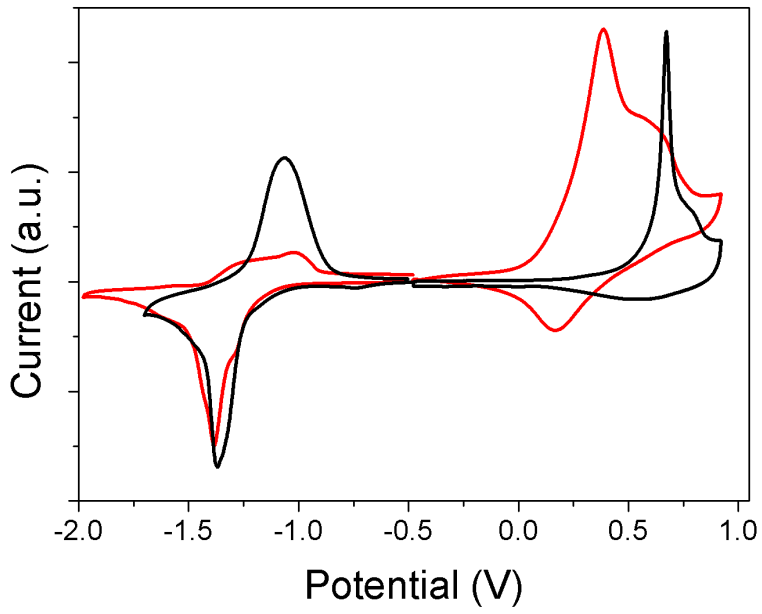

Figure 6.6 *Cyclic voltammetry of p(BDP-bisEDOT) (red) and p(BDP-bisEDTT) (black).*

The optical properties were characterised by UV-visible spectroscopy. Polymers p(BDP-bsEDOT) and p(BDP-bisEDTT) show broad absorption, Figure 6.7 and 6.8. The UV-visible absorption spectra show two distinctive peaks for each polymer in solution. For p(BDP-bisEDOT) there is a sharp peak at 426 nm and another at 818 nm. For p(BDP-bisEDTT) the peaks are at 405 nm and 648 nm. The peaks at shorter wavelengths can be easily mistaken for compound **4**, shown in Figure 6.2 as BODIPY is well known for having a strong absorption peak at lower wavelengths. However, the peaks belong to the EDOT units [37] or EDTT units. The absorption is impressive in solid state, particularly, for p(BDP-bisEDOT) as it absorbs from 400 nm to 1100 nm. In solid state the peaks are red shifted. The longer wavelengths are shifted to 669 nm and 821 nm for p(BDP-bisEDTT) and p(BDP-bisEDOT), respectively. The optical band-gaps have been calculated from the onset of absorption and found to be 1.18 eV for p(BDP-bsEDOT) and 1.35 eV for p(BDP-bisEDTT), as the onsets are 1050 nm and 919 nm, respectively.

The cyclic voltammetry and the UV-vis spectra show p(BDP-bisEDOT) to have a lower band-gap than p(BDP-bisEDTT). The reason for this is that the EDTT units in bisEDTT can be expected to be twisted [7]. However, the EDOT units in bisEDOT are likely to adopt a more planar spatial configuration. This is due to interactions between the atoms of adjacent EDOT units [41]. Solution measurements were carried out in dichloromethane, Figure 6.5 (a). For solid state measurements a thin-film of each polymer was deposited from a dichloromethane solution. It is worth mentioning that dichloromethane has a low boiling point of 39.6 °C. Therefore, we can expect a red-shift in optical absorption when depositing films from chlorobenzene, ortho-dichlorobenzene or trichlorobenzene as these solvents all have a higher boiling point ($>$ 130 °C), allowing for more crystalline domains. The solid state absorption spectra combined with energy levels and polymer band-gaps, make polymers p(BDP-bisEDOT) and p(BDP-bisEDTT) suitable for organic optoelectronics. The HOMO level of the polymers is well-matched to the electrode work functions of a typical device. Furthermore, the LUMO levels have a favourable energy offset ($\geq$ 0.3 eV) with the acceptor [6,6]-Phenyl-C_{71}-butyric acid methyl ester ($PC_{71}BM$) which is essential for charge separation and device performance.

Table 6.1 *Electrochemical and optical band-gaps of p(BDP-bisEDOT) and p(BDP-bisEDTT). The HOMO and LUMO levels were determined from the onset of the first oxidation and reduction[a]. The optical band-gaps were calculated from the onset of absorption[b].*

Polymer	**HOMO [eV][a]**	**LUMO [eV][a]**	**Eg [eV][a]**	**Eg [eV][b]**
p(BDP-bisEDOT)	-5.00	-3.65	1.35	1.18
p(BDP-bisEDTT)	-5.27	-3.62	1.65	1.35

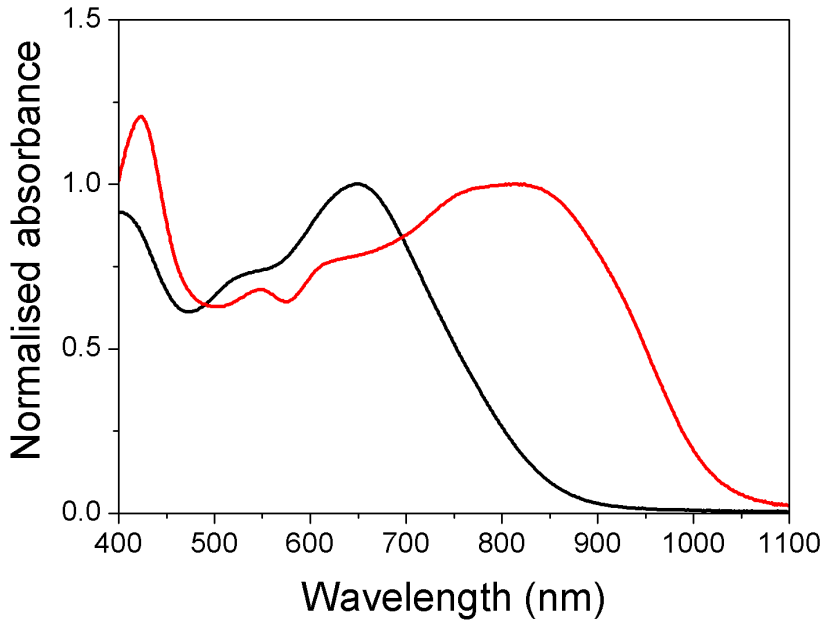

Figure 6.7 *UV-visible absorption of p(BDP-bisEDOT) (red) and p(BDP-bisEDTT) (black) in solution.*

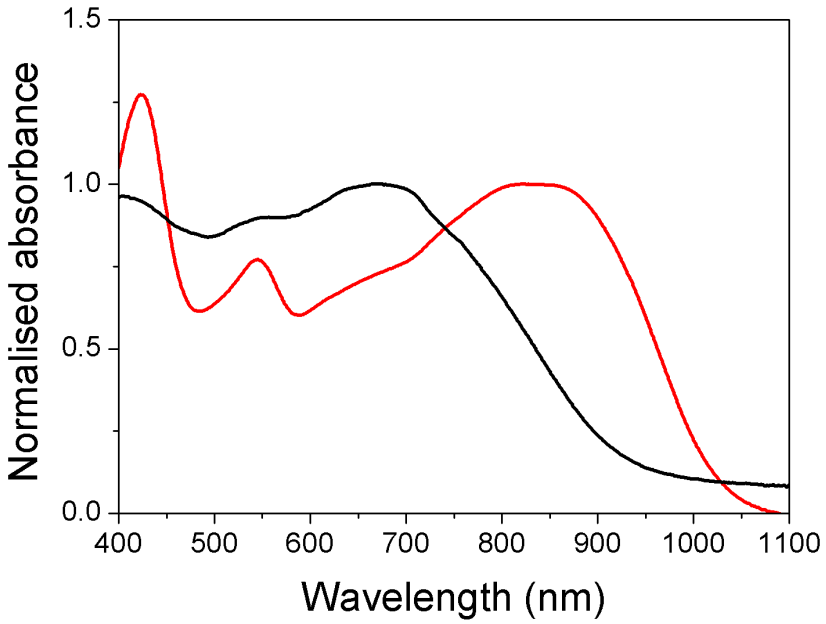

Figure 6.8 *UV-visible absorption of p(BDP-bisEDOT) (red) and p(BDP-bisEDTT) (black) in solid state.*

6.3 Polymer OPVs

I have shown polymers p(BDP-bisEDOT) and p(BDP-bisEDTT) to have favourable electrochemical and optical properties for organic optoelectronics. However, as the active component of a solution-processable organic optoelectronic device, it is essential that the polymers are soluble and exhibit a suitable morphology when blended with an acceptor, where excitons produced in the active layer, diffuse to the donor-acceptor interface within the exciton diffusion length, for dissociation, and after, the interpenetrating network should enable charges to travel within the percolated pathways to the adjacent electrodes. The most suitable morphology is achieved by adjusting film preparation conditions systematically. Here, I discuss the fabrication, optimisation and characterisation of two types of organic optoelectronic device with p(BDP-bisEDOT) or p(BDP-bisEDTT) as the active component, photovoltaic cells for solar energy harvesting and photodiode for sensing. The optimisation involves the fabrication and characterisation of devices. Devices are fabricated varying control parameters such as the acceptor, solvent, donor-acceptor ratio and the use of additives. These parameters alter the morphology and hence the recombination of excitons and charge in the active layer. Monitoring the performance parameters enables us to reduce the various loss mechanisms and therefore improve device performance.

6.3.1 Fabrication

Solar cells were prepared on indium tin oxide (ITO) coated glass substrates, purchased from Xin Yan Technology Ltd (15 Ω per □). The substrates were masked and etched in hydrochloric acid (37 %) for 20 minutes defining a 4 mm wide bottom contact and subsequently cleaned in an ultrasonic bath with deionised water, acetone and isopropanol successively for 15 minutes. The substrates were then dried with a nitrogen gun before being placed in an oxygen plasma asher for 5 minutes. Poly(3, 4-ethylenedioxythiophene) :poly(styrenesulfonate) (PEDOT:PSS) from H. C. Starck (Baytron AI4083) was spin-coated on top of the ITO at 4000 rpm and dried on a hot plate at 120 °C for 20 minutes. For active layer deposition, substrates were placed in a nitrogen-filled glove box. Active layers of various compositions with unique morphologies were deposited on top of the PEDOT:PSS by spin-coating. The devices were then placed into a vacuum chamber for aluminium deposition. 1.4 mm wide and 200 nm thick aluminium electrodes were thermally evaporated at a pressure of 1.8×10^{-6} mbar and a deposition rate of 0.4 nm s^{-1} producing devices with an active area of 0.06 cm^2. After back electrode deposition, devices were annealed for 20 minutes at 120 °C. Immediately after annealing, devices were encapsulated with a glass cover slip using a UV activated optical adhesive from Thorlabs. Devices were removed from the glove box and characterised, in air, using a K. H. Steuernagel AM 1.5 G solar simulator and a Keithley 2400 source-measure unit. Light intensities were verified with a calibrated thermopile from coherent model

number LM-1. IPCE spectra were measured using a NPL calibrated photodiode, Bentham TMc300 monochromator and a Keithley 6517A picoammeter.

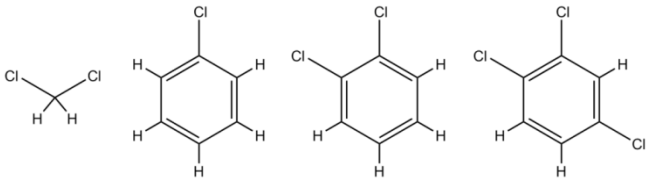

Figure 6.9 *Chemical structure of solvent dichloromethane, chlorobenzene, o-dichlorobenzene and trichlorobenzene (left to right).*

The active layers were deposited from a 20 mg ml^{-1} solution. The thickness was permanently maintained at ~100 nm. This was achieved by varying the ramp and spin speed. Film thicknesses were measured using a Dektak 150 M stylus profilometer. Devices were fabricated with a variety of acceptors. The acceptors investigated with what was thought to be a sufficient LUMO offset were Perylene-diimide (PDI), [6,6]-phenyl-C_{61}-butyric acid methyl ester-FLAVIN ($PC_{61}BM$-FLA), [6,6]-phenyl-C_{61}-butyric acid methyl ester ($PC_{61}BM$), [6,6]-phenyl-C_{71}-butyric acid methyl ester ($PC_{71}BM$) and [6,6]-phenyl C_{84} butyric acid methyl ester ($PC_{84}BM$). The donor-acceptor ratio was varied for the most promising acceptors in several different solvents. Optimum devices consisting solely of polymer were prepared from a 15 mg ml^{-1} solution, whilst, the bulk devices were spin-coated from a 20 mg ml^{-1} solution. A few drops of carbon disulfide (CS_2) were added to each chlorobenzene solution, before spin coating to enhanced solubility. Spin coating BHJ was at 1000 rpm, this produced films of ~110 nm thickness.

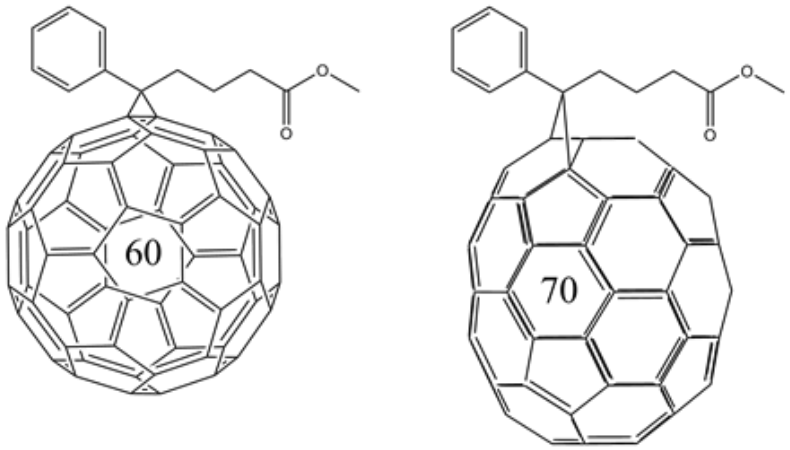

Figure 6.10 *Chemical structure of $PC_{61}BM$ (left) and $PC_{71}BM$ (right).*

The polymers p(BDP-bisEDOT) and p(BDP-bisEDTT) or **10** and **11**, respectively, demonstrate excellent solubility in dichloromethane. However, dichloromethane is not an ideal solvent for device fabrication. The quality of films spin-coated from the solvent is often poor, particularly, for films containing both polymer and fullerene. The low boiling point of the solvent, 39.6 °C, hinders intermixing and crystal growth. Solvents with higher boiling points for example chlorobenzene, dichlorobenzene and trichlorobenzene, Figure 6.9, have boiling points > 130 °C. Higher boiling point solvents increase the drying time during spin-coating and subsequent annealing [42]. Polymer fullerene films spin-coated from chlorobenzene or trichlorobenzene were mediocre. Clusters of insoluble polymer were present and this limited device performance. To improve solubility carbon disulphide was used as an additive, Figure 6.11.

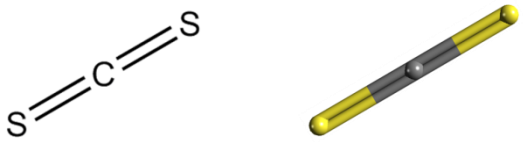

Figure 6.11 *Chemical structure of carbon disulfide (left) with ball-stick (right).*

The discovery of solvent additives [43] and their ability to radically improve the performance of organic photovoltaic cells, has raised considerable interest among the research community [44]. Yongye Liang et al. showed that as little as 3 % total volume of 1, 8-diiodoctane (DIO) to chlorobenzene could increase the PCE from 3.92 % to 7.4 % [45]. The additives are used to improve the solubility of the lesser soluble component within the BHJ and control the morphology of BHJ [46]. The use of solvent additives is not at all times intuitive. However, it is well-known that the additive must have a different boiling point to the host solvent. In our study carbon disulfide (CS_2) was selected as it has a boiling point of 46.3 °C and the polymers demonstrated exceptional solubility at high concentrations, 30 mg ml^{-1}. Films spin-coated from trichlorobenzene with CS_2 were of poor quality. However, films from chlorobenzene with CS_2 were exceptional. This is possibly due to the large difference in boiling point between the solvents, 131 °C for chlorobenzene and 214.4 °C for trichlorobenzene.

BHJ containing $PC_{61}BM$ or $PC_{71}BM$ demonstrated a photovoltaic response. The performance of $PC_{71}BM$ surpassed $PC_{61}BM$. The donor-acceptor ratio was varied. The optimum ratio was determined to be 1:4. The energy levels for the optimum BHJ for p(BDP-bisEDOT), **10**, and p(BDP-bisEDTT), **11**, are presented in Figure 6.12 (top) and Figure 6.13 (top), respectively. The device structures are presented in Figure 6.12 (bottom) and Figure 6.13 (bottom) for p(BDP-bisEDOT) and p(BDP-bisEDTT), respectively. The active layer is sandwiched between the PEDOT:PSS and Aluminium electrode. The UV activated epoxy and glass cover slip have been omitted from the diagram.

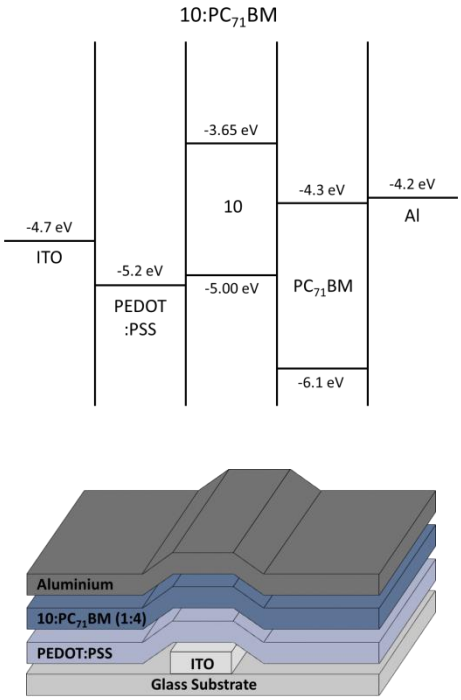

Figure 6.12 *Energy levels (top) and device structure (bottom) for p(BDP-bisEDOT)* ***10****:$PC_{71}BM$ (1:4).*

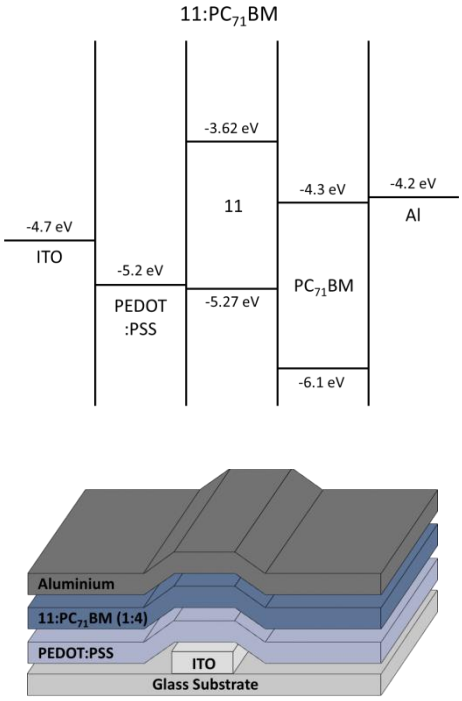

Figure 6.13 *Energy levels (top) and device structure (bottom) for p(BDP-bisEDTT)* ***11****:$PC_{71}BM$ (1:4).*

6.3.2 Optimisation

The optimisation of organic photovoltaic cells can be challenging. By nature, each cell is unique. Small variations in the fabrication or characterisation can dramatically alter device performance. However, if the correct protocols are followed, it is possible to optimise, even if the photovoltaic cell demonstrates poor performance. As fundamentally important as the band-gap is, it is by no means the bottleneck. Material properties, such as solubility and mobility, can limit performance. As such, it is imperative for device physicists to collaborate with chemists to ensure that the materials synthesised are feasible for optoelectronics. The focus of the device physicist is to discover the optimum morphology of the composite, and determine if the materials are suitable for optoelectronics.

To optimise, it is imperative to ensure that the electrochemical and optical properties are suitable. Solubility in common organic solvents is advantageous. If a material shows solid state emission it can be used to determine an appropriate acceptor, by time-resolved fluorescence techniques or steady state photoluminescence quantum yield (PLQY) measurements. On deciding on the most suitable acceptor, devices can be fabricated and the film quality and morphology investigated. If the film quality is good, then various donor-acceptor ratios can be explored, whilst maintaining the active layer thickness. On determining the optimum donor-acceptor ratio one can explore the use of thermal annealing, additives, low work function electrodes and inverted structures.

Here, I will discuss the optimisation of BODIPY-based conjugated polymer optoelectronic devices for sensing and harvesting. The J-V characteristics in this section were acquired under 100 mW cm^{-2} illumination with a standard AM1.5 G source. The statistics can be found in the appendix, Table 6.3.

It was not possible to probe the solid state emission and determine a suitable acceptor by the quenching of photoluminescence. Therefore, to determine an appropriate acceptor it was necessary to fabricate devices. Polymer **10** was dissolved in dichloromethane with a number of different acceptors, at a donor-acceptor ratio of 1:1. Only two of the five devices demonstrated a satisfactory photovoltaic response, **10**: $PC_{61}BM$ and **10**: $PC_{71}BM$, Figure 6.14. The PCEs were 0.04 % and 0.09 % for **10**: $PC_{61}BM$ and **10**: $PC_{71}BM$, respectively. The higher PCE for **10**: $PC_{71}BM$ arises from a larger FF and a Jsc almost double that of **10**: $PC_{61}BM$. The FF was 30 % for **10**: $PC_{71}BM$ and 24 % for **10**: $PC_{61}BM$. The Jsc for **10**: $PC_{61}BM$ and **10**: $PC_{71}BM$ was 0.59 mA cm^{-2} and 1.14 mA cm^{-2}, respectively. Device **10**: $PC_{71}BM$ has a larger Jsc as the fullerene $PC_{71}BM$ is likely to be contributing to the overall photocurrent. Furthermore, there is a larger driving force for charge separation, reducing recombination. However, the larger driving force is at a cost. The larger driving force is due to the LUMO of $PC_{71}BM$ being lower than that of $PC_{61}BM$. Having a lower LUMO reduces the gap between the HOMO of the donor and the LUMO of the acceptor. The theoretical maximum Voc is defined

as the $HOMO_D$-$LUMO_A$ [38-40] for this reason a slightly lower Voc is observed for $PC_{71}BM$, 0.26 V, compared to 0.28 V for $PC_{61}BM$.

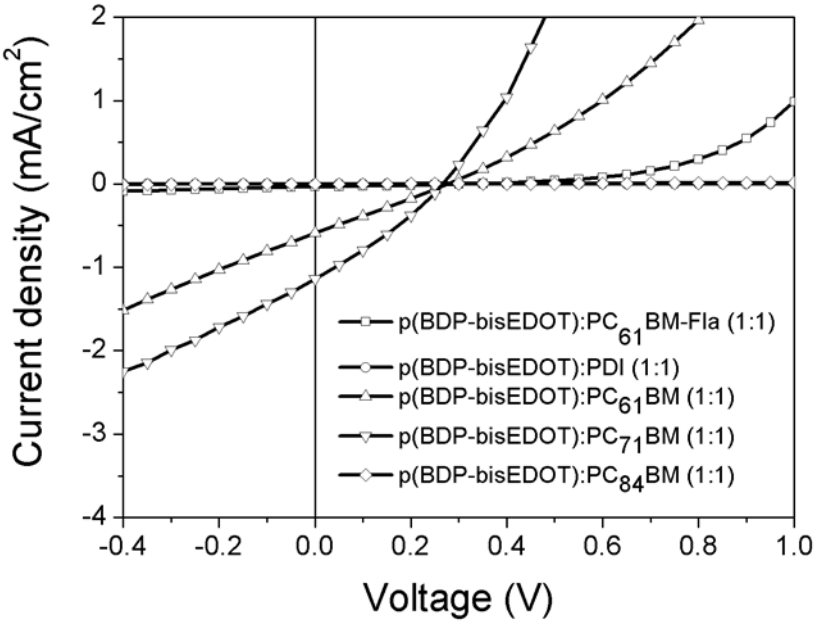

Figure 6.14 *J-V characteristics of polymer* ***10*** *with a number of different acceptors.*

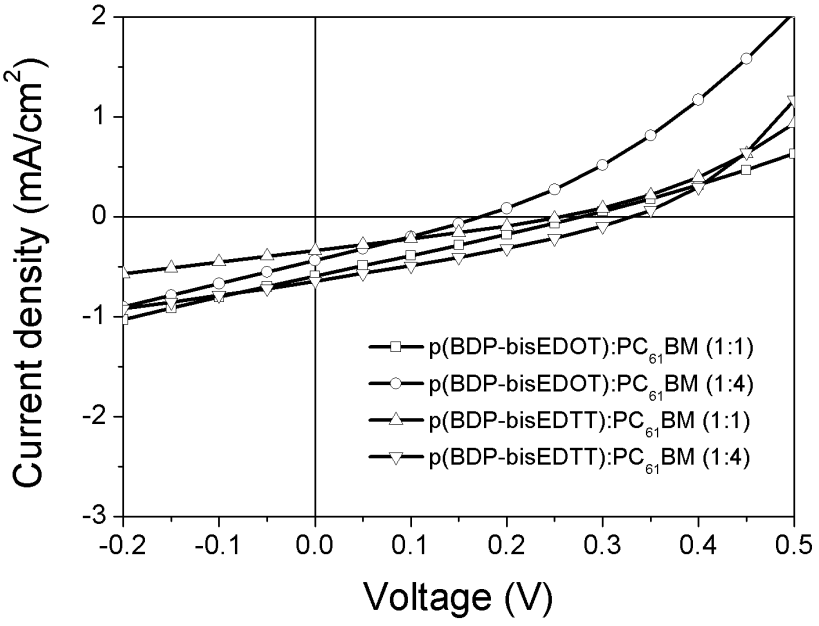

Figure 6.15 *J-V characteristics of polymer* ***10*** *and* ***11*** *with acceptor, $PC_{61}BM$, at a ratio of 1:1 and 1:4 in dichloromethane.*

To confirm if $PC_{71}BM$ was the correct choice of acceptor, devices were fabricated with $PC_{61}BM$ and polymers **10** and **11**. Films containing donor-acceptor ratios 1:1 and 1:4 were deposited from a dichloromethane solution, Figure 6.15. Polymer **10** devices at ratio 1:1 and 1:4 had PCEs 0.04 % and 0.02 % respectively. Devices fabricated with polymer **11** had PCEs 0.02 % and 0.06 % for ratio 1:1 and 1:4, respectively.

With its low boiling point dichloromethane is far from an ideal solvent for device fabrication. Following the same procedure devices were fabricated with chlorobenzene, Figure 6.16. For polymer **10** a slight improvement was observed with PCEs of 0.1 % and 0.08 % for 1:1 and 1:4, respectively. There was no improvement for polymer **11** devices.

Polymer **10** devices with $PC_{71}BM$ were fabricated with a number of different solvents, Figure 6.17. The PCE increased from 0.09 % for dichloromethane and o-dichlorobenzene to 0.16 % for chlorobenzene and trichlorobenzene. Confirming that $PC_{71}BM$ is the appropriate acceptor and that dichloromethane is not a suitable solvent.

Devices were fabricated with polymer **10** and **11** with acceptor, $PC_{71}BM$, at a donor-acceptor ratio of 1:2, 1:4 and 1:6. For polymer **10** the PCE for 1:2 and 1:6 were <0.1 % and for 1:4, 0.26 %. The device demonstrated a Jsc of 3.61 mA cm^{-2}, Voc of 0.2 V and a FF of 36 %, making 1:4 the optimum ratio for polymer **10**. The optimum donor-acceptor ratio for polymer **11** was 1:4 with a PCE of 0.25 %. The PCE for 1:2 and 1:6 was <0.1 % with Jsc ~ 1.0 mA cm^{-2}. The Jsc for the 1:4 device was >3 mA cm^{-2}, Figure 6.18.

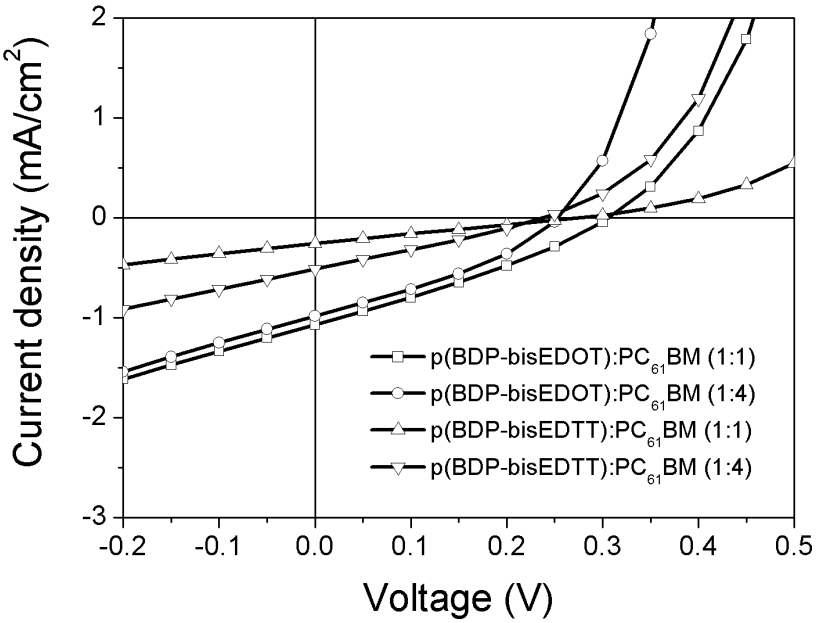

Figure 6.16 *J-V characteristics of polymer **10** and **11** with acceptor, $PC_{61}BM$, at a ratio of 1:1 and 1:4 in chlorobenzene.*

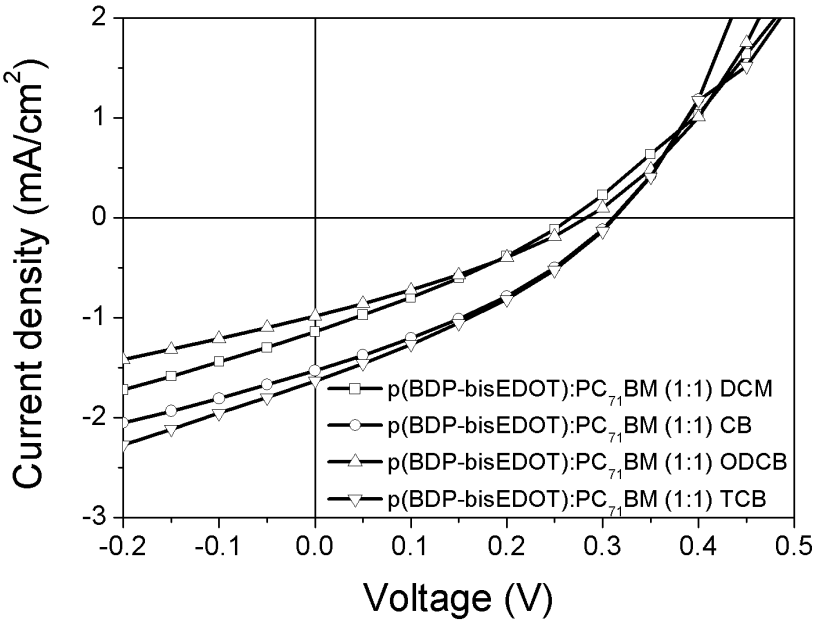

Figure 6.17 *J-V characteristics of polymer* ***10*** *with $PC_{71}BM$ in a number of different solvents.*

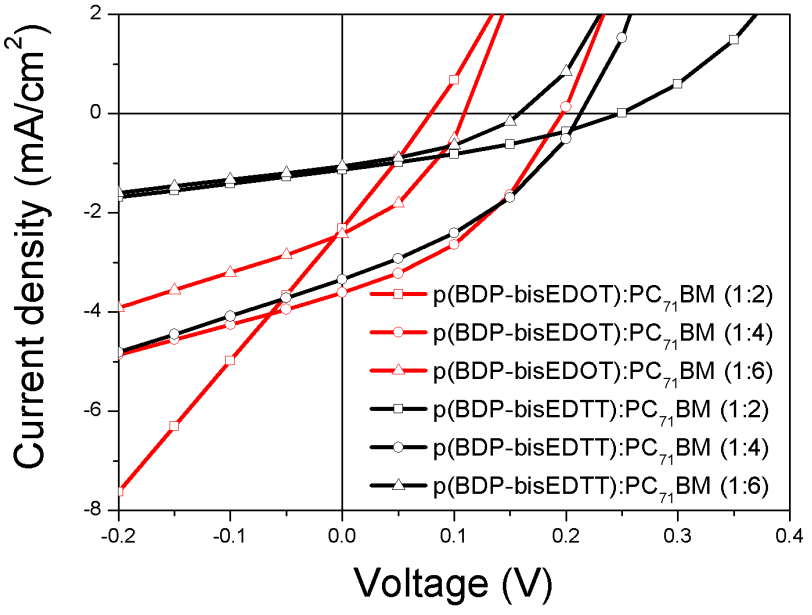

Figure 6.18 *-V characteristics of polymer* ***10*** *and* ***11*** *with acceptor, $PC_{71}BM$, at a ratio of 1:2, 1:4 and 1:6 in trichlorobenzene.*

The solubility of the polymers limited device performance. Figure 6.19 shows a tapping mode height image of polymer **10** from an Atomic force microscope (AFM). The root mean square (RMS) roughness was calculated to be around ~22 nm for a 10 μm×10μm scan area. The small bead-like structures are not of concern. However, some of these small structures are closely packed, forming clusters that are > 60 nm in height.

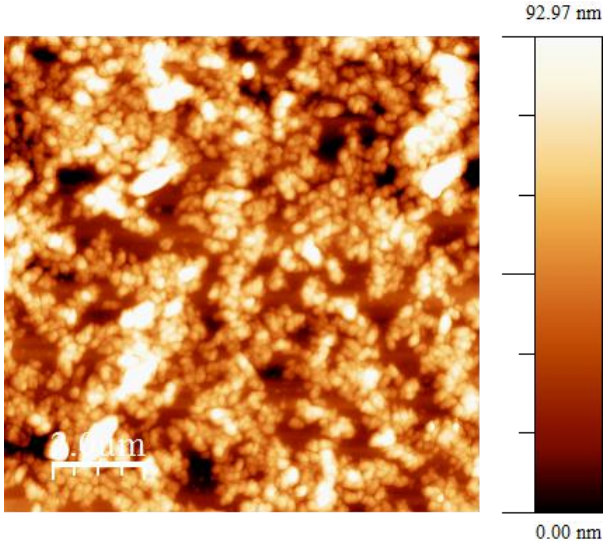

Figure 6.19 *Tapping mode atomic force microscope (AFM) height image.*

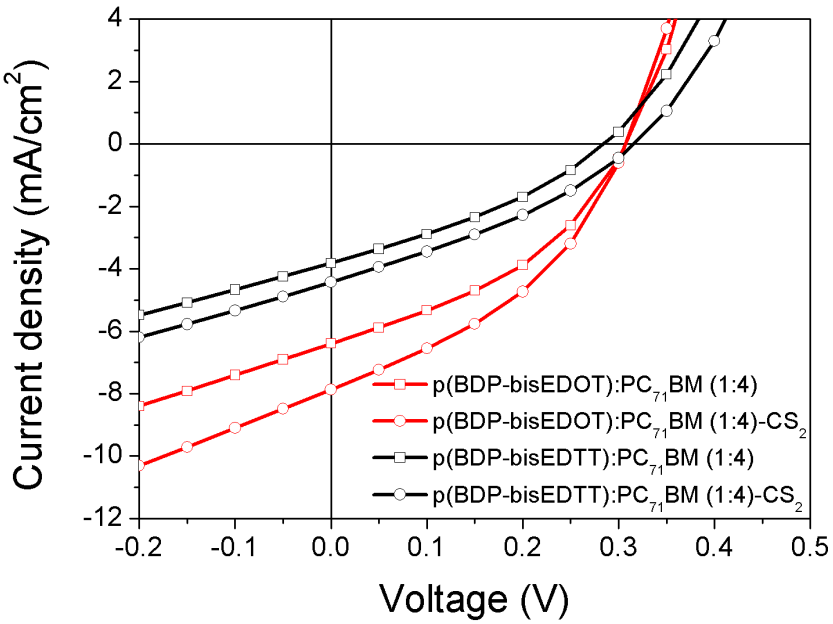

Figure 6.20 *J-V characteristics of polymer **10** and **11** with acceptor, $PC_{71}BM$, at a ratio of 1:4 in chlorobenzene with and without additive, carbon disulfide.*

6.3.3 Characterisation

To improve the solubility of polymer **10** and **11**, CS_2, was added to the solutions prior to spin-coating the active layer. The use of CS_2 as an additive improved device performance, as can be seen in Figure 6.20. For polymer **10** the PCE increased from 0.78 % to 0.95%. For polymer **11** the PCE increased from 0.35 % to 0.45 %. The increase in PCE for **10** and **11** is a direct result of an in increase in Jsc with the addition of CS_2.

In Figure 6.21 the J-V characteristics for polymer **10** and **11** are shown. The short circuit current density is high for photovoltaic cells consisting solely of polymer. The short circuit current densities were 1.18 mA cm^{-2} for **10** and 0.62 mA cm^{-2} for **11**. The high short circuit currents for polymer only devices indicate ambipolar charge transport.

The addition of an electron acceptor at a donor-acceptor ratio of 1:4 dramatically improves performance. The PCE increased from 0.13 % to 0.95 % for **10** and from 0.06 % to 0.45 % for **11**. The observed decrease in Voc for the polymer-fullerene devices can be attributed to the energy loss arising from electron transfer between the donor and the acceptor.

Polymer **10** performance surpassed that of polymer **11** for polymer only and polymer fullerene devices. Figure 6.21 and Figure 6.22 show the illuminated and dark currents for the optimum polymer and polymer-fullerene compositions, respectively.

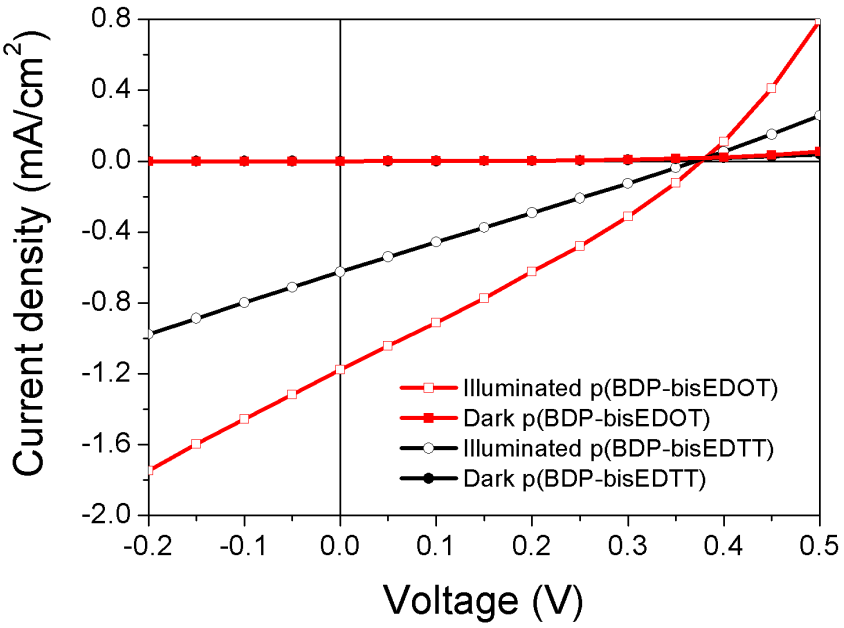

Figure 6.21 *J-V characteristics for polymer only devices dark and under illumination at 100 mW $cm^{-2}$with an AM1.5 G source.*

The statistics for polymer and polymer-fullerene photovoltaic cells are shown in Table 6.2. The results show that BODIPY-based conjugated polymers p(BDP-bisEDOT) and p(BDP-bisEDTT), **10** and **11**, respectively, are suitable for solar energy harvesting. The Jsc for **10** is similar to that of P3HT: $PC_{61}BM$. A fill factor of 39 % is encouraging. The only issue is the Voc and if this were to be improved then it is reasonable to assume that similar efficiencies to that of P3HT: $PC_{61}BM$ would be realised. It is also interesting that the polymers perform reasonably well without an acceptor.

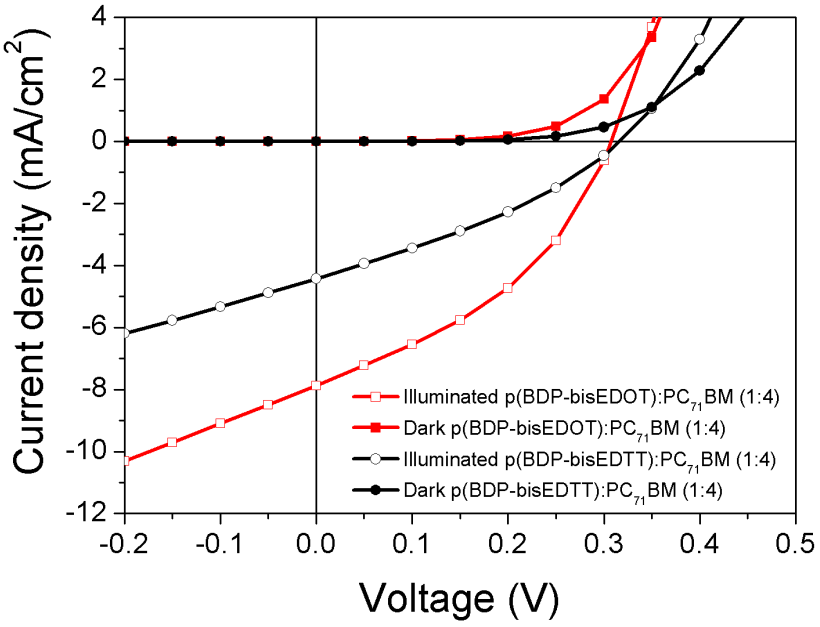

Figure 6.22 *J-V characteristics for polymer-fullerene devices dark and under illumination at 100 mW cm^{-2} with an AM1.5 G source.*

Table 6.2 *Performance statistics for polymer and polymer-fullerene devices under illumination at 100 mW cm^{-2} with an AM1.5 G source.*

Active layer	**Jsc [mA/cm^2]**	**Voc [V]**	**FF [%]**	**PCE [%]**
10	1.18	0.38	29	0.13
11	0.62	0.37	26	0.06
10:$PC_{71}BM$ (1:4)	7.87	0.31	39	0.95
11:$PC_{71}BM$ (1:4)	4.42	0.32	32	0.45

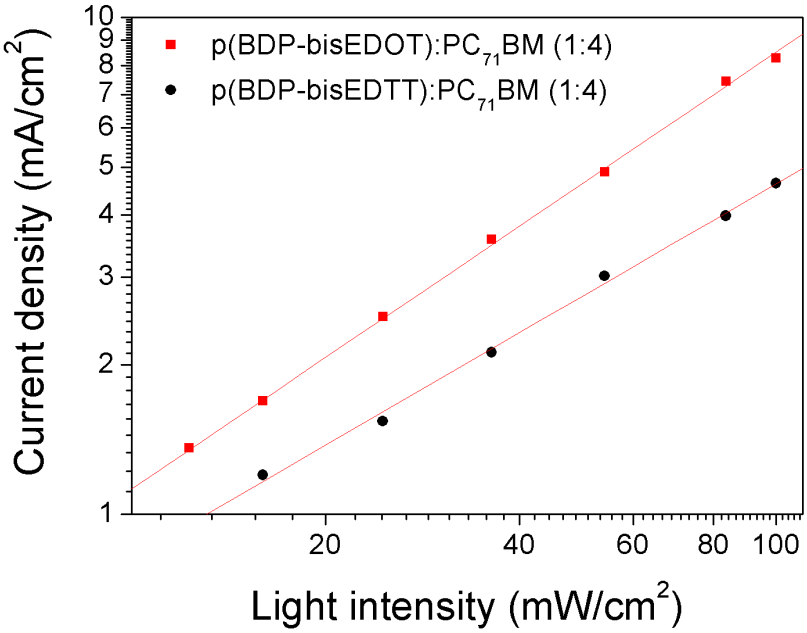

Figure 6.23 *Short circuit current densities for a number of light intensities.*

The ultrafast photo-induced electron transfer from polymer to fullerene [10] and fast temporal responses with high sensitivity of polymer-fullerene devices [47-49] allow organic semiconductors to be used in the fabrication of photodiodes. Furthermore, with low band-gap polymers a device can be sensitive across the UV-VIS-NIR region.

Today, broad-band photodiodes are fabricated with a number of materials with a variety of band-gaps to get the UV-VIS-NIR wavelength (λ) range. These systems are important for a wide variety of industrial and scientific applications. However, they can be expensive to manufacture and to operate, as some require cooling.

Xiong Gong et al demonstrated organic photodiodes with a broad-band spectral response from 400 nm to 1450 nm. However, their EQEs were relatively low across the entire region, from 400 nm to 600 nm the EQEs were $<$ 10 % and from 600 nm to 1450 nm the EQEs were $<$ 5 %, without an external bias [50].

To demonstrate my devices for sensing I show that the devices can be used for an absolute measure of light intensity, Figure 6.23, and that they have a broad-band spectral response, by measuring the EQE under short circuit conditions and under reverse bias, Figure 6.24 and 6.25. Both polymer-fullerene blends show a broad spectral response from 400 nm to 1100 nm, Figure 6.24 and 6.25.

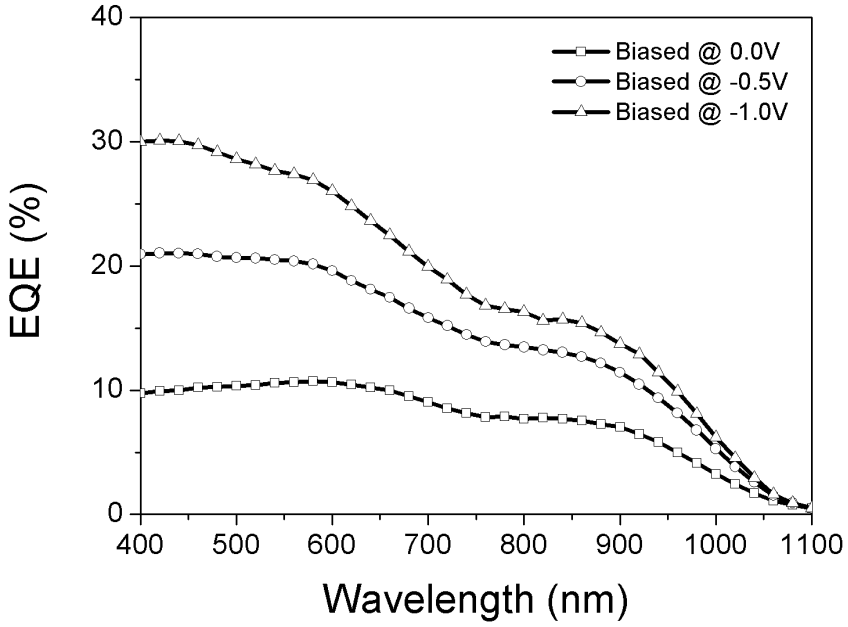

Figure 6.24 *Incident photon to converted electron (IPCE) ratio for p(BDP-bisEDOT): $PC_{71}BM$ at a 1:4 ratio with and without an external bias.*

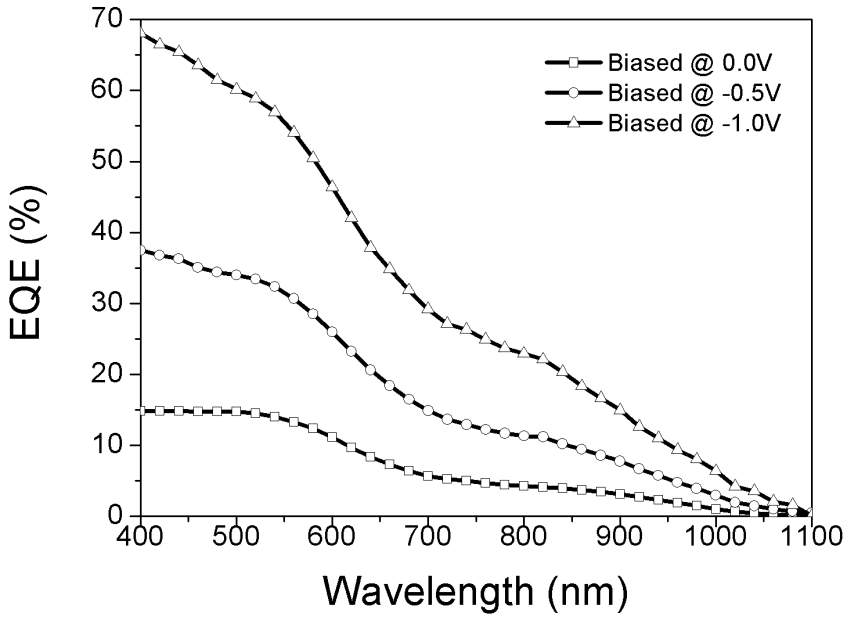

Figure 6.25 *Incident photon to converted electron (IPCE) ratio for p(BDP-bisEDTT): $PC_{71}BM$ at a 1:4 ratio with and without an external bias.*

For **10**: $PC_{71}BM$, Figure 6.24, an EQE of ~10, 20, 30 % is observed from 400–600 nm under 0.0, −0.5, −1.0 V bias, respectively. There is a steady decrease in EQE from 600–900 nm. However, the EQE remains > 5 % without an external bias. The EQE at 950 nm under 0.0, −0.5, −1.0 V bias is approximately half of that between 400 nm and 600 nm. A sharp fall in EQE is observed between 900 and 1100 nm.

For **11**: $PC_{71}BM$, Figure 6.25, an impressive EQE of 15 % is observed from 400 nm to 550 nm without an applied bias. In the same wavelength (λ) range with a bias of -0.5 V or -1.0 V an EQE of ~ 30 % or ~50 % is observed, respectively. From 550 nm to 1100 nm the EQE decreases because of the decreased absorption of polymer **11** and $PC_{71}BM$.

The large EQE from 400 nm to 700 nm can be attributed to the absorption of $PC_{71}BM$ and its ability to effectively dissociate excitons into free charge carriers, allowing them to contribute to photocurrent.

Polymers **10** and **11** demonstrate unusually high short circuit currents in photovoltaic cells without an acceptor, indicating ambipolar charge transport. To further understand this behaviour, electron and hole mobility measurements were carried out using a time of flight (TOF) technique.

Polymer **10** was selected for the study as it exhibited a Jsc almost double that of polymer **11**. In Figure 6.26 (a) the linear hole photocurrent transient for an electric field of 1.8×10^5 V cm^{-1} is shown. The transit time was determined by plotting the photocurrent transient in a log-log scale and fitting straight lines before and after the knee, Figure 6.26 (b). Using the relation $\mu=d^2/(V\times T)$, where d is the film thickness, V the applied field and T the transit time, it was possible to calculate the mobility. For an applied field of 1.8×10^5 V cm^{-1} the transit time was 39 μs, corresponding to a hole mobility value of 1.5×10^{-5} cm^2 V^{-1} s^{-1}. The linear electron photocurrent transient is shown in Figure 6.27 (a) for an applied field of 1.8×10^5 V cm^{-1}. The transit time from the log-log plot was 7 μs, Figure 6.27 (b), corresponding to an electron mobility value of 7.7×10^{-5} cm^2 V^{-1} s^{-1}.The schematic for the hole and electron mobility TOF experimental setup is shown in Figure 6.26 (a) and 6.27 (a). The thickness of the active layer, measured with a Dektak profiler, was found to be 1.1 μm. This was achieved by drop-casting. The photo-generation of charge carriers was at 580 nm with a pulsed dye laser. For electron mobility measurements the sample was illuminated through the negatively biased ITO contact and the electrons were collected at the aluminium contact, whilst for the hole mobility measurements the sample was illuminated through the positively biased aluminium contact and the hols collected at the ITO contact.

In order to demonstrate that polymer **10** is an ambipolar charge transport carrier material, TOF electron and hole mobility measurements were performed for a wide range of electric fields.

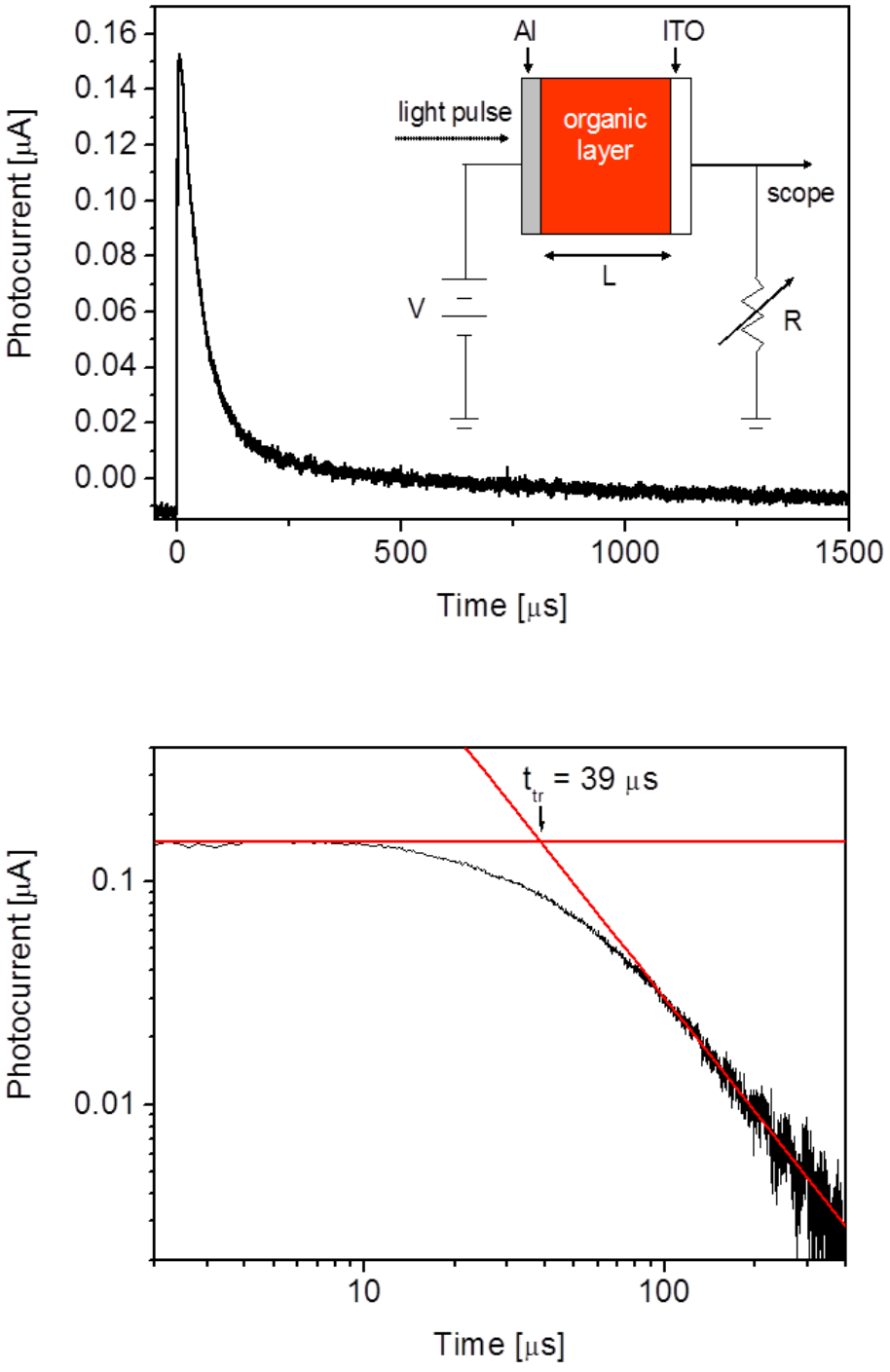

Figure 6.26 *Hole photocurrent transient of* ***10*** *at an electric field of 1.8 x 10^5 Vcm^{-1} both in linear (top) and log-log (bottom) scale. Schematic of the TOF experimental set-up for the mobility measurements (inset).*

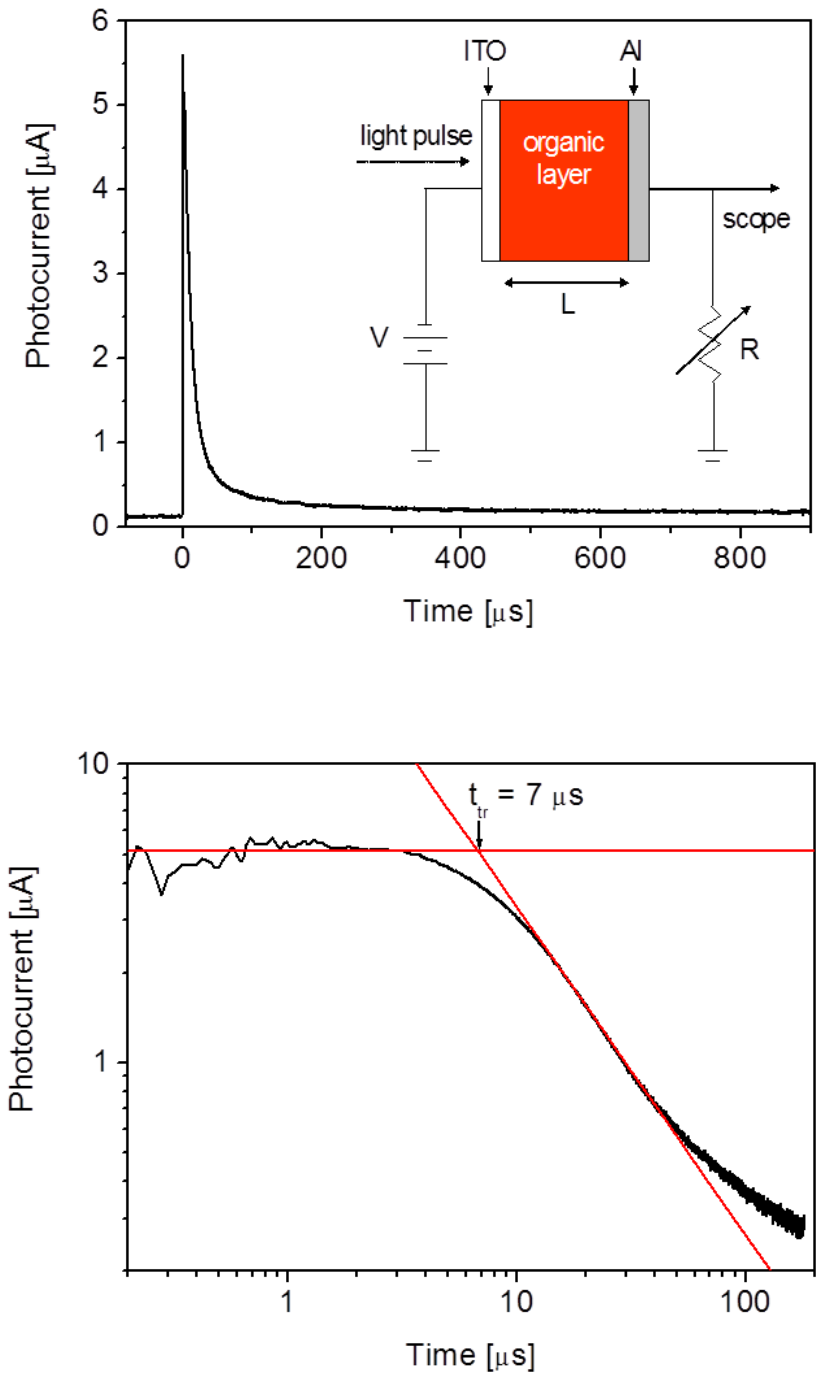

Figure 6.27 *Electron photocurrent transient of* ***10*** *at an electric field of 1.8 x* 10^5 Vcm^{-1} *both in linear (top) and log-log (bottom) scale. Schematic of the TOF experimental set-up for the mobility measurements (inset).*

To investigate the mobility field dependence TOF electron and hole mobility measurements were performed for a number of electric fields. In Figure 6.28 the electron (squared dots) and hole mobility (circular dots) are plotted as a function of the square root of the applied electric field.

In the photovoltaic devices polymer **10** was used as an electron donor, so it is surprising to see the electron mobility > hole mobility. It implies that it may be possible for polymer **10** to be used as an electron acceptor.

It is also interesting that the electron and hole mobility are of the same order of magnitude. This behaviour is entirely unexpected for an electron donor material. Usually, the electron mobility would be orders of magnitude lower than the hole mobility. Here, it is seen that the electron mobility values are approximately three times higher than the hole mobility values, verifying our suspicions of ambipolar behaviour.

The ambipolar behaviour of BODIPY has recently been confirmed by Bura, T. et al. Furthermore, they demonstrate BODIPY-based small molecules with a PCE ~ 4.7 % with $PC_{61}BM$ [51]. Efficiencies for BODIPY based conjugated polymers remain < 1 % [52]. However, a state of the art device was recently reported with an efficiency of > 2 % [33]. These studies confirm if the electrochemical properties were favourable for $PC_{61}BM$, it is possible that efficiencies > 1 % would have been achieved.

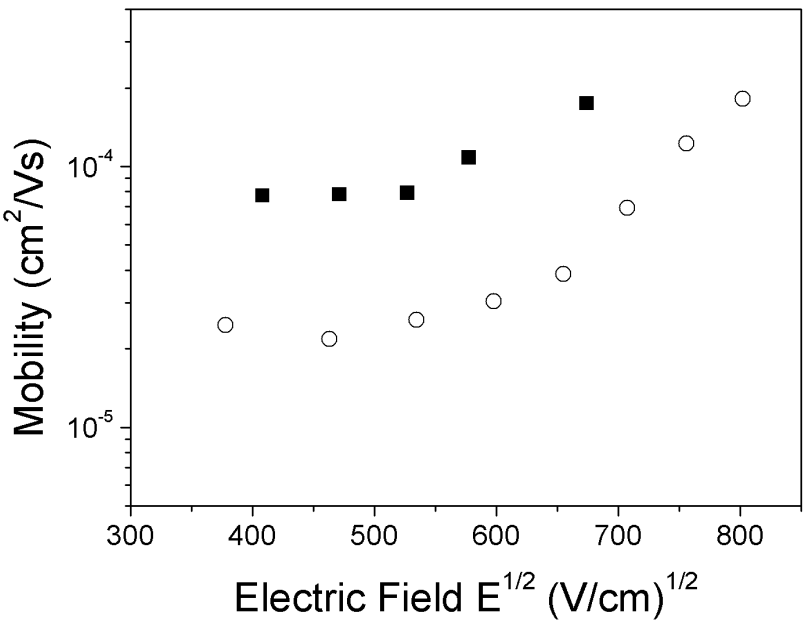

Figure 6.28 *Electron (squared dots) and hole (circular dots) mobility for polymer* ***10*** *for a number of applied electric fields.*

6.4 Conclusion

Two novel low band-gap conjugated polymers based on the 4, 4-difluoro-4-bora-3*a*, 4*a*-diaza-*s*-indacene (BODIPY) core, and either bis (3, 4-ethylenedioxythiophene) (bisEDOT) or the all-sulfur analogue bis (3, 4-ethylenedithiathiophene) (bisEDTT) have been introduced and shown to have properties suitable for optoelectronics. Optoelectronic devices were fabricated, characterised and optimised. The optimum devices demonstrate broad-band sensing and solar energy harvesting in organic photodiodes and photovoltaic cells, respectively.

The performance of photovoltaic cells consisting solely of polymer p(BDP-bisEDOT) or p(BDP-bisEDTT) as the active component, surpasses the typical performance expected of an organic photovoltaic cell without an acceptor, indicating polymers p(BDP-bisEDOT) and p(BDP-bisEDTT) to be ambipolar. Polymer p(BDP-bisEDOT) was selected for mobility measurements as the short circuit current was 1.18 mA cm^{-2} compared to 0.62 mA cm^{-2} for p(BDP-bisEDOT). Time of flight (TOF) mobility measurements show electron and hole mobility values to be of the same order of magnitude, confirming p(BDP-bisEDOT) as an ambipolar charge transport material.

The performance of photovoltaic devices dramatically increases with the addition of the acceptor, $PC_{71}BM$. From 0.13 % to 0.95 % for p(BDP-bisEDOT):$PC_{71}BM$ and from 0.06 % to 0.45 % for p(BDP-bisEDTT):$PC_{71}BM$. The optimum donor-acceptor ratio for both polymers was 1:4. The p(BDP-bisEDOT):$PC_{71}BM$ device demonstrated a short circuit current similar to that of P3HT:$PC_{61}BM$. However, a lower PCE is observed as the Voc is half that of P3HT:$PC_{61}BM$. The solubility of polymer p(BDP-bisEDOT) and p(BDP-bisEDTT) is one of the issues limiting device performance. However, using CS_2 as an additive it is possible to improve the solubility. Devices fabricated with the additive demonstrated superior performances to those without additive.

The polymer-fullerene devices are shown to be suitable for sensing applications. The EQE was measured under short circuit conditions and under reverse bias. The photodiodes demonstrate a broad spectral response from 400 nm to 1100 nm and are shown to be capable for an absolute measurement of light intensity.

To further performance modification of the chemical structure is required, with the aim of tuning the energy levels and improving the solubility of the polymers. The inclusion of a moiety with an alkyl chain could facilitate with the solubility, whilst altering the energy levels of the polymer. The choice of moiety is critical; it would be wonderful if both the HOMO and LUMO level of the polymers were moved towards Vacuum, ensuring a good Ohmic contact and a larger Voc. Recently, Bura, T. et al. confirmed the ambipolar behaviour of the BODIPY core and with a Thienyl-BODIPY small molecule derivative in combination with $PC_{61}BM$ achieved organic photovoltaic devices nearing 5 % [51]. That said, the PCE for BODIPY based conjugated polymers remain low at 2 % [33].

6.5 Appendix

Table 6.3 Performance statistics for p(BDP-bisEDOT) and p(BDP-bisEDTT).

Active layer	Solvent	Jsc [mA/cm^2]	Voc [V]	FF [%]	PCE [%]
10:$PC_{61}BM$-Fla (1:1)	DCM	0.03	0.3	00	0.00
10:PDI (1:1)	DCM	0.00	0.00	00	0.00
10:$PC_{61}BM$ (1:1)	DCM	0.59	0.28	24	0.04
10:$PC_{71}BM$ (1:1)	DCM	1.14	0.26	30	0.09
10:$PC_{84}BM$ (1:1)	DCM	0.00	0.00	00	0.00
10:$PC_{61}BM$ (1:1)	DCM	0.59	0.28	24	0.04
10:$PC_{61}BM$ (1:4)	DCM	0.43	0.17	27	0.02
11:$PC_{61}BM$ (1:1)	DCM	0.33	0.26	23	0.02
11:$PC_{61}BM$ (1:4)	DCM	0.64	0.33	28	0.06
10:$PC_{61}BM$ (1:1)	CB	1.07	0.30	31	0.1
10:$PC_{61}BM$ (1:4)	CB	0.98	0.25	33	0.08
11:$PC_{61}BM$ (1:1)	CB	0.26	0.24	32	0.02
11:$PC_{61}BM$ (1:4)	CB	0.51	0.27	29	0.04
10:$PC_{71}BM$ (1:1)	DCM	1.14	0.26	30	0.09
10:$PC_{71}BM$ (1:1)	CB	1.53	0.31	34	0.16
10:$PC_{71}BM$ (1:1)	ODCB	0.98	0.28	33	0.09
10:$PC_{71}BM$ (1:1)	TCB	1.63	0.31	32	0.16
10:$PC_{71}BM$ (1:2)	TCB	2.31	0.08	27	0.05
10:$PC_{71}BM$ (1:4)	TCB	3.61	0.20	36	0.26
10:$PC_{71}BM$ (1:6)	TCB	2.43	0.11	34	0.09
11:$PC_{71}BM$ (1:2)	TCB	1.13	0.25	32	0.09
11:$PC_{71}BM$ (1:4)	TCB	3.34	0.21	36	0.25
11:$PC_{71}BM$ (1:6)	TCB	1.06	0.16	35	0.06
10:$PC_{71}BM$ (1:4)	CB	6.40	0.31	39	0.78
10:$PC_{71}BM$ (1:4)	CB+CS_2	7.87	0.31	39	0.95
11:$PC_{71}BM$ (1:4)	CB	3.82	0.29	32	0.35

11:$PC_{71}BM$ (1:4)	$CB+CS_2$	4.42	0.32	32	0.45

6.6 References

1. Shirakawa, H., et al., *Synthesis of electrically conducting organic polymers: halogen derivatives of polyacetylene, (CH).* Journal of the Chemical Society, Chemical Communications, 1977. **0**(16): p. 578-580.
2. Chiang, C.K., et al., *Electrical Conductivity in Doped Polyacetylene.* Physical Review Letters, 1977. **39**(17): p. 1098.
3. Diaz, A.F., K.K. Kanazawa, and G.P. Gardini, *Electrochemical polymerization of pyrrole.* Journal of the Chemical Society, Chemical Communications, 1979. **0**(14): p. 635-636.
4. Kroon, R., et al., *Small Bandgap Polymers for Organic Solar Cells (Polymer Material Development in the Last 5 Years).* Polymer Reviews, 2008. **48**(3): p. 531-582.
5. Thompson, B.C. and J.M.J. Fréchet, *Polymer–Fullerene Composite Solar Cells.* Angewandte Chemie International Edition, 2008. **47**(1): p. 58-77.
6. Dennler, G., M.C. Scharber, and C.J. Brabec, *Polymer-Fullerene Bulk-Heterojunction Solar Cells.* Advanced Materials, 2009. **21**(13): p. 1323-1338.
7. Cortizo-Lacalle, D., et al., *BODIPY-based conjugated polymers for broadband light sensing and harvesting applications.* Journal of Materials Chemistry, 2012. **22**(28): p. 14119-14126.
8. Yu, G., et al., *POLYMER PHOTOVOLTAIC CELLS - ENHANCED EFFICIENCIES VIA A NETWORK OF INTERNAL DONOR-ACCEPTOR HETEROJUNCTIONS.* Science, 1995. **270**(5243): p. 1789-1791.
9. Halls, J.J.M., et al., *Efficient photodiodes from interpenetrating polymer networks.* Nature, 1995. **376**(6540): p. 498-500.
10. Sariciftci, N.S., et al., *PHOTOINDUCED ELECTRON-TRANSFER FROM A CONDUCTING POLYMER TO BUCKMINSTERFULLERENE.* Science, 1992. **258**(5087): p. 1474-1476.
11. Shaw, P.E., A. Ruseckas, and I.D.W. Samuel, *Exciton Diffusion Measurements in Poly(3-hexylthiophene).* Advanced Materials, 2008. **20**(18): p. 3516-3520.
12. Ruseckas, A., P.E. Shaw, and I.D.W. Samuel, *Probing the nanoscale phase separation in binary photovoltaic blends of poly(3-hexylthiophene) and methanofullerene by energy transfer.* Dalton Transactions, 2009(45): p. 10040-10043.
13. H. Chen, J.H., S. Zhang, Y. Liang, G. Yang, Y. Yang, L. Yu,, et al.
14. He, Z., Zhong, Chengmei, Su, Shijian, Xu, Miao, Wu, Hongbin, Cao, Yong, *Enhanced power-conversion efficiency in polymer solar cells using an inverted device structure.* Nat Photon, 2012(591–595
).
15. Ma, W., et al., *Thermally Stable, Efficient Polymer Solar Cells with Nanoscale Control of the Interpenetrating Network Morphology.* Advanced Functional Materials, 2005. **15**(10): p. 1617-1622.
16. Zeng, L., C.W. Tang, and S.H. Chen, *Effects of active layer thickness and thermal annealing on polythiophene: Fullerene bulk heterojunction photovoltaic devices.* Applied Physics Letters, 2010. **97**(5): p. 053305-3.
17. Roncali, J., *Synthetic Principles for Bandgap Control in Linear π-Conjugated Systems.* Chemical Reviews, 1997. **97**(1): p. 173-206.
18. Mishra, A. and P. Bäuerle, *Small Molecule Organic Semiconductors on the Move: Promises for Future Solar Energy Technology.* Angewandte Chemie International Edition, 2012. **51**(9): p. 2020-2067.
19. Zhou, H., L. Yang, and W. You, *Rational Design of High Performance Conjugated Polymers for Organic Solar Cells.* Macromolecules, 2012. **45**(2): p. 607-632.
20. Brabec, C.J., et al., *A Low-Bandgap Semiconducting Polymer for Photovoltaic Devices and Infrared Emitting Diodes.* Advanced Functional Materials, 2002. **12**(10): p. 709-712.
21. Becerril, H.A., et al., *Transistor and solar cell performance of donor-acceptor low bandgap copolymers bearing an acenaphtho[1,2-b]thieno[3,4-*

e]pyrazine (ACTP) motif. Journal of Materials Chemistry, 2009. **19**(5): p. 591-593.
22. Bijleveld, J.C., et al., *Poly(diketopyrrolopyrrole−terthiophene) for Ambipolar Logic and Photovoltaics.* Journal of the American Chemical Society, 2009. **131**(46): p. 16616-16617.
23. Treibs, A. and F.-H. Kreuzer, *Difluorboryl-Komplexe von Di- und Tripyrrylmethenen.* Justus Liebigs Annalen der Chemie, 1968. **718**(1): p. 208-223.
24. Loudet, A. and K. Burgess, *BODIPY Dyes and Their Derivatives: Syntheses and Spectroscopic Properties.* Chemical Reviews, 2007. **107**(11): p. 4891-4932.
25. Ziessel, R., G. Ulrich, and A. Harriman, *The chemistry of Bodipy: A new El Dorado for fluorescence tools.* New Journal of Chemistry, 2007. **31**(4): p. 496-501.
26. Ulrich, G., R. Ziessel, and A. Harriman, *The Chemistry of Fluorescent Bodipy Dyes: Versatility Unsurpassed.* Angewandte Chemie International Edition, 2008. **47**(7): p. 1184-1201.
27. Bonardi, L., et al., *Fine-Tuning of Yellow or Red Photo- and Electroluminescence of Functional Difluoro-boradiazaindacene Films.* Advanced Functional Materials, 2008. **18**(3): p. 401-413.
28. Nepomnyashchii, A.B. and A.J. Bard, *Electrochemistry and Electrogenerated Chemiluminescence of BODIPY Dyes.* Accounts of Chemical Research, 2012. **45**(11): p. 1844-1853.
29. García, O., et al., *Synthetic Strategies for Hybrid Materials to Improve Properties for Optoelectronic Applications.* Advanced Functional Materials, 2008. **18**(14): p. 2017-2025.
30. Bozdemir, O.A., et al., *Selective Manipulation of ICT and PET Processes in Styryl-Bodipy Derivatives: Applications in Molecular Logic and Fluorescence Sensing of Metal Ions.* Journal of the American Chemical Society, 2010. **132**(23): p. 8029-8036.
31. Kolemen, S., et al., *Optimization of distyryl-Bodipy chromophores for efficient panchromatic sensitization in dye sensitized solar cells.* Chemical Science, 2011. **2**(5): p. 949-954.
32. Erten-Ela, S., et al., *A Panchromatic Boradiazaindacene (BODIPY) Sensitizer for Dye-Sensitized Solar Cells.* Organic Letters, 2008. **10**(15): p. 3299-3302.
33. Kim, B., et al., *Bodipy-backboned polymers as electron donor in bulk heterojunction solar cells.* Chemical Communications, 2010. **46**(23): p. 4148-4150.
34. Arroyo, I.J., et al., *The Smallest and One of the Brightest. Efficient Preparation and Optical Description of the Parent Borondipyrromethene System.* The Journal of Organic Chemistry, 2009. **74**(15): p. 5719-5722.
35. Benniston, A.C. and G. Copley, *Lighting the way ahead with boron dipyrromethene (Bodipy) dyes.* Physical Chemistry Chemical Physics, 2009. **11**(21): p. 4124-4131.
36. Cihaner, A. and F. Algı, *A new conducting polymer bearing 4,4-difluoro-4-bora-3a,4a-diaza-s-indacene (BODIPY) subunit: Synthesis and characterization.* Electrochimica Acta, 2008. **54**(2): p. 786-792.
37. Forgie, J.C., et al., *New Redox Stable Low Band Gap Conjugated Polymer Based on an EDOT−BODIPY−EDOT Repeat Unit.* Chemistry of Materials, 2009. **21**(9): p. 1784-1786.
38. Halls, J.J.M., et al., *Charge- and energy-transfer processes at polymer/polymer interfaces: A joint experimental and theoretical study.* Physical Review B, 1999. **60**(8): p. 5721-5727.
39. Mihailetchi, V.D., et al., *Cathode dependence of the open-circuit voltage of polymer:fullerene bulk heterojunction solar cells.* Journal of Applied Physics, 2003. **94**(10): p. 6849-6854.
40. Scharber, M.C., et al., *Design Rules for Donors in Bulk-Heterojunction Solar Cells—Towards 10 % Energy-Conversion Efficiency.* Advanced Materials, 2006. **18**(6): p. 789-794.

41. Spencer, H.J., et al., *The first direct experimental comparison between the hugely contrasting properties of PEDOT and the all-sulfur analogue PEDTT by analogy with well-defined EDTT-EDOT copolymers.* Journal of Materials Chemistry, 2005. **15**(45): p. 4783-4792.
42. Ruderer, M.A., et al., *Solvent-Induced Morphology in Polymer-Based Systems for Organic Photovoltaics.* Advanced Functional Materials, 2011. **21**(17): p. 3382-3391.
43. Peet J, K.J., Coates NE, Ma WL, Heeger AJ, Moses D, Bazan GC, *Efficiency enhancement in low-bandgap polymer solar cells by processing with alkane dithiols.* Nat Mater, 2007, 6:497–500. doi:10.1038/nmat1928.
44. Lin, R., M. Wright, and A. Uddin, *Effects of solvent additive on inverted structure PCPDTBT:PC71BM bulk heterojunction organic solar cells.* physica status solidi (a), 2013: p. n/a-n/a.
45. Liang, Y., et al., *For the Bright Future—Bulk Heterojunction Polymer Solar Cells with Power Conversion Efficiency of 7.4%.* Advanced Materials, 2010. **22**(20): p. E135-E138.
46. Lee, J.K., et al., *Processing Additives for Improved Efficiency from Bulk Heterojunction Solar Cells.* Journal of the American Chemical Society, 2008. **130**(11): p. 3619-3623.
47. Schilinsky, P., C. Waldauf, and C.J. Brabec, *Recombination and loss analysis in polythiophene based bulk heterojunction photodetectors.* Applied Physics Letters, 2002. **81**(20): p. 3885-3887.
48. Peumans, P., V. Bulovic, and S.R. Forrest, *Efficient, high-bandwidth organic multilayer photodetectors.* Applied Physics Letters, 2000. **76**(26): p. 3855-3857.
49. O'Brien, G.A., et al., *A Single Polymer Nanowire Photodetector.* Advanced Materials, 2006. **18**(18): p. 2379-2383.
50. Gong, X., et al., *High-Detectivity Polymer Photodetectors with Spectral Response from 300 nm to 1450 nm.* Science, 2009. **325**(5948): p. 1665-1667.
51. Bura, T., et al., *High-Performance Solution-Processed Solar Cells and Ambipolar Behavior in Organic Field-Effect Transistors with Thienyl-BODIPY Scaffoldings.* Journal of the American Chemical Society, 2012. **134**(42): p. 17404-17407.
52. Economopoulos, S.P., et al., *Novel BODIPY-based conjugated polymers donors for organic photovoltaic applications.* RSC Advances, 2013. **3**(26): p. 10221-10229.

Chapter 7

BODIPY-based solution-processable small molecules with a DPP core for organic photovoltaics

Overview

In the previous chapter I reported and discussed the electrochemical, photophysical and optoelectronic properties of two solution-processable BODIPY-based conjugated polymers. Having been impressed with the properties of BODIPY we decided to further investigate. Here, I introduce two small molecules containing BODIPY and diketopyrrolopyrrole, DPP. The small molecules were fully characterised and their photovoltaic properties investigated. The addition of two thiophenes red shifts the absorption. However, it does not lead to improved device performance, instead, a propensity to aggregate, limiting device efficiency. The aggregation was investigated with microscopy. PLQY measurements show the aggregation to quench luminescence. The study shows that it is important to control aggregation for efficient devices

This work was performed under the supervision of Professor Ifor D. W. Samuel at the University of St Andrews. The synthesis and electrochemical characterisation was by Dr Diego Cortizo-Lacalle under the supervision of Professor Peter J. Skabara at the University of Strathclyde.

7.1 Introduction

The majority of research within the field of organic photovoltaics has focused on developing conjugated polymers as electron donors for the bulk heterojunction (BHJ). As conjugated polymers have a propensity to form an interpenetrating nano-scale network which facilitates in exciton dissociation and charge transport [1, 2]. At present conjugated polymers are the most promising materials for organic photovoltaic cells, with power conversion efficiencies in excess of 9 % [3]. In spite of achieving efficiencies in the vicinity of the desired 10 % milestone with polymer-fullerene photovoltaic cells [4], practicalities other than OPV lifetime also prevent their commercialisation. These include molecular weight polydispersity, end group contamination and batch to batch variations [5]. For this reason, there has recently been considerable interest in using small molecules as electron donors [6-10]. Small molecules do not suffer from polydispersity or end group variation. Hence, they have a well-defined chemical structure with completely reproducible properties. The ease of purification, shorter synthetic routes and suitability for deposition by thermal evaporation, makes them practical for commercialisation. Furthermore, their ability to self-assemble into ordered domains yields high charge carrier mobilities [7, 11].

The efficiencies of small molecule single junction organic photovoltaic cells are generally low, particularly, for those fabricated from solution. Small molecules generally favour deposition by thermal evaporation [7]. However, progress is being made. Recently, a solution-processable small molecule photovoltaic device achieved a certified efficiency of 7.10 % [12].

Most of the small molecules used in organic photovoltaic cells are based on oligothiophenes and their derivatives [7], as they are well-known for their very good charge transport properties, high polarisability and easily tuneable optical and electrochemical properties [13]. However, it is not uncommon to see push-pull molecules or dyes [10]. Of late, there has been a great deal of interest in synthesising DPP core containing polymers and small molecules for optoelectronics [14-18]. This is not too surprising, as to date, DPP core containing polymers have shown some of the highest mobility values reported for organic semiconductors [15]. The extraordinary aggregating properties of DPP moieties allow for strong intermolecular interaction by π-π stacking [17] and it this which is responsible for the high mobility values and excellent photovoltaic performances [19].

In this section, I introduce two small molecules containing DPP and BODIPY. The structure of these molecules is interesting as they contain two dyes in a single small molecule. I report their photophysical, electrochemical and photovoltaic properties and discuss further improvements. The addition of a thiophene increases the conjugation length and therefore red shifts the absorption. However, it does not improve device performance, instead, poor solubility, limits device efficiency.

7.2 Materials-Small molecules

The first section of this chapter introduced the 4, 4-difluoro-4-bora-3*a*, 4*a*-diaza-*s*-indacene (BODIPY) core. The BODIPY core was shown to have favourable properties for organic optoelectronics [20-22]. I showed that it is possible to make organic photovoltaics and photodiodes with BODIPY-based conjugated polymers [23]. The PCE for BODIPY based conjugated polymers remains low with the state of the art device > 2 % [24]. However, a recent BODIPY-based small molecule photovoltaic cell achieved an impressive PCE of 4.7 % [25]. Relating to the DPP core, Nguyen et al, investigated several DPP-based small molecules for organic photovoltaics and attained respectable efficiencies [10, 17, 26, 27]. The most promising combination was a benzofuran substituted DPP-OT-3, 6-bis(5-(benzofuran-2-yl)thiophen-2-yl)-2,5-bis(2-ethylhexyl)pyrrolo[3,4-c]pyrrole-1,4-dione (DPP(TBFu)$_2$). The small molecule was designed to be used with the acceptor, PC$_{71}$BM. The driving force between the LUMO of the donor and acceptor was > 0.6 eV, whilst the energy difference between the HOMO of the donor and the LUMO of the acceptor was 1.2 eV. This enabled the combination to achieved PCE values greater than 4 %, made possible by the large Voc ~ 1.0 V [19]. Interestingly, there have been reports of DPP containing small molecules being used as acceptors in organic photovoltaic cells. In one circumstance a small molecule containing DPP was used as an acceptor, replacing the PC$_{61}$BM, with the well-known poly(3-hexylthiophene) (P3HT), resulting in PCE values ~ 1 % [28]. The success as an acceptor highlights the ambipolar behaviour of the compound. Initial mobility studies reported ambipolar mobilities of 0.1 cm^2/Vs [13, 15]. To date, record p-type mobilities of 8.2 cm^2/Vs and n-type mobilities of 1.56 cm^2/Vs have been reported [14, 29].

Here, we consider small molecules containing the DPP core **1** and the BODIPY core **2**, Figure 7.1, as donors for organic photovoltaics. There have been reports of dyads and triads containing both the DPP and BODIPY core [8, 9, 30]. However, these small molecules have not been used in organic photovoltaic cells. The small molecules presented here are BODIPY-DPP-BODIPY triads linked with Thionyl bridges.

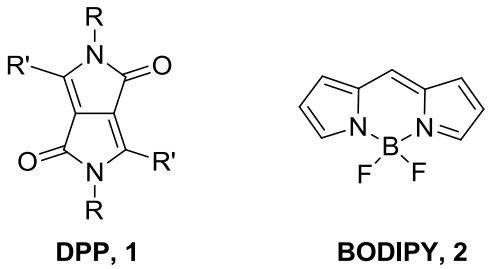

Figure 7.1 *Chemical structures of DPP core* ***1*** *and BODIPY core* ***2****.*

7.2.1 Molecular structures

The synthetic approach was to prepare BODIPY derivatives bearing a brominated thiophene **6** or thiophenes **7**, on the meso-position of the BODIPY core. This would allow for the coupling of the BODIPY, **6** or **7,** to the DPP core, **8,** via Suzuki coupling, resulting in BDP-DPP-BDP small molecules **9** or **10**. This was achieved by acidic catalysis condensation of 5-bromothiophene-2-carbaldehyde with 3-ethyl-2, 4-dimethylpyrrole, DDQ for the oxidation, deprotonation with triethylamine and treatment with borontrifluoride diethyl etherate. For the synthesis of **7** an α-brominated derivative of a bis-thionyl carbaldehyde was used following the synthetic route described by Benniston, A. C., et al. [16]. To synthesise the bis-thiophene the compound was treated with phosphorous oxychloride and N, N-dimethyl-formide via Vilsmeier-Haack. Bromination was achieved with the chemical reagent N-Bromosuccinimide (NBS). Compounds **6** and **7** were prepared with the same procedure. The functionalised DPP core, **8**, [18] was reacted with the brominated BODIPY derivatives, **6** or **7**, to attain DPP containing small molecules **9** or **10**, respectively.

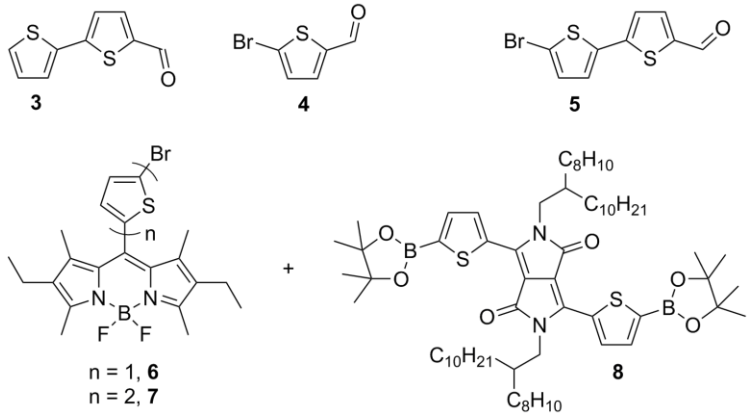

Figure 7.2 *Synthesis of DPP-based small molecules.*

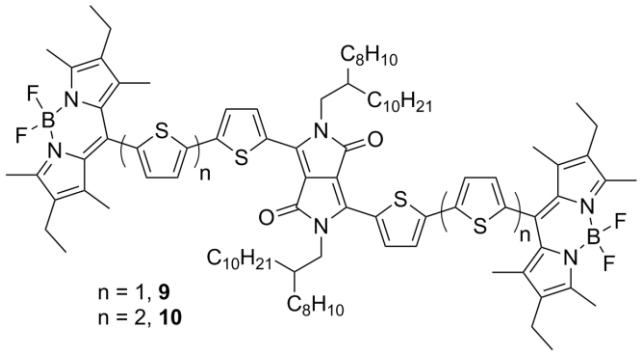

Figure 7.3 *Chemical structures of DPP-based small molecules.*

7.2.2 Electrochemical and optical properties

The cyclic voltammetry for polymers p(BDP-bisEDOT) and p(BDP-bisEDTT), Figure 6.6, were attained by depositing a film of each polymer on a glassy electrode. The experiment was carried out in acetonitrile in the presence of Bu_4NPF_6. Silver was used as the reference electrode and platinum as the counter electrode. The HOMO and LUMO levels were determined from the onset of the first oxidation and reduction with reference to ferrocene (-4.8 eV). It may be a surprise for some that the electrochemical study was carried out in solid state. However, this is the state that they are used within our organic photovoltaic cells. The same procedure was carried out for small molecules **9** and **10**. However, the cyclic voltammetry was difficult to interpret. Hence, I report the cyclic voltammogram for solution and solid state, Figure 7.4.

For solution, on oxidation, **9** shows two reversible peaks at +0.42 and +0.83 V, whilst **10** shows three reversible peaks at +0.37, +0.57 and +0.73 V. The first oxidation wave for **9** and **10** can be assigned to the formation of a radical cation on the terthiophene-DPP section of the molecule. Compound **10** has a lower oxidation potential compared to **9**, due to the extension of the oligothiophene chain. The second oxidation wave of **9**, the third for **10** is from oxidation of the BODIPY core. The formation of a radical dication is responsible for the second oxidation of **10** and is due to the two additional thiophene rings. For reduction, compound **9** shows a quasi-reversible peak at -1.48 V, a reversible peak at -1.58 V and an irreversible peak at -2.01 V. The reduction behaviour for **10** is complex as several processes overlap. It would appear that there are three quasi-reversble peaks at -1.48, -1.55 and -1.90 V and an irreversible peak at -2.09 V. The first two reduction processes are due to the reduction of the BODIPY and DPP core. It is possible that the reduction waves for the higher negative potentials are due to the reduction of the oligothiophene units.

The interpretation of the solid state cyclic voltammogram was the same as solution measurements. Like polymers p(BDP-bisEDOT) and p(BDP-bisEDTT), it is the HOMO and LUMO energy levels in the solid state, which are relevant for photovoltaic cells. The energy levels for **9** and **10** were determined from the first onset of oxidation and reduction.

Within the field of organic photovoltaics it is possible to improve solar absorption with extending the conjugation, resulting in a bathochromic shift by decreasing the gap between the HOMO and LUMO energy level. However, the statistics obtained from the cyclic voltammograms for solution and solid state show a higher HOMO-LUMO gap for **10** than **9** It is also interesting that the HOMO-LUMO gap is smaller in solution than solid state, as the molecular interactions are expected to be stronger in the solid state than in solution.

The HOMO and LUMO energy levels for **9** in solution were determined as -5.13 eV and -3.50 eV, respectively, giving a HOMO-LUMO gap of 1.63 eV. For solid state the HOMO was -5.31 eV and the LUMO -3.57 eV, giving a HOMO-LUMO gap of 1.74 eV. For compound **10** the HOMO and LUMO energy levels in solution were determined to be -5.10 eV and -3.40 eV,

respectively, giving a HOMO-LUMO gap of 1.70 eV. The HOMO and LUMO energy levels of **10** in solid state were determined as -5.25 eV and -3.44 eV, respectively, giving a HOMO-LUMO gap of 1.81 eV. Statistics significant for device fabrication are shown in Table 7.2.

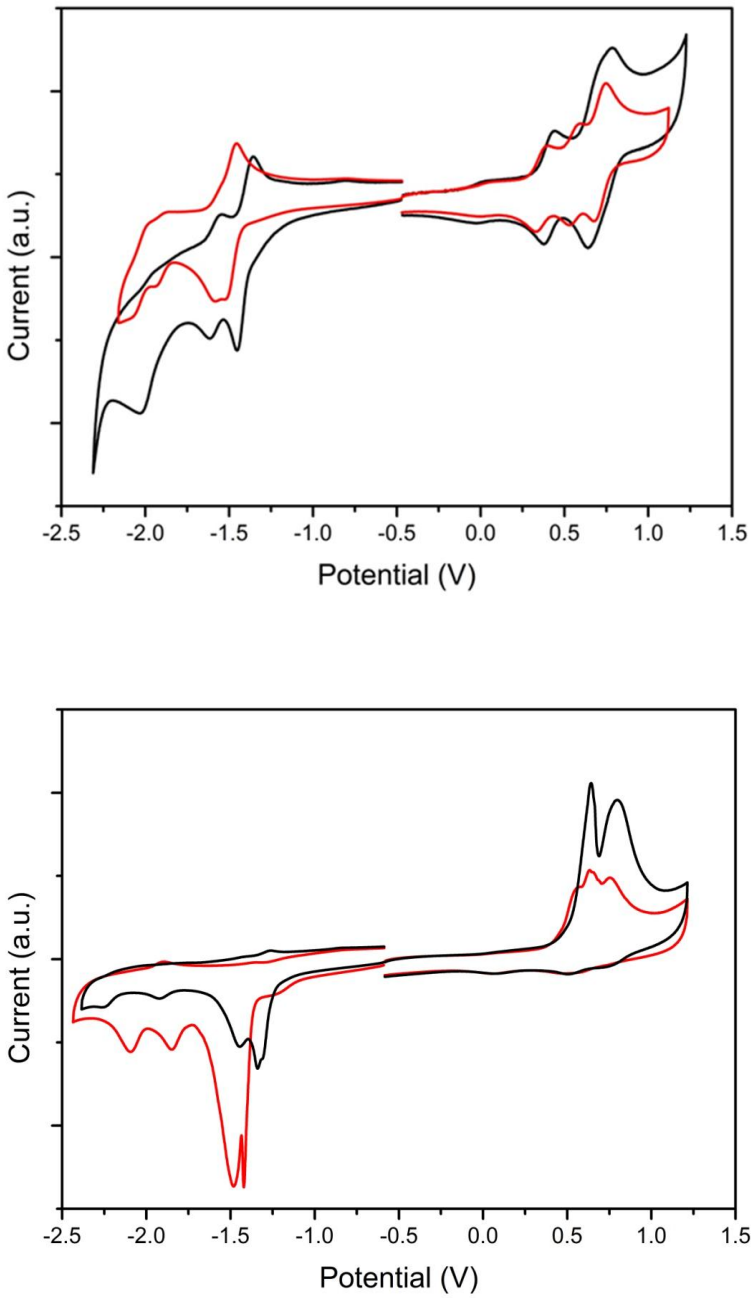

Figure 7.4 *Cyclic voltammetry of* ***9*** *(black) and* ***10*** *(red) in solution (top) and film (bottom).*

The absorption spectra for **9** and **10** in solution and solid state are shown in Figure 7.6 and 7.8, respectively. All the spectra have been normalised. To further understand the absorption spectra of **9** and **10**, an absorption spectrum for a small molecule containing a thieno-DPP core **11** was attained.

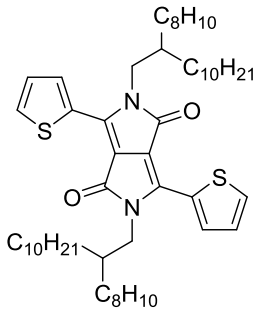

Figure 7.5 *Chemical structure of thieno-DPP core **11**.*

Compounds **9** and **10** have an absorption peak at ~ 542 nm. One could easily be mistaken for thinking that this peak is associated with the DPP core, considering **11**. However, BODIPY is well-known for having an absorption peak in this region. The value of the peak, ~ 542 nm, is the same reported for several BODIPY derivatives, substitued with oligothiophenes at the meso-position [16]. Therefore, the inclusion of the DPP core and additional thiophenes does not alter the absorption peak associated with the BODIPY moieties. However, there is a bathochromic shift with the addition of two thiophenes, which is what we would expect from extending the conjugation.

Compound **11** has two distinctive peaks, one at 512 nm and the other at 548 nm. The peaks are dramitcally shifted in compound **9** and **10**. The red-shifts are 72 nm and 74 nm for compound **9** (584 nm and 622 nm) and for compound **10**, 95 nm and 97 nm (607 nm and 645 nm).

The optical band-gaps were calculated from the onset of the absorption for **9** and **10** in solution. The onset of absorption for compund **9** was ~ 675 nm, corresponding to 1.83 eV. The onset of absorption for compund **10** was ~ 710 nm, corresponding to 1.75 eV.

A similar absorption profile is observed for the solid state measurements. However, for both **9** and **10** the peak associated with the BODIPY units has red-shifted by ~ 10 nm. The intensity of this peak is less prominent in the solid state than in solution, it is possible that π-π stacking is responsible for the decrease in intensity.

The absorption associated to the terthiophene-DPP is dramatically red-shifted. This is expected as the solid state films will have a higher degree of order than the solutions. A large shoulder at longer wavelenths (λ) is observed. This is due to the pressence of aggregates in the films.

The optical band-gaps were determined for solid state films. As seen from the absorption spectra, the tail at longer wavelengths (λ) can make calculations of the optical band-gap speculative. However, a value of 710 nm was obtained for **9** and ~ 740 nm for **10**, corresponding to optical band-gaps of ~ 1.75 eV and ~ 1.68 eV, respectively. The sbsorption spectra for compounds **9**, **10** and **11** in solution are shown in Figure 7.6. The graph shows that the compounds are suitably dissolved and that there are no aggregates present. The optical band-gaps calculated from the onset of absorption for solution are shown in Table 7.1 with the values obtained from the electrochemistry. Unlike polymers p(BDP-bisEDOT) and p(BDPibisEDTT) in Chapter 6, it was possible to attain photoluminescence for the compounds, Figure 7.7. The peaks, associated with the thieno-DPP core are at 660 nm for **9** and 690 nm for **10**.

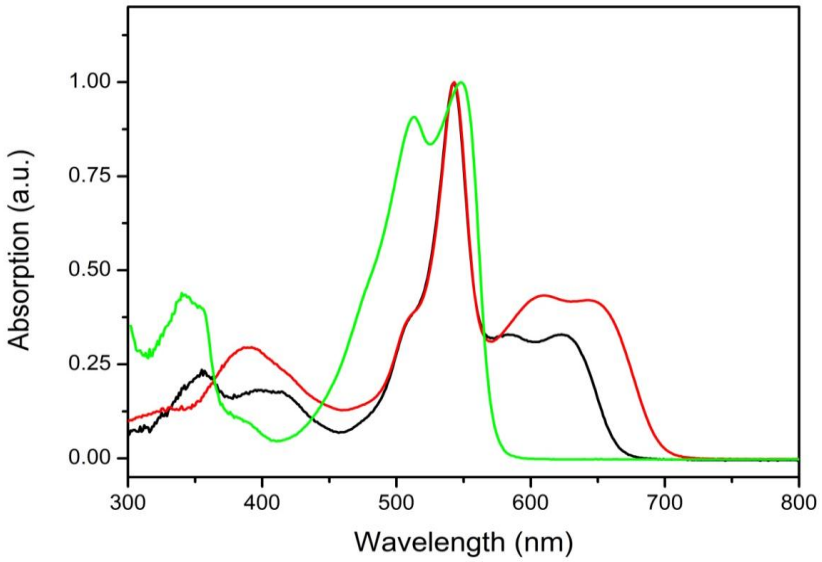

Figure 7.6 *Normalised absorption spectra for* ***9*** *(black),* ***10*** *(red) and* ***11*** *(green) in solution.*

Table 7.1 *Electrochemical and optical band-gaps for* ***9*** *and* ***10*** *in solution. The HOMO and LUMO levels were determined from the onset of the first oxidation and reduction[a]. The optical band-gaps were calculated from the onset of absorption[b].*

Small molecule	HOMO [eV][a]	LUMO [eV][a]	Eg [eV][a]	Eg [eV][b]
9	-5.13	-3.50	1.63	1.84
10	-5.10	-3.40	1.70	1.75

The absorption spectra for compounds **9** and **10** in solid state are shown in Figure 7.8. The optical band-gaps calculated from the onset of absorption are shown in Table 7.2, with the values obtained from the electrochemistry in solid state.

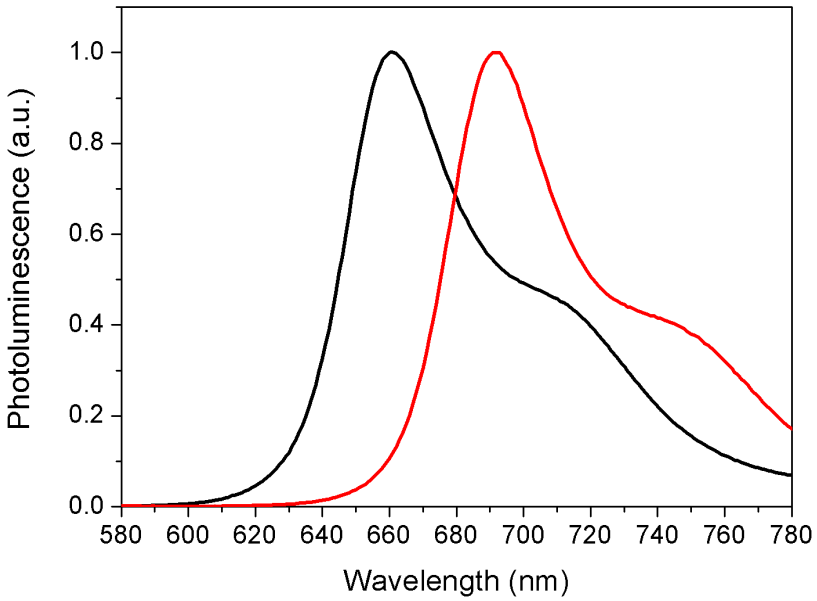

Figure 7.7 *Emission spectra of* ***9*** *(black) and* ***10*** *(red) acquired from 400 nm excitation (solution).*

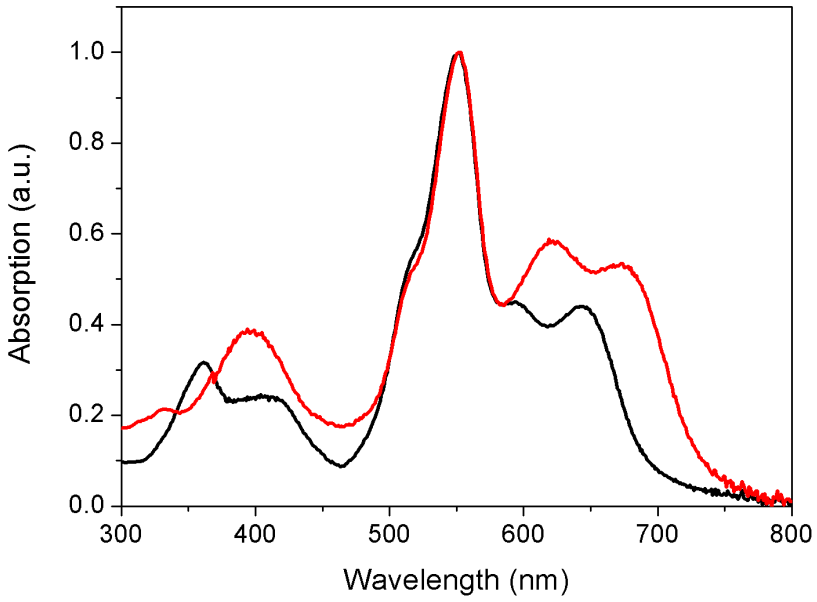

Figure 7.8 *Normalised absorption spectra for* ***9*** *(black) and* ***10*** *(red) in solid state.*

Table 7.2 *Electrochemical and optical band-gaps for* ***9*** *and* ***10*** *in solid state. The HOMO and LUMO levels were determined from the onset of the first oxidation and reduction[a]. The optical band-gaps were calculated from the onset of absorption[b].*

Small molecule	HOMO [eV][a]	LUMO [eV][a]	Eg [eV][a]	Eg [eV][b]
9	-5.31	-3.57	1.74	1.75
10	-5.25	-3.44	1.81	1.68

7.3 Small molecule OPVs

The optical band-gaps and absorption spectra make **9** and **10** interesting for organic photovoltaics. The spectra show absorption in the region between 500 nm and 700 nm. The absorption between 300 nm and 400 nm is low in comparison to wavelengths (λ) > 500 nm. However, when blended with $PC_{71}BM$, the most suitable acceptor considering the LUMO energy levels, we see good absorption from 300 nm to 700 nm, Figure 7.9. Whilst the photoluminescence spectra, Figure 7.7 may not provide information relating to solid state behaviour, it allows us to predict, where the emission will be in the solid state, allowing photophysical measurements. Despite having a HOMO energy level imperfect for an Ohmic contact, organic photovoltaics with **9** and **10** were investigated.

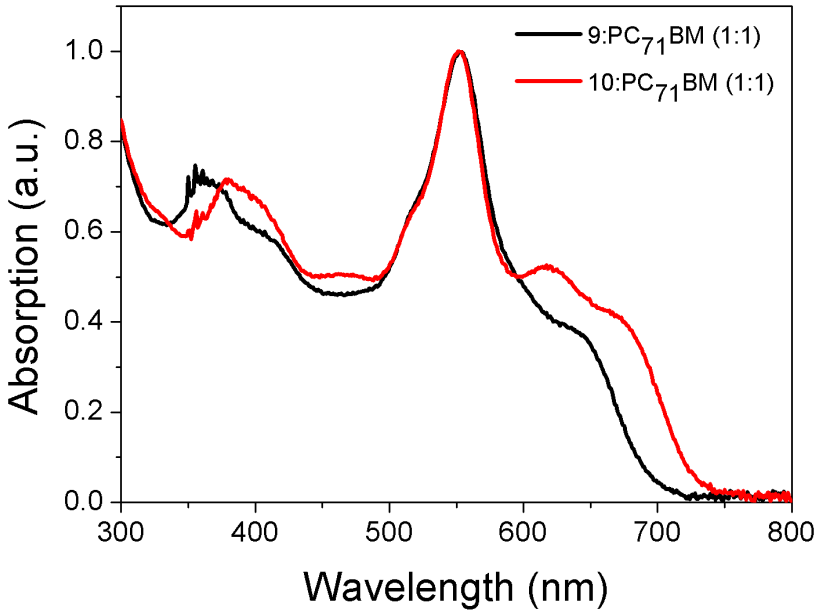

Figure 7.9 *Solid state absorption spectra for* ***9****:$PC_{71}BM$ (1:1) (black) and* ***10****:$PC_{71}BM$ (1:1) (red).*

7.3.1 Fabrication

The fabrication of organic photovoltaics cells was similar to those containing polymers p(BDP-bisEDOT) and p(BDP-bisEDTT). The cells were prepared on ITO coated glass (15 Ω per □). The ITO coated substrates were masked and etched in hydrochloric acid (37 %) for 20 minutes. The mask was removed and the substrates cleaned by sonication in deionised water, acetone and isopropanol. The substrates were then dried with nitrogen and placed in oxygen plasma for 3 minutes. Poly(3, 4-ethylenedioxythiophene): poly(styrenesulfonate) (PEDOT:PSS) from Clevios (AI4083) was spin-coated on top of the ITO. The PEDOT: PSS coated ITO samples were placed on a hotplate within a nitrogen-filled glove box and baked at 120 °C for 20 minutes. On removing the samples from the hotplate, films containing various donor/acceptor ratios were spin-coated from a 20 mg ml^{-1} Chlorobenzene solution. The devices were then annealed for 20 minutes at 140 °C before being placed into an evaporator for back electrode deposition. 20 nm of Calcium and 200 nm of Aluminium were thermally evaporated at a pressure of 2×10^{-6} mbar. After back electrode deposition the devices were encapsulated with a glass cover slip and a UV activated optical adhesive from Thorlabs. Characterisation was in air using a Keithley 2400 source-measure unit and a Steuernagel AM 1.5 G solar simulator at 100 mW cm^{-2}. The illumination intensity was verified and calibrated with an NREL calibrated mono-silicon detector and KG-5 filter. External quantum efficiency (EQE) measurements were obtained with an incident photon to charge carrier efficiency (IPCE) setup consisting of a NPL calibrated photodiode, Keithley 6517A picoammeter and a TMc300 monochromator. To verify the J-V measurements the short-circuit current density (Jsc) was calculated from the IPCE under AM 1.5 G.

The energy levels and device architecture are shown in Figure 7.11 and 7.12. The optimum donor-acceptor ratio was determined to be 1:3. To investigate the aspects limiting device performance the active layer was prepared on fused silica substrates for microscopy and photophysical studies. Film thicknesses were measured using a Dektak 150 M stylus profiler. Absorption and emission spectra were obtained with a Varian Cary 300 UV-visible Spectrophotometer and a Photoluminescence Quantum Yield (PLQY) measurement system (model: C9920-02G), respectively. Solution emission spectra were attained for samples dissolved in dichloromethane with a FluoroMax 2 spectrometer. For microscopy a WiTec AlphaSNOM was used for wide-field images and a Veeco scanning probe microscope (SPM) was used in tapping mode for atomic force microscopy (AFM).

7.3.2 Optimisation

Absorption is important; however, as previously discussed it is not the sole process in the operation of an organic solar cell. The dissociation of the coulombically bound electron-hole pair or exciton into free charge and their transport to the electrodes are critical for device operation [31]. Dissociation and transport are two processes that are strongly linked with the morphology of the active layer [32]. To determine the optimum morphology the donor-acceptor ratio was varied. The most promising ratio was determined to be 1:3, Figure 7.10. As the concentration of the acceptor is increased from 2:1 to 1:3 an increase in short-circuit current (Jsc), open circuit voltage (Voc) and Fill Factor (FF) is observed. If we continue to increase the concentration of the acceptor to 1:4 we see a decrease in Jsc, Voc and FF, Table 7.3.

.

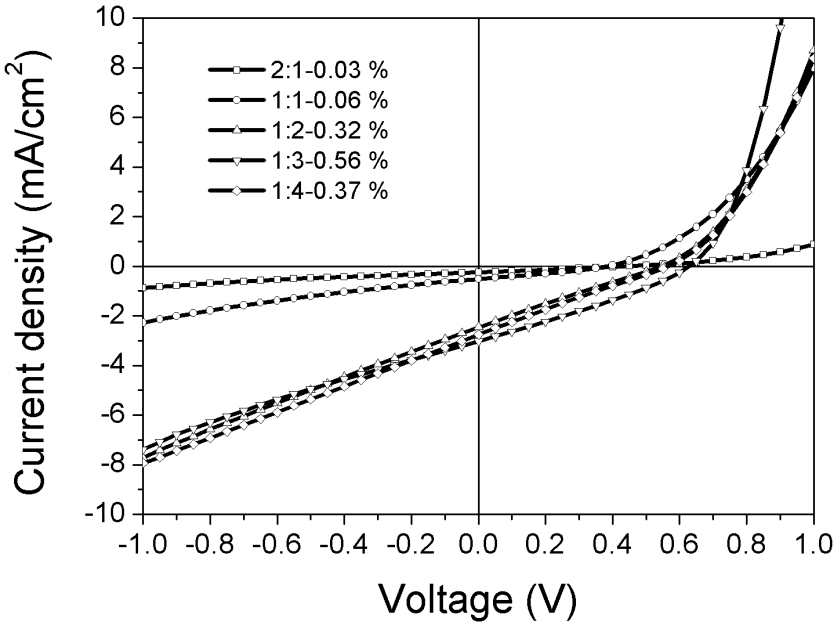

Figure 7.10 *J-V characteristics of* ***9****:$PC_{71}BM$ varying donor-acceptor ratios under 100 mW cm^{-2} illumination with a standard AM 1.5 G source.*

Table 7.3 *Statistics for different donor-acceptor ratios of* ***9****:$PC_{71}BM$.*

Donor-Acceptor Ratio	Jsc [mA/cm^2]	Voc [V]	FF [%]	PCE [%]
2:1	0.24	0.44	28	0.03
1:1	0.51	0.39	30	0.06
1:2	2.46	0.56	23	0.32
1:3	3.02	0.62	30	0.56
1:4	2.76	0.57	24	0.37

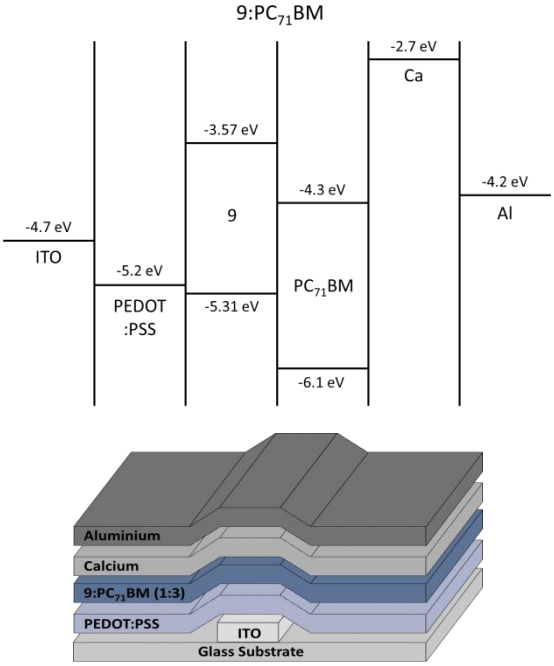

Figure 7.11 *Energy levels (top) and device structure (bottom) for 9:$PC_{71}BM$ (1:3).*

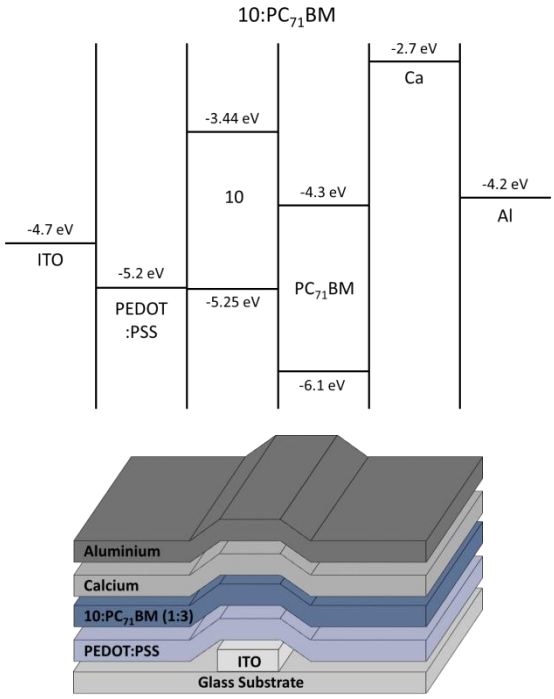

Figure 7.12 *Energy levels (top) and device structure (bottom) for 10:$PC_{71}BM$ (1:3).*

7.3.3 Characterisation

Small molecules **9** and **10** were used as donors in solution-processable organic photovoltaics cells. The PCEs for the optimum photovoltaics, were 0.65 % for **9** and 0.64 % for **10**. This is low in comparison with some of the DPP or BODIPY core small molecules reported in the literature, PCE > 4 % [19, 25]. Even when used as an acceptor with P3HT, DPP can have a PCE of ~ 1 % [28]. The low PCE values are a result of fill factors < 30 % and short circuit current densities < 5 mA/cm^2. The Voc is lower than what we would expect for this electron donor acceptor combination. However, for **9**, the Voc is larger than that attainable with P3HT:$PC_{61}BM$ [33]. To determine the aspects limiting performance the films were studied on fused silica.

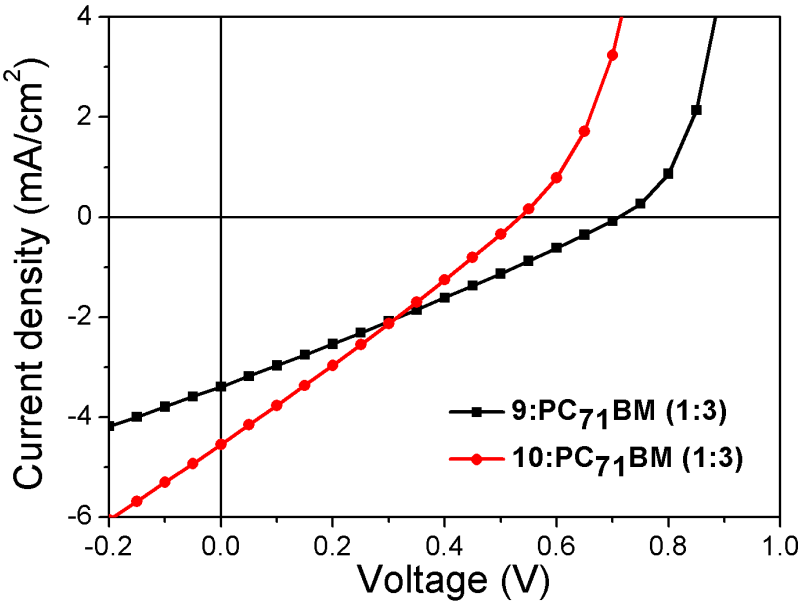

Figure 7.13 *J-V for* ***9****:$PC_{71}BM$ (1:3) and* ***10****:$PC_{71}BM$ (1:3) under illumination at 100 mW cm^{-2} with an AM1.5 G source.*

Table 7.4 *Performance statistics for* ***9****:$PC_{71}BM$ (1:3) and* ***10****:$PC_{71}BM$ (1:3) under illumination at 100 mW cm^{-2} with an AM1.5 G source.*

Active layer	Jsc [mA/cm^2]	Voc [V]	FF [%]	PCE [%]
9:$PC_{71}BM$ (1:3)	3.39	0.71	27	0.65
10:$PC_{71}BM$ (1:3)	4.55	0.53	26	0.64

The dark J-V curves and EQE spectra corresponding to the photovoltaic cells in Figure 7.13 are shown in Figure 7.15 and Figure 7.16, respectfully. It is important to mention that I noticed an issue relating to the photo-degradation of these materials. I have not provided any quantitative analysis of this behaviour as it is out with the remit of the study. However, it is seen when we compare the calculated and measured short circuit current densities (Jsc). The calculated Jsc for **9** was 3.66 mA cm^{-2} compared to a measured 3.36 mA cm^{-2}. For **10**, 3.49 mA cm^{-2} was calculated and a value of 4.55 mA cm^{-2} measured. The percentage difference between the measured and calculated Jsc for **9** is < 10 %. Whilst the percentage difference for **10** is ~ 30 %. For **9** the EQE measurement was carried out prior to J-V under 100 mW cm^{-2} illumination, whilst for **10**, the EQE measurement was carried out after illumination with 100 mW cm^{-2}. As the EQE measurements were carried out at low intensity it is reasonable to assume that the prior illumination with 100 mW cm^{-2} of **10** resulted in lower EQE values. Hence the measured and calculated Jsc mismatch.

We observe a dramatic difference in Voc between **9**:$PC_{71}BM$ and **10**:$PC_{71}BM$ of 0.71 V and 0.53 V, respectively. A favourable dark current is observed with **9**:$PC_{71}BM$ when compared with **10**:$PC_{71}BM$, Figure 7.15. There are several possible reasons why we observe a lower Voc with **10**:$PC_{71}BM$ than **9**:$PC_{71}BM$. The first being that **10**:$PC_{71}BM$ when compared with **9**:$PC_{71}BM$ has a shallow HOMO and the theoretical maximum Voc out of a device is proportional to the energy difference between the LUMO of the acceptor and the HOMO of the donor [34]. However, this difference is small. A more compelling reason is that **10**:$PC_{71}BM$ has a propensity to aggregate. I carried out an investigation into the morphology of the optimised blends. Wide-field images indicate more aggregates in the **10**:$PC_{71}BM$ (1:3) than in **9**:$PC_{71}BM$ (1:3). These aggregates are contained within red circles. Figure 7.14. The images show five regions where aggregates are observed for **9**:$PC_{71}BM$ (1:3) (a) and seventeen for **10**:$PC_{71}BM$ (1:3) (b).

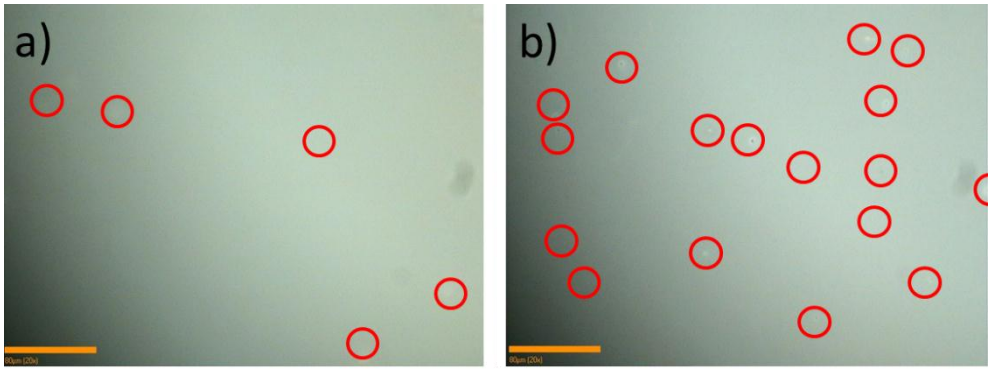

Figure 7.14 *Wide-field micrograph of* ***9****:$PC_{71}BM$ (1:3) (left) and* ***10****:$PC_{71}BM$ (1:3) (right). The scale bar in the bottom left hand corner of each image represents 80 μm and the red circles highlight aggregates in the film.*

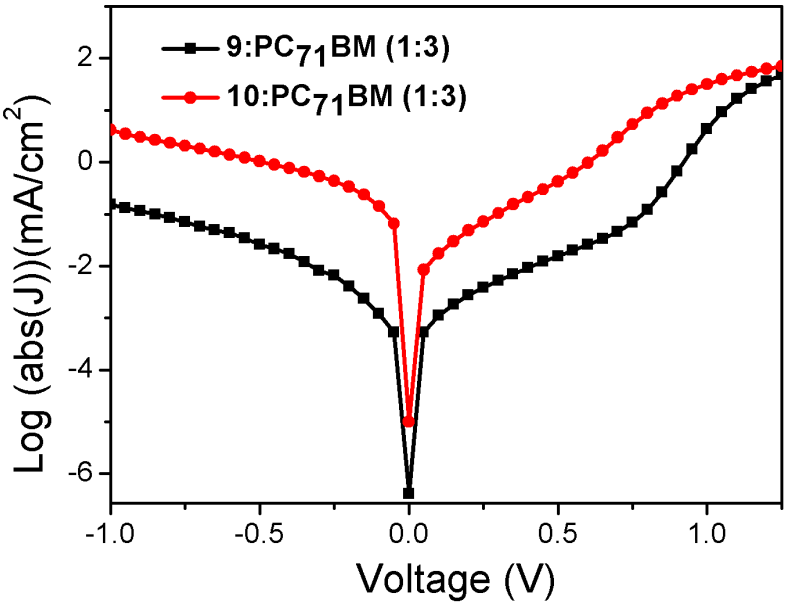

Figure 7.15 *J-V for* ***9****:$PC_{71}BM$ (1:3) and* ***10****:$PC_{71}BM$ (1:3) in the dark.*

The absorption spectra of **9**:$PC_{71}BM$ (1:1) and **10**:$PC_{71}BM$ (1:1) is good for a photovoltaic cell, Figure 7.9. However, at the optimum donor-acceptor ratio for dissociation and charge transport the active layer contains only 25 % of the donor. Therefore, the overall contribution to absorption by the donor is less, Figure 7.17. As the concentration of the acceptor has been increased there is strong absorption in the region 300-500 nm. Which is not ideal for a photovoltaic cells as the majority of the solar spectrum is at longer wavelengths (λ) above 500 nm.

In Figure 7.16 the incident photon to current conversion efficiency (IPCE) ratio or alternatively the external quantum efficiency (EQE) is shown for our full optimised devices. The spectral response of **9**:$PC_{71}BM$ (1:3) and **10**:$PC_{71}BM$ (1:3) is from 300 nm to 750 nm, which is impressive. The EQE spectra show that the small molecules are indeed contributing to the overall photocurrent of the photovoltaic cells. For both **9**:$PC_{71}BM$ (1:3) and **10**:$PC_{71}BM$ (1:3) photovoltaic cells there is a peak fixed at ~ 550 nm. This peak is associated with the BODIPY moieties. The two additional thiophenes in small molecule **10** allow absorption at slightly longer wavelengths.

The EQE values are ~ 20 % for **9**:$PC_{71}BM$ (1:3) and **10**:$PC_{71}BM$ (1:3) from 400 to 500 nm. From 500 to 550 the EQE increases to 24 % for **9**:$PC_{71}BM$ (1:3) and 21 % for **10**:$PC_{71}BM$ (1:3). From 550 -750 nm the EQE falls off following the tail of the absorption, with a slight shoulder at 650 nm for **9**:$PC_{71}BM$ (1:3) and 680 nm for **10**:$PC_{71}BM$ (1:3).

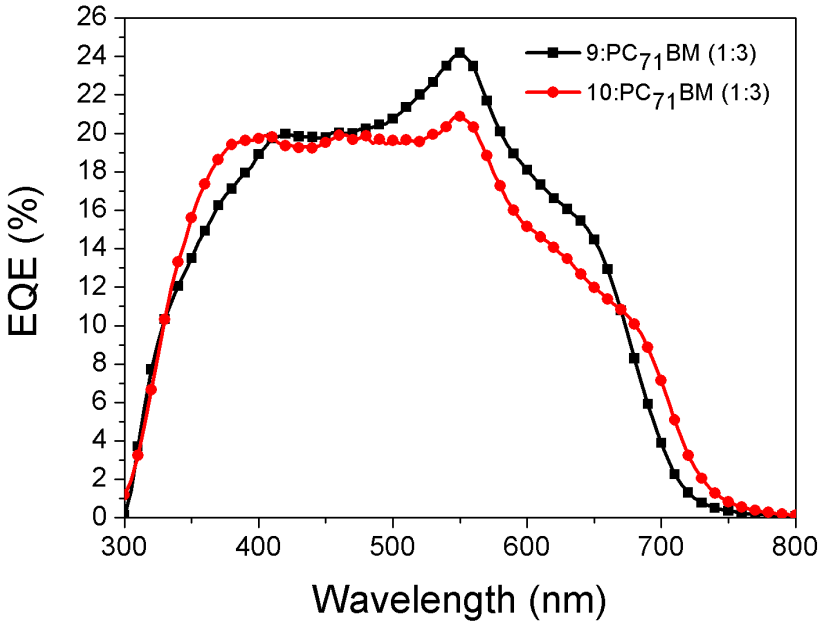

Figure 7.16 *Incident photon to converted electron (IPCE) ratio or external quantum efficiency (EQE) for* ***9****:$PC_{71}BM$ (1:3) (black) and* ***10****:$PC_{71}BM$ (1:3) (red).*

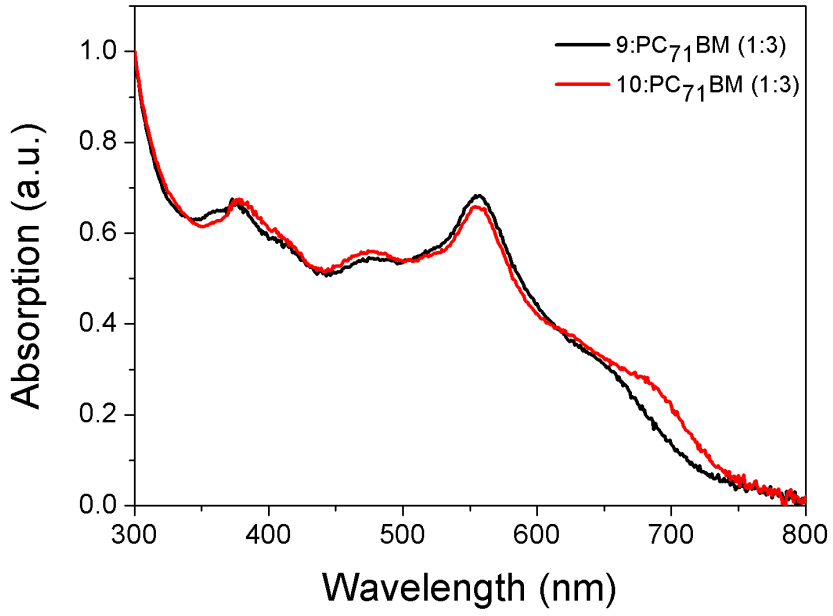

Figure 7.17 *Absorption spectra for* ***9****:$PC_{71}BM$ (1:3) (black) and* ***10****:$PC_{71}BM$ (1:3) (red).*

In order to understand the aspects limiting performance the morphology was investigated using tapping mode atomic force microscopy (AFM). The AFM height images show large bead-like structures for **9**:PC71BM (1:3) and **10**:PC71BM (1:3), Figure 7.18. These bead like structures are larger for **10**:PC71BM (1:3) than **9**:PC71BM (1:3). The maximum height observed with **10**:PC71BM (1:3) is 4.3 nm compared to 2.2 nm for **9**:PC71BM (1:3). The true height of these aggregates are not observed by AFM as the aggregates are too large for the AFM to image. It would appear that for **10**:$PC_{71}BM$ (1:3) the bead-like structures cluster together forming larger aggregates. There is no doubt that these aggregates are limiting photovoltaic performance, particularly the aggregates we are unable to AFM due to their size, which are shown in the wide-field images, Figure 7.14. The profiler measurements show aggregates hundreds of nanometres in size, Figure 7.22 (Appendix). With the active layer only ~ 80 nm thick, Figure 7.21 (Appendix), the aggregates act as recombination centres, preventing excitons from diffusing to the donor-acceptor interface within the exciton diffusion length and impeding the transport of free charge carriers to the adjacent electrodes.

To further investigate the aggregation, films containing only **9** or **10** were prepared on fused silica substrates for PLQY measurements. At an excitation wavelength of 550 nm, PLQY values of 1.5 % and 0.8 % were attained for **9** and **10**. The emission spectra from the integrating sphere are shown in Figure 7.19 and 7.20 for **9** and **10**, respectively. This difference in PLQY is a firm indication of small molecule 10's doggedness to aggregate.

The small molecules are of interest for photovoltaic applications. However, there are issues which require attention. The first concerns the device architecture. The HOMO of **9** and **10** is below that of the PEDOT: PSS, Figure 7.11 and 7.12. Therefore, the contact at the anode is not an ideal Ohmic contact. Finally, the solubility must be improved. These issues can be solved with chemical alterations of the small molecules.

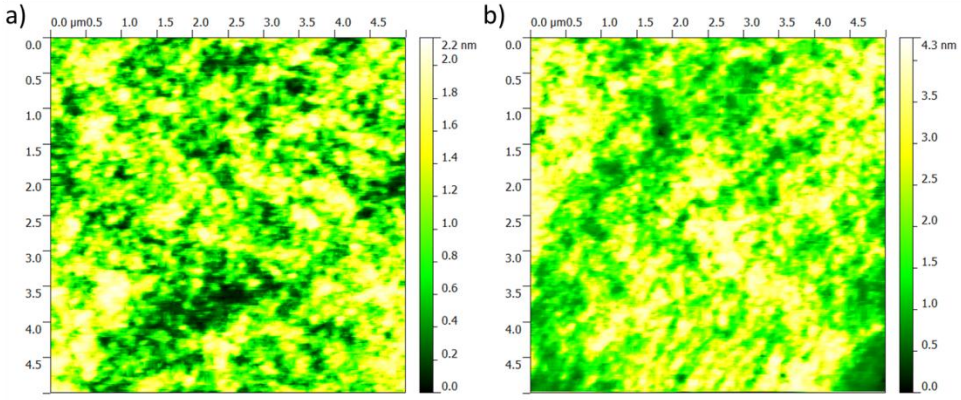

Figure 7.18 *Tapping mode AFM height images for* ***9****:*$PC_{71}BM$ *(1:3) (a) and* ***10****:*$PC_{71}BM$ *(1:3) (b) on fused silica.*

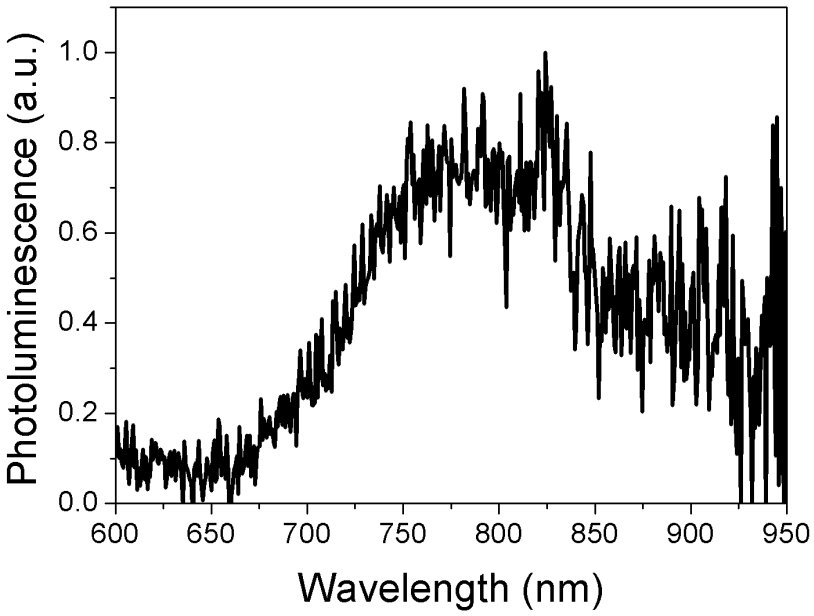

Figure 7.19 Emission spectrum of **9** acquired with a 550 nm excitation (solid state).

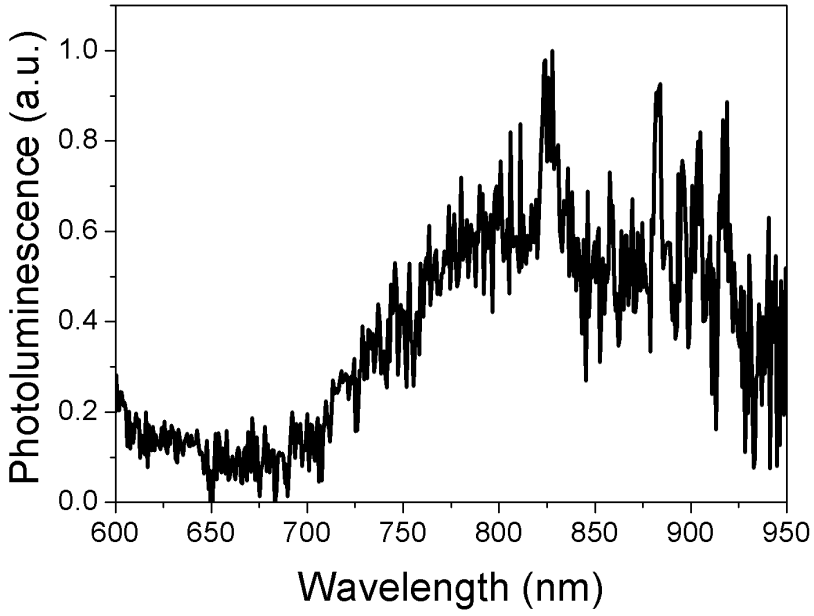

Figure 7.20 Emission spectrum of **10** acquired with a 550 nm excitation (solid state).

7.4 Conclusion

Two small molecules **9** and **10** were introduced and shown to have optical and electrochemical properties suitable for organic photovoltaic cells. The small molecules have a central diketopyrrolopyrrole (DPP) core with thionyl bridges extending to 4, 4-difluoro-4-bora-3*a*, 4*a*-diaza-*s*-indacene (BODIPY).

The absorption spectra for **9** and **10** in solution show three distinctive peaks. The absorption peak associated with the BODIPY moiety is at ~ 542 nm for both **9** and **10**. Two absorption peaks are observed for the DPP core and thionyl bridges, for **9** at 548 nm and 622 nm and for **10** at 607 nm and 645 nm. The two additional thiophenes in **10** extend the conjugation, resulting in a bathochromic shift. The solid state absorption is similar to the solution measurements. However, the spectra are red-shifted. This is expected as the solid state films have a higher degree of order than the solutions. The absorption for **9** is from 300 nm to 710 nm and for **10** from 300nm to 740 nm. The absorption between 300 nm and 400 nm is low in comparison to wavelength (λ) > 500 nm. The optical band-gaps for **9** and **10** were 1.75 eV and 1.68 eV, respectively. These were calculated from the onset of absorption, 710 nm for **9** and 740 nm for **10**. Similar values were determined from the electrochemistry. The HOMO and LUMO for **9** were -5.31 eV and -3.57 eV, respectively. For **10** the HOMO and LUMO were determined as -5.25 eV and -3.44 eV, respectively. Despite having a HOMO imperfect for an Ohmic contact, organic photovoltaic cells were fabricated, characterised and optimised.

The optimum donor-acceptor ratio was determined to be 1:3 with PCEs of 0.65 % and 0.64 % for **9**:$PC_{71}BM$ (1:3) and **10**:$PC_{71}BM$ (1:3), respectively. The low PCE values were a result of fill factors < 30 % and short-circuit current densities (Jsc) < 5 mA cm^{-2}. The Voc was lower than what we would expect from this donor-acceptor combination. However, for **9**, the Voc is larger than the attainable with P3HT:$PC_{61}BM$. To determine the aspects limiting performance, the morphology was investigated.

Microscopy and PLQY measurements were used to study the aggregation in **9** and **10**. It was believed that the two additional thiophenes in **10** would red-shift the absorption and improve performance. However, the studies concluded that their inclusion within the small molecule resulted in a propensity to aggregate, reducing Voc and hence device performance.

Aggregates of **9** and **10** within the photovoltaic cells act as recombination centres, preventing excitons diffusing to the donor-acceptor interface within the exciton diffusion length and inhibiting the transport of free charge carriers to the electrodes.

The chemical structures of the small molecules in this chapter are interesting as they incorporate two successful photovoltaic moieties, BODIPY and DPP. It has been shown that these molecules can be used as donors for solution-processable organic photovoltaic cells. However, the PCEs achieved with these, are low compared to those acquired with the state of the art small

molecules (> 6 %) [35] and those consisting of either DPP (> 4 %) [19] or BODIPY (> 2 %) [36-38]. In order to make these photovoltaic materials competitive further optimisation of the chemical structure is necessary to improve solubility and the energy levels.

7.5 Appendix

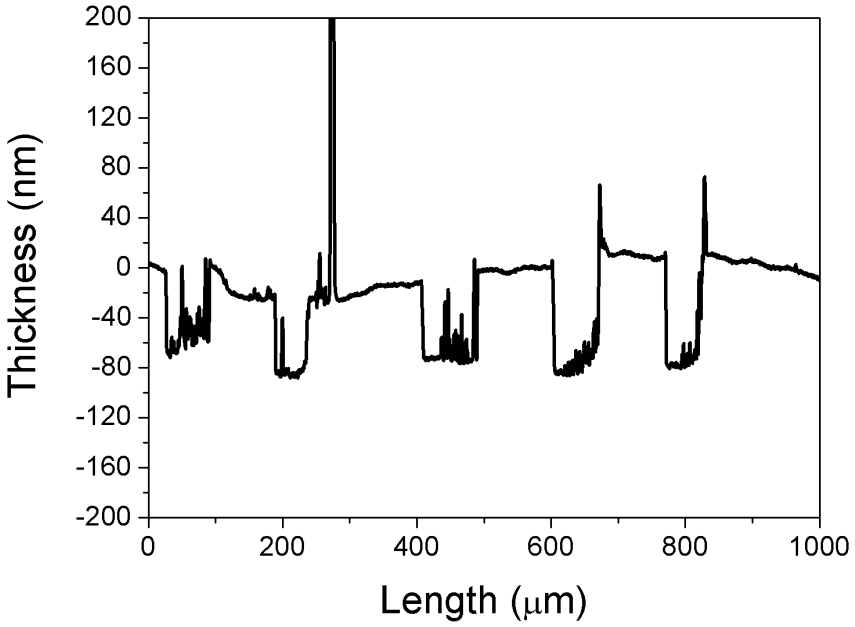

Figure 7.21 *Thickness of* ***9****:$PC_{71}BM$ (1:3) from Dektak profiler. To get an indication of thickness the film has been removed from five separate regions.*

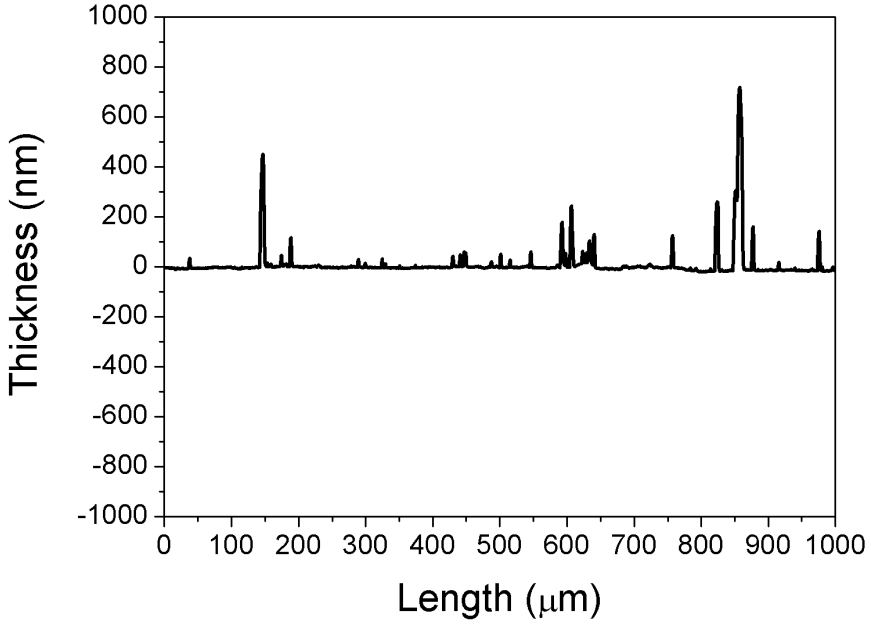

Figure 7.22 *Film of* ***10****:$PC_{71}BM$ (1:3) from Dektak profiler showing aggregates.*

7.6 References

1. Halls, J.J.M., et al., *Efficient photodiodes from interpenetrating polymer networks.* Nature, 1995. **376**(6540): p. 498-500.
2. Yu, G., et al., *POLYMER PHOTOVOLTAIC CELLS - ENHANCED EFFICIENCIES VIA A NETWORK OF INTERNAL DONOR-ACCEPTOR HETEROJUNCTIONS.* Science, 1995. **270**(5243): p. 1789-1791.
3. He, Z., Zhong, Chengmei, Su, Shijian, Xu, Miao, Wu, Hongbin, Cao, Yong, *Enhanced power-conversion efficiency in polymer solar cells using an inverted device structure.* Nat Photon, 2012(591–595
).
4. Ma, W., et al., *Thermally Stable, Efficient Polymer Solar Cells with Nanoscale Control of the Interpenetrating Network Morphology.* Advanced Functional Materials, 2005. **15**(10): p. 1617-1622.
5. Wright, I.A., et al., *Oligothiophene Cruciform with a Germanium Spiro Center: A Promising Material for Organic Photovoltaics.* Angewandte Chemie International Edition, 2012. **51**(19): p. 4562-4567.
6. Roncali, J., *Molecular Bulk Heterojunctions: An Emerging Approach to Organic Solar Cells.* Accounts of Chemical Research, 2009. **42**(11): p. 1719-1730.
7. Mishra, A. and P. Bäuerle, *Small Molecule Organic Semiconductors on the Move: Promises for Future Solar Energy Technology.* Angewandte Chemie International Edition, 2012. **51**(9): p. 2020-2067.
8. Hablot, D., A. Harriman, and R. Ziessel, *Using a Photoacid Generator to Switch the Direction of Electronic Energy Transfer in a Molecular Triad.* Angewandte Chemie International Edition, 2011. **50**(34): p. 7833-7836.
9. Hablot, D., et al., *Unsymmetrical p-Carborane Backbone as a Linker for Donor–Acceptor Dyads.* Chemistry – A European Journal, 2012. **18**(7): p. 1890-1895.
10. Proctor, C.M., et al., *Nongeminate Recombination and Charge Transport Limitations in Diketopyrrolopyrrole-Based Solution-Processed Small Molecule Solar Cells.* Advanced Functional Materials, 2013. **23**(28): p. 3584-3594.
11. Kippelen, B. and J.-L. Bredas, *Organic photovoltaics.* Energy & Environmental Science, 2009. **2**(3): p. 251-261.
12. Economopoulos, S.P., et al., *Novel BODIPY-based conjugated polymers donors for organic photovoltaic applications.* RSC Advances, 2013. **3**(26): p. 10221-10229.
13. Wienk, M.M., et al., *Narrow-Bandgap Diketo-Pyrrolo-Pyrrole Polymer Solar Cells: The Effect of Processing on the Performance.* Advanced Materials, 2008. **20**(13): p. 2556-2560.
14. Chen, Z., et al., *High-Performance Ambipolar Diketopyrrolopyrrole-Thieno[3,2-b]thiophene Copolymer Field-Effect Transistors with Balanced Hole and Electron Mobilities.* Advanced Materials, 2012. **24**(5): p. 647-652.
15. Bürgi, L., et al., *High-Mobility Ambipolar Near-Infrared Light-Emitting Polymer Field-Effect Transistors.* Advanced Materials, 2008. **20**(11): p. 2217-2224.
16. Benniston, A.C., et al., *Thermoresponsive fluorescent polymers based on a quaterthiophene-containing boron dipyrromethene (Bodipy) dyad dispersed in silicone rubber.* Journal of Materials Chemistry, 2011. **21**(8): p. 2601-2608.
17. Tamayo, A.B., et al., *Design, Synthesis, and Self-assembly of Oligothiophene Derivatives with a Diketopyrrolopyrrole Core.* The Journal of Physical Chemistry C, 2008. **112**(39): p. 15543-15552.
18. Cortizo-Lacalle, D., et al., *Incorporation of fused tetrathiafulvalene units in a DPP-terthiophene copolymer for air stable solution processable organic field effect transistors.* Journal of Materials Chemistry, 2012. **22**(22): p. 11310-11315.

19. Walker, B., et al., *Nanoscale Phase Separation and High Photovoltaic Efficiency in Solution-Processed, Small-Molecule Bulk Heterojunction Solar Cells.* Advanced Functional Materials, 2009. **19**(19): p. 3063-3069.
20. Ulrich, G., R. Ziessel, and A. Harriman, *The Chemistry of Fluorescent Bodipy Dyes: Versatility Unsurpassed.* Angewandte Chemie International Edition, 2008. **47**(7): p. 1184-1201.
21. Loudet, A. and K. Burgess, *BODIPY Dyes and Their Derivatives: Syntheses and Spectroscopic Properties.* Chemical Reviews, 2007. **107**(11): p. 4891-4932.
22. Ziessel, R., G. Ulrich, and A. Harriman, *The chemistry of Bodipy: A new El Dorado for fluorescence tools.* New Journal of Chemistry, 2007. **31**(4): p. 496-501.
23. Cortizo-Lacalle, D., et al., *BODIPY-based conjugated polymers for broadband light sensing and harvesting applications.* Journal of Materials Chemistry, 2012. **22**(28): p. 14119-14126.
24. Kim, B., et al., *Bodipy-backboned polymers as electron donor in bulk heterojunction solar cells.* Chemical Communications, 2010. **46**(23): p. 4148-4150.
25. Bura, T., et al., *High-Performance Solution-Processed Solar Cells and Ambipolar Behavior in Organic Field-Effect Transistors with Thienyl-BODIPY Scaffoldings.* Journal of the American Chemical Society, 2012. **134**(42): p. 17404-17407.
26. Kim, C., et al., *Influence of Structural Variation on the Solid-State Properties of Diketopyrrolopyrrole-Based Oligophenylenethiophenes: Single-Crystal Structures, Thermal Properties, Optical Bandgaps, Energy Levels, Film Morphology, and Hole Mobility.* Chemistry of Materials, 2012. **24**(10): p. 1699-1709.
27. Walker, B., C. Kim, and T.-Q. Nguyen, *Small Molecule Solution-Processed Bulk Heterojunction Solar Cells†.* Chemistry of Materials, 2010. **23**(3): p. 470-482.
28. Sonar, P., et al., *Solution processable low bandgap diketopyrrolopyrrole (DPP) based derivatives: novel acceptors for organic solar cells.* Journal of Materials Chemistry, 2010. **20**(18): p. 3626-3636.
29. Chen, H., et al., *Highly π-Extended Copolymers with Diketopyrrolopyrrole Moieties for High-Performance Field-Effect Transistors.* Advanced Materials, 2012. **24**(34): p. 4618-4622.
30. Hablot, D., P. Retailleau, and R. Ziessel, *Substituted Diketopyrrolopyrroles as Input Energy Units in Soluble Donor–Acceptor Dyads.* Chemistry – A European Journal, 2010. **16**(45): p. 13346-13351.
31. Shaw, P.E., A. Ruseckas, and I.D.W. Samuel, *Exciton Diffusion Measurements in Poly(3-hexylthiophene).* Advanced Materials, 2008. **20**(18): p. 3516-3520.
32. Dang, M.T., et al., *Controlling the Morphology and Performance of Bulk Heterojunctions in Solar Cells. Lessons Learned from the Benchmark Poly(3-hexylthiophene):[6,6]-Phenyl-C61-butyric Acid Methyl Ester System.* Chemical Reviews, 2013. **113**(5): p. 3734-3765.
33. Tremolet de Villers, B., et al., *Improving the Reproducibility of P3HT:PCBM Solar Cells by Controlling the PCBM/Cathode Interface.* The Journal of Physical Chemistry C, 2009. **113**(44): p. 18978-18982.
34. Potscavage, W.J., A. Sharma, and B. Kippelen, *Critical Interfaces in Organic Solar Cells and Their Influence on the Open-Circuit Voltage.* Accounts of Chemical Research, 2009. **42**(11): p. 1758-1767.
35. Sun, Y., et al., *Solution-processed small-molecule solar cells with 6.7% efficiency.* Nat Mater, 2012. **11**(1): p. 44-48.
36. Rousseau, T., et al., *A tailored hybrid BODIPY-oligothiophene donor for molecular bulk heterojunction solar cells with improved performances.* Chemical Communications, 2010. **46**(28): p. 5082-5084.
37. Rousseau, T., et al., *Multi-donor molecular bulk heterojunction solar cells: improving conversion efficiency by synergistic dye combinations.* Journal of Materials Chemistry, 2009. **19**(16): p. 2298-2300.

38. Rousseau, T., et al., *BODIPY derivatives as donor materials for bulk heterojunction solar cells.* Chemical Communications, 2009(13): p. 1673-1675.

Chapter 8

Oligothiophene with a Germanium Spiro-centre: A promising photovoltaic material with a fascinating packing motif

Overview

In this chapter, I introduce a small molecule with a Germanium-bridged Spiro-centre and discuss the molecule's capability to pack in a way that is favourable for charge transport and device performance. In addition, I demonstrate photovoltaic devices fabricated with the molecule. The molecule is a promising material for organic photovoltaics, as the molecular shape of the material facilitates two-dimensional charge transport. To help establish the significance of this material to the field of organic solar cells (OSCs), I will in this chapter; (1) provide an overview of the material's properties, (2) compare the field dependent mobility with several other compounds, (3) show the mobility to vary with annealing, using two independent techniques, charge generation layer (CGL) time of flight (TOF) and organic field effect transistor (OFET) measurements, (4) discuss how the change in mobility with annealing was investigated using optical, electron and scanning probe microscopy, and found to be concomitant with the change in morphology, (5) prove by means of a planar heterojunction, that through the implementation of a well-defined annealing method, it is possible to control the morphology and by extension the mobility of the material, which can lead to improved device performance, (6) demonstrate the material and a slightly altered version of the material, which has yet to be reported in the literature, as donors for solution-processable bulk-heterojunction (BHJ) OSCs, and finally, (7) discuss the opportunity of exploring similar materials for photovoltaic applications.

Time of flight (TOF) mobility measurements were in collaboration with project student Stuart A. J. Thomson and Dr Salvatore Gambino, under the supervision of Professor Ifor D. W. Samuel at the University of St Andrews. At the University of Strathclyde, under the supervision of Professor Peter J. Skabara; Dr Iain Wright synthesised and completed the electrochemical characterisation, Dr Anto R. Inigo performed organic field effect transistor (OFET) mobility measurements, Dr Fiona Coomer carried out X-ray diffraction (XRD) measurements and finally, Joseph Cameron was responsible for the density functional theory (DFT) calculations.

8.1 Introduction

To date, most of the research in the field of organic solar cells (OSCs) has focussed on developing conjugated polymers as donors for polymer/fullerene derivative bulk heterojunction (BHJ) OSCs. What has made conjugated polymers so attractive for OSCs, is their ability to form, when blended with a fullerene acceptor, a bicontinuous interpenetrating network which provides efficient exciton dissociation and charge transport [1, 2]. In addition, conjugated polymers are solution-processable semiconductors, and device fabrication via solution processing increases output and reduces the cost of fabrication [3]. At present the best OSCs are fabricated with this type of donor [4].

In spite of their superior power conversion efficiencies (PCEs) and film-forming properties, polymeric materials suffer from molecular weight polydispersity, end group contamination, and batch to batch variations [5]. Small molecules and oligomers, on the other hand, have well-defined chemical structures and are created from mono-dispersed compounds with completely reproducible properties. Small molecules are also more prone to self-assemble into ordered domains, thus yielding high charge-carrier mobilities [6-8]. Hence, small molecules are excellent candidates for OSCs [9].

The use of small molecules as donors for OSCs appeared a few years after the development of the BHJ [1, 2]. However great the work on evaporated small molecules, enthusiasm was short-lived, as solution-processing was challenging and the OSCs exhibited low PCEs. In the previous chapter, I demonstrated the difficulty in obtaining films of sufficient quality necessary to achieve OSCs with reasonable PCEs, i.e. greater than or equal to 1 %.

The earliest solution-processable small molecule OSCs included BHJs of phthalocyanine/perylene [10] and hexabenzocoronene/perylene [11]. These early OSCs, including those small molecule/fullerene BHJ OSCs, achieved PCEs several orders of magnitude lower than similar systems fabricated with conjugated polymers [12]. It was only in 2006, more than a decade after the discovery of the BHJ, that solution-processable BHJ OSCs with small molecules as donors achieved noteworthy PCEs of 0.3-1.0 % [13-15]. These promising efficiencies renewed interest in small molecule OSCs, and by means of careful material design and device engineering [9], it was not long before small molecule OSCs become a fashionable photovoltaic topic and a feasible technology [8, 16-21].

The tremendous desire for small molecule OSCs has led to the design and use of some very interesting small molecules for OSC applications, these include, but are not exclusive to; dendritic oligothiophenes [22], star- or X shaped molecules [7, 15, 20, 23], linear donor-acceptor-donor (D-A-D) structures [24-26] and organic dyes [27-29].

Charge transport is an important aspect of OSC material design, particularly for small molecules, as improving absorption by means of

increasing the active layer thickness, requires materials with good charge transport properties.

A promising strategy for improving charge transport, and thus electronic device performance, is to increase the dimensionality of the intermolecular interactions in the organic semiconducting material [7, 23]. The most studied multi-dimensional conjugated systems for organic electronics are based on star- or X shaped oligomers and dendrimers, which exhibit improved device performance when compared to their linear analogues [30, 31].

In this chapter, I present a multi-dimensional material with a Germanium Spiro-centred oligothiophene cruciform structure, as a promising donor for solution-processable OSCs. The choice of oligothiophene is no accident. A vast majority of organic semiconducting materials contain oligothiophenes because of their good charge transport and tuneable optical and electronic properties [8]. The use of oligothiophene cruciform structures for applications in organic electronics is also not new. Swivel-type oligothiophene cruciforms have been shown to form crystalline films and perform well in field effect transistors [32]. Whilst, rigid Spiro-centred cruciform structures like the Ge Spiro-centred cruciform, were believed to discourage aggregation and were therefore considered suitable for applications as highly luminescent materials [33].

In stark contrast with rigid Spiro-centred cruciforms, our Ge Spiro-centred cruciform, here after known as the Ge-cruciform, has a propensity to aggregate in a way that is beneficial for charge transport and device performance. This is achieved by means of self-assembly, with the formation of efficient π-π stacking in two mutually orthogonal directions. The interesting packing motif provides us with a semiconducting material with multi-directional intermolecular interactions for applications in OSCs. It is well-known that controlling the morphology of BHJs is important for efficient OSCs [34-37]. BHJ OSCs with the Ge-cruciform are no exception. Through careful control of the morphology, it is possible, using the Ge-cruciform as donor, to fabricate OSCs with PCEs two orders of magnitude greater than solution processable derivatives of sexithiophene [38]. Whilst this is an exciting result, a rather more interesting aspect, is how the morphology of the aforementioned material is affected by post-processing thermal treatment. To my knowledge, this is the first organic semiconducting material to exhibit such a morphological change [5]. Controlling the morphology of this two-dimensional (2D) packing motif through post thermal treatment, allows us, to gain control of charge transport and by extension device performance.

The Ge-cruciform with its novel structure and interesting packing motif, brings to light new possibilities for OSC material design. This class of material is in the early stages of development and considering the efficiencies achieved thus far, we can expect future materials with improved absorption and by means of exploiting the multi-dimensional nature of self-assembly to achieve PCEs greater than that in our study.

8.2 Materials

Oligothiophenes have been actively investigated as conjugated materials for electronic devices [39], but they usually exhibit wider band gaps than polymers and favour deposition by means of thermal evaporation rather than solution-processing. For this reason, the majority of solution-processable oligothiophene OSCs demonstrate PCEs lower than their polymer counterparts. For example, whilst it is possible to exceed a PCE of 2 % with an OSC fabricated by thermal evaporation of sexithiophene and C70 [8], a solution-processed OSC fabricated with a blend of α, ω-dihexylsexithiophene and $PC_{61}BM$ will not exceed 0.01 % [38].

Promising methods for improving the performance of the aforementioned OSCs, include but are not limited to: increasing the solubility, absorption cut-off and dimensionality of the donor molecules [5]. Increasing the dimensionality of the donor molecules, in an attempt to match the intrinsically three-dimensional (3D) character of intermolecular interactions of the fullerene acceptor, has been a subject of intense research in the last decade [12].

Roncali and co-workers were the first to extend the dimensionality of the donor molecule in order to improve OSC device performance [23]. They achieved a PCE of 0.3 % (under 80 mW/cm^2 illumination) with a tetrahedral star-shaped silicon-centred system, compound **1** Figure 8.1, blended with $PC_{61}BM$. The low PCE was due to the OSC having a short-circuit current density (Jsc) of 1.15 mA/cm^2, a result of the absorption cut-off of λ=440 nm, which corresponds to an optical band-gap of approximately 2.8 eV. With the active layer only able to absorb a small fraction of the solar spectrum, large photocurrents were impossible [17]. Understanding the limitations of the material, Ponomarenko et al synthesised a similar 3D material, compound **2** Figure 8.1, with an absorption cut-off of λ=500 nm. Using $PC_{71}BM$ as an acceptor, they were able to achieve a PCE of 1.4 % [40]. With the same acceptor, Zhan et al, achieved a PCE of 1.54 % using an X-shaped oligothiophene, compound **3** Figure 8.1, with an absorption cut-off of λ=600 nm. Arguably, the most pronounced effect of extending dimensionality upon OSC performance was achieved by Bauerle et al, where they achieved a PCE of 1.7 % using a dendritic oligothiophene, compound **4** Figure 8.1, with an absorption cut-off of λ=600 nm, blended with the acceptor $PC_{61}BM$ [22].

Although these 3D architectures provide motifs for the most isotropic charge transporting properties, the most efficient aggregation can be achieved with 2D π-π stacking in mutually orthogonal directions [5]. An example of such an interaction has been demonstrated with a crystal structure of 2,6-bis-(4-hexylthiophen-2-yl)-benzo[1,2-d;4, 5-d′]bisthiazole, compound **1** Figure 8.2, wherein assembly in the third dimension and the origin of an orthogonal arrangement is provided by non-covalent sulfur-nitrogen interactions [41], shown in Figure 8.3 (a).

Hence, a cruciform arrangement with mutually orthogonal conjugated backbones obtained by means of covalent bonding would allow for the creation of a stable tecton for supramolecular assembly and provide the possibility for electronic conjugation between the arms of the molecule. Spiro-centred X-shaped systems are ideal candidates for achieving such a molecular cruciform arrangement [42]. Oligomers in a cruciform arrangement with a C or Si Spiro-centre typically show no electronic communication [5]. However, it is possible, under certain circumstances, for there to be some degree of conjugation, for example, in the case of 9,9′-Spiro-bifluorene and 9,9′-Spiro-bi(9-silafluorene), if the p orbitals around the Spiro-centre in each of the two orthogonal conjugated systems are anti-symmetric to one another [43], the value of the coupling is higher for the more compact carbon Spiro-centre [44].

In terms of material design, for efficient charge transport, conjugation between the two orthogonal backbones in a Spiro system is of great importance. In contrast, for efficient intermolecular interactions the two conjugated parts of the cruciform should be separated from each other by a sufficient distance. For this reason, our material was synthesised with a Germanium Spiro-centre. Ge has certain advantages over C or Si as a Spiro-centre. It gives better spatial separation of the oligomers in the Spiro structure and also has a full d-shell which may participate in the Spiro conjugation [5].

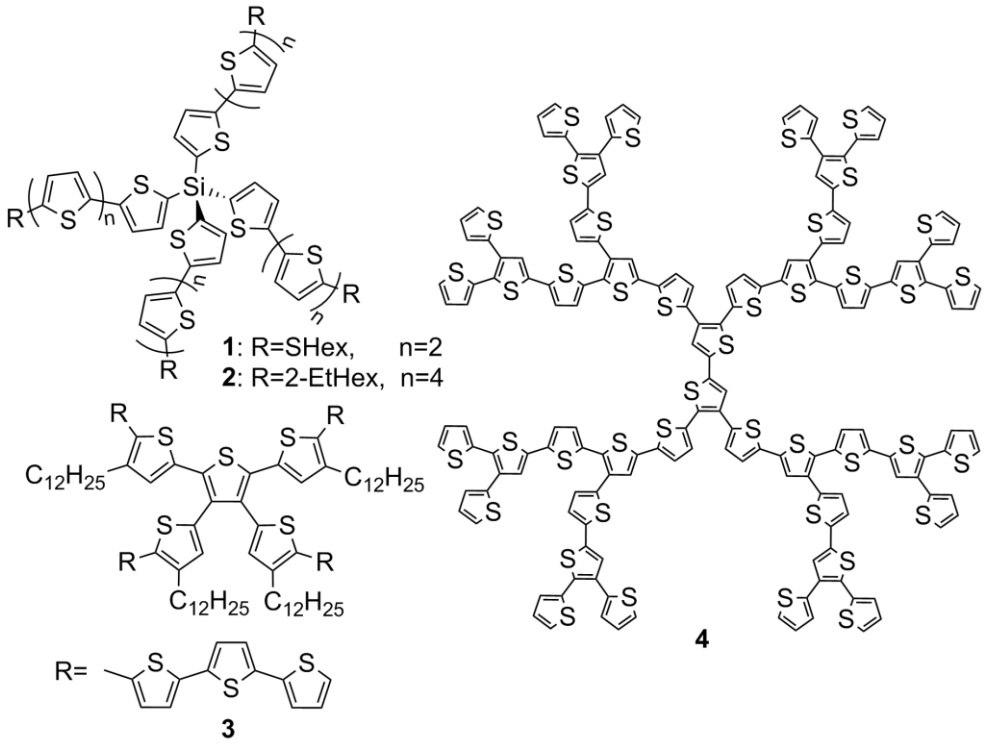

Figure 8.1 *Chemical structures of donor molecules with extended dimensionality previously used in the fabrication of BHJ OPVs.*

8.2.1 Molecular structures

The synthesis of bis(dithiolate) compounds with Si, Ge, Sn, and Pb Spiro-centres were first reported by Fink et al in 1966 [45]. Since, there have only been few reports of bis(dithiolate)germanium(IV) [46, 47], including the fused Spirobi[(1,3,2)dithiagermole] tetrathiafulvalene (TTF) system, compound **2** of Figure 8.2 [48], from which none have been considered for applications in the field of organic electronics. Here, I introduce the Ge-cruciform, compound **7** of Figure 8.2, which is a fused spirobi[(1,3,2)dithiagermole]quinquithiophene system. The full synthesis and characterisation can be found in [5].

In summary, compound **7** Figure 8.2 has been synthesised by treating dithiolone, compound **3** Figure 8.2, with sodium methoxide and reacting the resulting sodium dithiolate with germanium (IV) bromide.

For comparison, in addition to compound **8**, a compound bearing two septithiophene fragments bridged with a fused TTF unit, compound **6** Figure 8.2, is considered. This compound was first reported in the literature by Samuel et al in 2011 [49]. The end-capped oligothiophene, compound **3** Figure 8.2, having a fused dithiolone unit is similar to that of compound **4** Figure 8.2, which was used for the synthesis of compound **6** Figure 8.2. Both compounds can be used as synthetic equivalents of dinucleophilic synthons for constructing Spiro structures with the sulfur handles providing space separation of the two conjugated backbones and the possibility for Spiro conjugation.

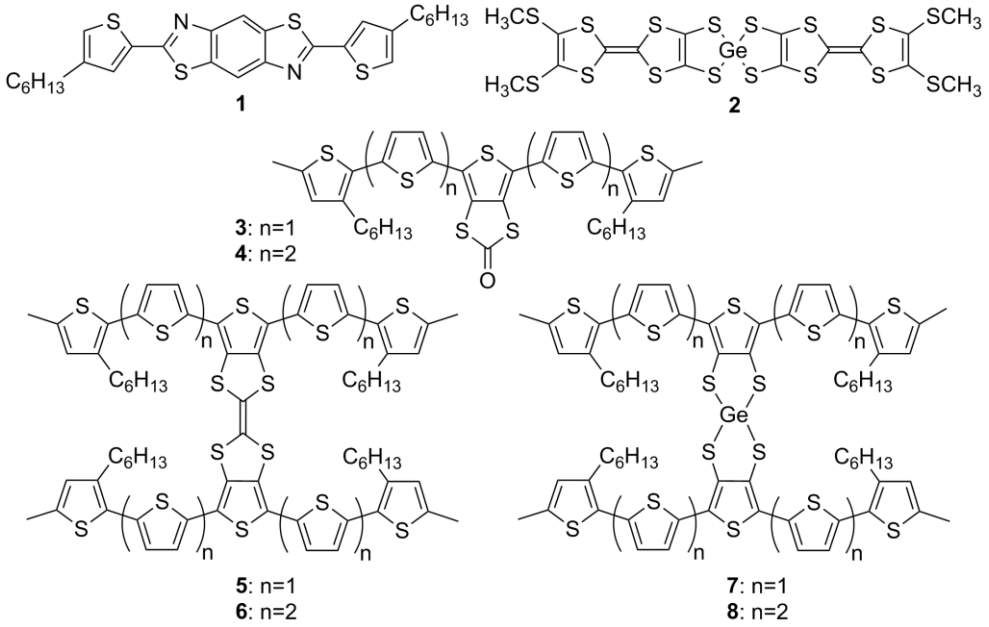

Figure 8.2 *Chemical structures of electro-active compounds* ***1*** *and* ***2****, and precursor* ***3*** *and* ***4*** *for constructing TTF bridged* ***5*** *and* ***6****, and Ge spiro centred* ***7*** *and* ***8****.*

Previous reports have suggested that conjugated cruciform oligomers are not prone to aggregate [33, 43]. In contrast, the Ge-cruciform has a propensity to aggregate. Control of the aggregation was achieved by adding a small amount of CS_2 for solution processing.

X-ray analysis on crystals of compound **1** and **7**, showed 2D stacking, Figure 8.3 (a) and (b), respectively. For the latter, the crystal structure revealed two types of stacking interactions. The oligothiophene of each cruciform molecule containing a bithiophene unit in a syn-orientation within the central part of the chain (see red plates with a small twist on one end, Figure 8.3 (c)) is involved in a stacking interaction with an identical chain of another molecule. These two molecules relate to each other by a centre of symmetry, which means that the other part of the cruciform (quinquithiophene represented by blue vertical plates in Figure 8.3 (c)) is located on different sides from the site of the π-π stacking. These quinquithiophenes stack in a second, perpendicular orientation with translation space symmetry. The inter-plane distances for these two types of stacking are 3.417 Å and 3.704 Å, respectively. For further information relating to the XRD measurements, please see the appendix.

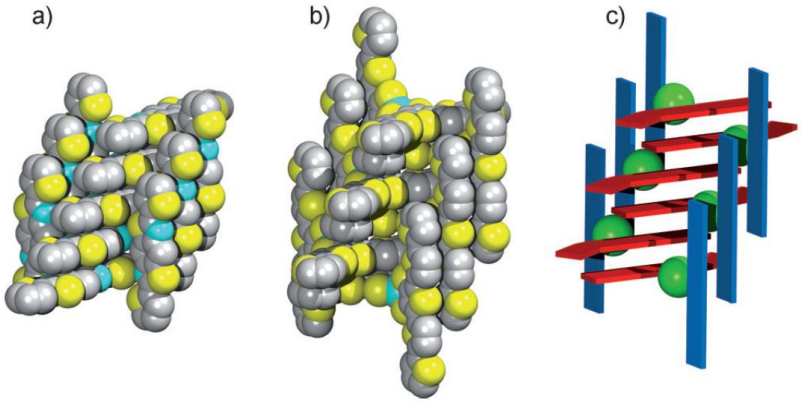

Figure 8.3 *Space filling model of 2-dimensional π-π stacking for compounds: (a)* ***1*** *and (b)* ***7*** *(alkyl substituents and hydrogen atoms omitted for clarity); and (c) schematic representation of intermolecular interactions for compound* ***7*** *(green spheres represent GeS_4-spiro centres, red plates-oligothiophenes which stack in a vertical direction with an inter-planar distance of 3.427 Å, blue plates are quinquithiophenes with a stacking distance of 3.704 Å, in the horizontal direction. Reproduced from Ref. [5] with permission from John Wiley and Sons.*

8.2.2 Electrochemical and optical properties

The cyclic voltammetry for compounds **3** and **7** can be found in the Supporting Information of the aforementioned article [5]. The results for compound **8** have yet to be reported but have been provided courtesy of Professor Peter J. Skabara.

In solution, Figure 8.4, compounds **7** and **8** have a λ_{max} of 430 and 465 nm, and an absorption onset of 521 and 582 nm, respectively. Emission spectra were obtained with an excitation wavelength of λ=420 nm, and show two peaks, 512 and 544 nm for compound **7** and, 556 and 590 nm for compound **8**. Calculating the HOMO-LUMO gap from the absorption onset gives for compound **7** and **8**, a gap of 2.38 eV and 2.13 eV, respectively. The discrepancy of 0.09 eV in [5] for compound **7**, possibly arises from the use of CS_2, which would prevent the formation of aggregates.

From the cyclic voltammetry the HOMO's for compounds **3**, **7** and **8** were found to be -5.21, -5.00 and -5.02 eV, with LUMO's -2.88, -3.64 and -3.47 eV, respectively. Hence, providing HOMO-LUMO gaps of 2.33 (2.44), 1.36 (2.47) and 1.55 (2.13) eV for compounds **3**, **7** and **8**, respectively. The optical HOMO-LUMO gaps calculated from the onset of absorption are shown in the brackets.

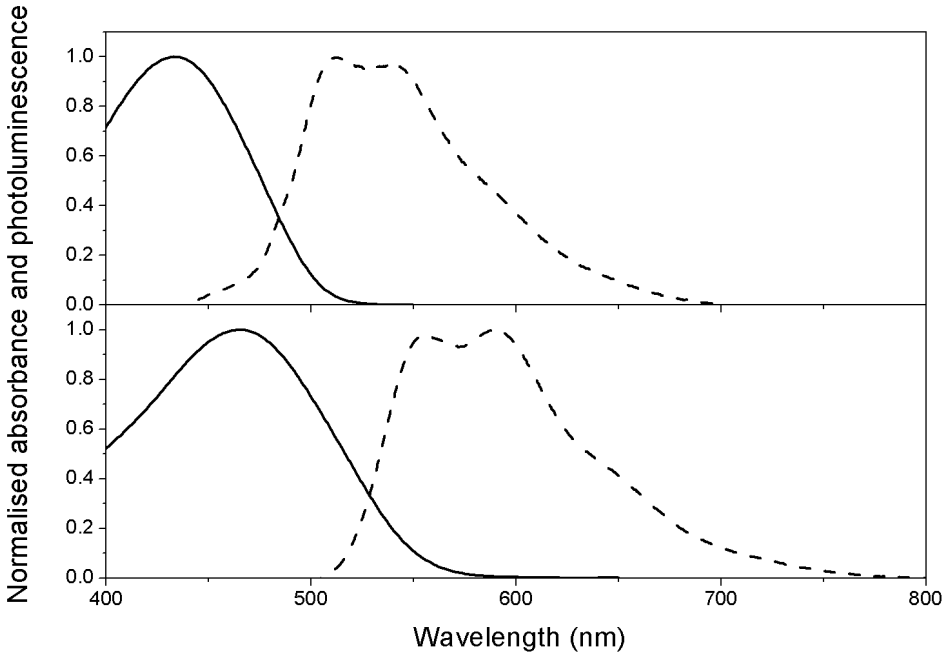

Figure 8.4 *Absorption and emission spectra for* ***7*** *(top) and* ***8*** *(bottom) in chlorobenzene solution. Emission spectra recorded with an excitation wavelength of 420 nm.*

There is a large decrease of the LUMO energy level, going from compound **3** to compound **7**. Whilst, the difference in HOMO energy level between the two compounds, is possibly due to substituent effects, compound **3** containing carbonyl versus compound **7** containing germanium.

The discrepancy between the optically and electrochemically determined HOMO-LUMO gaps for compound **7,** and to a certain extent compound **8**, suggest the Ge Spiro centre to be an electro-active subunit within the compounds, as the optically measured HOMO-LUMO gap exclusively represents the π-π* transition of the quinquithiophene chain.

In thin-film, Figure 8.5, compound **7** and **8** show a λ_{max} of 446 and 476 nm, with an absorption onset of 550 and 610 nm, respectively. For light harvesting applications the spectra for compound **7** and **8** are not ideal. This is emphasised in the comparison with the spectra of a well-studied OSC material, P3HT, which shows broad absorption at longer wavelengths compared to **7** and **8** with an absorption onset of 700 nm.

Comparing solution, Figure 8.4, with thin-film, Figure 8.5, we see disorder in solution, whereas in thin-film we have structure as our films show ordered organisation. The red-shift going from solution to thin-film for both compounds **7** and **8** is greater than 10 nm.

The aggregation in thin-film made it difficult to measure solid state emission. However, it was possible to obtain results for time-resolved fluorescent measurements, which is discussed in the latter part of this chapter.

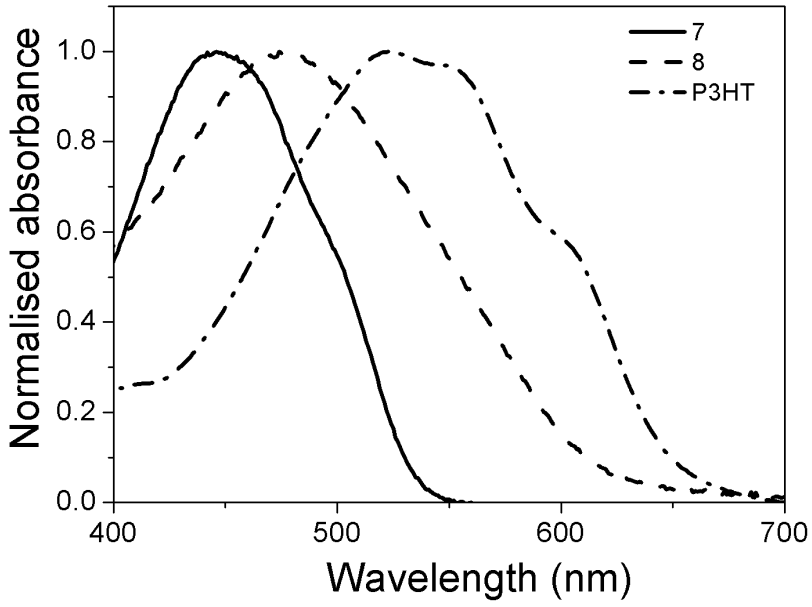

Figure 8.5 *Thin-film absorption spectra.*

8.2.3 Stacking in mutually orthogonal directions

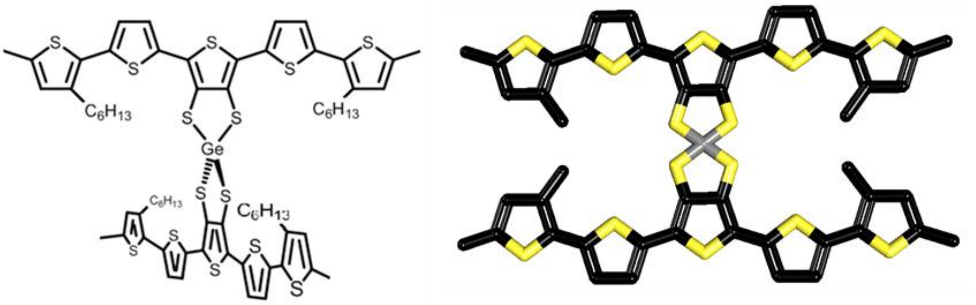

Figure 8.6 *Chemical structure of Ge-cruciform.*

Figure 8.6 shows a 3D representation of the Ge-cruciform, compound **7**, alongside its chemical structure. As mentioned, the onset of absorption for the Ge-cruciform is at shorter wavelengths than ideal for light harvesting applications. Nevertheless, the Ge-cruciform is a promising OSC material, as it exhibits a stacking structure, which I will demonstrate to be favourable for charge transport and by extension device performance. Hence, it would be of scientific interest to synthesise, using the Ge-cruciform as a template, novel materials with a reduced energy gap and cruciform structure, which would have improved absorption to that of the Ge-cruciform and exhibit similar self-assembly for good charge transport and device performance. Charge transport within the Ge-cruciform is facilitated through 2D dimensional stacking in mutually orthogonal directions. The use of a germanium atom instead of C or Si ensures a more delocalised HOMO across both arms. This central bridging atom of the molecule provides a tetrahedral geometry and promotes aggregation by allowing the arms of the cruciform to stack. The packing motif, shown in Figure 8.7, enables these long range molecular interactions in 2D. Computational methods were applied to the Ge-cruciform and the optimised structure was determined to be similar to the structure obtained by means of crystallography. The computational studies, in addition, provided evidence suggesting the Ge Spiro centre to be an electro-active subunit within the compound [5].

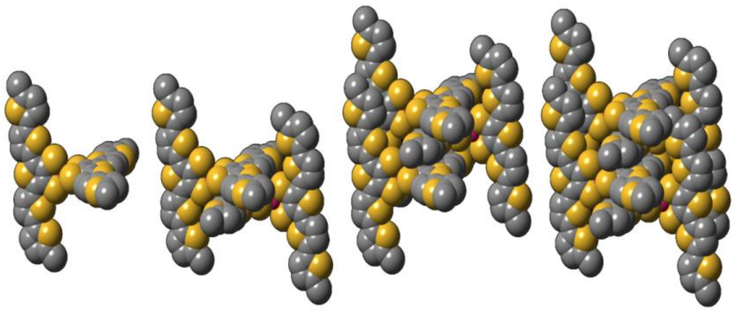

Figure 8.7 *Schematic representation of stacking for Ge-cruciform, courtesy of Professor Peter J. Skabara.*

8.3 Mobility measurements

To demonstrate the effect of stacking on the mobility of holes, I compare the field-dependent hole mobility for the Ge-cruciform, compound **7**, in carbon disulfide (CS_2) and chlorobenzene (C_6H_5Cl) with several other compounds, Figure 8.8. The field-dependent mobility measurements were measured by charge-generation layer (CGL) time of flight (TOF). It is worth mentioning that the measurements do not by themselves indicate 2D packing. The comparison is merely to show that the cruciform has a higher mobility than the analogues and that this is facilitated by the packing motif. The measurements are similar to those in earlier chapters, measuring charge mobility in the direction perpendicular to the film, which is the direction most relevant to OSCs. By incorporating a CGL the semiconductor can be the same thickness as used in an OPV, as the laser excites charge within the CGL and not the semiconductor under study. The field-dependent mobility is the result of organic semiconductors exhibiting disorder. The higher the disorder the more localised the states, transport occurs via hopping between states, as opposed to band transport found in inorganic semiconductors. Applying an electric field lowers the energy barrier for hopping, leading to an increase in mobility with field. The precursor of the Ge-cruciform, compound **3**, and the Ge-cruciform, compound **7**, both showed dispersive charge transport [5]. The mobility measurements for the fused TTF bridged septithiophene unit, compound **6**, and associated precursor, compound **4**, have been reproduced from [49]. Figure 8.8, shows the aforementioned compounds having a strong field dependent mobility.

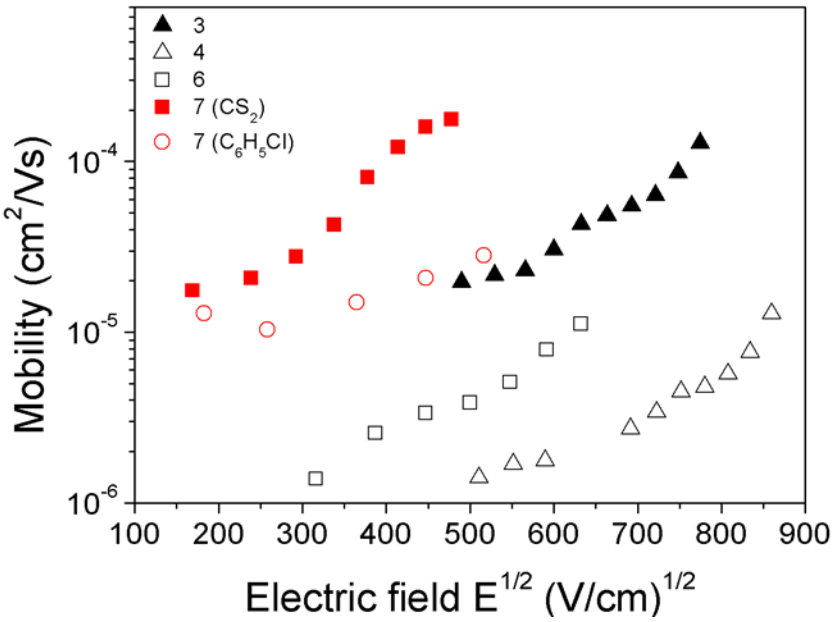

Figure 8.8 CGL-TOF hole field dependent mobility measurements.

For compound **3**, as the field increases from 2.4×10^5 to 6.0×10^5 V cm^{-1}, the mobility increases from 1.97×10^{-5} to 1.28×10^{-4} cm^2 V^{-1} s^{-1}, respectively. Whilst, for the Ge-cruciform, compound **7** dissolved in carbon disulfide (CS_2), as the field increases from 0.29×10^5 to 2.3×10^5 V cm^{-1}, the mobility increases from 1.75×10^{-5} to 1.76×10^{-4} cm^2 V^{-1} s^{-1}, respectively. Where the applied electric fields of the two compounds almost overlap, there is an order of magnitude difference in the hole mobility.

It is interesting to compare the results with other mobility measurements in the direction perpendicular to the film on related materials. The mobility measured at an electric field of 1.1×10^5 V cm^{-1} for compound **1** (data not shown) and the Ge-cruciform, compound **7**, was 6×10^{-6} and 4.2×10^{-5} cm^2 V^{-1} s^{-1}, respectively [5].

For the fused TTF bridged septithiophene unit, compound **6**, as the electric field was increased from 1×10^5 to 4×10^5 V cm^{-1}, the mobility increased from 1.38×10^{-6} to 1.12×10^{-5} cm^2 V^{-1} s^{-1}, respectively. Whilst, the mobility for the associated precursor, compound **4**, increased from 1.4×10^{-6} to 1.28×10^{-5} cm^2 V^{-1} s^{-1}, when the electric field was increased from 2.6×10^5 to 7.4×10^5 V cm^{-1}, respectively.

The results show, for the precursors, that going from a septithiophene unit, compound **4**, to a quinquithiophene unit, compound **3**, there is an order of magnitude increase in the hole mobility. A possible reason for such a large difference in the mobility, is likely due to compound **4** having a propensity to aggregate in a way that is not favourable for charge transport [49]. A likely result of large crystallised structures forming within the film, made possible by the compound having a longer chain unit. A similar effect was observed for compound **8**, synthesised from compound **4** for use in OSC applications with improved absorption of the solar spectrum to that of compound **7**. However, the longer chain unit disrupted the cruciform structure with the formation of large crystallised structures. Hence, device performance for compound **8** was less than that of compound **7**, shown in the latter part of this chapter. When dissolved in chlorobenzene (C_6H_5Cl) the Ge-cruciform, compound **7**, no longer shows strong mobility field dependence, as previously observed when dissolved in carbon disulfide (CS_2). The reduced mobility at higher electric field strengths in chlorobenzene is possibly due to the stacking structure not being as efficient as previously demonstrated in carbon disulfide. As carbon disulfide has a boiling point of 46.3 °C, whereas chlorobenzene has a boiling point of 131 °C. The larger boiling point of chlorobenzene, allows the growth of large crystal structures in random directions, acting as defects and preventing efficient charge transfer, shown later. Nevertheless, the mobility measurements for the

Ge-cruciform, compound **7**, in chlorobenzene are still larger than the precursor, with the hole mobility increasing from 1.29×10^{-5} to 2.81×10^{-5} cm^2 V^{-1} s^{-1}, with the electric field increasing from 0.33×10^5 to 2.67×10^5 V cm^{-1}, respectively. The mobility of the Ge-cruciform is an order of magnitude higher than that reported for sexithiophene [50], and the same order of magnitude as that reported for P3HT [51, 52].

The morphology of the Ge-cruciform is greatly affected by post-processing thermal treatment. This change in morphology can lead to favourable charge transport and improved device performance. To demonstrate the effect of post-processing thermal treatment, I show mobility measurements, measured by two independent techniques, time of flight (TOF) and organic field effect transistor (OFET) configurations, Figure 8.9. The TOF measurements, measure charge mobility in the direction perpendicular to the film, whilst the OFET measurements, measure charge mobility in the direction parallel to the film. Measurements were performed on two sets of samples. One set was annealed in successive step temperatures of 50, 75, 100 and 120 °C, with an annealing time of 20 minutes for each temperature step. Whilst, the other set of samples were annealed straight to 120 °C from room temperature (RT) for 20 minutes. All measurements were performed at RT.

For OFET measurements performed in the bottom gate bottom contact configuration, the mobility increases by an order of magnitude from 4×10^{-6} cm^2 V^{-1} s^{-1} (not annealed) to 4×10^{-5} cm^2 V^{-1} s^{-1} after step-annealing to 120 °C, with a gradual increase in mobility at each temperature step (50, 75 and 100 °C). However, for those samples annealed straight to 120 °C from RT, the mobility is much lower than that of the samples step-annealed to 120 °C (data not shown) [53].

TOF measurements were measured using the CGL-TOF technique. The Ge-cruciform was deposited from chlorobenzene as the field dependent mobility was not as strong as that observed for carbon disulfide, Figure 8.8. In addition, during the OFET measurements, discolouration of the gold electrode was observed for films deposited from carbon disulfide, making the results unreliable. The TOF mobility field dependent measurements at different stages of post-thermal treatment are shown in Figure 8.41 of the appendix. The results clearly show films deposited from chlorobenzene not to exhibit strong mobility field dependence, as previously observed with carbon disulfide. Hence, it is possible to compare the TOF and OFET measurements, Figure 8.9. Both

OFET and TOF measurements show a gradual increase in mobility with step-annealing, with the hole mobility for the TOF measurements increasing by an order of magnitude from 1×10^{-5} cm^2 V^{-1} s^{-1} to 1×10^{-4} cm^2 V^{-1} s^{-1}, going from RT to 100 °C with an applied electric field of 3.3×10^4 V cm^{-1}.

The aforementioned techniques for measuring mobility are not only different from a geometric perspective, but are governed by different physical phenomena, for example low level charge carrier density in TOF as opposed to high charge carrier density in OFETs [53]. Hence, the absolute value of the mobility at each annealing step observed for the TOF and OFET measurements are different, as shown in Figure 8.9.

Both the TOF and OFET mobility methods show an increase in mobility with step-annealing. These measurements provide further confirmation of the interesting packing motif observed with XRD and demonstrate a semiconducting material with a mobility that can be easily controlled through post-thermal treatment to be used for improved device performance, shown in the latter part of this chapter.

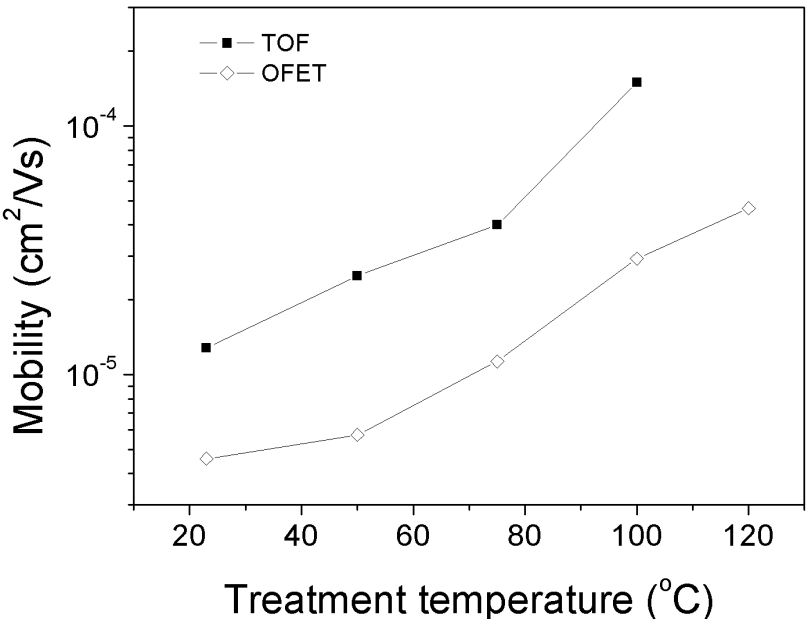

Figure 8.9 *Mobility measurements for the Ge-cruciform measured by time of flight (TOF) and organic field effect transistor (OFET) methods. The mobility has been measured at RT between each temperature step. Reproduced from Ref. [53] with permission from The Royal Society of Chemistry.*

8.3.1 Morphological studies

Organic semiconducting materials have been known to exhibit improved performance after annealing closer to their glass transition temperature [54-56], a large variation in mobility due to step annealing is very interesting and may play a direct role in the efficiency of OSCs.

To help understand the change in mobility with post-processing thermal treatment, morphological studies were carried out using a variety of scanning microscopies.

Tapping mode AFM height images show the surface structure of as-cast films to be amorphous, Figure 8.42 of the appendix. In the same figure, images are shown for samples step-annealed. These AFM images were measured post annealing at a given temperature step for 20 minutes.

At 50 °C crystalline structures start to form. There is no significant difference in the size of crystalline structures for samples annealed at temperatures between 50 and 100 °C. However, the RMS surface roughness for samples annealed at 75 and 100 °C is almost double compared to samples annealed at 50 °C [53]. Step-annealing samples to 120 °C reveals a very different surface structure with broken rod-like crystalline domains of ~200 nm length and ~20 nm widths, Figure 8.10.

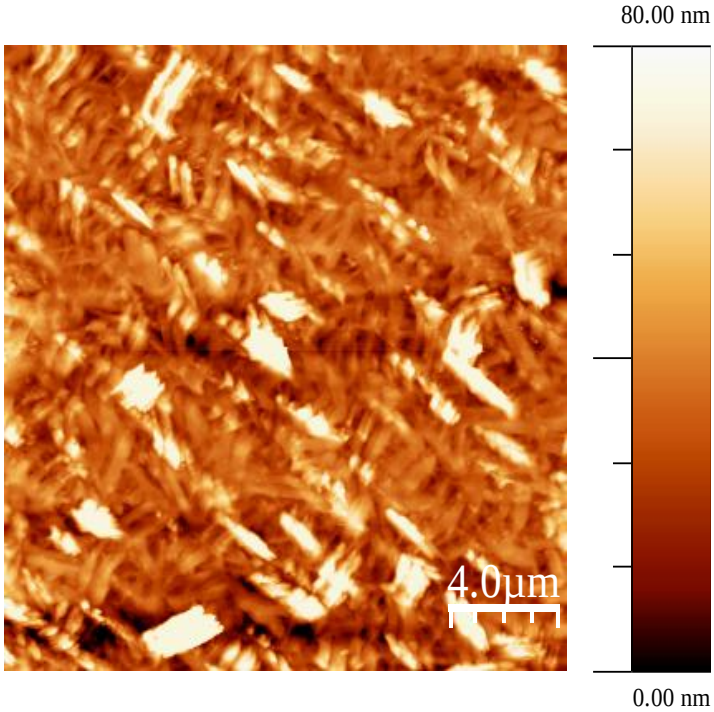

Figure 8.10 *Tapping mode AFM of Ge-cruciform annealed at 120 °C for 20 minutes after annealing at 50, 75 and 100 °C in 20 minutes steps. Reproduced from Ref. [53] with permission from The Royal Society of Chemistry.*

For samples annealed straight to 120 °C, the tapping mode AFM height images show branching fibrillar structures, Figure 8.11. These crystalline rod-like structures are ~10 μm in length and ~1 μm wide. They are randomly aligned with horizontal separations as long as ~8 μm. The shape, size and random alignment of these structures are detrimental for charge transport, as the charge carriers would have to overcome rough interfaces and unfavourable alignment with the direction of the electric field.

Annealing the samples straight to 120 °C may give all the molecules a relatively similar molecular mobility so they can form a thermodynamically stable structure. In contrast, successive step-annealing and cooling up to 120 °C may reduce molecular mobility due to the early formation of smaller crystalline domains at temperatures less than or equal to 100 °C. The AFM images show that faster annealing promotes growth over the nucleation of crystalline domains; although molecular mobility is important, the rate of nucleation is presumably the dominating factor for the difference in morphologies under these annealing conditions. Once the temperatures are further raised to 120 °C, the crystalline structures already formed at temperatures less than or equal to 100 °C may block the movement of mobile molecules to form a dense, short-range ordered (DSRO) medium. This type of medium would be favourable for any type of organic electronic device based on charge transport, such as OPVs and OFETs [53].

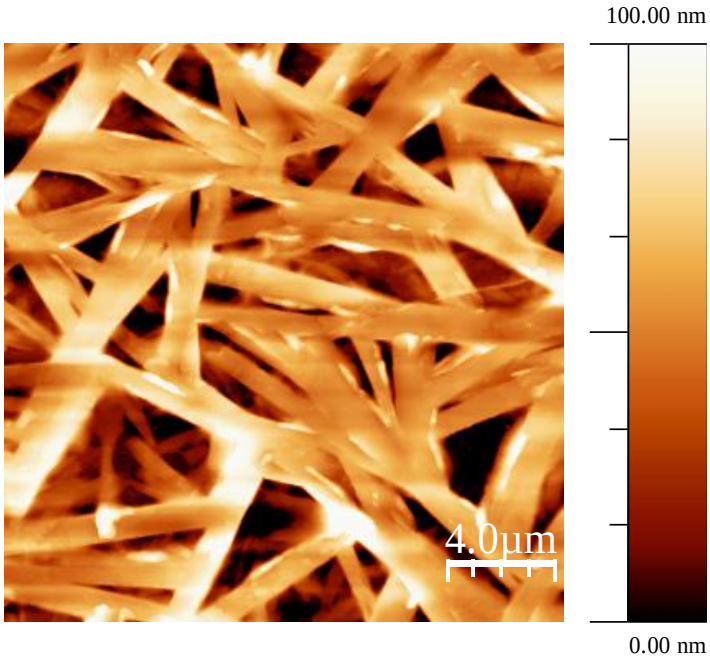

Figure 8.11 *Tapping mode AFM of Ge-cruciform annealed at 120 °C for 20 minutes. Reproduced from Ref. [53] with permission from The Royal Society of Chemistry.*

To demonstrate the effect of post-processing thermal treatment on device performance, OPVs were fabricated with a planar heterojunction structure, shown in Figure 8.16. The fabrication of such devices required a careful selection of solvent. It was necessary for the solvent to have a low boiling point to ensure rapid drying of the films to reduce intermixing and yet allow for crystal growth when annealed straight to 120 ^{o}C. For this, carbon disulphide was selected, as it had previously demonstrated its ability to control the aggregation of the cruciform [5]. To confirm carbon disulphide as a suitable solvent, films of the cruciform were spun from carbon disulphide or chlorobenzene, and compared with SEM. At room temperature (RT) the films exhibit a similar morphology, Figure 8.12 (a) and (c). Figure 8.12 (b) is a larger area section of (a) and shows the effectiveness of carbon disulphide as a solvent, in that the cruciform is thoroughly dissolved. Due to the low boiling point of carbon disulphide (46.3 ^{o}C), on annealing we see the formation of smaller crystalline rod-like structures than those observed in the AFM with chlorobenzene, Figure 8.12 (d). These are also shown to inhibit mobility [53].

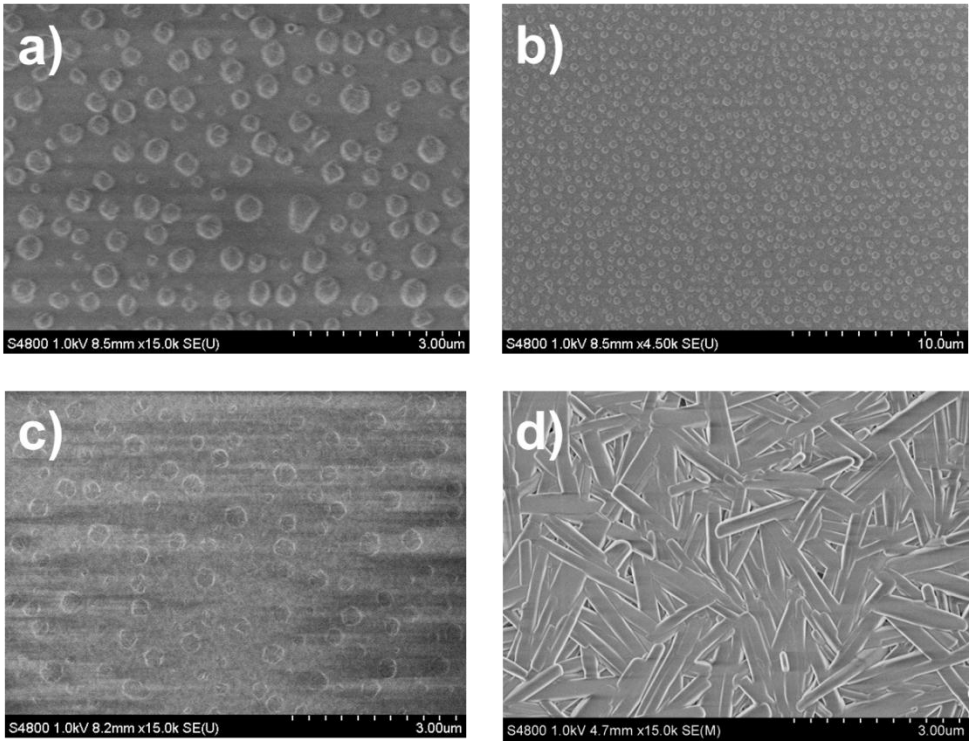

Figure 8.12 *SEM images of Ge-cruciform. (a) and (b) are of a single film spun from Carbon disulphide (CS_2). Film (c) was prepared with Chlorobenzene (C_6H_5Cl). Film (d) was deposited from CS_2 and annealed 120 ^{o}C for 20 minutes. Reproduced from Ref. [53] with permission from The Royal Society of Chemistry.*

The absorption spectra for un-annealed films deposited from carbon disulphide or chlorobenzene, Figure 8.13, are similar to the spectra observed in solution, Figure 8.4 (top), with a red shift of λ_{max} from 430 to 452 nm, going from solution to film, respectively. In addition, the solid state absorption spectra show slightly more structure compared to solution, which is to be expected with more ordered organisation of the material.

Similar absorption spectra are observed for films deposited from carbon disulphide or chlorobenzene when annealed straight to 120 °C. However, below 450 nm we see some variation due to the size of the structures in the film deposited from carbon disulphide. The spectra are broad, indicating lots of disorder. The peaks are 452, 472 and 511 nm for carbon disulphide and 452, 470 and 507 nm for chlorobenzene. The absorption for the step-annealed sample is similar to the un-annealed sample with a λ_{max} of 452 nm. Less scattering at longer wavelengths with carbon disulphide further confirm CS_2 as an appropriate solvent.

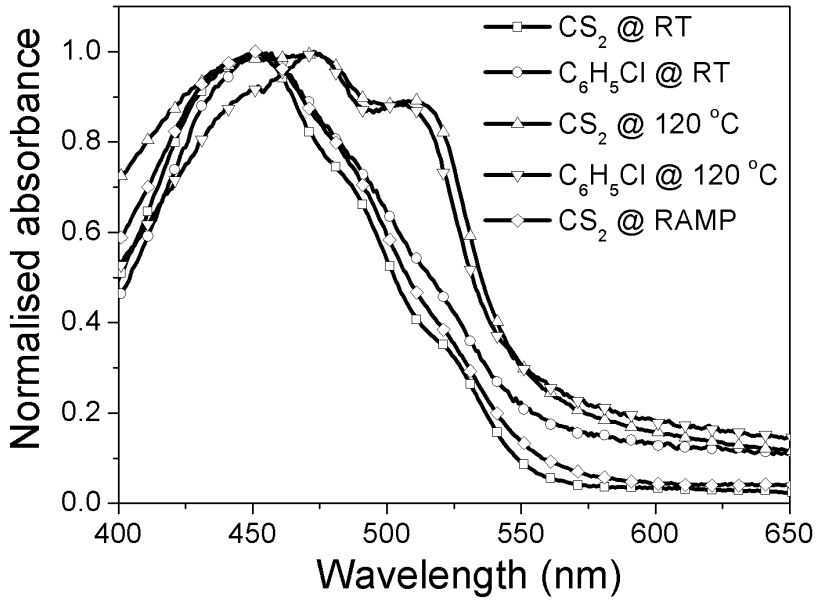

Figure 8.13 *Absorption spectra for Ge-cruciform films prepared from Carbon Disulphide (CS_2) or Chlorobenzene (C_6H_5Cl). Two films for each solvent, one of each annealed straight to 120 °C for 20 minutes. An additional film was prepared from CS_2. The film was annealed for 20 minutes at each of the following temperatures 50, 75, 100 and 120 °C in successive order. Reproduced from Ref. [53] with permission from The Royal Society of Chemistry.*

8.4 Planar heterojunctions

Fluorescent microscopy was used to image un-annealed, step-annealed and annealed straight to 120 °C films, Figure 8.44 of the appendix. The un-annealed films appeared to be amorphous, whilst those annealed straight to 120 °C showed crystalline structures. Interestingly, it was not possible to obtain an image for the step-annealed films. A possible reason for this is that the surface structures are too small or/and the fluorescent signal too weak to acquire an image. Figure 8.14 and 8.15 are of films step-annealed or annealed straight to 120 °C, respectively. Both of these films were used in the fabrication of planar heterojunction devices. To demonstrate the charge transporting properties of the Ge-cruciform within the planar heterojunction devices, thick films were required. To get an indication of the film thickness, each film was scratched several times before being measured with a profiler. The large structures observed in the films are most likely a result of material removal. The films step-annealed and annealed straight to 120 °C had similar thicknesses of approximately 250 nm, shown in Figure 8.14 and 8.15, respectively. Large crystalline structures are observed in the latter.

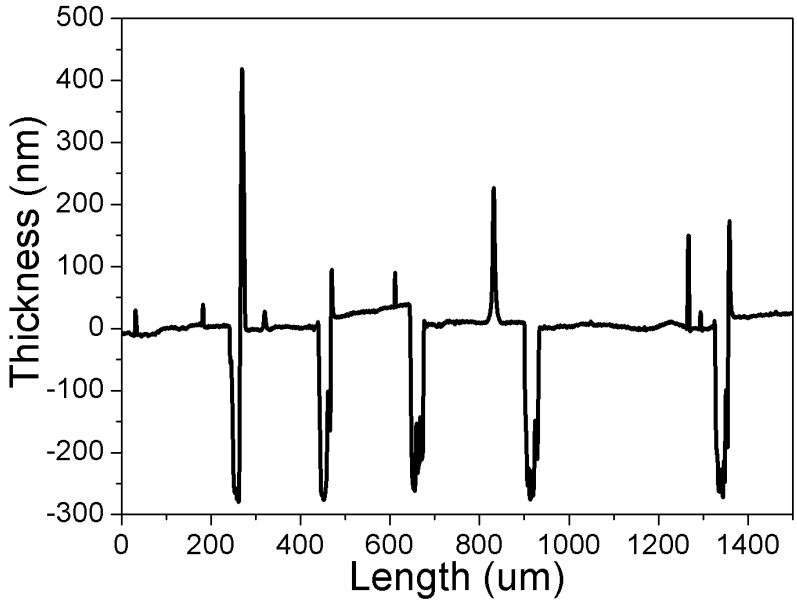

Figure 8.14 *Measurement of film thickness from Dektak profiler for Ge-cruciform spun from CS_2 and annealed at 50, 75, 100 and 120 °C in 20 minute steps. To get an indication of film thickness the films were scratched 5 times. The film thickness is shown to be approximately 250 nm. Reproduced from Ref. [53] with permission from The Royal Society of Chemistry.*

The fluorescent microscopy images and profiler measurements show the difference in morphology between films step-annealed and annealed straight to 120 °C. These measurements are consistent with the morphological observations discussed in the previous section. To achieve a similar morphology within a device as previously discussed, a single un-annealed device was measured at RT, and then annealed at 50 °C for 20 minutes and re-measured. This process was repeated with the device being subsequently annealed at temperatures 75, 100, and 120 °C. Between each temperature step of 20 minutes an incident photon to converted electron efficiency (IPCE) measurement was taken. In addition to this device, several un-annealed samples were annealed straight to a given temperature, and after acceptor and back electrode deposition they were characterised.

The short-circuit density (Jsc) under AM1.5 G was calculated for each device by integrating the IPCE. The reason for calculating the Jsc and not measuring it with the use of a solar simulator, is due to the comparatively large error inherent in measuring the Jsc with a solar simulator [57].

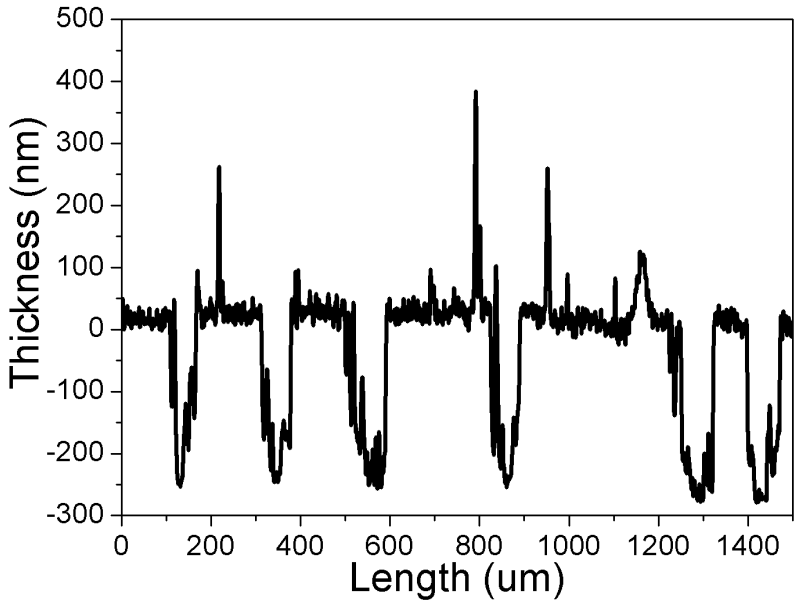

Figure 8.15 *Measurement of film thickness from Dektak profiler for Ge-cruciform spun from CS_2 and annealed straight to 120 °C for 20 minutes. The film was scratched 6 times and shown to be approximately 250 nm thick. Reproduced from Ref. [53] with permission from The Royal Society of Chemistry.*

8.4.1 Fabrication

Planar heterojunction devices were prepared on Indium tin oxide (ITO) coated glass substrates. The substrates were masked and etched in hydrochloric acid (37 %) for 20 minutes. The mask was removed and the substrates cleaned by sonication in deionised water, acetone and isopropanol. The substrates were then dried and placed in oxygen plasma for 5 minutes. Poly (3, 4-ethylenedioxythiophene):poly(styrenesulfonate) (PEDOT:PSS) from Clevios (AI4083) was spin-coated on the ITO. The PEDOT:PSS coated substrates were placed on a hotplate at 120 °C for 20 minutes in a nitrogen filled glovebox. The substrates were removed from the hotplate and left standing for 10 minutes. A ~250 nm film of the Ge-cruciform was spin-coated from a carbon disulphide solution on top of each substrate. Before depositing the acceptor and back electrode the substrates were annealed at a single temperature (either RT, 50, 75, 100 or 120 °C) for 20 minutes. The acceptor [6, 6]-phenyl-C_{71}-butyric acid methyl ester ($PC_{71}BM$) from Solenne B. V. Company was spin-coated on top of the Ge-cruciform film from a chlorobenzene solution, producing a film of ~30 nm thickness [58]. The Ge-cruciform has poor solubility in chlorobenzene and as we are annealing, i.e. making the films more crystalline, it is reasonable to assume that spin-coating the acceptor will not significantly alter the underlying donor layer. Film thicknesses were measured using a Dektak 150 M Stylus profilometer. The samples were then inserted into an evaporator for back electrode deposition. A ~20 nm calcium layer and a ~200 nm aluminium cathode were thermally evaporated at a pressure of 2×10^{-6} mbar. Figure 8.16, shows the planar heterojunction device architecture fabricated with the Ge-cruciform.

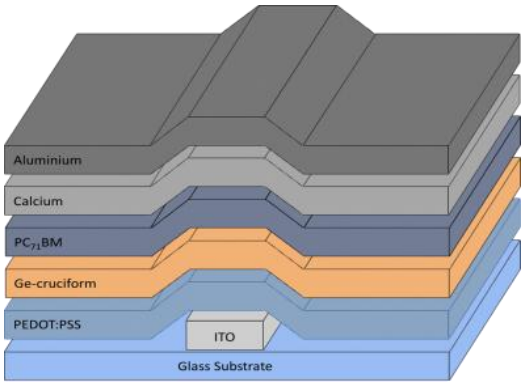

Figure 8.16 *Architecture for Ge-cruciform planar heterojunction device. Reproduced from Ref. [53] with permission from The Royal Society of Chemistry.*

Immediately after back electrode deposition, to prevent degradation by exposure to air and moisture, the fully fabricated planar heterojunction devices were removed from the evaporator and encapsulated with a glass cover slip and a UV activated optical adhesive from Thorlabs. The devices were then removed from the glovebox and characterised in air using an incident photon to converted electron efficiency (IPCE) setup, which consisted of an NPL calibrated photodiode, Keithley 6517A Pico-ammeter and a TMc300 monochromator. A single device that was not annealed straight to a given temperature was step-annealed at temperatures 50, 75, 100 and 120 °C in succession. The annealing time for each temperature step was 20 minutes. The IPCE measurement was carried out between each temperature step. The short-circuit current density (Jsc) under AM1.5 G was calculated for each IPCE measurement. Figure 8.17, shows the approximate energy level alignment for each electronically active component within the planar heterojunction.

For scanning electron microscopy (SEM) and photophysical studies, films were prepared on fused silica substrates from carbon disulphide or chlorobenzene. Samples for OFET, TOF and OPV were produced using the same procedure. SEM images were recorded with a HITACHI S-4800 scanning electron microscope and the UV-visible absorption spectra were acquired with a Varian Cary 300 spectrophotometer.

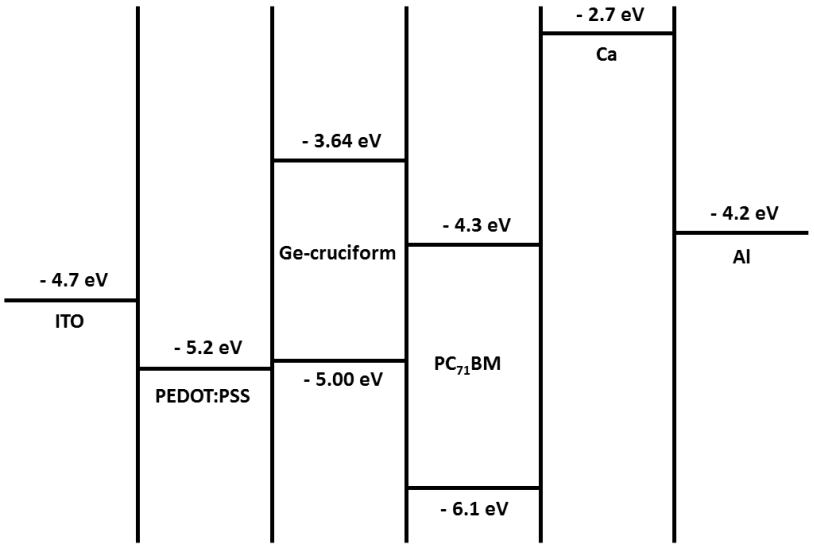

Figure 8.17 *Energy levels for Ge-cruciform planar heterojunction device. Reproduced from Ref. [53] with permission from The Royal Society of Chemistry.*

8.4.2 Characterisation

The results for a single device step-annealed to 120 °C are shown in Figure 8.18. At each temperature step we see an increase in the IPCE, with little change in the overall shape. The increase in IPCE on step annealing is observed between 350 and 650 nm. Within this wavelength range the percentage difference between un-annealed and step-annealed to 120 °C can be more than 10 %. There is no observed change in the wavelength of the peaks (380, 470 and 550 nm) within the IPCE between each temperature step. Below 350 nm the percentage difference between un-annealed and step annealed is less than 3 %, whilst above 650 nm, the percentage difference is less than or equal to 5 %.

Comparing the step-annealed device to those devices annealed straight to a given temperature for 20 minutes, we see a very different result, Figure 8.19. Noticeably, at temperatures greater than 75 °C there is a change in the IPCE, with a sharp fall for those devices annealed straight to 100 or 120 °C. The peaks observed in Figure 8.19 are similar to those in Figure 8.18 (380 and 470 nm with a shoulder at 550 nm).

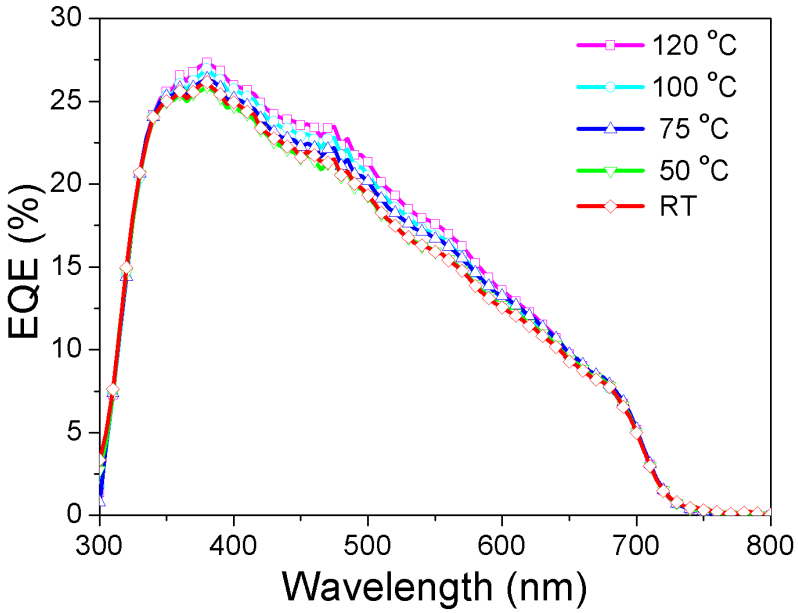

Figure 8.18 *Single device measured at RT, then annealed at 50 °C for 20 minutes and re-measured. This process was repeated for 75, 100 and 120 °C. An EQE measurement was taken between each temperature step of 20 minutes. Reproduced from Ref. [53] with permission from The Royal Society of Chemistry.*

Interestingly, those devices annealed straight to a given temperatures great than or equal to 75 °C show a peak at ~350 nm. The percentage difference at 350 and 650 nm between un-annealed and device's annealed straight to 120 °C for 20 minutes is great than 110 %, very different to the step-annealed device. The short-circuit current density (Jsc) was calculated for devices step-annealed and annealed straight to a given temperature, Figure 8.20 top and bottom, respectively. When we compare the results by calculating the Jsc, we see similarities with the aforementioned mobility measurements, Figure 8.9. The Jsc for the step-annealed device at RT and 50 °C was calculated as 3.26 mA cm^{-2}. At 75 °C a slight increase was observed in the calculated Jsc of 0.02 mA cm^{-2} to 3.28 mA cm^{-2}. A larger Jsc was determined for 100 and 120 °C of 3.4 and 3.5 mA cm^{-2}, respectively. Those devices annealed straight to a given temperature less than or equal to 75 °C, show a small variation in the calculated Jsc when compared to devices annealed straight to temperatures greater than 75 °C. At temperatures greater than 75 °C the Jsc falls off sharply from 3.15 mA cm^{-2} at 75 °C to 0.81 mA cm^{-2} at 120 °C. The IPCE and associated Jsc for the device annealed straight to 50 °C indicates that the device may not have been characterised correctly or alternatively the device may be dissimilar to the other devices, as the shape of the IPCE and value for the Jsc is different to the device measured at RT or 75 °C.

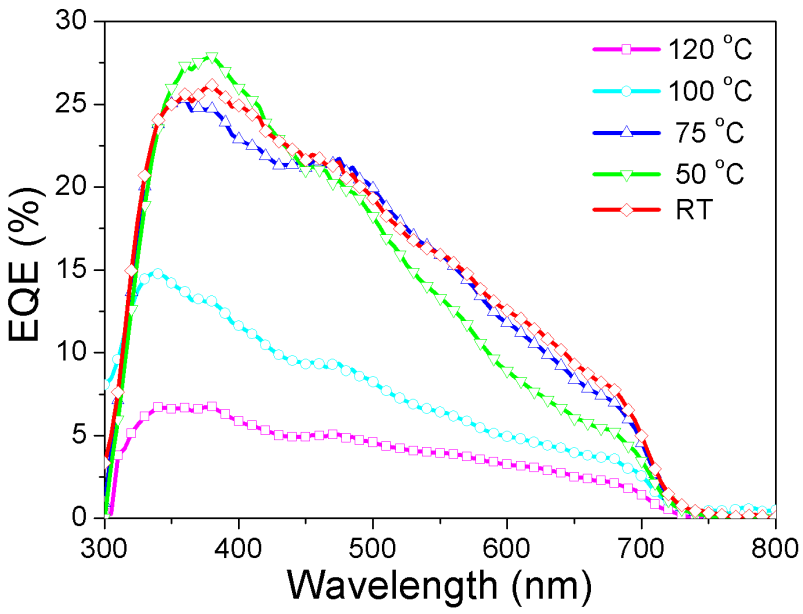

Figure 8.19 *EQE for several devices annealed straight to a given temperature for 20 minutes. Reproduced from Ref. [53] with permission from The Royal Society of Chemistry.*

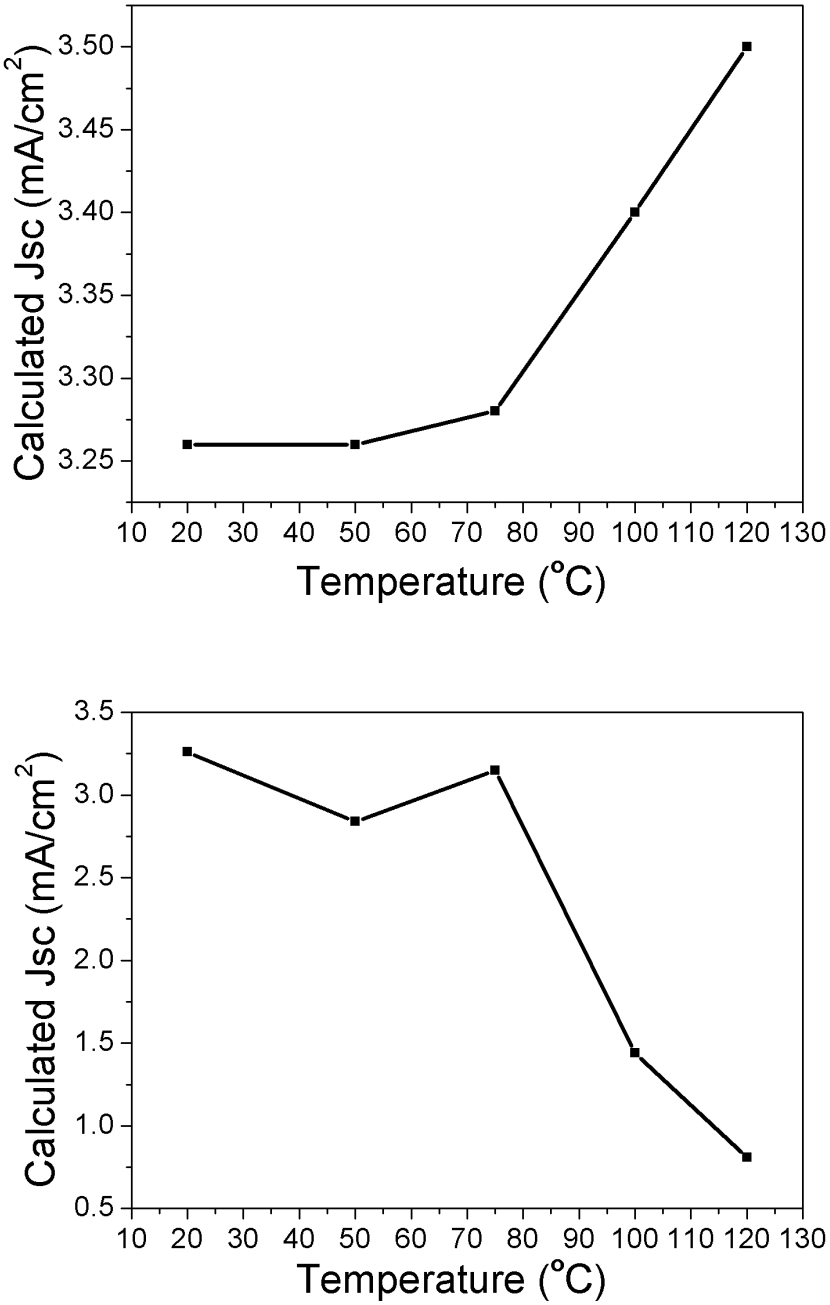

Figure 8.20 *Short-circuit current calculated for a single device measured at RT, then step-annealed at 50, 75, 100 and 120 °C with measurements taken between each temperature step of 20 minutes (top). Devices annealed straight to a given temperature for 20 minutes (bottom). Reproduced from Ref. [53] with permission from The Royal Society of Chemistry.*

To summarise, the morphology of the Ge-cruciform, a semiconducting material, is greatly influenced by the thermal annealing process and the induced morphological change affects the mobility. Controlling this process through step-annealing allows us to achieve favourable charge transport for improved device performance. For devices annealed straight to 100 or 120 °C we see the formation of large crystalline structures. These structures are shown to be unfavourable for charge transport and hence lead to poor device performance.

The measurements on OPV devices, combined with OFET and TOF results, suggest that the mobilities observed perpendicular to the plane of the substrates by OPV and TOF measurements, and parallel to the plane of the substrate by OFET measurements, are influenced by different annealing methods as a function of the material's unique 2-dimentional π-π stacking.

The results emphasise the importance of organic semiconducting materials with bulk dimensionality and how controlling the morphology of these multi-dimensional semiconducting materials is important for device performance.

8.5 Bulk heterojunctions

For efficient OPVs it is necessary to fabricate devices with bulk heterojunction architectures [1, 2]. The only exception, is with tandem OPVs, where it is possible to achieve efficiencies greater than 10 % with a series of planar heterojunction devices [9]. Hence, bulk heterojunction solar cells were fabricated with the Ge-cruciform [5]. However, it would be interesting to observe the Ge-cruciform in devices with a tandem architecture, even if not used as an active component in solar harvesting but as a charge transporting medium [53].

It is common practice in the field of OPV to investigate similar materials with improved solar absorption, achieved by means of extending the conjugation, resulting in a bathochromic shift and a decrease in the gap between the HOMO and LUMO energy level [59]. Here, two additional thiophene units have been added to each arm in the Ge-cruciform, compound **7**, adjacent to the Ge spiro centre, compound **8**. For comparison, in addition to compound **7**, bulk heterojunction solar cells were fabricated, characterised and optimised with compound **8**, in hope that the red-shift in the absorption spectra, shown in Figure 8.4, would result in improved device performance.

The motivation for investigating the possibility of successfully incorporating compounds **7** or **8** as donors in solution-processable bulk heterojunction solar cells, arises from the difficulty in achieving efficient

solution-processable devices with small molecules [13, 22, 23, 60], as small molecules usually have low molecular weights compared to polymers [8]. Hence, when deposited from solution, small molecules typically tend not to form the bicontinuous, interpenetrating network consisting of donor and acceptor phases, which is responsible for efficient OPVs [12]. For this reason small molecules are usually processed by thermal evaporation, which is less convenient for mass production. However, it can be argued that the most successful OPV material is PCBM, which is responsible for the realisation of efficient OPVs. PCBM is a multi-dimensional solution processable (n-type) semi-conducting material, and is a small molecule. Therefore, it is of interest to search for a multi-dimensional semi-conducting material, which is the donor analogue (p-type) of PCBM.

8.5.1 Fabrication

Bulk heterojunction devices were prepared on indium tin oxide (ITO) coated glass substrates purchased from Xin Yan Technology LTD (15 Ω/□). The substrates were etched in hydrochloric acid (37 %) for 20 minutes to attain a 4-mm-wide bottom contact. The patterned ITO coated glass substrates were subsequently cleaned in an ultrasonic bath with deionised water, acetone and isopropanol successfully for 15 minutes, followed by oxygen plasma ashing for a further five minutes. A 40-nm-thick layer of Poly(3, 4-ethylenedioxythiophene): poly(styrenesulfonate) (PEDOT: PSS) from H. C. Starck (Baytron AI4083) was deposited on top of the ITO at 4000 rpm. The substrates were then heated on a hot plate at 120 °C for 20 minutes, before being placed in a nitrogen-filled glovebox for active layer deposition. Active layers consisting of compounds **7** or **8** were deposited with and without an acceptor. Two acceptors were investigated: [6, 6]-phenyl-C_{61}-butyric acid methyl ester ($PC_{61}BM$) and [6, 6]-phenyl-C_{71}-butyric acid methyl ester ($PC_{71}BM$), purchased from Solenne B. V. Company. A variety of post deposition thermal annealing conditions were explored. The most suitable annealing condition was imposed on active layers of ~90-nm-thinkness, consisting of various donor acceptor concentrations. The layers were spin-coated at 1000 rpm for 30 seconds with a ramp of five, from a 20 mg/ml chlorobenzene solution containing carbon disulphide (8μl of carbon disulphide for every 0.1ml of chlorobenzene). The thicknesses of the active layers were recorded with a Dektak 150 M stylus profilometer.

For top contact deposition the substrates were placed into a vacuum chamber. Four 2-mm-width, 100-nm-thick, aluminium electrodes were thermally evaporated at a pressure of 2.0×10^{-6} mbar, with a deposition rate of 0.4 nm s^{-1}, defining an active area of 0.08 cm^2. A low work-function metal,

calcium, was used in combination with aluminium as the top contact for the optimal device with thicknesses of 20 and 100 nm, respectively. Devices with aluminium as a top contact were thermally annealed post electrode deposition, whereas those devices with calcium and aluminium as a top contact were annealed before electrode deposition.

Post electrode deposition and thermal annealing, as with the planar heterojunction devices, to prevent degradation by exposure to air and moisture, the devices were encapsulated with a glass cover slip and a UV activated optical adhesive from Thorlabs. On completion of the fabrication, the devices, shown in Figure 8.21, were removed from the glovebox and immediately characterised, in air, using a K. H. Steuernagel AM 1.5 G solar simulator at 100 mW cm^{-2} and a Keithley 2400 source measure unit. The light intensity was measured using a calibrated thermopile (Coherent model LM-1). As with the planar heterojunction devices, IPCE measurements were performed with an NPL calibrated photodiode, Keithley 6517A Pico-ammeter and a TMc300 monochromator.

To correct for the spectral error in the measured short-circuit current density (Jsc), arising from the difference in 1) spectral irradiance between the source and reference spectrum and 2) spectral response of the reference detector and test cell, a spectral mismatch correction factor was calculated and applied to the optimal device, fabricated with compound **7** or **8**.

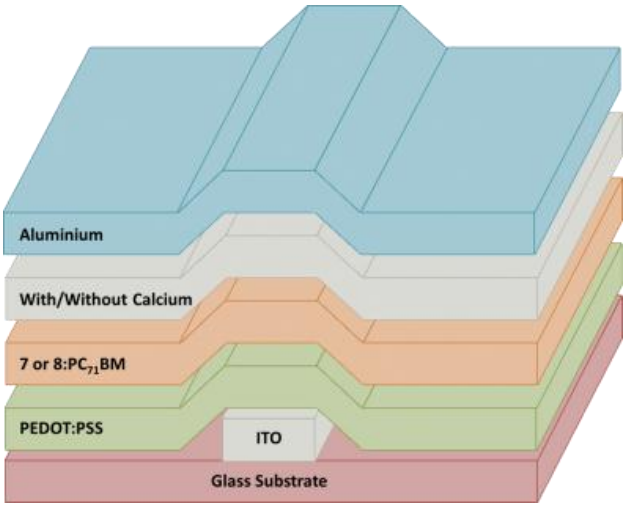

Figure 8.21 *Architecture of bulk heterojunction device.*

8.5.2 Optimisation

The discovery of the BHJ [1, 2] has enabled efficient OPVs [9, 61, 62]. Whilst progress in our understanding of the distribution of donor and acceptor components [63] within the BHJ has facilitated the fabrication of efficient devices [64-66], the optimisation of the donor-acceptor blend remains challenging [67].

Obviously, there are many factors other than the BHJ morphology that can limit the efficiency of an organic solar cell, for example the cathode-polymer interface [68]. However, the morphology of the BHJ, which at times can be extremely complex [69], plays an important role in achieving efficient devices, as fundamental processes, critical to device operation occur within the BHJ, for example exciton dissociation and charge transport [70]. Other factors that can limit the efficiency in terms of the active layer, include but are not limited to; light absorption and the mobility mismatch between the donor and acceptor components [68].

To improve device efficiency the majority of research in the field of organic solar cells has focussed on reducing the impact of these efficiency limiting factors, by means of investigating novel materials with enhanced exciton diffusion [71], light absorption [69] and mobility [53] or alternatively, trying to address these factors by investigating OPV device design, for example by fabricating tandem cells, modules with nanostructures or through the control of the molecular packing and BHJ morphology [63].

In this section I discuss the optimisation of organic solar cells with donor compounds **7** and **8**. The optimisation largely focused on morphological studies. However, the cathode-polymer interface was also investigated.

Typically, BHJ optimisation is achieved by means of controlling the morphology with a tool box. The tools available to the device physicist are constantly growing, but at present the most effective tools for controlling the active layer morphology and by extension device efficiency, are the choice of solvent, additives, deposition method and annealing [72]. Through understanding the main device performance parameters, short-circuit current density (Jsc), open-circuit voltage (Voc), and fill factor, and by monitoring them and their dependence when using the aforementioned tools, it is possible to optimise an OPV.

Knowing the correct fabrication procedure to follow when investigating a novel material can be challenging. What makes the fabrication and optimisation of an OPV challenging is the complex morphology and control thereof to improve device efficiency. The ideal situation would be a scenario where we are able to change a single variable which would have a well-defined

change on the morphology that we can observe, understand and reproduce, rather than just monitoring the impact on the performance. However, this is time consuming and extremely difficult to achieve in practice. In addition, it is worth mentioning that no typical blend exists, for example, the systems of P3HT:$PC_{61}BM$ and PTB7:$PC_{71}BM$ are extremely different from each other and hence require a different set of device fabrication parameters to achieve optimal performance [73].

Often the changing of a single condition, for example: solvent, annealing, donor-acceptor ratio, additives, electrode deposition etc. will result in more than one morphological change [74]. Whilst, there has been informative research on these morphological controlling conditions and they have facilitated in the fabrication of devices with enhanced efficiencies for given systems [35, 58, 65, 69, 75-77], implementing these on novel material where there is limited supply of material and resources in terms of equipment, cost and time, makes morphological studies which are critical to our understanding to improve device performance, difficult. Nevertheless, many microscopies are easy to perform and not time consuming and can aid in our understanding of morphology and enable us to fabricate organic solar cells with improved device efficiencies.

After selecting the required donor and acceptor components for inclusion in the device by means of considering the energy levels, the first and foremost requirement is to determine a common solvent that can dissolve both donor and acceptor components in the BHJ. For example, the acceptors: $PC_{61}BM$ and $PC_{71}BM$ are well-known to have good solubility in 1, 2, 4-Trichlorobenzene, whilst donor compounds for example, P3HT, have limited solubility at concentrations necessary for device fabrication [77]. The choice of solvent also affects the distribution of donor and acceptor phases within the BHJ, a good example of this is in the case of PTB7:$PC_{71}BM$ devices fabricated with chlorobenzene or dichlorobenzene. The change in morphology is so dramatic that the PCE increases from 3.92 % to 6.22 % going from chlorobenzene to dichlorobenzene, respectively [78].

In my study various solvents were considered. This involved dissolving donor compounds **7** and **8** with $PC_{71}BM$ at device fabrication concentrations and probing the resulting solutions with a white light source to ensure good solubility. Chlorobenzene was selected as a suitable solvent for device fabrication. Active layers consisting of **7**:$PC_{71}BM$ and **8**:$PC_{71}BM$ at ratios of 1:1 were deposited from a 20 mg ml^{-1} chlorobenzene solution. In addition, neat active layers consisting of only **7** and **8** were investigated with the blends using the standard device architecture without the use of a low work-function back electrode, shown in Figure 8.21.

Post aluminium back electrode deposition two devices containing **7**:$PC_{71}BM$ and **8**:$PC_{71}BM$ were annealed at 120 °C for 20 minutes. After annealing, all the devices (not annealed, annealed and devices containing only compounds **7** and **8**) were encapsulated, removed from the glovebox and characterised. The preliminary results, shown in Figure 8.22, show the successful incorporation of compounds **7** and **8** as donors in solution-processable bulk heterojunction organic solar cells i.e. when compounds **7** and **8** are blended with an acceptor we see a photovoltaic response. For the not annealed **7**:$PC_{71}BM$ device we have a Jsc of 1.27 mA cm^{-2}, Voc of 0.75 V and fill factor of 23 %, providing us with a PCE of 0.23 %. A lower Jsc and Voc are observed with annealing, 0.68 mA cm^{-2} and 0.44 V, respectively. The larger fill factor on annealing of 27 % is not enough to compensate for the lower Jsc and Voc. Hence, the PCE for the annealed device is 0.08 % compared to 0.23 % for the not annealed device. The opposite is observed for **8**:$PC_{71}BM$. For the not annealed device we have a Jsc of 1.56 mA cm^{-2}, Voc of 0.32 V and fill factor of 28 %, providing us with a PCE 0.14 %. The PCE is lower than that of the not annealed **7**:$PC_{71}BM$ device, which is the direct result of a lower Voc of 0.32 V compared to 0.75 V. On annealing, we observe a substantially larger Jsc of 3.45 mA cm^{-2}, Voc of 0.42 V and fill factor of 39 %, providing us with a PCE four times that of the not annealed device of 0.56 %.

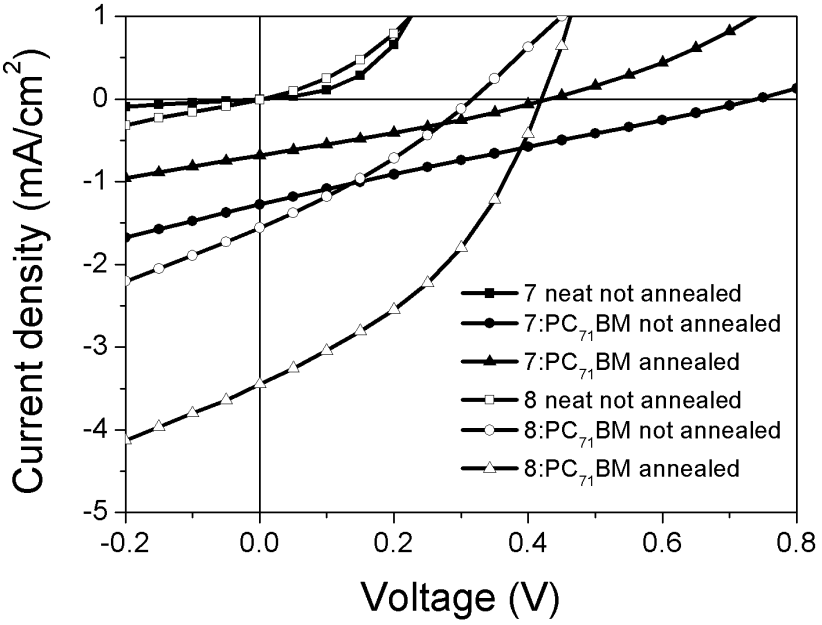

Figure 8.22 *J-V characteristics of* ***7*** *and* ***8*** *with and without acceptor for annealed and not annealed devices.*

Whilst, these PCEs are low, they are extremely encouraging for devices yet to be optimised. Typically, a device that has not been optimised that has a PCE greater than or equal to 0.1 % is worth pursuing. However, as efficiencies for organic solar cells increase with time, the bench mark for an efficient device changes [79]. The most promising device shown in Figure 8.22 is the annealed **8**:$PC_{71}BM$ (1:1) device with a PCE of 0.56 %. During fabrication small un-dissolved aggregates were observed in the films. To improve solubility the additive carbon disulfide was utilized. In addition, in an attempt to increase the Voc, devices were fabricated with $PC_{61}BM$, as $PC_{61}BM$ has a shallow LUMO compared to $PC_{71}BM$ [62, 80] and therefore would exhibit a larger theoretical Voc [81]. In practice, a very different result was observed. The results are shown in Figure 8.23. For purposes of comparison, devices containing **8**:$PC_{61}BM$ and **8**:$PC_{71}BM$ were annealed at 90, 110 or 130 °C for 20 minutes before being characterised. The devices annealed at 110 and 130 °C outperform those obtained at 120 °C, indicating that the addition of carbon disulfide is facilitating a favourable morphology for improved device performance. For the device annealed at 110 °C we have a Jsc of 5.08 mA cm^{-2}, Voc of 0.46 V and fill factor of 37 %, providing us with a PCE 0.87 %. Whilst, for the device annealed at 130 °C we have a Jsc of 5.82 mA cm^{-2}, Voc of 0.42 V and fill factor of 41 %, giving us a PCE of 1.01 %, making 130 °C the optimal annealing condition for **8**:$PC_{71}BM$.

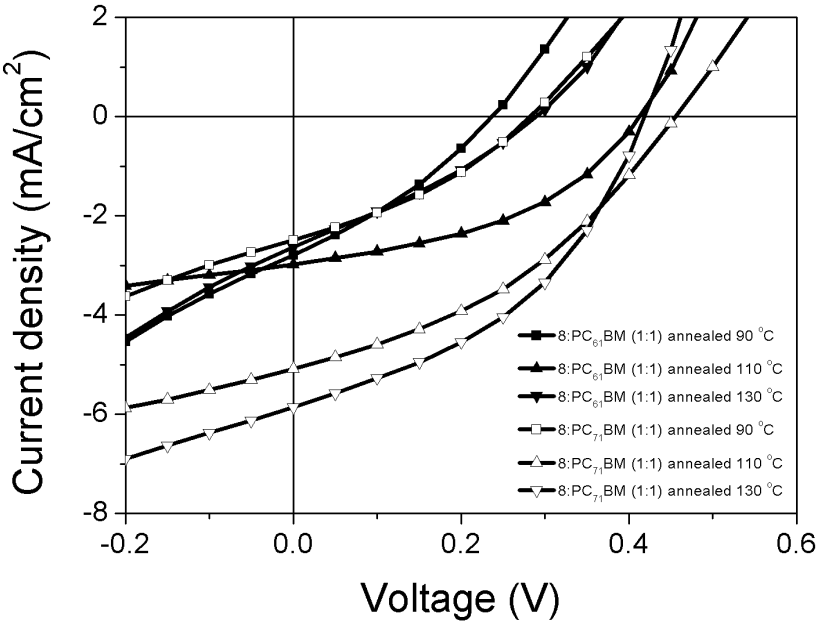

Figure 8.23 *J-V characteristics of* ***8*** *with $PC_{61}BM$ or $PC_{71}BM$ at a ratio of 1:1 for a variety of annealing conditions.*

The results shown in Figure 8.23 reinforce that our choice of acceptor, $PC_{71}BM$, is appropriate. The acceptor, $PC_{61}BM$, appears not to be suitable for exciton dissociation, as the open-circuit voltages (Voc) are much lower for devices containing **8**:$PC_{61}BM$ than those containing **8**:$PC_{71}BM$. In addition, $PC_{61}BM$ does not absorb strongly in the visible [82]. $PC_{71}BM$, on the other hand is well-known for having good absorption for an acceptor in the visible [69]. We know from the absorption measurements of our compounds that their absorption in the visible is far from ideal for OPV applications and therefore for efficient OPV based on our compounds the acceptor will have an important role in the absorption of light. The IPCE measurement, shown in Figure 8.24, is for the **8**:$PC_{61}BM$ and **8**:$PC_{71}BM$ device annealed at 130 °C for 20 minutes and supports our argument. The calculated short-circuit current density (Jsc) is almost double for the device containing $PC_{71}BM$ compared to $PC_{61}BM$. Both IPCE measurements have a peak in the IPCE at ~450 nm. It is difficult to know which component is largely responsible for this peak as both components have a peak near 450 nm [69]. However, looking at the solid state absorption for compound **8**, Figure 8.5, and knowing that $PC_{61}BM$ contributes to photocurrent [66] I would argue that it is the $PC_{71}BM$ which is largely responsible for the photovoltaic response shown in Figure 8.23.

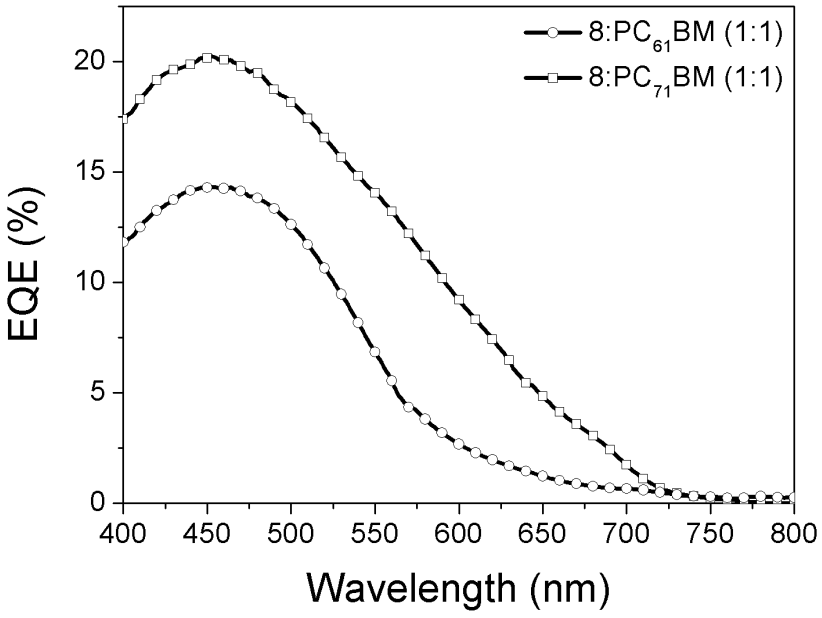

Figure 8.24 *Incident photon to converted electron (IPCE) ratio for* ***8*** *with acceptor* $PC_{61}BM$ *or* $PC_{71}BM$.

It is interesting that the performance of OPVs fabricated with compounds **7** and **8** vary with annealing. Whilst it is well-established that the performance of P3HT:PCBM OPVs can be improved with annealing [83], this is the exception rather than the rule [69, 84]. In the majority of cases, it is where the OPV materials tend to form crystalline structures, exhibiting a strong morphological change on annealing that is responsible for the performance dependence. What makes compounds **7** and **8** so interesting is that when we anneal devices containing compound **7** the efficiency decreases, whilst on annealing devices fabricated with compound **8**, we see an increase in the performance.

It is difficult to know precisely the reason for the difference in performance between compound **7** and **8** on annealing. However, as our previous measurements showed that annealing compound **7** straight to a given temperature for 20 minutes results in the formation of large crystalline structures, which are unfavourable for charge transport and by extension device performance. It is reasonable to assume, as we are dealing with a donor-acceptor blend with a ratio of 1:1 that for compound **7**, a similar morphological change, as observed in the previous measurements, is responsible for the comparatively low device performance observed in the annealed device to that of the not annealed device. If compound **8** is not forming crystalline aggregates on annealing, then we need to understand what is happening in terms of the morphology on annealing and why does it happen to compound **8** and not **7** i.e. what makes compound **7** different from compound **8**?

The only difference between compound **7** and **8** is the chemical structure; compound **8** has **7** thiophene units along each arm, whilst compound **7** has 5. To understand why we observe improved device performance on annealing, films similar to those used in the device fabrication, containing compound **8** with $PC_{71}BM$ at a donor-acceptor ratio of 1:1 were deposited onto fused silica substrates and annealed at 90, 110 and 130 °C. The morphology was investigated using tapping mode atomic force microscopy (AFM). The blends, annealed at 90, 110 and 130 °C are shown in Figures 8.25, 8.26 and 8.27, respectively.

The results provide some insight into how the morphology differs at different annealing temperatures. The phase contrast decreases with increasing temperature. In addition, the structures appear to decrease in size with increasing annealing temperature. As it is well-known that PCBM based acceptors aggregate on annealing [64, 65], we can assume that the dark regions within the AFM images correspond to compound **8**. Therefore, it would appear that by annealing the devices we are improving the distribution of the donor within the blend. This is consistent with the device results, as we observe a larger Voc, Jsc and fill factor with annealing at the same donor-acceptor concentration.

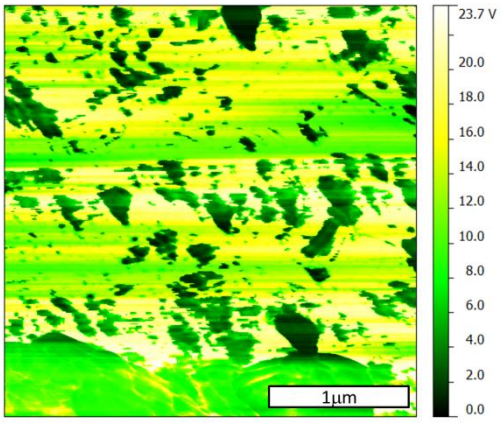

Figure 8.25 *Phase measurement from an AFM (tapping mode) of compound* ***8*** *with $PC_{71}BM$ at a ratio of 1:1 post annealing at 90 °C for 20 minutes.*

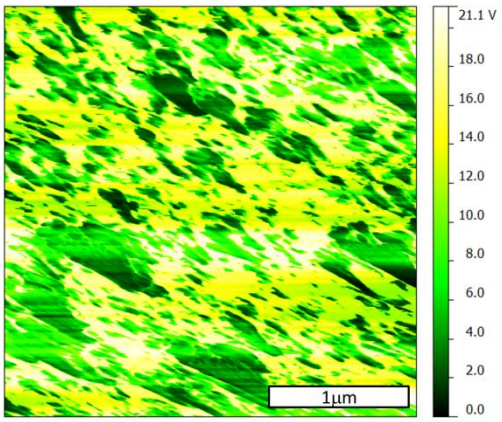

Figure 8.26 *Phase measurement from an AFM (tapping mode) of compound* ***8*** *with $PC_{71}BM$ at a ratio of 1:1 post annealing at 110 °C for 20 minutes.*

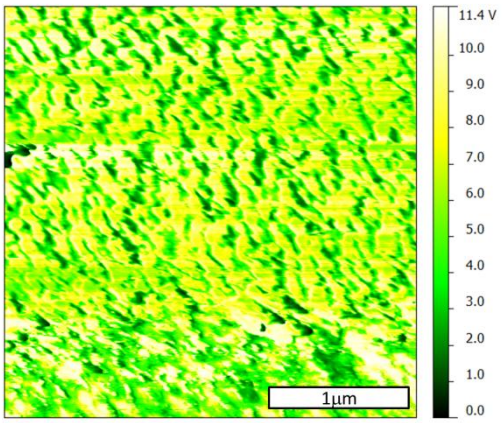

Figure 8.27 *Phase measurement from an AFM (tapping mode) of compound* ***8*** *with $PC_{71}BM$ at a ratio of 1:1 post annealing at 130 °C for 20 minutes.*

The next stage in the optimisation investigated the donor-acceptor ratio. The solubility of compounds **7** and **8** within the BHJ suggested that a donor-acceptor ratio where the concentration of the donor is less than the acceptor is necessary to achieve good film quality. Furthermore, if the acceptor is largely contributing to the photocurrent, then increasing the concentration of the acceptor may improve the Jsc. Therefore, **7**:$PC_{71}BM$ and **8**:$PC_{71}BM$ devices at ratios 1:2, 1:4, 1:6 and 1:8 were fabricated and characterised. **7**:$PC_{71}BM$ and **8**:$PC_{71}BM$ devices were annealed at 120 °C for 20 minutes before characterisation. The justification for annealing, and my choice of acceptor, was a consequence of having achieved efficient OPVs with **8**:$PC_{71}BM$. Previous studies showed that annealing compound **7** straight to 120 °C results in the formation of crystalline structures and that these structures are unfavourable for charge transport and device performance. This phenomenon is believed to be responsible for the poor performing **7**:$PC_{71}BM$ annealed OPV. Nevertheless, for a direct comparison between **7**:$PC_{71}BM$ and **8**:$PC_{71}BM$ devices, it was necessary to follow the same fabrication procedure for devices fabricated with **7** and **8**, and as the most efficient devices were the annealed **8**:$PC_{71}BM$ devices, the same fabrication procedure was repeated for all the devices in the donor-acceptor optimisation. Furthermore, if the crystalline structures are limiting the performance of devices with compound **7**, then decreasing the concentration of the donor in the blend would likely result in improved device performance.

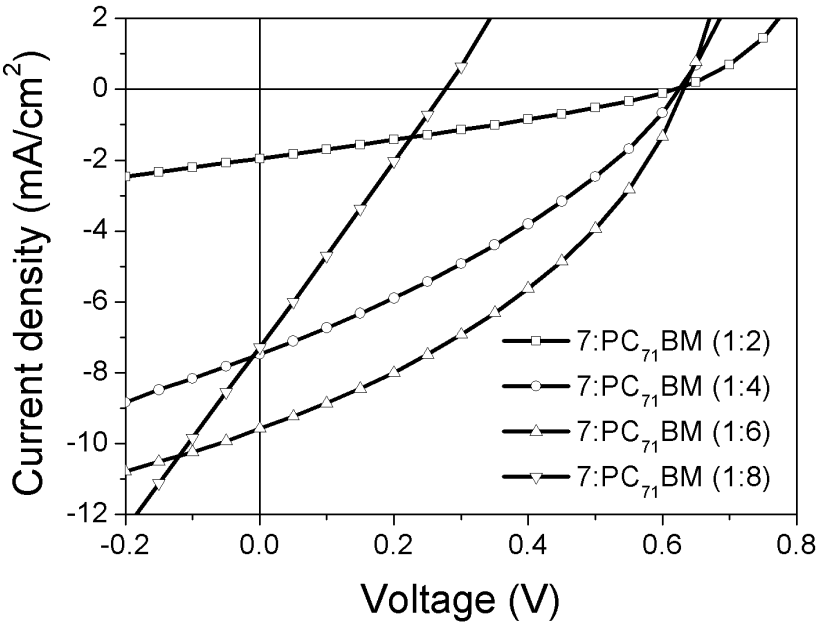

Figure 8.28 *J-V characteristics of* ***7****:$PC_{71}BM$ for different donor acceptor ratios.*

The J-V characteristics in Figure 8.28 show the donor-acceptor optimisation for devices fabricated with compound **7**. Comparing **7**:$PC_{71}BM$ (1:1) in Figure 8.22 with **7**:$PC_{71}BM$ (1:2) in Figure 8.28, we see an improvement in the performance going from a ratio of 1:1 to 1:2. For 1:1 the Jsc, Voc, fill factor and PCE were 0.68 mA cm^{-2}, 0.44 V, 27 % and 0.08 %, respectively. Whilst, for 1:2 a Jsc of 1.95, Voc of 0.62 V and a fill factor of 29 % was achieved, resulting in a PCE of 0.35 %. The PCE of the 1:2 is more than four times greater than the 1:1. It is worth mentioning that the donor-acceptor ratio is not the only variable altered going from 1:1 to 1:2, as the devices shown in Figure 8.28 contain additive carbon disulfide.

Increasing the concentration of the acceptor to a donor-acceptor ratio of 1:4, a large improvement in performance is observed. For 1:4 a Jsc, Voc, fill factor and PCE of 7.48 mA cm^{-2}, 0.62 V, 33 % and 1.53 % was achieved, respectively. Again, greater than a four-fold increase in PCE was observed. These large increases in PCE are mainly the result of improved short-circuit current densities (Jsc). It is reasonable to assume that by increasing the concentration of the acceptor and decreasing the concentration of the donor we are limiting compound **7**'s ability to form crystalline structures and improving the light absorption. The most efficient OPV for compound **7** was achieved with a donor-acceptor ratio of 1:6. Here, a Jsc of 9.57 mA cm^{-2}, Voc of 0.63 V, fill factor of 37 % and a PCE of 2.25 % was ascertained. Comparing this result with the aforementioned results we see that the increase in PCE is largely due to the improvement in the Jsc and fill factor. Further increasing the concentration of the acceptor to a donor-acceptor ratio of 1:8 we observe a dramatic decrease in the Voc, fill factor and PCE of 0.28 V, 25 % and 0.5 %, respectively, whilst the Jsc has decreased to 7.28 mA cm^{-2}.

The distribution of the donor and acceptor within the BHJ plays an important role in the Voc, as it is at the donor-acceptor interface where almost all charge carrier separation (exciton dissociation) and recombination occurs. Hence, the Voc is largely governed by the difference between the HOMO of the donor and the LUMO of the acceptor [85]. Therefore, considering the results of Figure 8.22 we see that on annealing a **7**:$PC_{71}BM$ device the Voc goes from 0.75 V to 0.44 V. It is reasonable to assume that annealing results in the formation of crystalline structures and that these structures are increasing recombination at the donor-acceptor interface. With the use of carbon disulphide and by means of reducing the concentration it has been possible to improve the Voc on annealing, allowing us to fabricate an efficient OPV. Increasing the Voc by reducing the donor-acceptor interfacial area is not new and was first established by Koen Vandewal et al [86]. A similar effect is observed in the OPV with a donor acceptor ratio of 1:8. Here, with the device that has the largest acceptor

concentration, the Voc is 0.28 V, which is low compared to the 0.63 V for the device with a donor-acceptor ratio of 1:6. The donor-acceptor optimisation for devices fabricated with compound **8** is shown in Figure 8.29. The solubility of compound **8** made device fabrication and reproducibility challenging.

It is important to consider conformation when comparing molecules. For this reason we selected a TTF bridged compound, compound 6 shown in Figure 8.2, for comparison with **8**. Here, the effective conjugation length is already reached (one terminal thiophene in each chain is twisted out of co-planarity with the rest of the oligomer chain) [49]. It is possible that compound **8** is similar. There is little change in performance for devices fabricated at 1:2 and 1:4. These devices are comparable to the 1:1 device in Figure 8.22 and have a lower PCE than those devices annealed to 110 and 130 °C, shown in Figure 8.23. It is unclear why the performance of these devices is low in comparison i.e. what is responsible for the decrease in the Voc and Jsc. The results for 1:6 and 1:8 are more reliable. The Jsc, Voc and fill factor for the 1:6 was 8.82 mA cm^{-2}, 0.51 V and 39 %, respectively, resulting in a PCE of 1.76 %. A similar Voc of 0.51 V was observed for 1:8 with a slightly lower fill factor of 34 % and PCE of 0.72 %. The low PCE for 1:8 is the result of a Jsc of 4.18 mA cm^{-2}. The results from the optimisation indicated that for efficient OPVs, devices of **7**:$PC_{71}BM$ and **8**:$PC_{71}BM$ should be fabricated at a D-A ratio of 1:6. Therefore, a ratio of 1:6 was used in subsequent studies.

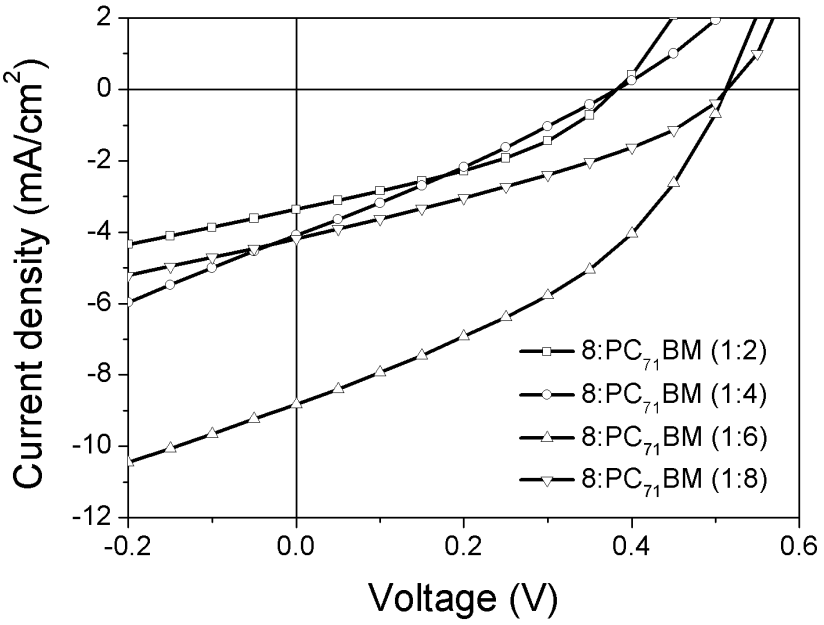

Figure 8.29 *J-V characteristics of* ***8****:$PC_{71}BM$ for different donor acceptor ratios.*

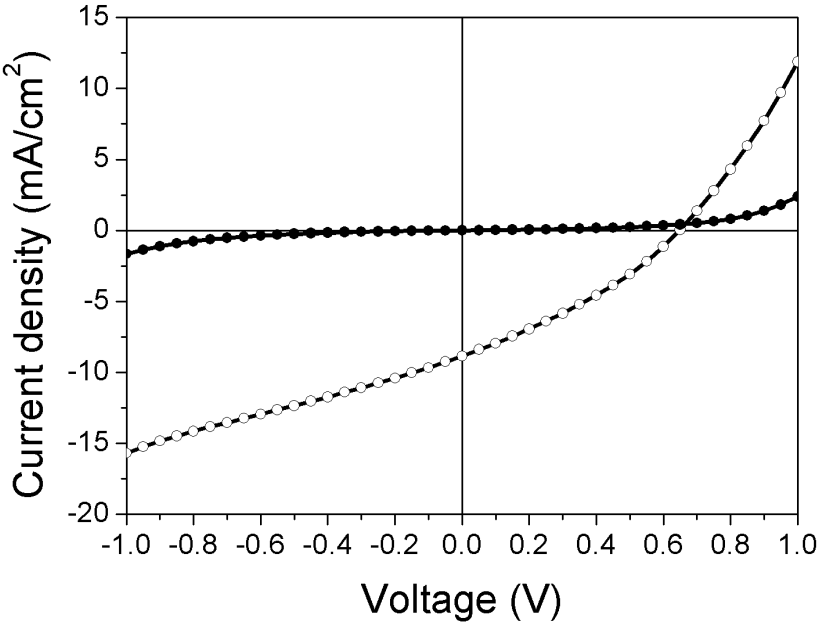

Figure 8.30 *J-V characteristics of* ***7****:$PC_{71}BM$ at a ratio of 1:6 with an aluminium back electrode.*

Another factor that can limit the efficiency of an organic solar cell is the cathode-polymer interface [68]. This can be assessed by means of looking at the dark current. With an aluminium top electrode we see significant current leakage, shown in Figure 8.30. Here, we have poor rectification due to a non-Ohmic contact at the cathode-polymer interface. As a result, the shunt resistance (Rsh) is low. Hence, the Voc decreases with increasing current. To obtain a high Rsh we need to reduce the leakage current across the device. To do this, it is necessary to find an alternative top electrode. Organic solar cells have been successfully fabricated with a plethora of metal contacts, for example Al, Ag, Au, Pd [87] etc. or combinations, for example LiF/Al, Ca/Al, Ba/Al [88] etc. In addition, buffers which act as electron transporting (hole blocking) or hole transporting (electron blocking) layers have been explored with great success [62, 89-91]. To determine a suitable top electrode for our devices, it is necessary to understand how we can achieve an Ohmic contact at the cathode-polymer interface. When materials like compound **7** and the top electrode, aluminium, are brought together, there is an equalization of the chemical potential, i.e. the Fermi level. At this interface, we can either have a Schottky (rectifying) or an Ohmic (non-rectifying) contact. The work-function of each material plays an important role in determining the type of contact we attain.

For an n-type semiconductor, for example $PC_{71}BM$, in order to achieve an Ohmic contact, i.e. an accumulation layer within the semiconductor with no barriers to the flow of electrons. It is necessary for the work-function of the metal, Φm, to be less than the work-function of the semiconductor, Φs, i.e. Φm less than Φs. If, as in our case Φm greater than Φs, then we have a Schottky (rectifying) contact due to the formation of a depletion layer within the semiconductor. This barrier prevents electron flow and is caused by the electrons diffusing from the semiconductor to the metal on contact, due to the material carrier density mismatch. Therefore, to achieve an Ohmic contact a low work-function metal is required such that Φm less than Φs. Hence, subsequent devices were fabricated with a Ca/Al back electrode, Figure 8.31 and 8.32. For organic solar cells where the contacts are non-Ohmic the Voc is determined by the work-function difference of the electrodes. Whilst, for Ohmic contacts the Voc has been shown to be proportional to the difference between the HOMO of the donor and the LUMO of the acceptor [85]. The HOMO of the donor for compound **7** from the electrochemistry is -5.00 eV. For $PC_{71}BM$ the LUMO is typically between -3.7 and -4.3 eV [92-94]. Therefore, in the best case scenario the maximum theoretical Voc is ~1.3 V. However, we can lose ~ 0.2 V at each electrode [85]. Hence, a theoretical Voc of ~0.9 V is attainable and achieved in Figure 8.31.

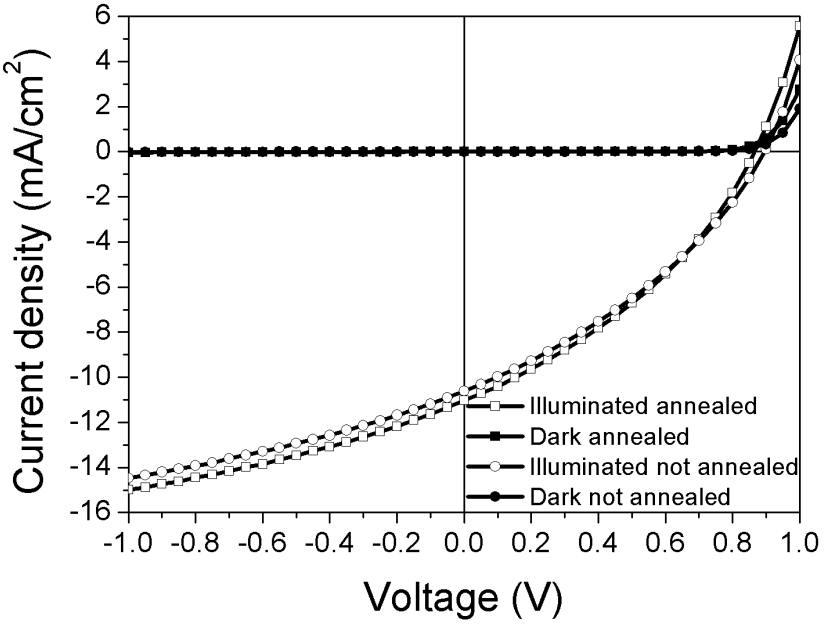

Figure 8.31 *J-V characteristics of* ***7****:$PC_{71}BM$ (1:6) with a calcium/aluminium back electrode.*

The J-V characteristics in Figure 8.31 show for a calcium/aluminium top electrode an Ohmic (non-rectifying) contact. At a glance it is apparent that the dark currents shown in Figure 8.31 have a higher shunt resistance (Rsh) than that shown in Figure 8.30.

The shunt resistance (Rsh) was calculated for each device following the standard convention, i.e. taking the reciprocal of the dark current at V=0 [95]. In doing so, we determine for an annealed **7**:$PC_{71}BM$ device with an aluminium top electrode a shunt resistance (RshA) of ~4.5 kΩ cm^2, Figure 8.46 of the appendix. Whilst, for an annealed and not annealed device with a calcium/aluminium top electrode, we determine a shunt resistance (RshA) of ~76 kΩ cm^2 and ~147.3 kΩ cm^2, respectively, shown in Figure 8.47 and 8.48 of the appendix. These values are typical for organic solar cells; however, it is surprising that we observe a decrease in Rsh on annealing, as previous reports document an increase in Rsh with annealing [63], the implications of which are that we have more charge recombination and current leakage on annealing.

This result is in good agreement with previous observations of compound **7** forming crystallised structures when annealed straight to 120 °C. However, as the concentration of the donor within the blend in these devices is only ~14 % of the active layer, serious implications on device performance are mitigated. Hence, on annealing we observe a slightly lower Voc of 0.86 V compared to 0.90 V. These open-circuit voltages (Voc) are large when compared to those obtained from devices with only an aluminium top electrode. The largest Voc achieved thus far with a **7**:$PC_{71}BM$ (1:6) device with an aluminium top electrode being 0.65 V. The short circuit current densities are slightly larger with a calcium/aluminium top electrode than those obtained with only an aluminium top electrode. With a calcium/aluminium top electrode we measured for the not annealed and annealed device a Jsc of 10.62 mA cm^{-2} and 11.04 mA cm^{-2}, respectively. The large open-circuit voltages (Voc) of 0.90 and 0.86 V are responsible for the large PCEs of 3.36 and 3.35 %, for the not annealed and annealed device, respectively, as the fill factor for both devices was 35 %.

The effect of metal electrodes on the performance of organic solar cells has been well-studied [93, 96-98]. An increase in PCE attributed to an increase in the Voc, resulting from the deposition of a low work function metal in combination with aluminium for an Ohmic contact, has been observed with lithium fluoride/aluminium [85, 87]. Here, they observe a similar increase in the Jsc with the Voc increasing from 0.674 to 0.902 V with approximately no change in the fill factor. Therefore, by depositing a thin layer of calcium (20 nm) pre aluminium deposition we achieve a low leakage current, a larger shunt resistance (Rsh) and efficient devices.

Figure 8.32 shows J-V characteristics for **8**:$PC_{71}BM$ devices with a calcium/aluminium top electrode. The dark currents for annealed and not annealed devices show we have an Ohmic (non-rectifying) contact. As in our previous measurements we observe on annealing improved performance. For the device not annealed we measure a Jsc, Voc and fill factor of 7.16 mA cm^{-2}, 0.38 V and 32 %, respectively. This results in a PCE of 0.87 %. For the device annealed straight to 120 °C for 20 minutes we attain a Jsc of 10.27 mA cm^{-2}, Voc of 0.56 V and fill factor of 37 %, which results in a PCE of 2.1 %. The improvement in performance on annealing is largely a result of an increase in Voc and Jsc. Previous device measurements with an aluminium top electrode showed that we can obtain higher fill factors by annealing to greater temperatures. For 90, 110 and 130 °C we obtained fill factors of 34, 37 and 41 %, respectively. It is interesting to observe a similar trend with devices with a calcium aluminium top electrode. As there is strong evidence suggesting that thermal annealing induces a better contact between the blend and the aluminium, which reduces recombination, resulting in higher fill factors and improved Jsc [63]. However, we observe a similar response for devices with aluminium as calcium/aluminium, although devices with calcium/aluminium were annealed before electrode deposition, whilst, devices with aluminium were annealed post electrode deposition. For the device not annealed we have a fill factor of 32 %. On annealing to 120 °C for 20 minutes the fill factor is 37 %. Annealing to 130 °C we attain a fill factor of 45 %, shown in Figure 8.33.

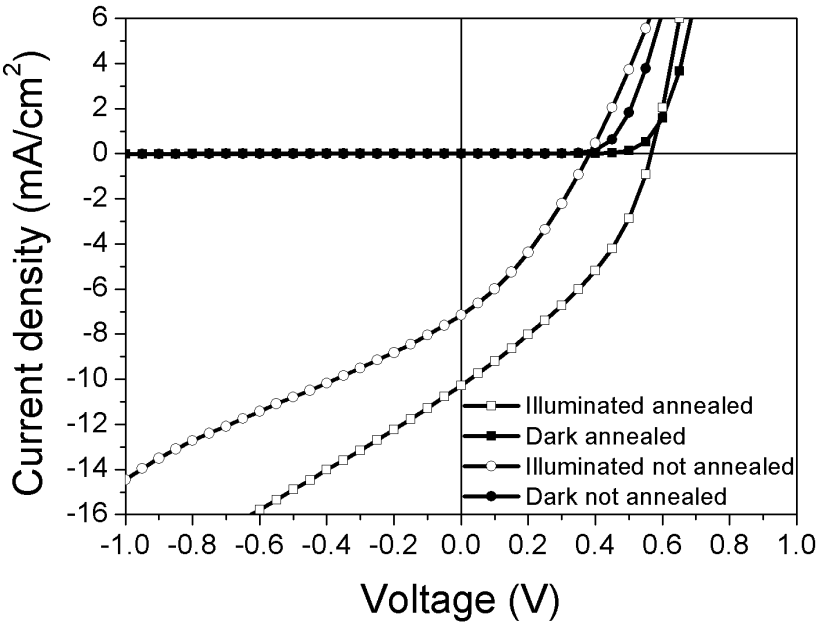

Figure 8.32 *J-V characteristics of* ***8****:$PC_{71}BM$ (1:6) with a calcium/aluminium back electrode.*

8.5.3 Characterisation

In earlier chapters, I investigated photovoltaic cells where the spectral response of the reference cell was similar to that of our test cells. In addition, the active layer of our tests cells absorbed strongly in the visible. Hence, it was not necessary to calculate and apply a spectral mismatch correction factor to our data. This was confirmed by means of calculating the short-circuit current density (Jsc) from the EQE spectra which was obtained through IPCE and compared with the Jsc measured under the AM 1.5 G solar simulator at 100 mW cm^{-2}. However, for our **7**:$PC_{71}BM$ and **7**:$PC_{71}BM$ devices the active layer absorbs strongly in a region where the spectral irradiance of our solar simulator deviates from AM 1.5 G. It is well-known that it is difficult and costly to obtain a solar simulator that can closely follow AM 1.5 G for a broad spectral range [57, 99]. For this reason when purchasing a solar simulator it is necessary to consider the photovoltaic cells to be tested. The percentage deviation of our solar simulator with AM 1.5 G was determined to be 24.1 % from 400 to 500 nm. This large deviation resulted in a discrepancy between the Jsc calculated from the EQE and the Jsc measured under the solar simulator. To correct the spectral error, a spectral mismatch correction factor was calculated and applied to the optimal **7**:$PC_{71}BM$ and **8**:$PC_{71}BM$ devices. The J-V characteristics for the raw and corrected datasets are shown in Figure 8.33.

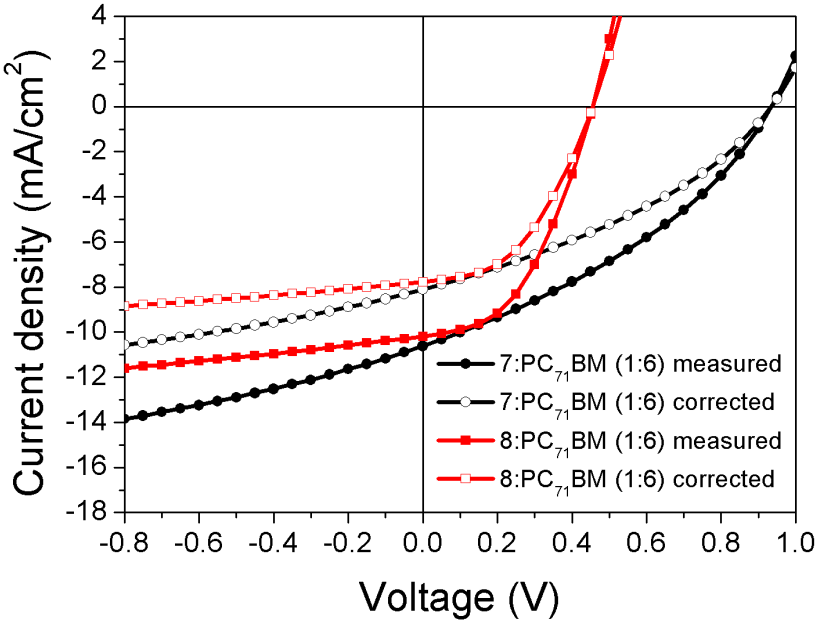

Figure 8.33 *J-V characteristics of* ***7****:$PC_{71}BM$ (1:6) and* ***8****:$PC_{71}BM$ (1:6) with a calcium/aluminium back electrode.*

The devices selected as optimal include: the not annealed **7**:$PC_{71}BM$ (1:6) device and the **8**:$PC_{71}BM$ (1:6) device annealed to 130 °C for 20 minutes. The reason for selecting the **8**:$PC_{71}BM$ (1:6) device annealed to 130 °C, was due to the relatively large fill factor for a small molecule OPV [6, 39] of 45 %. Comparing the result in Figure 8.33 to Figure 8.32, it is obvious that the device annealed to 130 °C is a better device, even though both devices exhibit a PCE of 2.1 %.

The spectral mismatch correction factor, M, was calculated as 1.31 for **7**:$PC_{71}BM$ and **8**:$PC_{71}BM$, as they both show a similar spectral response, shown in Figure 8.34. This is not surprising as in both cases the active layer consists of ~86 % $PC_{71}BM$. The light intensity was measured using a calibrated thermopile (Coherent model LM-1) with a quantum efficiency of unity. Hence, the only consideration other than the calculated and measured Jsc was the deviation between the source and reference spectrum. This value may appear large, but if you consider a photovoltaic device with a similar spectral response to that of our devices, MEH-PPV:PCBM (1:4), where the light intensity has been calibrated with a thermal detector, the spectral mismatch factor is 1.35 [99]. The corrected performance statistics for the devices shown in Figure 8.33 are depicted in table 8.1. The application of a spectral mismatch factor does not change the value of the Voc and fill factor. The correction is applied to the Jsc and hence alters the PCE. For the **7**:$PC_{71}BM$ device the Jsc is 10.61 mA cm^{-2}, after the correction the Jsc is 8.10 mA cm^{-2}. This change in Jsc results in the PCE going from 3.36 to 2.66 %. With the **8**:$PC_{71}BM$ device the Jsc changes from 10.19 to 7.78 mA cm^{-2} with the application of the correction factor, resulting in a PCE change from 2.10 to 1.60 %. If we compare these results with that of P3HT:PCBM, we see that for **7**:$PC_{71}BM$ we have managed to fabricate a device with a similar PCE to that of P3HT:PCBM, PCE=2.53 %, shown in Figure 8.43 of the appendix. All the performance statistics for the optimisation of **7**:$PC_{71}BM$ and **8**:$PC_{71}BM$ devices can be found in Table 8.2 of the appendix.

Table 8.1 *Performance statistics for polymer and polymer-fullerene devices under illumination at 100 mW cm^{-2} with an AM1.5 G source.*

Active layer	**Jsc [mA/cm^2]**	**Voc [V]**	**FF [%]**	**PCE [%]**
7:$PC_{71}BM$ (1:6)	8.10	0.93	35	2.66
8:$PC_{71}BM$ (1:6)	7.78	0.46	45	1.60

The EQE spectra obtained from the IPCE for the not annealed **7**:$PC_{71}BM$ (1:6) and annealed straight to 130 °C for 20 minutes **8**:$PC_{71}BM$ (1:6) device are shown in Figure 8.34. As previously mentioned, the EQE spectra for **7**:$PC_{71}BM$ (1:6) and **8**:$PC_{71}BM$ (1:6) are similar, as the active layers for both OPVs, i.e. the absorbing layers, are ~86 % $PC_{71}BM$. We observe a red-shift of the peak at ~450 nm of ~30 nm in the EQE spectra going from the **7**:$PC_{71}BM$ (1:6) to the **8**:$PC_{71}BM$ (1:6) device. This red-shift is to be expected as compound **8** has two additional thiophenes on each arm (Figure 8.2) compared to compound **7**, resulting in a bathochromic shift. This is evident in Figure 8.5, where we see in the solid state neat films, peaks at 446 and 476 nm for compound **7** and **8**, respectively. These peaks are also observed in the solid state absorption of the blend at a donor acceptor ratio of 1:6, shown in Figure 8.35. However, the peaks are further red-shifted as these films were annealed straight to 120 °C for 20 minutes before being measured. The subtle peaks observed in the EQE spectra are at similar wavelengths to those observed in the absorption measurements and hence, it is reasonable to suggest that compounds **7** and **8** are contributing to the overall photocurrent of the devices. However, as the absorption onsets for compound **7** and **8** are 550 and 610 nm, respectively, and the fact that ~86 % of the active layer is $PC_{71}BM$, it is unmistakable that the acceptor is largely responsible for the photovoltaic response seen in these devices. This is an exciting result as the charge transport properties of our small molecule have facilitated in the fabrication of OPVs with an active layer consisting of ~86 % acceptor that are as efficient as OPVs fabricated with P3HT:PCBM, shown in Figure 8.43 of the appendix, with a Voc that is greater than 60 % that of P3HT:PCBM. The EQEs are impressive and similar in magnitude to that of P3HT:PCBM [65, 75, 100, 101]. Unfortunately, the EQE spectra are not as broad as that of P3HT:PCBM and is blue shifted, which is not ideal for absorption of the solar spectrum [99]. However, this can be advantageous in the fabrication of tandem cells, where subsequent modules absorb light in the region where the OPV is redundant. Alternatively, as we have demonstrated the effectiveness of $PC_{71}BM$ as an OPV material, replacing compound **7** with a material that exhibits similar charge transport properties with broad absorption i.e. absorbing in the region where $PC_{71}BM$ is ineffective, may lead to devices with enhanced power conversion efficiency. An excellent example of this was recently reported by Guodan Wei et al, where by means of fabricating devices containing Squaraine in combination with $PC_{71}BM$ at a donor acceptor ratio of 1:6, they managed to achieve PCEs of greater than 5.0 %. [102].

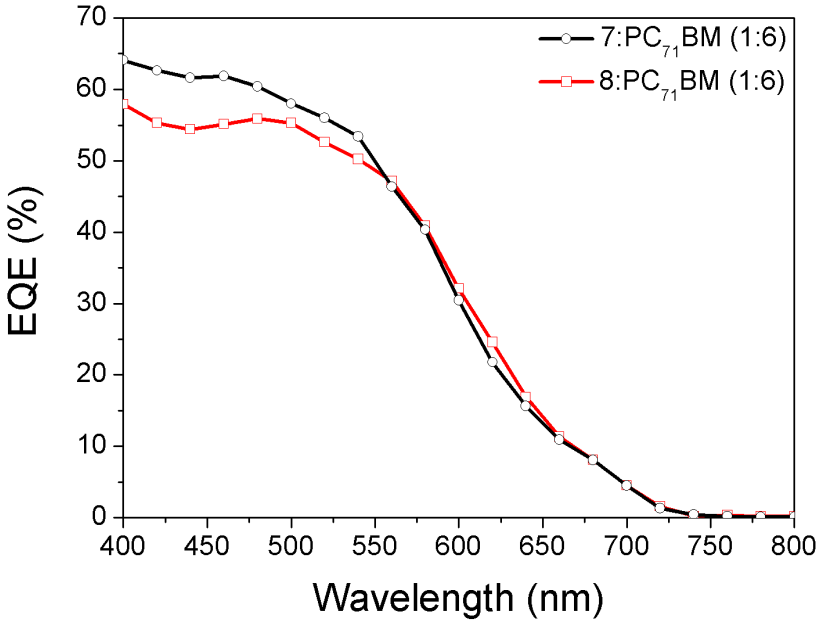

Figure 8.34 *Incident photon to converted electron (IPCE) ratio for not annealed* ***7****:$PC_{71}BM$ (1:6) and annealed* ***8****:$PC_{71}BM$ (1:6) with a calcium/aluminium back electrode.*

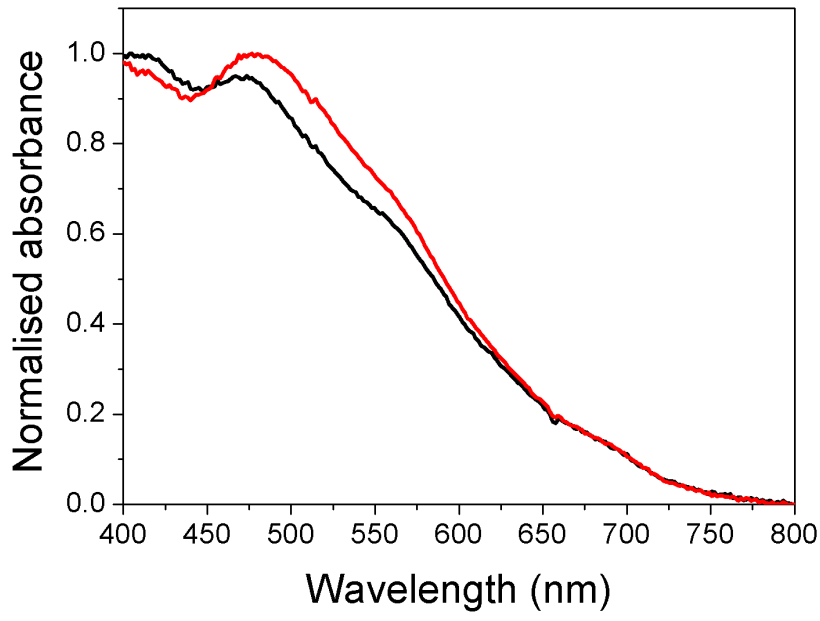

Figure 8.35 *Absorption spectra for* ***7****:$PC_{71}BM$ (1:6) and* ***8****:$PC_{71}BM$ (1:6) deposited on fused silica substrates and annealed at 120 °C.*

8.6 Time-resolved photophysics

The OPV devices reported by Guodan Wei et al. are very impressive. However, in order to achieve these extremely efficient devices it was necessary to carefully control the phase separation of the blend. This was achieved with solvent-assisted annealing in combination with monitoring the change in morphology with advanced morphological probing techniques, for example X-ray diffraction (XRD) and transmission electron microscopy (TEM) etc. Through gaining control of the morphology and by optimising the molecular ordering of the blend they ensured efficient exciton dissociation and low resistance charge transport by way of maximising the interface between the donor and acceptor, and maintaining sufficiently large charge transport pathways, respectively [102]. These results do not diminish those obtained with compound **7**; on the contrary, they are inspiring, as we have achieved PCEs similar to those of P3HT:PCBM without the need for post deposition thermal annealing techniques, required by both SQ:$PC_{71}BM$ and P3HT:PCBM. It is unfortunate that in our attempt to red-shift the absorption spectrum, by inclusion of additional thiophenes, for broad solar absorption we have inadvertently damaged the quality of our films with the deposition of large aggregates of compound **8**, shown in Figure 8.44 of the appendix.

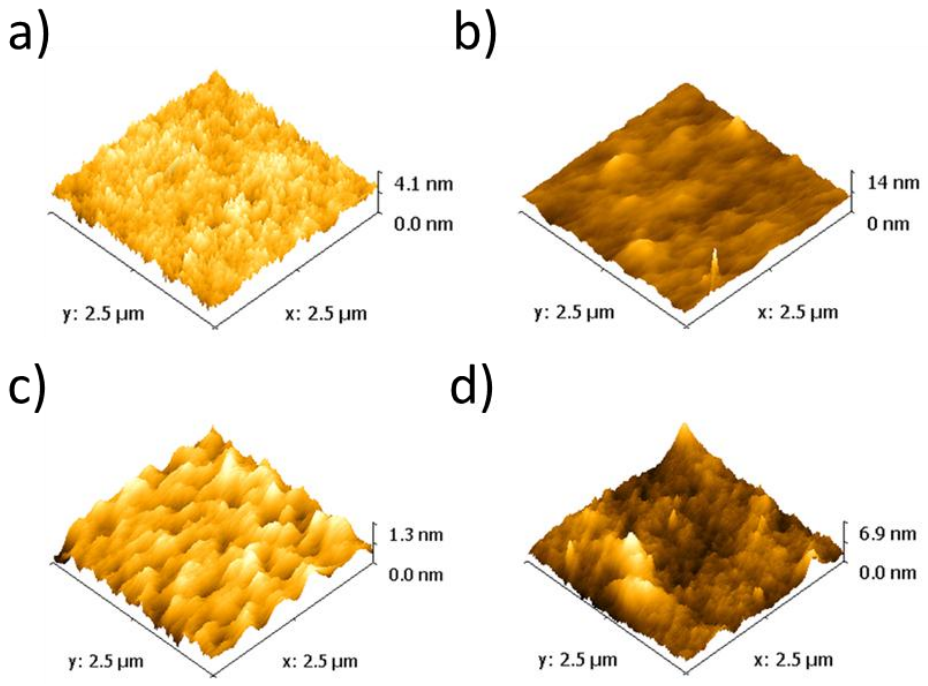

Figure 8.36 *Tapping mode AFM for* ***7****:$PC_{71}BM$ (1:6) not annealed (a) and annealed (b), and* ***8****:$PC_{71}BM$ (1:6) not annealed (c) and annealed (d).*

These aggregates are detrimental to device performance as they act as recombination centres [55, 64-67, 103]. For this reason when we compare our optimal devices, we observe for the device fabricated with compound **8** a PCE that is 1 % lower than that achieved with the device fabricated with compound **7**. Nevertheless, as shown in the results reported by Guodan Wei et al., there is nothing wrong with our methodology. However, instead of trying to improve the absorption by extending the conjugation length in future studies it may be worth including benzothiadiazole (BT) units into compound **7**. These units appear to facilitate absorption via intramolecular D-A charge transfer and have good solubility in common solvents [104]. The tapping mode AFM images shown in Figure 8.36 are of annealed and not annealed films containing **7**:$PC_{71}BM$ or **8**:$PC_{71}BM$ at a donor acceptor ratio of 1:6. These images have been plotted with a colour scale going from black to weight for the minimum and maximum height, respectively. Comparing the not annealed films for **7**:$PC_{71}BM$ and **8**:$PC_{71}BM$, Figure 8.36 (a) and (b), respectively. We observe for **7**:$PC_{71}BM$ a large number of small peaks with a maximum height of 4.1. For **8**:$PC_{71}BM$ we observe a comparatively small number of peaks that are stretched in the direction parallel to the film. The maximum height for these peaks is 1.3 nm. The difference in morphology between these two films is likely due to solubility. The wide-field images shown in Figure 8.44 of the appendix show the difference in solubility between compound **7** and **8** in the solid state.

Hence, we observe more structure in the AFM for compound **7** than **8**, as compound **7** is more soluble than **8**. On annealing, we observe something very interesting. For **7**:$PC_{71}BM$, the film appears to be smooth with the exception of a large aggregate of height 14 nm, it is possible that on annealing diffusion has resulted in the formation of a crystallite, as previously observed in films solely containing compound **7** [53], the formation of which is not uncommon in blends when subjected to post deposition thermal annealing [64, 65, 67]. For **8**:$PC_{71}BM$, the film is no longer smooth. Instead there are large aggregates with a maximum height of 6.9 nm, and the smaller peaks appear to be similar to those observed for the not annealed **7**:$PC_{71}BM$ film. This is consistent with early observations of compound **8** attained by AFM. The AFM and wide-field images provide insight into the difference in the way compound **7** and **8** respond on annealing and how this is related to device performance. It is worth mentioning the AFM images are notoriously difficult to interpret and here we can only postulate. To try and get a better understanding of how effective our materials are within the blend for applications in OPV, critical processes essential to device performance were investigated with time-resolved photoluminescence (PL) measurements. Time-resolved PL measurements have

been shown to be an extremely useful tool for probing the fundamental mechanisms that govern optoelectronic device operation [76, 105, 106]. In terms of organic solar cells, time-resolved measurements have been used to determine the exciton diffusion length (L_D) by means of surface quenching [70] and volume quenching [76]. In addition, the exciton dissociation efficiency has been valuable in improving our understanding of how state of the art organic solar cells operate [69]. The PL decays can provide us with invaluable knowledge of how efficiently a molecule dissipates excess energy or how quickly non-radiative deactivation pathways remove excitons. Here, PL measurements have been measured using a streak camera to help us understand why, at a donor acceptor ratio of 1:6; our OPVs are so efficient, with power conversion efficiencies of 2.66 and 1.60 %, for compounds **7** and **8**, respectively. For purposes of comparison it was necessary to extract values from our data. To do this it was necessary to fit our data with exponential decays. The PL decays, with fits are shown in the appendix, Figure 8.49 to 8.53. The data without the fits are shown in Figures 8.37 to 8.40. The reasoning behind the measurement was to evaluate the acceptor's ability to quench the photoluminescence of the donor and vice versa, and in doing so to be able to provide further evidence as to why we observe different PCEs for devices fabricated with compound **7** and **8**. The decays obtained for films consisting solely of compound **7** or **8** are shown in Figure 8.37 and 8.38, respectively.

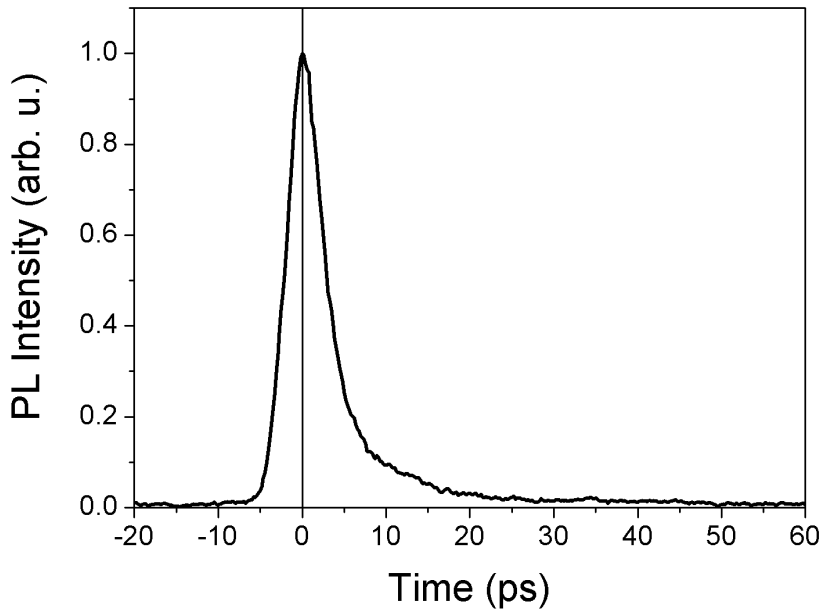

Figure 8.37 *The PL decay of* ***7*** *in film.*

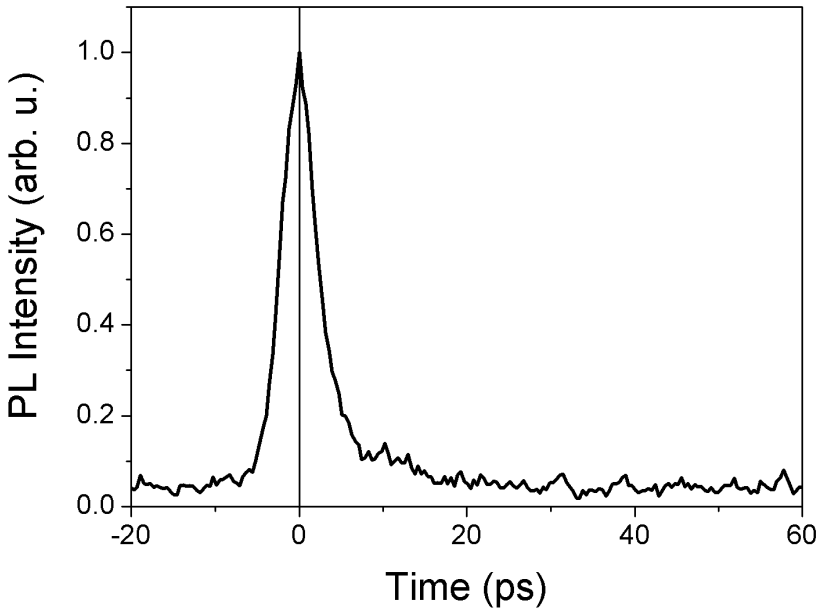

Figure 8.38 *The PL decay of* ***8*** *in film.*

The fits show for compound **7** an instrument limited lifetime of less than 2 ps (90 %) and a slightly larger non-instrument limited lifetime of **7** ps (10 %). A similar result was observed for compound **8**, an instrument limited lifetime of less than 2 % (97 %) with a larger 13 ps (3 %) lifetime. Unfortunately, the ultrafast decay of compound **7** and **8** make monitoring the PL decay of the donor when blended with the acceptor, $PC_{71}BM$, impossible with this technique. However, the PL decay for the aforementioned acceptor was promising in this regard, shown in Figure 8.39. Here, we observe two comparably long lifetimes of 130 ps (40 %) and 430 ps (60 %), Figure 8.51. The longer lifetimes observed with $PC_{71}BM$ enable us to see just how effective our small molecules are at quenching the PL of the acceptor. As the optimal blends contain ~14 % small molecule combined with the observation of aggregates, one may perceive that for compound **8** quenching of the acceptor's PL would be less efficient than with compound **7**, owing to the small molecule not being suitably distributed throughout the film. However, in practice, using the same experimental procedure employed to achieve the optimal OPVs, we observe very different results, shown in Figure 8.40. For the blend containing compound **7** we have fitted a tri-exponential decay, shown in Figure 8.52 of the appendix, and observe an instrumented limited lifetime of less than 2 ps (51 %) and two additional lifetimes of 17 ps (47 %) and greater to or equal than 200

ps (2 %). With compound **8**, a bi-exponential was fitted to the decay, Figure 8.53 of the appendix. Here we observe an instrument limited response of less than 2 ps (83 %) and a longer lifetime of 12 ps (17 %). The signal to noise of the PL decays for the blends is not ideal. Hence, we should be careful when drawing conclusions from the results shown in Figure 8.40. However, the results show for films with ~14 % of either compound **7** or **8**, effective quenching of the acceptor's PL. Hence, it is reasonable to postulate as compound **7** and **8** are similar in their ability to quench, that the recombination processes brought about by having larger domains of compound **8** are responsible for the lower PCEs achieved with compound **8** when compared with **7**.

The J-V characteristics combined with wide-field and AFM images support this argument that the recombination centres are responsible for the low open-circuit voltages (Voc), which leads to the comparatively low operational performance for those devices fabricated with compound **8**. The Voc for the optimal device containing compound **8** is approximately half that obtained with compound **7**, even though both compounds have similar energy levels. On annealing, we observe improved distribution of the donor within the blend and a concomitant increase in Voc.

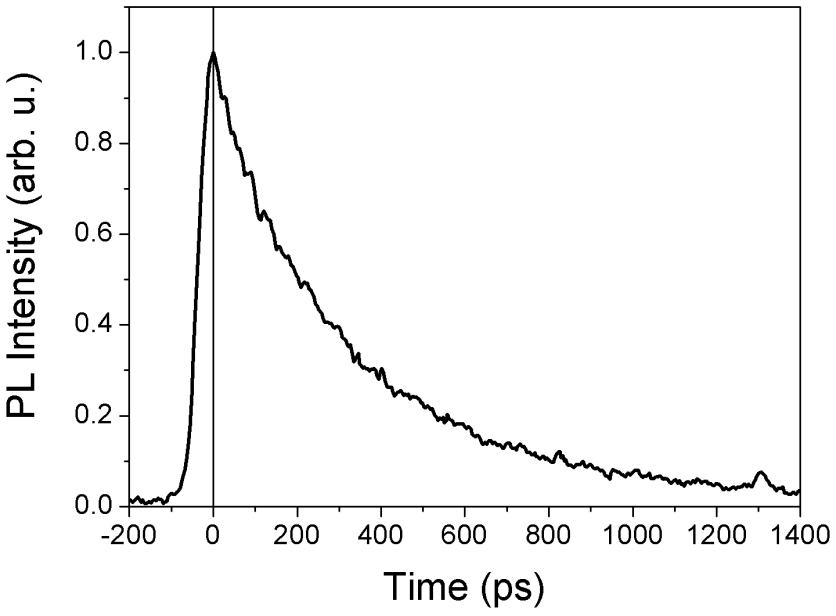

Figure 8.39 *The PL decay of $PC_{71}BM$ in film.*

Therefore, as it appears that we have reached the effective conjugation length limit with compound **8**, as reported with a similar compound that has a TTF bridge, compound 6 [49], to improve absorption of the solar spectrum a different methodology is required, such as incorporating units with some acceptor character into the backbone.

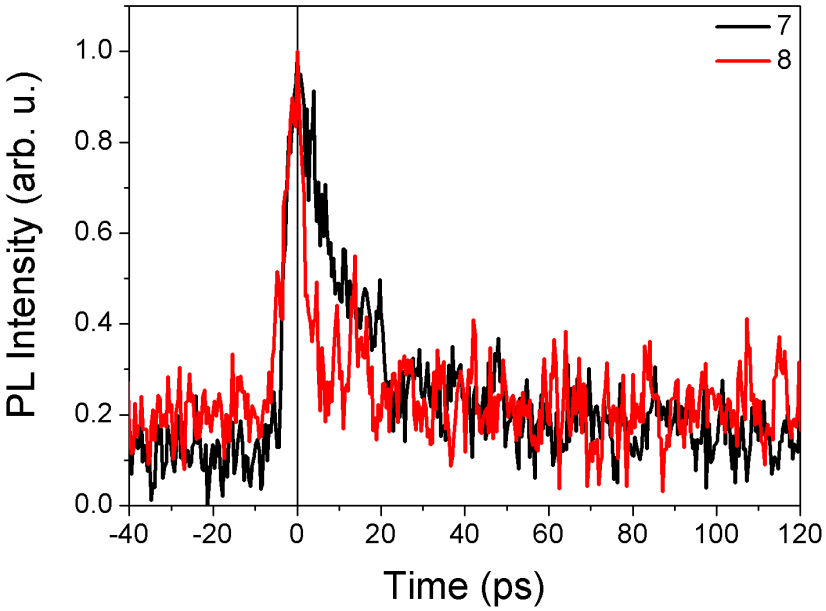

Figure 8.40 *The PL decay of* ***7*** *or* ***8*** *with* $PC_{71}BM$ *at a ratio of 1:6 in film.*

8.7 Conclusions

Small-molecules are attractive for organic solar cells as they have well-defined molecular structures and do not suffer from polydispersity. Hence, it is possible to synthesise with high purity and in good quantity semiconducting materials without batch to batch variations [5, 8, 104]. This, reproducibility, is an important requirement for commercialisation [107] and hence small molecule OPVs are a hot photovoltaic topic [8, 12, 19, 27, 39, 40]. However, only recently, have efficient solution-processable small molecule organic solar cells been realised [19, 26, 108], as small-molecule semiconducting materials typically favour deposition by means of thermal evaporation [39]. With the use of thermal evaporation and tandem architectures small molecules have facilitated OPVs with PCEs of 12 % [21, 109].

In this chapter, I introduced a solution-processable small molecule semiconducting material, compound **7**, with a Germanium-bridged spiro-centre and discussed the molecular, electrochemical and optical properties of the material. In addition, a small molecule similar to compound **7** with an extended conjugation length, compound **8**, was discussed. I demonstrated with the aid of TOF and OFET measurements compound **7**'s ability to pack in a way that is favourable for charge transport. The two-dimensional charge transporting nature of the material was shown to vary with annealing. The change in mobility with annealing was investigated with optical, electron and scanning probe microscopies, and shown to be concomitant with morphological changes. By controlling the morphology with the implementation of a well-defined annealing method it was possible to improve the device performance of OFETs and planar-heterojunction OPVs. Solution-processable bulk-heterojunction organic solar cells were fabricated, characterised and optimised with compound **7** and the slightly modified version of the material, compound **8**.

The mobility measurements obtained with the TOF technique show the mobility of compound **7** to be greater than several other compounds investigated. These mobility measurements are an order of magnitude higher than TOF mobilities reported for sexithiophene [50] and are the same order of magnitude as that reported for the well-studied conjugated polymer P3HT [51, 52], showing the advantage of the 2D structure.

The temperature dependent mobility of compound **7** was measured with two independent techniques, TOF and OFET. The measurement's provide further evidence of the two-dimensional stacking interactions, and demonstrates that these interactions facilitate charge transport in more than one direction. In both cases, TOF and OFET, where we measure the charge carrier mobility

perpendicular and parallel to the plane of the substrate, respectively, we observe an increase in the mobility by applying a specific annealing condition i.e. step-annealing. However, without the application of the aforementioned annealing condition i.e. when annealed straight to a given temperature greater than 100 °C, we observe the formation of large crystalline, branching fibrillar structures and show that these structures are detrimental to charge transport.

Organic solar cells with planar-heterojunction device architecture were fabricated with the same annealing conditions. The devices were measured with IPCE and the Jsc calculated. The results show how the change in the morphology, brought about by applying various annealing conditions, can influence the mobility and by extension OPV device performance. In addition, they highlight the importance of increasing the bulk dimensionality of organic semiconductors for improved device performance [48], which in our case is provided by the 3-D molecular architecture of compound **7** [5].

For efficient organic solar cells it was necessary to fabricate bulk-heterojunction organic solar cells [1, 2] with compound **7** and **8**. The optimal devices for compound **7** and **8** were fabricated with a donor acceptor ratio of 1:6. $PC_{71}BM$ was determined to be the appropriate acceptor. To prevent poor rectification, it was necessary to deposit a metal with a low work function, calcium, before deposition of the aluminium electrode. Not annealed and annealed devices containing compound **7** showed similar efficiencies. The optimal compound **7** device exhibited a PCE of 2.66 %, which was shown to be similar to that of devices fabricated with P3HT:PCBM. However, unlike P3HT:PCBM, our devices, fabricated with compound **7** do not require post deposition thermal annealing. To achieve efficient devices with compound **8**, it was necessary to anneal the devices to 130 °C. Unfortunately, extending the conjugation length resulted in poor solubility and an insufficient bathochromic shift to enhance the absorption. Hence, the PCE for the optimal OPV fabricated with compound **8** was 1.60 %.

In future studies, longer wavelength absorption is needed. This can be achieved by means of inclusion of benzothiadiazole (BT) units in an attempt to improve absorption of the solar spectrum, as extending the conjugation length has been shown to be ineffective. BT units have been shown to have good solubility in common organic solvents and have previously been used to extend the absorption via intramolecular interactions. An excellent example of this was reported by Huixia Shang et al. where they incorporated a BT unit into a solution-processable 3-D star-shaped molecule. The incorporation of the BT unit red-shifted the spectrum by 83 nm and facilitated very efficient devices with PCEs greater than 4.0 % [104].

8.8 Appendix

X-ray diffraction measurements were acquired with a Bruker-Nonius KappaCCD area detector placed at a window of a rotating anode. The structure was resolved using direct methods and refined with programs belonging to the SHELXL suite. Hydrogen atoms have been included in the analysis for refinement, but were constrained to the atoms they were bonded. The data has also been corrected for absorption effects with SADABS. There is some positional disorder in two of the alkyle chains (C30, C31 and C63) with occupancy of approximately 70:30% between the major and minor orientations. Data collection and refinement parameters at 120(2) K with MoK_a(λ = 0.71073Å): M = 1414.72, Triclinic, P-1, a = 7.9940(2), b = 18.3520(7), c = 24.8770(8) Å, α = 69.322(2), β = 82.751(2), γ = 86.023(2)°, V = 3385.99(19) Å^3, Z = 2, 53939 measured reflections, 15562 unique reflections (Rint = 0.1466), R = 0.1509, wR = 0.2378. The crystallography data can also be found in the Cambridge Crystallographic Data Centre database, reference number CCDC853611. Information regarding XRD has been reproduced from [5] with permission from John Wiley and Sons.

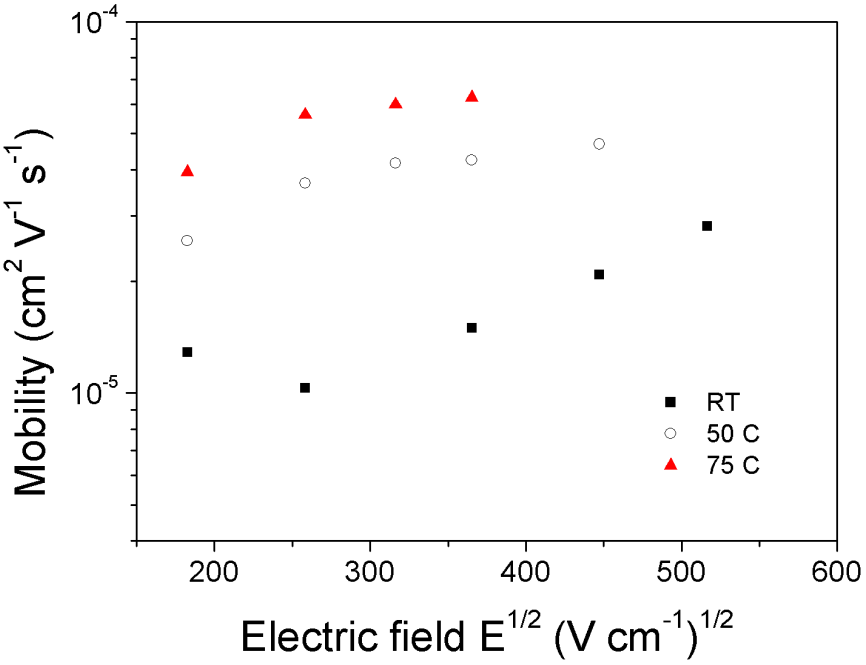

Figure 8.41 *Field dependent hole mobility for Ge-cruciform at RT and after subsequent step annealing measured using time of flight method. Reproduced from Ref. [53] with permission from The Royal Society of Chemistry.*

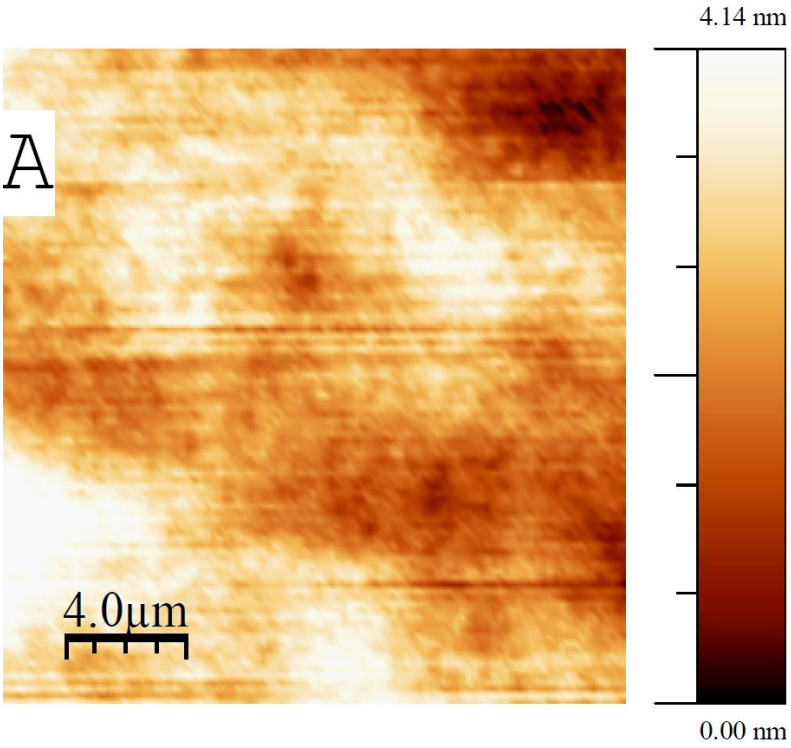
4.14 nm
A
4.0µm
0.00 nm

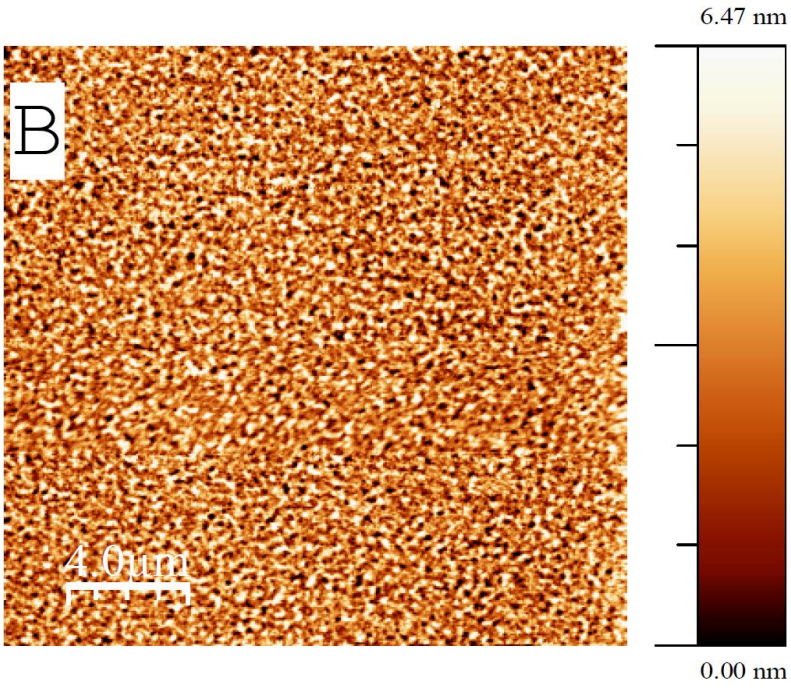
6.47 nm
B
4.0µm
0.00 nm

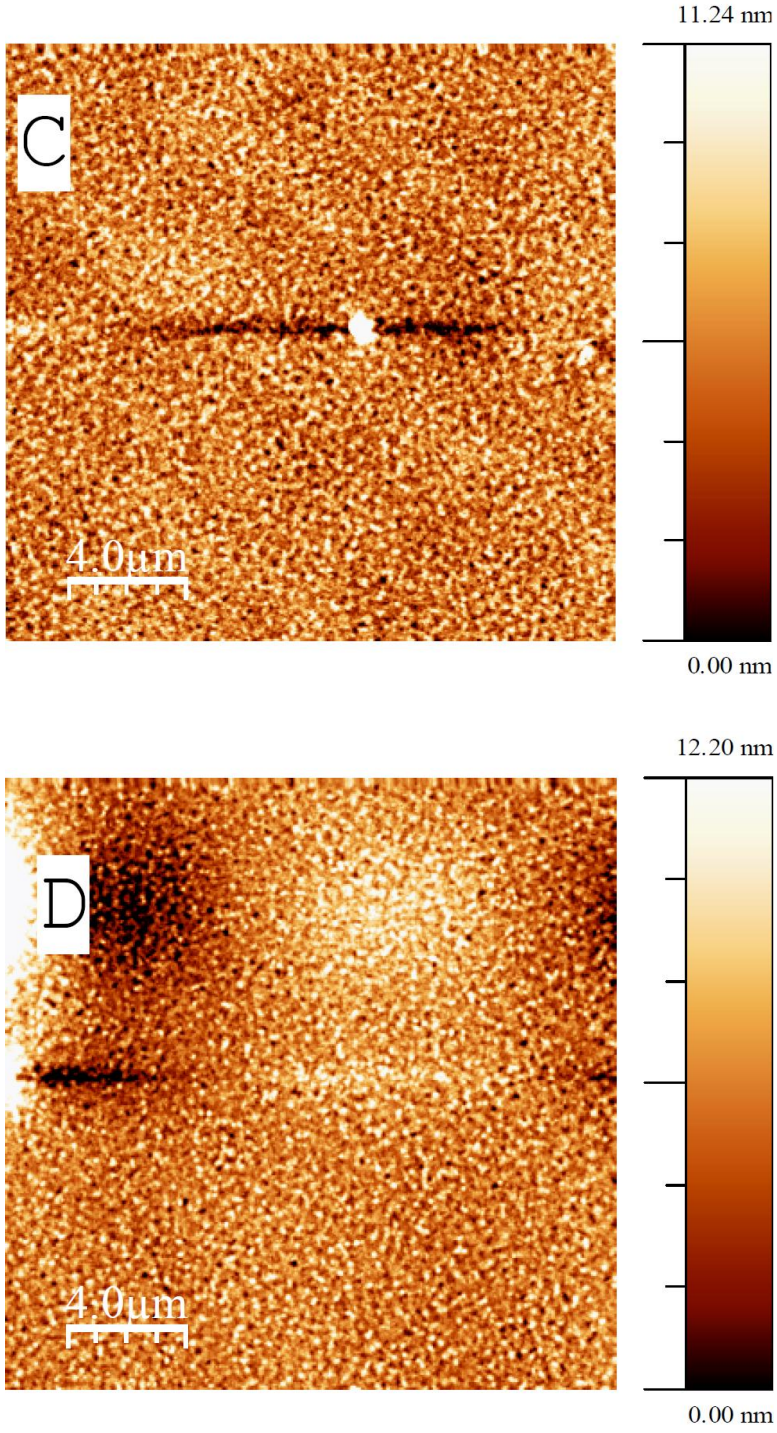

Figure 8.42 *AFM height images of Ge-Cruciform a) un-annealed, b) 50 °C, c) 75 °C, and d) 100 °C. Reproduced from Ref. [53] with permission from The Royal Society of Chemistry.*

Table 8.2 *Performance statistics for* ***7*** *and* ***8****.*

Active layer	Annealing [°C]	Jsc [mA/cm^2]	Voc [V]	FF [%]	PCE [%]
7	N/A	0	0	0	0
7:PC$_{71}$BM (1:1)	N/A	1.27	0.75	24	0.23
7:PC$_{71}$BM (1:1)	120	0.68	0.44	27	0.08
8	N/A	0	0	0	0
8:PC$_{71}$BM (1:1)	N/A	1.56	0.32	28	0.14
8:PC$_{71}$BM (1:1)	120	3.45	0.42	39	0.56
8:PC$_{61}$BM (1:1)	90	2.79	0.24	30	0.2
8:PC$_{61}$BM (1:1)	110	2.97	0.41	43	0.52
8:PC$_{61}$BM (1:1)	130	2.63	0.29	30	0.23
8:PC$_{71}$BM (1:1)	90	2.49	0.28	34	0.24
8:PC$_{71}$BM (1:1)	110	5.08	0.46	37	0.87
8:PC$_{71}$BM (1:1)	130	5.82	0.42	41	1.01
7:PC$_{71}$BM (1:2)	120	1.95	0.62	29	0.35
7:PC$_{71}$BM (1:4)	120	7.48	0.62	33	1.53
7:PC$_{71}$BM (1:6)	120	9.57	0.63	37	2.25
7:PC$_{71}$BM (1:8)	120	7.28	0.28	25	0.5
8:PC$_{71}$BM (1:2)	120	3.36	0.38	38	0.48
8:PC$_{71}$BM (1:4)	120	4.08	0.38	28	0.43
8:PC$_{71}$BM (1:6)	120	8.82	0.51	39	1.76
8:PC$_{71}$BM (1:8)	120	4.18	0.51	34	0.72
7:PC$_{71}$BM (1:6)	120	8.85	0.65	32	1.82
7:PC$_{71}$BM (1:6)	N/A	10.62	0.90	35	3.36
7:PC$_{71}$BM (1:6)	120	11.04	0.86	35	3.35
8:PC$_{71}$BM (1:6)	N/A	7.16	0.38	32	0.87
8:PC$_{71}$BM (1:6)	120	10.27	0.56	37	2.1
7:PC$_{71}$BM (1:6)	N/A	10.61	0.93	34	3.36
8:PC$_{71}$BM (1:6)	130	10.19	0.46	45	2.10

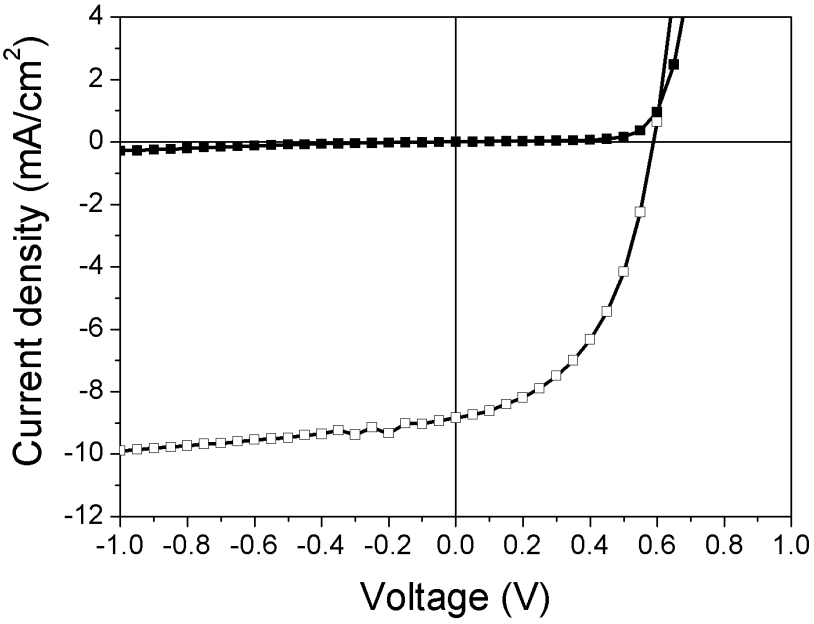

Figure 8.43 *J-V characteristics for a P3HT:$PC_{61}BM$ (1:1) photovoltaic device with a power conversion efficiency (PCE) of 2.53 %, a short-circuit current (Jsc) of 8.84 mA/cm^2, an open-circuit voltage (Voc) of 0.59 V and a fill factor of 48.55 %.*

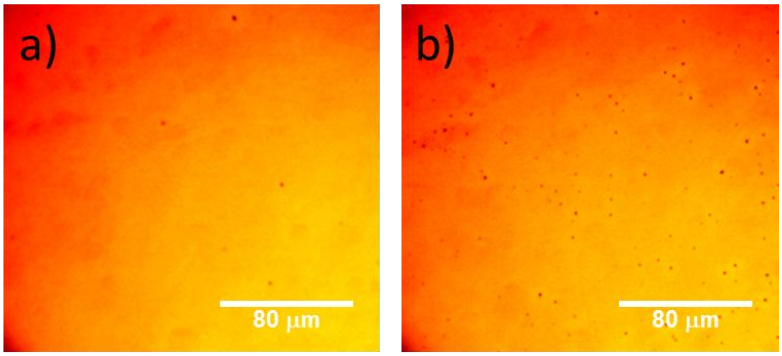

Figure 8.44 *Wide-field of* ***7****:$PC_{71}BM$ (1:6) (left) and* ***8****:$PC_{71}BM$ (1:6) (right).*

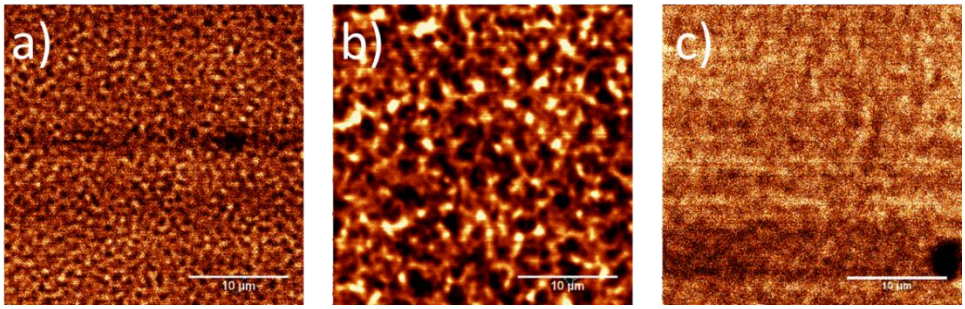

Figure 8.45 *Images obtained from a fluorescence microscope of Ge-cruciform a) not annealed, b) annealed straight to 120 °C for 20 minutes and c) annealed at 50, 75, 100 and 120 °C in 20 minute increments. Images obtained with an excitation wavelength of λ=532 nm.*

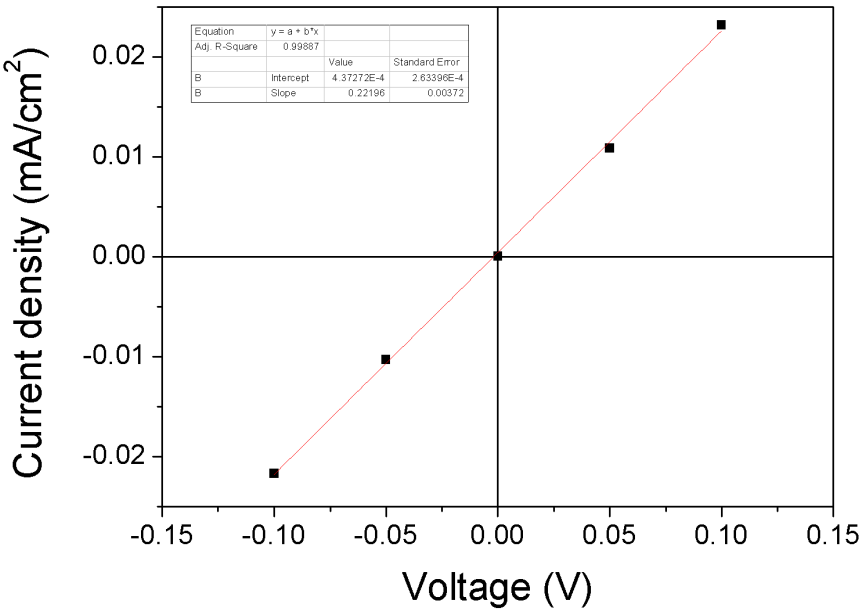

Figure 8.46 *J-V for a 7:$PC_{71}BM$ (1:6) photovoltaic device, dark current for an encapsulated annealed device with a non-Ohmic aluminium top electrode.*

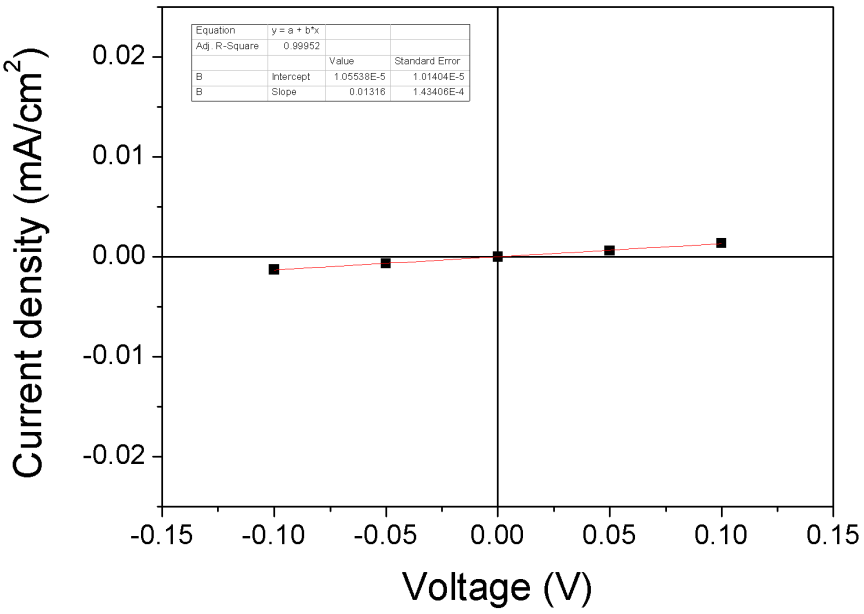

Figure 8.47 *J-V for a 7:$PC_{71}BM$ (1:6) photovoltaic device, dark current for an encapsulated annealed device with an Ohmic calcium/aluminium top electrode.*

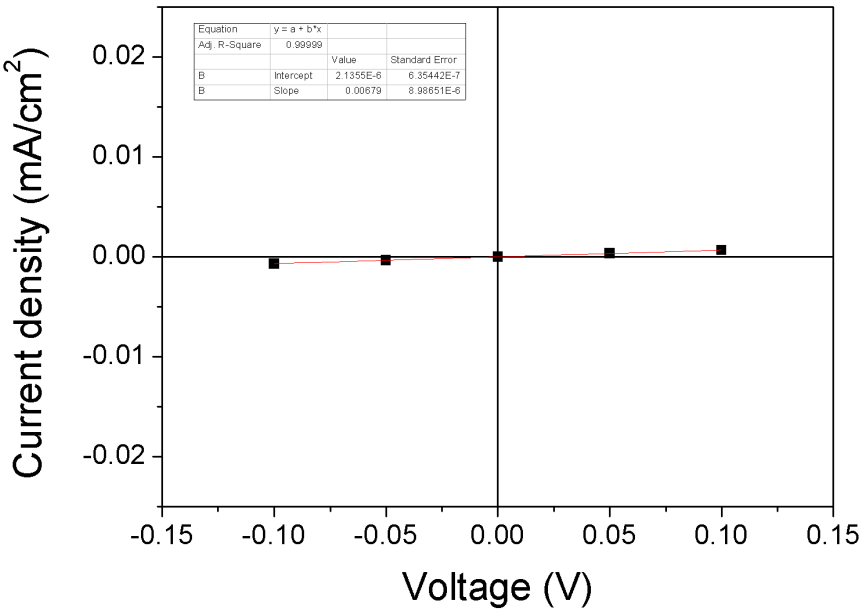

Figure 8.48 *J-V for a 7:$PC_{71}BM$ (1:6) photovoltaic device, dark current for an encapsulated not annealed device with an Ohmic calcium/aluminium top electrode.*

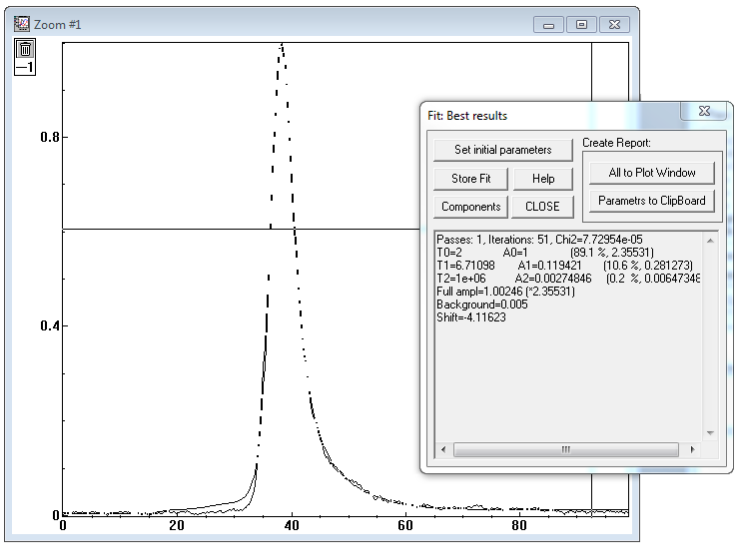

Figure 8.49 *The PL decay of* ***7*** *in film, lifetimes less than* 2 ps (90%), 7 ps (10%).

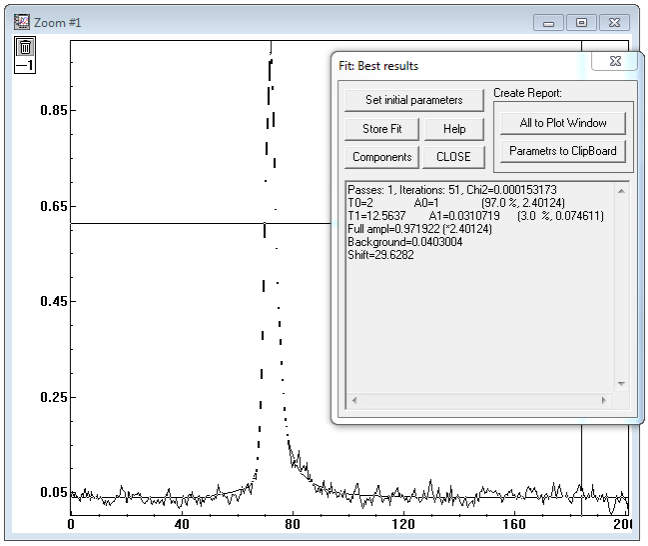

Figure 8.50 *The PL decay of* ***8*** *in film, lifetimes less than* 2 ps (97%), 13 ps (3%).

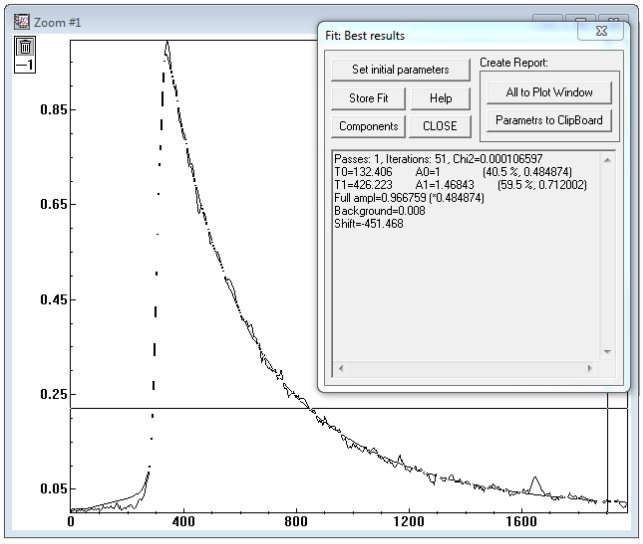

Figure 8.51 *The PL decay of* $PC_{71}BM$ *in film, lifetimes* 130 ps (40%), 430 ps (60%).

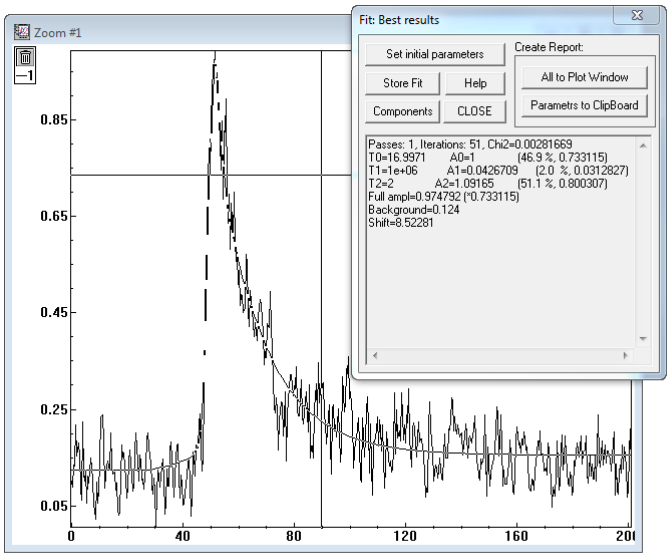

Figure 8.52 *The PL decay of* ***7*** *blend in film, lifetimes less than* 2 ps (51%), 17 ps (47%), long lived greater to or equal than 200 ps (2%).

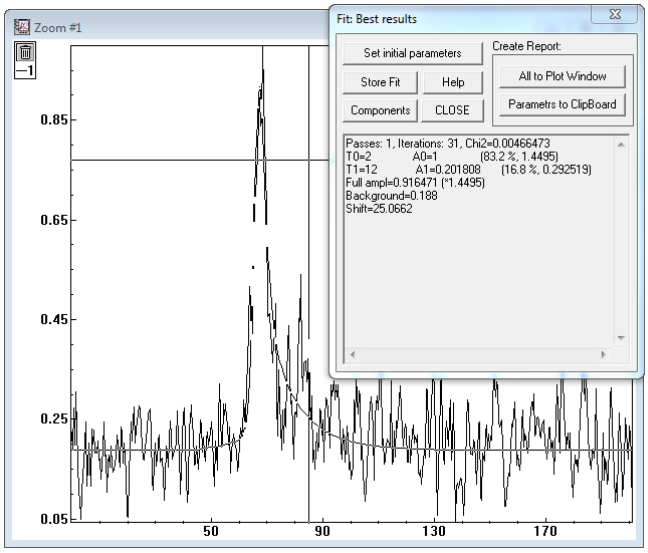

Figure 8.53 *The PL decay of* ***8*** *blend in film, lifetimes less than* 2 ps (83%), 12 ps (17%).

8.9 References

1. Halls, J.J.M., et al., *Efficient photodiodes from interpenetrating polymer networks.* Nature, 1995. **376**(6540): p. 498-500.
2. Yu, G., et al., *POLYMER PHOTOVOLTAIC CELLS - ENHANCED EFFICIENCIES VIA A NETWORK OF INTERNAL DONOR-ACCEPTOR HETEROJUNCTIONS.* Science, 1995. **270**(5243): p. 1789-1791.
3. Ma, C.-Q., et al., *Functionalized 3D Oligothiophene Dendrons and Dendrimers— Novel Macromolecules for Organic Electronics.* Angewandte Chemie International Edition, 2007. **46**(10): p. 1679-1683.
4. He, Z., et al., *Enhanced power-conversion efficiency in polymer solar cells using an inverted device structure.* Nat Photon, 2012. **6**(9): p. 591-595.
5. Wright, I.A., et al., *Oligothiophene Cruciform with a Germanium Spiro Center: A Promising Material for Organic Photovoltaics.* Angewandte Chemie International Edition, 2012. **51**(19): p. 4562-4567.
6. Lloyd, M.T., J.E. Anthony, and G.G. Malliaras, *Photovoltaics from soluble small molecules.* Materials Today, 2007. **10**(11): p. 34-41.
7. Sun, X., et al., *X-Shaped Oligothiophenes as a New Class of Electron Donors for Bulk-Heterojunction Solar Cells.* The Journal of Physical Chemistry B, 2006. **110**(15): p. 7702-7707.
8. Mishra, A. and P. Bäuerle, *Small Molecule Organic Semiconductors on the Move: Promises for Future Solar Energy Technology.* Angewandte Chemie International Edition, 2012. **51**(9): p. 2020-2067.
9. Liu, Y., et al., *Solution-processed small-molecule solar cells: breaking the 10% power conversion efficiency.* Sci. Rep., 2013. **3**.
10. Petritsch, K., et al., *Dye-based donor/acceptor solar cells.* Solar Energy Materials and Solar Cells, 2000. **61**(1): p. 63-72.
11. Schmidt-Mende, L., et al., *Self-Organized Discotic Liquid Crystals for High-Efficiency Organic Photovoltaics.* Science, 2001. **293**(5532): p. 1119-1122.
12. Walker, B., C. Kim, and T.-Q. Nguyen, *Small Molecule Solution-Processed Bulk Heterojunction Solar Cells†.* Chemistry of Materials, 2010. **23**(3): p. 470-482.
13. Roncali, J., et al., *Molecular and supramolecular engineering of π-conjugated systems for photovoltaic conversion.* Thin Solid Films, 2006. **511–512**(0): p. 567-575.
14. Wong, W.W.H., et al., *Self-Assembling Thiophene Dendrimers with a Hexa-peri-hexabenzocoronene Core−Synthesis, Characterization and Performance in Bulk Heterojunction Solar Cells.* Chemistry of Materials, 2009. **22**(2): p. 457-466.
15. He, C., et al., *Improving the efficiency of solution processable organic photovoltaic devices by a star-shaped molecular geometry.* Journal of Materials Chemistry, 2008. **18**(34): p. 4085-4090.
16. Hablot, D., A. Harriman, and R. Ziessel, *Using a Photoacid Generator to Switch the Direction of Electronic Energy Transfer in a Molecular Triad.* Angewandte Chemie International Edition, 2011. **50**(34): p. 7833-7836.
17. Proctor, C.M., et al., *Nongeminate Recombination and Charge Transport Limitations in Diketopyrrolopyrrole-Based Solution-Processed Small Molecule Solar Cells.* Advanced Functional Materials, 2013. **23**(28): p. 3584-3594.
18. Li, W., et al., *Benzothiadiazole-Based Linear and Star Molecules: Design, Synthesis, and Their Application in Bulk Heterojunction Organic Solar Cells.* Chemistry of Materials, 2009. **21**(21): p. 5327-5334.
19. Roncali, J., *Molecular Bulk Heterojunctions: An Emerging Approach to Organic Solar Cells.* Accounts of Chemical Research, 2009. **42**(11): p. 1719-1730.
20. Zhang, J., et al., *Solution-Processable Star-Shaped Photovoltaic Organic Molecule with Triphenylamine Core and Benzothiadiazole−Thiophene Arms.* Macromolecules, 2009. **42**(20): p. 7619-7622.

21. *Heliatek consolidates its technology leadership by establishing a new world record for organic solar technology with a cell efficiency of 12%.* Press release, 2013.
22. Ma, C.-Q., et al., *Solution-Processed Bulk-Heterojunction Solar Cells Based on Monodisperse Dendritic Oligothiophenes.* Advanced Functional Materials, 2008. **18**(20): p. 3323-3331.
23. Roquet, S., et al., *Three-dimensional tetra(oligothienyl)silanes as donor material for organic solar cells.* Journal of Materials Chemistry, 2006. **16**(29): p. 3040-3045.
24. Lincker, F., et al., *Fluorenone-Based Molecules for Bulk-Heterojunction Solar Cells: Synthesis, Characterization, and Photovoltaic Properties.* Advanced Functional Materials, 2008. **18**(21): p. 3444-3453.
25. Tamayo, A.B., et al., *A low band gap, solution processable oligothiophene with a dialkylated diketopyrrolopyrrole chromophore for use in bulk heterojunction solar cells.* Applied Physics Letters, 2009. **94**(10): p. -.
26. Walker, B., et al., *Nanoscale Phase Separation and High Photovoltaic Efficiency in Solution-Processed, Small-Molecule Bulk Heterojunction Solar Cells.* Advanced Functional Materials, 2009. **19**(19): p. 3063-3069.
27. Wei, G., et al., *Efficient, Ordered Bulk Heterojunction Nanocrystalline Solar Cells by Annealing of Ultrathin Squaraine Thin Films.* Nano Letters, 2010. **10**(9): p. 3555-3559.
28. Rousseau, T., et al., *A tailored hybrid BODIPY-oligothiophene donor for molecular bulk heterojunction solar cells with improved performances.* Chemical Communications, 2010. **46**(28): p. 5082-5084.
29. Burckstummer, H., et al., *Tailored merocyanine dyes for solution-processed BHJ solar cells.* Journal of Materials Chemistry, 2010. **20**(2): p. 240-243.
30. Kanibolotsky, A.L., I.F. Perepichka, and P.J. Skabara, *Star-shaped [small pi]-conjugated oligomers and their applications in organic electronics and photonics.* Chemical Society Reviews, 2010. **39**(7): p. 2695-2728.
31. Saragi, T.P.I., T. Fuhrmann-Lieker, and J. Salbeck, *Comparison of Charge-Carrier Transport in Thin Films of Spiro-Linked Compounds and Their Corresponding Parent Compounds.* Advanced Functional Materials, 2006. **16**(7): p. 966-974.
32. Zen, A., et al., *Organic Field-Effect Transistors Utilizing Solution-Deposited Oligothiophene-Based Swivel Cruciforms.* Chemistry of Materials, 2007. **19**(6): p. 1267-1276.
33. Pina, J., et al., *Spectral and Photophysical Studies on Cruciform Oligothiophenes in Solution and the Solid State.* The Journal of Physical Chemistry B, 2006. **110**(31): p. 15100-15106.
34. Dang, M.T., et al., *Controlling the Morphology and Performance of Bulk Heterojunctions in Solar Cells. Lessons Learned from the Benchmark Poly(3-hexylthiophene):[6,6]-Phenyl-C61-butyric Acid Methyl Ester System.* Chemical Reviews, 2013. **113**(5): p. 3734-3765.
35. Collins, B.A., et al., *Absolute Measurement of Domain Composition and Nanoscale Size Distribution Explains Performance in PTB7:PC71BM Solar Cells.* Advanced Energy Materials, 2013. **3**(1): p. 65-74.
36. Moulé, A.J. and K. Meerholz, *Controlling Morphology in Polymer–Fullerene Mixtures.* Advanced Materials, 2008. **20**(2): p. 240-245.
37. Lou, S.J., et al., *Effects of Additives on the Morphology of Solution Phase Aggregates Formed by Active Layer Components of High-Efficiency Organic Solar Cells.* Journal of the American Chemical Society, 2011. **133**(51): p. 20661-20663.
38. Muhammad, F.F. and K. Sulaiman, *Photovoltaic performance of organic solar cells based on DH6T/PCBM thin film active layers.* Thin Solid Films, 2011. **519**(15): p. 5230-5233.
39. Lin, Y., Y. Li, and X. Zhan, *Small molecule semiconductors for high-efficiency organic photovoltaics.* Chemical Society Reviews, 2012. **41**(11): p. 4245-4272.
40. Würthner, F. and K. Meerholz, *Systems Chemistry Approach in Organic Photovoltaics.* Chemistry – A European Journal, 2010. **16**(31): p. 9366-9373.

41. Pang, H., et al., *Advantageous 3D Ordering of π-Conjugated Systems: A New Approach Towards Efficient Charge Transport in any Direction.* Advanced Materials, 2007. **19**(24): p. 4438-4442.
42. Zen, A., et al., *Solution Processable Organic Field-Effect Transistors Utilizing an α,α'-Dihexylpentathiophene-Based Swivel Cruciform.* Journal of the American Chemical Society, 2006. **128**(12): p. 3914-3915.
43. Saragi, T.P.I., et al., *Spiro Compounds for Organic Optoelectronics.* Chemical Reviews, 2007. **107**(4): p. 1011-1065.
44. Schweig, A., et al., *Spiroconjugation.* Angewandte Chemie International Edition in English, 1973. **12**(4): p. 310-311.
45. Payne, D.A. and F.H. Fink, *Electronegativities and group IVA chemistry.* Journal of Chemical Education, 1966. **43**(12): p. 654.
46. Lavayssière, H., G. Dousse, and E.J. Satgé, *Quelques aspects de la chimie des dioxa- et dithia-germoles.* Recueil des Travaux Chimiques des Pays-Bas, 1988. **107**(6): p. 440-448.
47. Meller, A., J. Pfeiffer, and M. Noltemeyer, *Aza- und Thia-2-germa(II)-indane und entsprechende 2,2'-Spirobi(2-germaindane).* Zeitschrift für anorganische und allgemeine Chemie, 1989. **572**(1): p. 145-150.
48. Skabara, P.J., J.-B. Arlin, and Y.H. Geerts, *Close Encounters of the 3D Kind – Exploiting High Dimensionality in Molecular Semiconductors.* Advanced Materials, 2013. **25**(13): p. 1948-1954.
49. Wright, I.A., et al., *Electronic, redox and charge transport properties of an unusual hybrid structure: a bis(septithiophene) bridged by a fused tetrathiafulvalene (TTF).* Journal of Materials Chemistry, 2011. **21**(5): p. 1462-1469.
50. Delannoy, P., et al., *Transient electroluminescence of monolayer and bilayer sexithiophene diodes.* Synthetic Metals, 1994. **67**(1–3): p. 197-200.
51. Binh, N.T., L.Q. Minh, and H. Bässler, *Photoconduction in poly(3-alkylthiophene) II. Charge transport.* Synthetic Metals, 1993. **58**(1): p. 39-50.
52. Mozer, A.J., et al., *Charge carrier mobility in regioregular poly(3-hexylthiophene) probed by transient conductivity techniques: A comparative study.* Physical Review B, 2005. **71**(3): p. 035214.
53. Arumugam, S., et al., *Charge transport in a two-dimensional molecular organic semiconductor.* Journal of Materials Chemistry C, 2014. **2**(1): p. 34-39.
54. Baldwin, R.J., et al., *A comprehensive study of the effect of reactive end groups on the charge carrier transport within polymerized and nonpolymerized liquid crystals.* Journal of Applied Physics, 2007. **101**(2): p. -.
55. Kim, Y., et al., *A strong regioregularity effect in self-organizing conjugated polymer films and high-efficiency polythiophene:fullerene solar cells.* Nat Mater, 2006. **5**(3): p. 197-203.
56. Tan, C.H., et al., *The morphological dependence of charge transport in a soluble luminescent conjugated polymer.* Organic Electronics, 2002. **3**(2): p. 81-88.
57. Snaith, H.J., *The perils of solar cell efficiency measurements.* Nat Photon, 2012. **6**(6): p. 337-340.
58. Ayzner, A.L., et al., *Reappraising the Need for Bulk Heterojunctions in Polymerâ"Fullerene Photovoltaics: The Role of Carrier Transport in All-Solution-Processed P3HT/PCBM Bilayer Solar Cells.* The Journal of Physical Chemistry C, 2009. **113**(46): p. 20050-20060.
59. Cortizo-Lacalle, D., et al., *BODIPY-based conjugated polymers for broadband light sensing and harvesting applications.* Journal of Materials Chemistry, 2012. **22**(28): p. 14119-14126.
60. Sakai, J., et al., *Annealing effect in the sexithiophene:C70 small molecule bulk heterojunction organic photovoltaic cells.* Solar Energy Materials and Solar Cells, 2009. **93**(6–7): p. 1149-1153.

61. Liang, Y., et al., *For the Bright Future - Bulk Heterojunction Polymer Solar Cells with Power Conversion Efficiency of 7.4%.* Advanced Materials. **22**(20): p. E135-E138.
62. He, Z., Zhong, Chengmei, Su, Shijian, Xu, Miao, Wu, Hongbin, Cao, Yong, *Enhanced power-conversion efficiency in polymer solar cells using an inverted device structure.* Nat Photon, 2012(591–595
).
63. Kim, M.-S., B.-G. Kim, and J. Kim, *Effective Variables To Control the Fill Factor of Organic Photovoltaic Cells.* ACS Applied Materials & Interfaces, 2009. **1**(6): p. 1264-1269.
64. Campoy-Quiles, M., et al., *Morphology evolution via self-organization and lateral and vertical diffusion in polymer:fullerene solar cell blends.* Nat Mater, 2008. **7**(2): p. 158-164.
65. Agostinelli, T., et al., *Real-Time Investigation of Crystallization and Phase-Segregation Dynamics in P3HT:PCBM Solar Cells During Thermal Annealing.* Advanced Functional Materials, 2011. **21**(9): p. 1701-1708.
66. Nicolaidis, N.C., et al., *Fullerene Contribution to Photocurrent Generation in Organic Photovoltaic Cells.* The Journal of Physical Chemistry C, 2011. **115**(15): p. 7801-7805.
67. Wu, W.-R., et al., *Competition between Fullerene Aggregation and Poly(3-hexylthiophene) Crystallization upon Annealing of Bulk Heterojunction Solar Cells.* ACS Nano, 2011. **5**(8): p. 6233-6243.
68. Gupta, D., M. Bag, and K.S. Narayan, *Correlating reduced fill factor in polymer solar cells to contact effects.* Applied Physics Letters, 2008. **92**(9): p. -.
69. Hedley, G.J., et al., *Determining the optimum morphology in high-performance polymer-fullerene organic photovoltaic cells.* Nat Commun, 2013. **4**.
70. Shaw, P.E., A. Ruseckas, and I.D.W. Samuel, *Exciton Diffusion Measurements in Poly(3-hexylthiophene).* Advanced Materials, 2008. **20**(18): p. 3516-3520.
71. Luhman, W.A. and R.J. Holmes, *Enhanced exciton diffusion in an organic photovoltaic cell by energy transfer using a phosphorescent sensitizer.* Applied Physics Letters, 2009. **94**(15): p. 153304.
72. Li, G., et al., *High-efficiency solution processable polymer photovoltaic cells by self-organization of polymer blends.* Nat Mater, 2005. **4**(11): p. 864-868.
73. Lu, L. and L. Yu, *Understanding Low Bandgap Polymer PTB7 and Optimizing Polymer Solar Cells Based on It.* Advanced Materials, 2014: p. n/a-n/a.
74. Xie, Y., et al. *Solvent effect on the morphology of P3HT/PCBM films.* 2009.
75. Kim, Y.S., et al., *Effect of solvents on the performance and morphology of polymer photovoltaic devices.* Current Applied Physics. **In Press, Accepted Manuscript**.
76. Ruseckas, A., P.E. Shaw, and I.D.W. Samuel, *Probing the nanoscale phase separation in binary photovoltaic blends of poly(3-hexylthiophene) and methanofullerene by energy transfer.* Dalton Transactions, 2009(45): p. 10040-10043.
77. Machui, F., et al., *Determination of the P3HT:PCBM solubility parameters via a binary solvent gradient method: Impact of solubility on the photovoltaic performance.* Solar Energy Materials and Solar Cells, 2012. **100**(0): p. 138-146.
78. Liang, Y., et al., *For the Bright Future—Bulk Heterojunction Polymer Solar Cells with Power Conversion Efficiency of 7.4%.* Advanced Materials, 2010. **22**(20): p. E135-E138.
79. Poe, A.M., et al., *Small molecule BODIPY dyes as non-fullerene acceptors in bulk heterojunction organic photovoltaics.* Chemical Communications, 2014. **50**(22): p. 2913-2915.
80. Zhao, G., Y. He, and Y. Li, *6.5% Efficiency of Polymer Solar Cells Based on poly(3-hexylthiophene) and Indene-C60 Bisadduct by Device Optimization.* Advanced Materials, 2010. **22**(39): p. 4355-4358.

81. Scharber, M.C., et al., *Design Rules for Donors in Bulk-Heterojunction Solar Cells—Towards 10 % Energy-Conversion Efficiency.* Advanced Materials, 2006. **18**(6): p. 789-794.
82. Kim, J.Y., et al., *Efficient Tandem Polymer Solar Cells Fabricated by All-Solution Processing.* Science, 2007. **317**(5835): p. 222-225.
83. Huang, Y.-C., et al., *Study of the effect of annealing process on the performance of P3HT/PCBM photovoltaic devices using scanning-probe microscopy.* Solar Energy Materials and Solar Cells, 2009. **93**(6–7): p. 888-892.
84. Lin, R., M. Wright, and A. Uddin, *Effects of solvent additive on inverted structure PCPDTBT:PC71BM bulk heterojunction organic solar cells.* physica status solidi (a), 2013: p. n/a-n/a.
85. Mihailetchi, V.D., et al., *Cathode dependence of the open-circuit voltage of polymer:fullerene bulk heterojunction solar cells.* Journal of Applied Physics, 2003. **94**(10): p. 6849-6854.
86. Vandewal, K., et al., *Increased Open-Circuit Voltage of Organic Solar Cells by Reduced Donor-Acceptor Interface Area.* Advanced Materials, 2014. **26**(23): p. 3839-3843.
87. Mihailetchi, V.D., L.J.A. Koster, and P.W.M. Blom, *Effect of metal electrodes on the performance of polymer:fullerene bulk heterojunction solar cells.* Applied Physics Letters, 2004. **85**(6): p. 970-972.
88. Gupta, V., et al., *Barium: An Efficient Cathode Layer for Bulk-heterojunction Solar Cells.* Sci. Rep., 2013. **3**.
89. He, Z., et al., *Simultaneous Enhancement of Open-Circuit Voltage, Short-Circuit Current Density, and Fill Factor in Polymer Solar Cells.* Advanced Materials, 2011. **23**(40): p. 4636-4643.
90. Peumans, P., A. Yakimov, and S.R. Forrest, *Small molecular weight organic thin-film photodetectors and solar cells.* Journal of Applied Physics, 2003. **93**(7): p. 3693-3723.
91. Oh, H., et al., *Comparison of various sol–gel derived metal oxide layers for inverted organic solar cells.* Solar Energy Materials and Solar Cells, 2011. **95**(8): p. 2194-2199.
92. Yang, B., et al., *Solution-Processed Fullerene-Based Organic Schottky Junction Devices for Large-Open-Circuit-Voltage Organic Solar Cells.* Advanced Materials, 2013. **25**(4): p. 572-577.
93. Lampande, R., et al., *A highly efficient transition metal oxide layer for hole extraction and transport in inverted polymer bulk heterojunction solar cells.* Journal of Materials Chemistry A, 2013. **1**(23): p. 6895-6900.
94. Tatsuki, Y., et al., *Flexible PTB7:PC 71 BM bulk heterojunction solar cells with a LiF buffer layer.* Japanese Journal of Applied Physics, 2014. **53**(2S): p. 02BE05.
95. Li, Y., et al., *Evaluation of methods to extract parameters from current–voltage characteristics of solar cells.* Solar Energy, 2013. **90**(0): p. 51-57.
96. Armstrong, N.R., et al., *Oxide Contacts in Organic Photovoltaics: Characterization and Control of Near-Surface Composition in Indiumâ^'Tin Oxide (ITO) Electrodes.* Accounts of Chemical Research, 2009. **42**(11): p. 1748-1757.
97. Bradas, J.-L., et al., *Molecular Understanding of Organic Solar Cells: The Challenges.* Accounts of Chemical Research, 2009. **42**(11): p. 1691-1699.
98. Potscavage, W.J., A. Sharma, and B. Kippelen, *Critical Interfaces in Organic Solar Cells and Their Influence on the Open-Circuit Voltage.* Accounts of Chemical Research, 2009. **42**(11): p. 1758-1767.
99. Shrotriya, V., et al., *Accurate Measurement and Characterization of Organic Solar Cells.* Advanced Functional Materials, 2006. **16**(15): p. 2016-2023.
100. Tremolet de Villers, B., et al., *Improving the Reproducibility of P3HT:PCBM Solar Cells by Controlling the PCBM/Cathode Interface.* The Journal of Physical Chemistry C, 2009. **113**(44): p. 18978-18982.
101. Ameri, T., et al., *Performance Enhancement of the P3HT/PCBM Solar Cells through NIR Sensitization Using a Small-Bandgap Polymer.* Advanced Energy Materials, 2012. **2**(10): p. 1198-1202.

102. Wei, G., et al., *Solvent-Annealed Crystalline Squaraine: PC70BM (1:6) Solar Cells.* Advanced Energy Materials, 2011. **1**(2): p. 184-187.
103. Kirkpatrick, J., et al., *Ultrafast Transient Optical Studies of Charge Pair Generation and Recombination in Poly-3-Hexylthiophene(P3ht):[6,6]Phenyl C61 Butyric Methyl Acid Ester (PCBM) Blend Films.* The Journal of Physical Chemistry B, 2011. **115**(51): p. 15174-15180.
104. Shang, H., et al., *A Solution-Processable Star-Shaped Molecule for High-Performance Organic Solar Cells.* Advanced Materials, 2011. **23**(13): p. 1554-1557.
105. Shaw, P.E., A. Ruseckas, and I.D.W. Samuel, *Distance dependence of excitation energy transfer between spacer-separated conjugated polymer films.* Physical Review B (Condensed Matter and Materials Physics), 2008. **78**(24): p. 245201.
106. Hedley, G.J., A. Ruseckas, and I.D.W. Samuel, *Ultrafast Intersystem Crossing in a Red Phosphorescent Iridium Complex.* The Journal of Physical Chemistry A, 2008. **113**(1): p. 2-4.
107. Lim, N., et al., *High-Performance Organic Solar Cells with Efficient Semiconducting Small Molecules Containing an Electron-Rich Benzodithiophene Derivative.* Chemistry of Materials, 2014. **26**(7): p. 2283-2288.
108. Lloyd, M.T., et al., *Photovoltaic cells from a soluble pentacene derivative.* Organic Electronics, 2006. **7**(5): p. 243-248.
109. Heliatek, *Heliatek reaches efficiency record with 40 % transparent organic solar cells.* Press release, 2014.

Chapter 9

Conclusion

The greatest threat to humanity is its dependence on fossil fuels. One only needs to think of the humanitarian crisis that would develop if we were no longer able to burn fossil fuels. Humanity's strive for economic and technological gain has inadvertently resulted in a culture of mass consumerism and an unquenchable desire for more. As scientists, it is our duty to inform the public and governments of the world of the grave consequences that would result if we do not soon take affirmative action.

To ensure low food prices, access to clean water, wild-life preservation, disease prevention, economic growth, political stability and to slow down climate change, it is absolutely imperative that renewable technologies are developed. In 2012, the United States Census Bureau (USCB) estimated the world's human population to have exceeded 7 billion [1]. As the human population continues to grow, so too does our demand for resources. This demand, a consequence of such a large human population and a growing energy demand per capita, is putting significant commercial pressure on land-use and energy [2]. There are currently 2.7 billion living without the means to cook a healthy meal [2] and 1.3 billion without access to electricity [3], which is, frankly, unacceptable. Unfortunately, governments have only recently started to pave the way for reform, lacking the initiative and intellect in understanding the importance of implementing preventative measures. This results in governments to date only taking retrospective action, evident on the topic of climate change [4, 5], for example. With the demand for energy expected to grow by one-third by 2035 [3], double by the mid-century and treble at the turn of the next [6], the opportunity to intervene before major irreversible environmental alterations occur is reducing.

Renewable energy can help us meet the global demand for energy and reduce our dependency on fossil fuels. Decreasing our need to burn fossil fuels will help us reduce the emission of harmful pollutants, resulting in a positive impact on health and the environment. Renewable technologies have the capability of harnessing energy from our natural environment. A plethora of technologies have been developed. These include hydroelectricity, bio-energy, wind energy, geothermal energy, solar thermal energy and photovoltaic energy.

This thesis focused on the topic of photovoltaics, a promising renewable technology. A photovoltaic is an optoelectronic device that converts sunlight into electricity. The sun is the most abundant source of energy and delivers

more energy to the Earth in one hour than all the energy consumed in a year [6]. However, the cost of implementing the technology to harness this energy on a large scale is too expensive. Hence, photovoltaic technologies account for less than 0.1 % of energy production [7]. Therefore, there is a significant interest amongst the research community to achieve photovoltaic conversion with novel materials that are low cost in their manufacture and require limited infrastructure to implement [6]. Organic semiconductors are but one promising possibility [8, 9], and have been demonstrated in a wide variety of device applications including: photovoltaics (OPVs) [10], photodiodes [11], light-emitting diodes (OLEDs) [12], field-effect transistors (OFETs) [13, 14] and optically pumped tuneable lasers [15]. The possibility of being able to fabricate flexible, low-cost, light-weight devices from solution, with materials that have a readily tuneable band-gap, makes organic semiconductors attractive for photovoltaic applications [16]. The light weight, low cost and flexible nature of organic semiconductors has already resulted in their use as efficient low-glare OLED displays in portable devices [17].

The first research chapter of my Thesis was Chapter 5. In this chapter, I discussed the importance of controlling bulk-heterojunction morphology for efficient organic photovoltaics (OPVs), illustrated with PTB7-based polymer OPVs [18]. On determining the optimal bulk-heterojunction morphology, OPVs were optimised by altering the anode interlayer. This was achieved by doping poly(3,4-ethylenedioxylenethiophene):poly(styrenesulfonate)(PEDOT:PSS) with a sulfonic acid surfactant molecule or a sulfonic ionomer fluorinated polymer, perfluoroctaneessulfonic (PFOS) acid or perfluorinated ionomer (PFI), respectively.

Through doping of the anode interlayer it was possible to achieve OPVs with EQEs and PCEs that are amongst the highest reported with a conventional OPV device structure, containing a PEDOT:PSS anode and a calcium/aluminium cathode [19, 20]. In the best case scenario, when doped with PFOS, the PCE increased from 7.18 % to 8.26 %, a percentage increase of ~ 15 %. Here, the observed increase in PCE was a result of an increase in the open-circuit voltage (Voc), fill factor (FF) and short-circuit current density (Jsc). We observed an increase in the PCE with the PFI doped PEDOT:PSS. However, this improvement was a direct result of an increase in the Jsc. For PFOS or PFI doped PEDOT:PSS the increase in Jsc was from 15.94 mA cm^{-2} to 16.94 mA cm^{-2} or 16.89 mA cm^{-2}, respectively.

P3HT:$PC_{61}BM$ OPVs were fabricated with doped PEDOT:PSS interlayers. On increasing the concentration of PFI within the PEDOT:PSS, we observed PCEs of 1.49, 1.50, 2.39 and 2.96 % for concentrations

(PEDOT:PSS:PFI) of (1:6:1), (1:6:2.5), (1:6:13.4) and (1:6:30), respectively. Whilst, for those OPVs that had the PEDOT:PSS doped with PFOS, we observed PCEs of 2.59, 2.79, 2.84 and 2.91 %, respectively. For OPVs where the PEDOT:PSS interlayer was doped with PFI, at concentrations of 1:6:1 and 1:6:2.5, we observed an s-kink in the J-V characteristics, this was responsible for fill factors of ~ 30 % and ~ 28 %, respectively, compared to fill factors of > 47 %. These fill factors are responsible for the low PCEs attained at these PFI concentrations. The s-kink in the J-V characteristics is usually the result of one or more of the following: presence of interface dipoles [21], imbalance of charge carrier mobilities [22], and resistance of the interfacial layer [23-28].

At a concentration of 1:6:30 with PFI, we observed a Jsc, Voc and fill factor of 8.85 mA cm^{-2}, 0.618 V and 54.01 %, respectively, resulting in a PCE of 2.96 %. At the same concentration for PFOS, we obtained a Jsc of 8.63 mA cm^{-2}, Voc of 0.633 V and fill factor of 53.28 %, resulting in a PCE of 2.91 %. The reference OPV had a Jsc of 8.84 mA cm^{-2}, Voc of 0.589 V and fill factor of 48.55 %, resulting in a PCE of 2.53 %. Therefore, by doping PEDOT:PSS with PFI or PFOS it is possible to improve the PCE of P3HT:PC_{61}BM OPVs by ~ 15 %.

In order to understand why we observe an s-kink in the J-V characteristics for OPVs with certain concentrations of PFI doping, conductivity measurements were carried out. Unfortunately, the conductivity measurements were determined to be unreliable, as increases in conductivity were found to be concomitant with changes in the relative humidity (RH). On the other hand, this shows that organic semiconductors can also be used as humidity sensors [29]. For reliable conductivity measurements samples were prepared and sent to our collaborators. In addition, to the conductivity measurements they performed work function measurements.

The original proposition was to improve the Ohmic contact at the anode interface by means of altering the PEDOT:PSS interlayer work function through doping. There have been several reports on doping PEDOT:PSS with PFI for applications in organic optoelectronics. These reports focus on improving charge injection and electrode stability in OLEDs [30-32]. In these reports, they show the alteration of the PEDOT:PSS work function by means of doping. However, none of these are on the topic of organic photovoltaics, and to the best of my knowledge there have been no reports on the use of PFOS in the field of organic optoelectronics.

The work function values received from our collaborators are consistent with previous reports concerning PFI [30-32]. From Kelvin probe force microscopy (KPFM) we observed nanoscopic work functions 4.7, 5.4 and 4.9 eV

for un-doped, PFI doped and PFOS doped PEDOT:PSS, respectively. Whilst, the microscopic work functions showed 5.2, 5.72 and 5.56 eV, respectively. The values obtained via UPS were 5.19, 7.37 and 7.09 eV for the un-doped, PFI doped and PFOS doped PEDOT:PSS, respectively.

Unfortunately, the conductivity measurements were only measured at the optimal device concentration of 1:6:30. Hence we were unable to shed light on the s-kink. However, poor rectification was observed at these PFI concentrations. As the concentration of PFI is increased the poor rectification disappears. It is possible that the s-kink is concomitant with an increase in the conductivity, and as we move to larger concentrations of PFI the conductivity decreases. The conductivity of films containing PFI or PFOS was less than that measured for un-doped PEDOT:PSS.

The near-field microscopy measurements showed little change in film morphology on doping. However, contact angle measurements revealed a dramatic change in the wettability. This was evident in the deposition of the doped PEDOT:PSS and the active layer. Although, we observed a similar increase in PCE of 15 % with the P3HT:PC_{61}BM devices. It is difficult to be absolutely sure what process or combinations of processes are facilitating in these efficient devices. For PTB7:PC_{71}BM and P3HT:PC_{61}BM OPVs, at the optimal doping concentration we observed a reduced dark current. On illumination we observed an improved Jsc for all the optimal devices containing a doping agent. However, it is only with the P3HT:PC_{61}BM OPVs, where we observed an increase in Voc with doping. This combined with the fact that we observe an increase in the EQE with no change in the overall shape, leads me to think, that in this case, we are enhancing device performance by improving the Ohmic contact. This is consistent with previous observations [33, 34]. However, for the PTB7:PC_{71}BM OPVs we observed a non-uniform increase in the EQE, which results in a considerable change in the shape of the EQE spectra on doping. Therefore, the enhanced efficiency is more likely to be a result of increased contact selectivity brought about by the different wettability, evidenced by the change in contact angle, absorption and EQE. Reports on PFI doped PEDOT:PSS showed that by doping the PEDOT:SS interlayer it is possible to improve the performance and stability of OLEDs [32]. Hence, degradation studies were carried out with P3HT:PC_{61}BM OPVs. Our observations were consistent with those on OLEDs, and highlights the importance of using doped PEDOT:PSS. Alternatively, degradation can be slowed down through encapsulation or replacing the PEDOT:PSS interlayer with Molybdenum trioxide MoO_3 [19, 35-39].

The electrochemical, photophysical and optoelectronic properties of four solution-processable BODIPY derivatives were reported and discussed in Chapter 6 and 7.

In Chapter 6, two low band-gap BODIPY-based conjugated polymers, p(BDP-bisEDOT) and p(BDP-bisEDTT) were introduced and shown to have properties favourable for optoelectronics. The performance of photovoltaic cells consisting solely of p(BDP-bisEDOT) or p(BDP-bisEDTT) as the active component, surpassed the typical performance expected of an organic photovoltaic cell without an acceptor, indicating ambipolar behaviour, which was verified with time of flight (TOF) mobility measurements. The performance of the photovoltaic cells dramatically increased with the addition of a fullerene acceptor, $PC_{71}BM$. The polymer-fullerene devices demonstrated a Jsc similar to that of P3HT:$PC_{61}BM$. However, lower PCEs were observed as the Voc was half that of P3HT:$PC_{61}BM$. The lower Voc was a result of the gap between the HOMO of the donor and the LUMO of the acceptor being shorter than that for P3HT:$PC_{61}BM$. The polymer-fullerene devices were demonstrated for broadband sensing and solar energy harvesting [16].

In Chapter 7, two small molecules containing DPP and BODIPY were introduced. The small molecules were fully characterised and their photovoltaic properties investigated. The addition of two thiophenes red-shifted the absorption spectra, however, it did not improve device performance, instead, resulted in further aggregation, which limited the device efficiency.

I concluded that to further device performance, it is necessary to optimise the chemical structures of these BODIPY derivatives shown in Chapter 6 and 7, to improve their solubility and energy levels. This ensures the maximum number of excitons formed in the active layer can diffuse to the donor-acceptor interface within the exciton diffusion length for free charge generation and that these free charges can travel to the Ohmic contacts for collection.

In chapter 8, I introduced a solution-processable small molecule with a germanium spiro centre and an interesting packing motif. I discussed the molecular, electrochemical and optical properties of the material. In addition, a similar small molecule with an extended conjugation length was discussed. The packing motif was shown to be favourable for charge transport by comparing the time of flight (TOF) mobility measurements with several other compounds. The mobility measurements shown are an order of magnitude higher than that reported for sexithiophene [40] and the same order of magnitude as the well-studied conjugated polymer P3HT [41, 42].

The two-dimensional charge transporting nature of the material was verified with two independent techniques, time of flight (TOF) and organic field-effect transistor (OFET) measurements by measuring the charge carrier mobility perpendicular and parallel to the substrate, respectively. The mobility of the organic semiconducting material was shown to varying with annealing. The change, with annealing was believed to be concomitant with morphological changes. The morphology was studied with optical, electron and scanning probe microscopies, and shown to alter on annealing. Hence, by controlling the morphology with the implementation of a well-defined annealing method it was possible to improve the device performance. This improvement in device performance was demonstrated with OFETs and planar-heterojunction OPVs [43]. Solution-processable bulk-heterojunction organic solar cells were fabricated, characterised and optimised with the germanium spiro centred small molecule and the slightly modified version of the material with the longer conjugation length. Optimal devices were achieved with a donor acceptor ratio of 1:6. $PC_{71}BM$ was determined to be the appropriate acceptor. The dark-current J-V characteristics showed poor rectification. To prevent poor rectification, a metal with a low work function, calcium, was deposited before deposition of the aluminium electrode. In doing so, an Ohmic (non-rectifying) contact was achieved. The bulk-heterojunction OPVs fabricated with the original small molecule showed similar PCEs with and without annealing. However, in order to achieve efficient devices with the small molecule with the extended conjugation length, it was necessary to anneal the devices to 130 ^{o}C for 20 minutes. The optimal PCEs obtained with the original molecule were similar to those achieved with P3HT:$PC_{61}BM$ of 2.66 %. However, to achieve efficient OPVs with P3HT:$PC_{61}BM$ it is necessary to carry out post deposition thermal annealing [44-46]. Unfortunately, extending the conjugation length of the original small molecule resulted in poor solubility and an insufficient bathochromic shift to enhance the absorption. Hence, the PCE for the optimal OPV fabricated with the small molecule with extended conjugation length was determined to be 1.60 %. However, the dramatically different morphological changes observed in blends containing the small molecule with the extended conjugation length were extremely interesting for example, the observation of increasing Voc with increasing annealing temperature. The solution-processable oligothiophene small molecule containing a germanium spiro centre is a promising photovoltaic material [47]. The packing motif facilitates charge transport, making it an interesting organic optoelectronic semiconducting material. In future studies, it may be worth including benzothiadiazole (BT)

units in an attempt to improve absorption of the solar spectrum, as extending the conjugation length has been shown to be ineffective.

The field of organic photovoltaics is an exciting and fast moving field. In less than two decades we have seen a percentage increase of > 1000 % in power conversion efficiency (PCE) [48, 49]. However, there are many challenges including: degradation, batch to batch variations with conjugated polymers and the search for new interlayers, transparent electrodes and solution-processable small molecules.

To the best of my ability, I have tried to elucidate the current challenges we face in the field of organic photovoltaics and my contribution to the field. I am very grateful to all those who have helped me and in doing so facilitated this body of work. I think if anything, the field of organic solar cells is an excellent example of how science should happen, through the sharing of ideas and equipment by means of collaborations with different institutions and departments. I am extremely grateful to Professor Peter Skabara at the University of Strathclyde and his group for synthesising many of the organic semiconductors presented in this Thesis.

9.1 References

1. USCB, *U.S. and World Population Clock.* http://www.census.gov/popclock/ 2010 Census data and the most recent national population estimates.
2. Howells, M., et al., *Integrated analysis of climate change, land-use, energy and water strategies.* Nature Clim. Change, 2013. **3**(7): p. 621-626.
3. Agency, I.E., *World Energy Outlook.* IEA, 2011.
4. Luthi, D., et al., *High-resolution carbon dioxide concentration record 650,000-800,000[thinsp]years before present.* Nature, 2008. **453**(7193): p. 379-382.
5. Academies, J.S., *Statement: Global response to climate change.* 2001, 2005, 2007, 2008 and 2009.
6. Lewis, N.S., et al., *Basic Research Needs for Solar Energy Utilization. Report of the Basic Energy Sciences Workshop on Solar Energy Utilization, April 18-21, 2005*, 2005. p. Medium: ED.
7. BERNÈDE, J.C., *ORGANIC PHOTOVOLTAIC CELLS: HISTORY, PRINCIPLE AND TECHNIQUES.* Journal of the Chilean Chemical Society, 2008. **53**: p. 1549-1564.
8. Yu, G., et al., *POLYMER PHOTOVOLTAIC CELLS - ENHANCED EFFICIENCIES VIA A NETWORK OF INTERNAL DONOR-ACCEPTOR HETEROJUNCTIONS.* Science, 1995. **270**(5243): p. 1789-1791.
9. Halls, J.J.M., et al., *Efficient photodiodes from interpenetrating polymer networks.* Nature, 1995. **376**(6540): p. 498-500.
10. Tang, C.W., *Two-layer organic photovoltaic cell.* Applied Physics Letters, 1986. **48**(2): p. 183-185.
11. Harrison, M.G., J. Grüner, and G.C.W. Spencer, *Analysis of the photocurrent action spectra of MEH-PPV polymer photodiodes.* Physical Review B, 1997. **55**(12): p. 7831.
12. Friend, R.H., et al., *Electroluminescence in conjugated polymers.* Nature, 1999. **397**(6715): p. 121-128.
13. Garnier, F., et al., *All-Polymer Field-Effect Transistor Realized by Printing Techniques.* Science, 1994. **265**(5179): p. 1684-1686.
14. Dimitrakopoulos, C.D. and P.R.L. Malenfant, *Organic Thin Film Transistors for Large Area Electronics.* Advanced Materials, 2002. **14**(2): p. 99-117.
15. Ribierre, J.C., et al., *Amplified spontaneous emission and lasing properties of bisfluorene-cored dendrimers.* Applied Physics Letters, 2007. **91**(8): p. -.
16. Cortizo-Lacalle, D., et al., *BODIPY-based conjugated polymers for broadband light sensing and harvesting applications.* Journal of Materials Chemistry, 2012. **22**(28): p. 14119-14126.
17. Forrest, S.R., *The path to ubiquitous and low-cost organic electronic appliances on plastic.* Nature, 2004. **428**(6986): p. 911-918.
18. Hedley, G.J., et al., *Determining the optimum morphology in high-performance polymer-fullerene organic photovoltaic cells.* Nat Commun, 2013. **4**.
19. He, Z., Zhong, Chengmei, Su, Shijian, Xu, Miao, Wu, Hongbin, Cao, Yong, *Enhanced power-conversion efficiency in polymer solar cells using an inverted device structure.* Nat Photon, 2012(591–595
).
20. Gu, C., et al., *Achieving High Efficiency of PTB7-Based Polymer Solar Cells via Integrated Optimization of Both Anode and Cathode Interlayers.* Advanced Energy Materials, 2014. **4**(8): p. n/a-n/a.
21. Kumar, A., S. Sista, and Y. Yang, *Dipole induced anomalous S-shape I-V curves in polymer solar cells.* Journal of Applied Physics, 2009. **105**(9): p. -.
22. Tress, W., et al., *Imbalanced mobilities causing S-shaped IV curves in planar heterojunction organic solar cells.* Applied Physics Letters, 2011. **98**(6): p. -.

23. Wagner, J., et al., *Identification of different origins for s-shaped current voltage characteristics in planar heterojunction organic solar cells.* Journal of Applied Physics, 2012. **111**(5): p. -.
24. Pivrikas, A., et al., *A review of charge transport and recombination in polymer/fullerene organic solar cells.* Progress in Photovoltaics: Research and Applications, 2007. **15**(8): p. 677-696.
25. Tress, W., K. Leo, and M. Riede, *Influence of Hole-Transport Layers and Donor Materials on Open-Circuit Voltage and Shape of I–V Curves of Organic Solar Cells.* Advanced Functional Materials, 2011. **21**(11): p. 2140-2149.
26. Zhou, Y., et al., *Inverted organic solar cells with ITO electrodes modified with an ultrathin Al2O3 buffer layer deposited by atomic layer deposition.* Journal of Materials Chemistry, 2010. **20**(29): p. 6189-6194.
27. Saive, R., et al., *Understanding S-shaped current-voltage characteristics of organic solar cells: Direct measurement of potential distributions by scanning Kelvin probe.* Applied Physics Letters, 2013. **103**(24): p. -.
28. Wagenpfahl, A., et al., *S-shaped current-voltage characteristics of organic solar devices.* Physical Review B, 2010. **82**(11): p. 115306.
29. Jaruwongrungsee, K., et al. *High-sensitivity humidity sensor utilizing PEDOT/PSS printed quartz crystal microbalance*. in *Electrical Engineering/Electronics, Computer, Telecommunications and Information Technology (ECTI-CON), 2011 8th International Conference on*. 2011.
30. Park, J.K., et al., *Solution-processed electrophosphorescent devices with a thin fluoropolymer at the hole transport interfacial layer.* Journal of Information Display, 2011. **12**(4): p. 223-227.
31. Lee, T.W., et al., *Self-Organized Gradient Hole Injection to Improve the Performance of Polymer Electroluminescent Devices.* Advanced Functional Materials, 2007. **17**(3): p. 390-396.
32. Lee, T.-W., et al., *Hole-injecting conducting-polymer compositions for highly efficient and stable organic light-emitting diodes.* Applied Physics Letters, 2005. **87**(23): p. -.
33. Mihailetchi, V.D., L.J.A. Koster, and P.W.M. Blom, *Effect of metal electrodes on the performance of polymer:fullerene bulk heterojunction solar cells.* Applied Physics Letters, 2004. **85**(6): p. 970-972.
34. Mihailetchi, V.D., et al., *Cathode dependence of the open-circuit voltage of polymer:fullerene bulk heterojunction solar cells.* Journal of Applied Physics, 2003. **94**(10): p. 6849-6854.
35. Lampande, R., et al., *A highly efficient transition metal oxide layer for hole extraction and transport in inverted polymer bulk heterojunction solar cells.* Journal of Materials Chemistry A, 2013. **1**(23): p. 6895-6900.
36. Mayuko, K., et al., *Efficient Organic Photovoltaic Cells Using MoO 3 Hole-Transporting Layers Prepared by Simple Spin-Cast of Its Dispersion Solution in Methanol.* Japanese Journal of Applied Physics, 2013. **52**(2R): p. 020202.
37. Murase, S. and Y. Yang, *Solution Processed MoO3 Interfacial Layer for Organic Photovoltaics Prepared by a Facile Synthesis Method.* Advanced Materials, 2012. **24**(18): p. 2459-2462.
38. Hori, T., et al., *MoO3 buffer layer effect on photovoltaic properties of interpenetrating heterojunction type organic solar cells.* Thin Solid Films, 2009. **518**(2): p. 522-525.
39. Cattin, L., et al., *MoO3 surface passivation of the transparent anode in organic solar cells using ultrathin films.* Journal of Applied Physics, 2009. **105**(3): p. -.
40. Delannoy, P., et al., *Transient electroluminescence of monolayer and bilayer sexithiophene diodes.* Synthetic Metals, 1994. **67**(1–3): p. 197-200.
41. Mozer, A.J., et al., *Charge carrier mobility in regioregular poly(3-hexylthiophene) probed by transient conductivity techniques: A comparative study.* Physical Review B, 2005. **71**(3): p. 035214.
42. Binh, N.T., L.Q. Minh, and H. Bässler, *Photoconduction in poly(3-alkylthiophene) II. Charge transport.* Synthetic Metals, 1993. **58**(1): p. 39-50.

43. Arumugam, S., et al., *Charge transport in a two-dimensional molecular organic semiconductor.* Journal of Materials Chemistry C, 2014. **2**(1): p. 34-39.
44. Huang, Y.-C., et al., *Study of the effect of annealing process on the performance of P3HT/PCBM photovoltaic devices using scanning-probe microscopy.* Solar Energy Materials and Solar Cells, 2009. **93**(6–7): p. 888-892.
45. Kim, Y.S., et al., *Effect of solvents on the performance and morphology of polymer photovoltaic devices.* Current Applied Physics. **In Press, Accepted Manuscript**.
46. Agostinelli, T., et al., *Real-Time Investigation of Crystallization and Phase-Segregation Dynamics in P3HT:PCBM Solar Cells During Thermal Annealing.* Advanced Functional Materials, 2011. **21**(9): p. 1701-1708.
47. Wright, I.A., et al., *Oligothiophene Cruciform with a Germanium Spiro Center: A Promising Material for Organic Photovoltaics.* Angewandte Chemie International Edition, 2012. **51**(19): p. 4562-4567.
48. Heliatek, *Heliatek reaches efficiency record with 40 % transparent organic solar cells.* Press release, 2014.
49. *Heliatek consolidates its technology leadership by establishing a new world record for organic solar technology with a cell efficiency of 12%.* Press release, 2013.